Ambient Noise Interferometry and Surface-Wave Array Tomography in Southeastern Tibet

by

Huajian Yao

M.S. Geophysics, University of Science and Technology of China, Hefei, China, 2004
B.S. Geophysics, University of Science and Technology of China, Hefei, China, 2001

Submitted to the Department of Earth, Atmospheric, and Planetary Sciences
in partial fulfillment of the requirements for the degree of

Doctor of Philosophy

at the

MASSACHUSETTS INSTITUTE OF TECHNOLOGY

June 2009

Author:.....
Department of Earth, Atmospheric, and Planetary Sciences
May 22, 2009

Certified by:.....
Robert D. van der Hilst
Cecil and Ida Green Professor of Earth Sciences
Thesis Supervisor

Accepted by:.....
Maria T. Zuber
E. A. Griswold Professor of Geophysics
Head, Department of Earth, Atmospheric, and Planetary Sciences

Ambient Noise Interferometry and Surface-Wave Array Tomography in Southeastern Tibet

by

Huajian Yao

Submitted to the Department of Earth, Atmospheric, and Planetary Sciences
on May 22, 2009 in partial fulfillment of the requirements for the Degree of
Doctor of Philosophy in Geophysics

Abstract

The primary goal of my doctoral research is to understand the crustal and upper mantle structure and deformation in southeastern Tibet. To improve the resolution in the crust, we developed a new approach for surface-wave array tomography by combining inter-station phase velocity dispersion measurements from empirical Green's functions (EGFs) recovered from ambient noise interferometry and from traditional teleseismic surface-wave two-station (TS) analysis. The non-stationarity (e.g., seasonal changes) and non-uniform distribution of ambient noise sources may obstruct full reconstruction of the surface-wave Green's functions, which may, in turn, degrade the accuracy of the tomographic models. Under the assumption of plane-wave propagation, we developed an iterative method to estimate ambient noise energy distribution, phase velocity bias primarily due to uneven noise energy distribution, and azimuthally anisotropic phase velocity maps. With phase velocity dispersion measurements at periods 10 – 150 s from 1 year data of 75 broad band stations in SE Tibet, we performed inversion for wavespeed variations and azimuthal anisotropy. The tomographic images revealed widespread crustal low-velocity zones (LVZs) at middle/lower crustal depth beneath SE Tibet. There is substantial lateral and vertical variability of these zones and some may be truncated by large faults. The pattern of azimuthal anisotropy in the upper crust is consistent with clockwise rotation around the eastern Himalaya syntaxis and a predominance of simple shear and strike-slip faulting in SE Tibet. Comparison of splitting from SKS observations and from our 3D anisotropic model suggests that the contribution to splitting from the crust is at least as important as from the upper mantle in the region west of Sichuan Basin and north of 26°N. However, beneath Yunnan, splitting signal originates mainly from the upper mantle. The radial changes in deformation pattern argue against vertically coherent lithospheric deformation in Tibet. Combined with the widespread crustal LVZs, this supports models of ductile crustal flow beneath SE Tibet. However, the spatial variation in strength and depth of crustal LVZs and in pattern of azimuthal anisotropy suggests that the 3-D geometry of crustal weak layers is complex and that unhindered crustal flow over large regions may not occur.

Thesis supervisor: Robert D. van der Hilst
Title: Cecil and Ida Green Professor of Earth Sciences

Acknowledgements*

Having spent almost five years in the department of EAPS at MIT, I am indebted to many great people who gave me much support and love in my academic study, research, and life.

It is my greatest fortune and pleasure that professor Rob van der Hilst was my thesis supervisor. Without his insightful supervision and continuous support, I would not have been able to complete this thesis. Rob gave me inspiration and encouragement during the entire period of my doctoral study and research. Also, the freedom he gives me makes working with him is such a great pleasure. His broad knowledge and research interests really open my minds in the research. Besides, he is also a good friend in life who you can always ask for help and suggestions.

I would also like to thank the rest of my thesis committee, professor Wiki Royden (chair of the committee), Nafi Toksöz, Stéphane Rondenay, and Mike Ritzwoller. Wiki, Nafi, and Stéphane were also in the committee of my general exam. I have many discussions with Wiki about the Tibetan tectonics and crustal channel flow which was really helpful to my thesis work. Nafi gave me many suggestions to my research. Stéphane was always helpful and I benefited from the discussion with him and from a few great courses he gave in the department. I also owe much to professor Mike Ritzwoller in University of Colorado and his group, including Yingjie Yang and Fan-Chi Lin, for many helpful discussions related to ambient noise studies.

I appreciate professor Maarten de Hoop at Prudue University, Jean-Paul Montagner at IPG Paris, Caroline Beghein at UCLA, and Dr. Xander Campman at Shell for their great help and valuable suggestions during our research collaborations. Maarten gave me many ideas on the propagation of seismic waves and interferometry. Jean-Paul gave me great advice for the inversion of shear wave azimuthal anisotropy. Caroline taught me how to use the Neighborhood Algorithm. Xander shared with me many great suggestions in looking at the properties of recovered Green's function from seismic interferometry. I also appreciate the numerous discussions with Victor Tsai at Harvard University about ambient noise interferometry. I would like to thank professor Chen Ziliang in Chengdu Institute of Geology and Mineral Resources for his help in the deployment of MIT array in SW China and professor Anne Meltzer in Lehigh University for sharing the seismic data of Lehigh array in southern Tibet for surface wave analysis in Chapter 6 of this thesis.

My appreciation also goes to professor Brad Hager, who was the advisor of my general project. I learned a lot from him about geodynamic modeling of crustal channel flow, which broadened my knowledge and research interests. I also would like to thank professor Clark Burchfiel for insightful discussions on the geology of the Tibetan Plateau.

* The research presented in this thesis was supported by the Continental Dynamics Program of the National Science Foundation (under grant 6892042) and AFRL grants FA8718-04-C-0018 and FA8718-07-C-0001.

Many faculty members and researchers in EAPS and ERL also gave me a lot of help in the past a few years; I would especially thank Dan Burns, Mike Fehler, Alison Malcolm, Dale Morgan, Bill Rodi, and Zhenya Zhu.

My deep gratitude also goes to these Chinese brothers Youshun Sun, Ping Wang, and Chang Li in the department for their kindly and numerous help in the past, which let me and my family really feel the love and warmth even in a foreign country, especially in the first several years my family lived out of MIT campus. I also appreciate the friendship and help from many students and postdocs in EAPS, including Terry Blackburn, Scott Burdick, Qin Cao, Krystle Catalli, Chin-Wu Chen, Min Chen, Tianrun Chen, Kristen Cook, Xingding Fang, Pierre Gouedard, Hui Huang, Sichuan Huang, Kang Hyeun Ji, Mike Krawczynski, Rosalee Lamm, Einat Lev, Junlun Li, Maureen Long, Rongrong Lu, Jiangning Lü, Erwan Mazarico, Noah Mclean, Oleg Poliannikov, Xuefeng Shang, Maria Silva, Fuxian Song, Lili Xu, Min Xu, Haijiang Zhang, Xin Zhan, and Yang Zhang. In particular, I thank Einat for her help with my second general project.

Dr. Vicki Mckenna and Ms. Carol Sprague in the Department Education office, the administrative secretary Sue Turbak and Beth MacEachran provided me a lot of prompt help. Linda Meinke helped me solve many hardware and software problems. I heartily thank those great people in the department for their important contribution.

My appreciation also goes to my colleagues in China, who gave me much help and hospitality when I was in China for visiting, research collaborations, and meetings; I would especially thank the director Wu Yaoqiang, Lü Zhiyong, Deng Yiwei, Yi Guixi, Cheng Tianchang, Fan Jun, and Wen Xueze from Sichuan Earthquake Administration, professor Liu Qiyuan and his group (Chen Jiuhui, Li Yu, Guo Biao) in Institute of Geology of Chinese Earthquake Administration, professor Zhao Junmeng, Gao Xing, and Pei Shunping in the Tibetan Plateau Research Institute of Chinese Academy of Sciences (CAS), professor Zhu Rixiang, Sun Ruomei, Bai Denghai, Chen Lin, and Xu Tao in Institute of Geology and Geophysics in CAS, professor Shi Yaolin and Zhang Huai in the Graduate School of CAS, professor John Yongshun Chen in Peking University, and professor Xu Guoming, Fu Rongshan, Chen Xiaofei, Wu Xiaoping, and Ni Sidao in University of Science and Technology of China (USTC).

My special thanks also go to my B.S. and M.S. thesis supervisor, professor Xu Guoming in USTC, who opened the first door of scientific research for me. The geophysical background and research experiences I obtained from USTC were a great foundation for my doctoral thesis work at MIT.

My endless love goes to my wife Sun Shidan, my daughter Sunny Yao, my parents Yao Gecheng and Luo Yuanxiu, my parents-in-law Wu Jinlin and Sun Zhaonan, and my sister Yao Huaqin. They are the biggest supports for me anytime and anywhere. I share every happiness and difficulty with them. Without their love and continuing supports, it would have been impossible for me to finish this thesis work in five years.

Contents

List of figures

Chapter 1

Introduction

1.1 Structure and deformation of the crust and upper mantle of southeastern Tibet

The collision of the Indian and Eurasian plates (Figure 1-1), which began at approximately 50 Ma (Dewey et al., 1988; Molnar et al., 1993; Rowley, 1998; Royden et al., 2008), has produced (1) world's largest plateau, with average surface elevation of 5 km (Figure 1-2) and a crust thickness of up to 80 km (Mooney et al., 1998), (2) the magnificent mountain ranges of the Himalaya, Karakorum, Tien Shan, Kunlun Shan, Qilian Shan, and Longmen Shan, (3) transport of (crust and, perhaps, lithosphere) material from the central Tibetan plateau towards the east, with bifurcation around the rigid Sichuan Basin toward SW China and the northeastern Tibetan plateau margin (Figure 1-2) (Zhang et al., 2004; Royden et al., 2008), and (4) many active faults and numerous continental earthquakes inside the plateau proper and around the plateau margin (Figure 1-2), including the devastating Wenchuan earthquake (M = 8.0) of 12 May 2008 in the Longmen Shan fault zone of the eastern Tibetan plateau margin (Burchfiel et al., 2008). Furthermore, the creation of the Himalayas and the Tibetan plateau may have caused dramatic climate changes in southern Asia (Molnar et al., 1993).

The mechanism for the deformation of the Tibetan plateau is still hotly debated and several possibilities have been proposed, including rigid block extrusion (Molnar & Tapponnier, 1975), distributed crustal thickening (England & Houseman, 1986), injection of Indian crust into Tibetan lower crust (Zhao & Morgan, 1987), and lower or middle crustal channel flow (Figure 1-3) (Royden et al., 1997; Beaumont et al., 2001).

Deformation of the southeastern Tibetan plateau, around the eastern Himalayan syntaxis, is influenced by northward subduction of the Indian lithosphere along the Indus-Tsangpo suture (ITS) (Yin & Harrison, 2000; Li et al., 2008), eastward subduction of the Burmese microplate along the Burma arc (Ni et al., 1989; Li et al., 2008), and resistance to further eastward expansion of the Tibetan plateau by the (mechanically) rigid Sichuan basin (Cook & Royden, 2008). The southeastern margin of the Tibetan plateau is characterized by a gentle topographic slope, lack of large-scale (geologically) young crustal shortening, and a predominance of N-S-trending strike-slip faults (Royden et al., 1997) that enable clockwise rotation of crust fragments around the eastern Himalayan syntaxis (Wang and Burchfiel, 2000; Zhang et al., 2004). These characteristics have been explained by lateral (ductile channel) flow in a mechanically weak lower crust (Royden et al., 1997). Beaumont et al. (2001, 2004) invoked thermo-mechanical channel flow within a weak middle crust of southern Tibet and the Himalayas to explain, for instance, the southward extrusion of the Tibetan middle crust toward the Indian foreland (Hodges et al., 2001).

Such crustal flow models imply (and require) the existence of a large scale network of interconnected (mechanically) weak zones in the middle/lower crust with viscosity several orders lower than that of the upper rigid crust, so that the upper crustal deformation is largely decoupled from the motion of the underlying lithospheric upper mantle (Royden et al., 1997, 2008). The level of mechanical coupling between the upper crust and upper mantle in SE Tibet and SW China is still hotly debated (e.g., Royden et al., 1997; Holt, 2000; Flesch et al., 2005; Lev et al., 2006; Sol et al., 2007; Royden et al., 2008; Wang et al., 2008). For instance, Wang et al. (2008) used the joint analysis of shear wave splitting measurements and surface GPS observations to argue for vertically coherent deformation in the crust and upper mantle in Tibet and surrounding area, but the complexity of shear wave splitting (e.g., Lev et al., 2006) as well as mounting evidence for widespread existence of crustal zones with anomalously slow shear propagation (indicating low rigidity) seems, at least qualitatively, consistent with the crustal flow model.

Previous travel-time tomography and magnetotelluric studies (e.g., Huang et al., 2002; Wang et al., 2003; Sun et al., 2003; Bai et al., 2005; Unsworth et al., 2005) have indeed revealed the existence of crustal low velocity or low resistivity (possibly mechanically weaker) zones in SE Tibet. However, the spatial distribution in both lateral and vertical extent as well as the 3-D interconnectivity of these low velocity (or resistivity) zones are poorly understood either due to the resolution limitations of each of these methods or insufficient data coverage. More recently, analyses of surface wave dispersion (Yao et al., 2006, 2008; Li et al., 2009) and receiver functions (Xu et al., 2007; Liu et al., 2008; Wang et al., 2009) have begun to provide unequivocal evidence for the existence of crustal zones of low shear wavespeed and, presumably, rigidity.

Constraining lithosphere scale deformation in this region has been an enormous challenge. The Global Positioning System (GPS) provides accurate measurements of the present-day rate of displacement of crustal blocks but does not tell us much about the long term deformation history. Indeed, the GPS velocity field can only be compared to finite strain if one assumes a deformation mechanism (e.g., pure v.s. simple shear) and that the style of deformation has been the same over long periods of geological time. Shear wave splitting is often used as diagnostic of upper mantle azimuthal anisotropy, which, in turn, is used as a proxy for finite strain. Even though the depth resolution of splitting measurements is poor, many studies attribute the origin of the splitting signal to the shallow mantle and ignore the contribution from crustal anisotropy. In Tibet, however, the crustal material is not only highly deformed (and presumably highly anisotropic) but also very thick. Therefore, robust interpretation of shear wave splitting results in SE Tibet needs to consider the effect of crustal anisotropy. Considering these complexities, direct comparison of surface instantaneous strain field derived from GPS data with shear wave splitting measurements is fraught with uncertainty and should be done with care in order to obtain meaningful constraints on the crust and upper mantle deformation pattern.

1.2 Thesis objectives

In view of the above background, the general objective of my doctoral thesis is to investigate the structure and deformation of the lithosphere beneath SE Tibet in sufficient

detail to discriminate between competing tectonic and dynamics models, for instance to confirm or refute the above mentioned crustal flow model. Specific objectives include:

(1) Construct a high resolution 3-D shear velocity model with azimuthal anisotropy in crustal and upper mantle beneath SE Tibet;

(2) Investigate the 3-D architecture (e.g., geometry and interconnectivity) of crustal low velocity zones (LVZs) in SE Tibet;

(3) Probe possible relationship between the crustal LVZs and major faults (e.g., Xianshuihe faults);

(4) Constrain the deformation pattern of the crust and upper mantle deformation pattern (e.g., mechanically coupling or decoupling) in SE Tibet.

1.3 MIT array of broad band seismographs

Meeting these objectives requires careful analysis of broad band data from a dense seismograph network. For this purpose, MIT (in collaboration with Chengdu Institute of Geology and Mineral Resources (CIGMR) and with funding from the US National Science Foundation's Continental Dynamics Program) deployed between September 2003 and September 2004 25 broad band stations in SW China along the southeastern Tibetan plateau margin (Figure 1-4). The average inter-station distance was about 100 km. The (continuous) waveform data are freely available from the Data Management Center (DMC) of the Incorporated Research Institutions for Seismology (IRIS). Previous studies with data from this array (and from an array deployed by Lehigh University in about the same period of time) focused on azimuthal anisotropy from shear wave splitting (Lev et al., 2006; Sol et al., 2007), crustal thickness (Moho depth) from receiver function analysis (Xu et al., 2007), and variations in *P*-wavespeed in the upper mantle using travel time tomography (Li et al., 2006, 2008). My thesis work has focused on the development of new methods for high resolution surface wave array tomography with the aim of improving our understanding of the structure and (azimuthal) anisotropy in the crust and upper mantle.

1.4 Ambient noise interferometry and surface wave array tomography

Surface waves are evanescent and propagate along Earth's surface with phase (or group) velocities that depend on frequency (or period), and this dispersion can be used to study medium properties at different depths. At long periods (e.g., T > 100s) surface waves are mainly sensitive to the shear velocity structure at large depth (e.g., upper mantle), while at short periods (e.g., T < 30s) they sample shallow structure. As a corollary, the depth resolution of short period surface waves is much better than that of long period waves.

Surface waves propagating from earthquakes to one or more receivers have been widely used to study the crust and upper mantle structure on both regional and global scale. Various approaches have been used for regional surface wave array tomography, including the construction – and point-wise inversion – of phase (or group) velocity maps (Ritzwoller & Levshin, 1998; Curtis et al., 1998, and many others), the measurement of inter-station phase velocities through traditional two-station analysis (e.g., Passier et al., 1995; Yao et al., 2005), or (partitioned) waveform inversion (e.g., Nolet, 1991; Zielhuis and Van der Hilst, 1996; Simons et al., 1999). Forsyth and Li (2005) developed a two-plane-wave method to analyze the 2-D variation of surface wave phase velocities across arrays with small foot-prints (compared to the source-receiver distance). Surface waves can be used to investigate both the isotropic and anisotropic structure in the crust and upper mantle, which can help understand subsurface deformation. In fact, surface wave dispersion provides more direct constraints on depth variation in azimuthal and radial anisotropy (e.g., Montagner & Nataf, 1986; Montagner & Tanimoto, 1991; Simons et al., 2002; Sebai et al., 2006) than shear wave splitting of, for instance, *SKS* waves.

In Tibet and surrounding areas, numerous surface-wave tomographic studies have been conducted with earthquake data (e.g., Ritzwoller & Levshin, 1998; Griot & Montagner, 1998; Huang et al., 2003; Shapiro et al., 2004; Yao et al., 2005; Yi et al., 2008). However, due to the small number of stations in the high plateau region, the lateral resolution of these tomographic studies is usually quite poor (~300 – 500 km). Furthermore, it has been difficult to obtain reliable constraints on crustal structure from surface wave dispersion because at short periods (e.g., T < 25s) the waveforms are usually affected by scattering due to strong crustal heterogeneity. Besides, sparse and uneven distribution of

earthquake sources and the uncertainties of the spatial characteristics of surface-wave sensitivity kernel also limit the resolution and accuracy of traditional approaches of surface wave tomography.

The lateral resolution of tomographic images can be improved by increasing the number of stations in the study area, for example, through the deployment of temporary seismograph arrays. The deployment of arrays by MIT and Lehigh University in SE Tibetan (see above) represented a dramatic increase of the number of stations from which data are openly available, from two (that is, the Global Seismograph Network stations in Lhasa, LSA, and Kunming, KMI) to almost 75 (Figure 1-4).

To improve radial resolution one must extend the frequency bandwidth, in particular toward shorter periods. Research in ultrasonics and seismology (e.g., Lobkis & Weaver, 2001; Campillo & Paul, 2003; Shapiro & Campillo, 2004) demonstrates that the short-period surface wave Green's function (essentially, ground displacement due to a point source) between pairs of receivers can be extracted from the time-domain correlation of ambient noise and coda waves (i.e., scattered waves). Since the measurements can be made between each station pair, this approach leads to high resolution surface wave array tomography at short periods (e.g., Shapiro et al., 2005).

The measurement of dispersion at intermediate and long periods from interferometry is restricted by the range of inter-station distances (and the requirement of far-field surface wave propagation). For these longer periods we use a traditional two-station analysis. In early applications of ambient noise tomography only inter-station group velocity dispersion curves were measured (e.g., Shapiro et al., 2005; Sabra et al., 2005). However, the measurement of group velocity is usually less accurate than that of the phase velocity, and the group velocity measurement is mere easily biased by the distribution of ambient noise energy (Pedersen et al., 2007). One of the first objectives of my PhD research was, therefore, to develop a method for measuring inter-station phase velocity dispersion by means of ambient noise interferometry, and to combine measurements from ambient

noise interferometry and two-station analysis for high resolution surface wave array tomography of the crust and upper mantle beneath SE Tibet.

In theory, the recovery of Green's functions from ambient noise interferometry requires isotropic distribution of noise sources or diffuse wave fields with equipartitioning of energy (e.g., Weaver and Lobkis, 2004; Snieder, 2005; Roux et al., 2005). However, in the real world these requirements are difficult to satisfy, and in general the Green's function inferred from interferometry, hereinafter referred to as the empirical Green's function (EGF), deviates from the true Green's function (GF). This motivates the investigation of (1) uneven noise source distribution or non-diffuse wave fields on GF reconstruction; (2) the bias of dispersion measurements from EGFs for given distribution of noise sources; (3) the real distribution of ambient noise sources; and (4) the effect of uneven source distribution on the tomographic images of isotropic and anisotropic structure.

1.5 Thesis structure

This thesis contains six chapters. In Chapter 1 (this chapter), we review the previous studies related to this thesis work and present the motivation and objectives of this thesis research.

In Chapter 2, published as Yao et al. (2006), we provide a phase image analysis technique for the determination of phase velocity dispersion curve of surface-wave EGFs from ambient noise correlation. Then we develop a new approach for surface-wave array tomography and apply it in SE Tibet using broadband data from MIT array stations. This approach combines the phase velocity dispersion measurements from both EGFs and teleseismic surface-wave two-station analysis.

In Chapter 3, published as Yao et al. (2008), we determine the 3-D shear wave speed variations in the crust and upper mantle in the southeastern borderland of the Tibetan Plateau, SW China, from surface wave array tomography using ambient noise and two-station analysis, with the Neighborhood algorithm. We explore the spatial variation and

strength of the crustal low velocity layers and their relationship to major fault zones in SW China.

In Chapter 4, under review as Yao et al. (2009), we investigate how source distribution and scale lengths of medium heterogeneity influence Green's function construction in the period band of primary microseisms (10-20s). We also demonstrate that seasonal variation of cross-correlation functions correlate with changes in ocean activity and that the energy contributing to Green's function construction can be understood better with beamforming analysis.

In Chapter 5, under review as Yao & Van der Hilst (2009), we analyze the effect of uneven ambient noise distribution and medium heterogeneity and azimuthal anisotropy on phase velocities measured from EGFs with an asymptotic plane wave (far-field) approximation. The (normalized) azimuthal distribution of ambient noise energy can be directly estimated from the cross correlation functions obtained through ambient noise interferometry. We illustrate our method for noise energy estimation, phase velocity bias suppression, and ambient noise tomography (including azimuthal anisotropy) with data from a seismic array in SE Tibet.

In Chapter 6, which is in preparation for publication, we present a 3-D shear velocity model with azimuthal anisotropy in the crust and upper mantle in southeastern Tibet using data from 75 broadband stations from surface-wave array tomography. We illustrate the 3-D architecture of crustal low velocity layers, e.g., the spatial and depth extent as well as the interconnectivity and discuss its dynamic importance for the evolution of the southeastern Tibetan Plateau. We infer the pattern of deformation in the crust and upper mantle beneath SE Tibet with joint analysis from GPS observations and shear wave splitting measurements.

References cited

Bai, D., Meju, M., Arora, B., et al., 2006. Large crustal-mantle channel flow in central Tibet and eastern Himalaya inferred from magnetotelluric models, *Eos Trans. AGU*, 87(36), West. Pac. Geophys. Meet. Suppl., Abstract S45A-07.

Beaumont, C., Jamieson, R. A., Nguyen, M. H. and Lee, B., 2001. Himalayan tectonics explained by extrusion of a low-viscosity channel coupled to focused surface denudation, *Nature*, 414, 738-742.

Beaumont, C., R. A. Jamieson, M. H. Nguyen, and S. Medvedev (2004), Crustal channel flows: 1. Numerical models with applications to the tectonics of the Himalayan-Tibetan orogen, *J. Geophys. Res.*, 109, B06406, doi:10.1029/2003JB002809.

Burchfiel, B.C., Royden, L.H., van der Hilst, R.D., Hager, B.H., Chen, Z., King, Q.W., Li, C., Lu, J., Yao, H., and Kirby, E., 2008. A geological and geophysical context for Wenchuan earthquake of 12 May 2008, Sichuan, People's Republic of China, *GSA Today,* 18(7), doi:10.1130/GSATG18A.1

Campillo, M. and A. Paul, 2003. Long-Range correlations in the diffuse seismic coda, *Science*, 299, 547-549.

Chen, Z., Burchfiel, B.C., Liu., Y., King, R.W., Royden, L.H., Tang, W., Wang, E., Zhao, J., Zhang, X., 2000. Global positioning system measurements from eastern Tibet and their implications for India/Eurasia intercontinental deformation, *J. Geophys. Res* 105, 16215-16227.

Cook, K.L. and Royden, L.H., 2008. The role of crustal strength variations in shaping orogenic plateau, with application to Tibet, *J. Geophys. Res.*, 113, B08407, doi:10.1029/ 2007JB005457.

Curtis, A., Trampert, J., Snieder, R., 1998. Eurasian fundamental mode surface wave phase velocities and their relationship with tectonic structures. *J. Geophys. Res.* 103, 26919–26947.

Dewey, J. F., Shackleton, R. M., Chang, C. and Sun, Y., 1988. The tectonic evolution of the Tibetan Plateau, *Philos. Trans. R. Soc. London, Ser. A*, 327, 379-413.

Engdahl, E.R., Van der Hilst, R.D. & Buland, R.P., 1998. Global teleseismic earthquake relocation from improved travel times and procedures for depth determination, *Bull.seism. Soc. Am.,* 88, 722–743.

England, P. & Houseman, G., 1986. Finite strain calculations of continental deformation: 2, Comparison with the India-Asia collision zone, *J. Geophys. Res.*, 91, 3664-3676.

Flesch, L.M., Holt, W.E., Silver, P.G., Stephenson, M., Wang, C.-Y., and Chan, W.W., 2005. Constraining the extent of crust-mantle coupling in central Asia using GPS, geologic, and shear wave splitting data, *Earth Planet. Sci. Lett*, 238, 248-268.

Forsyth, D.W., and A. Li, 2005. Array-analysis of two-dimensional variations in surface wave phase velocity and azimuthal anisotropy in the presence of multipathing interference, in Seismic Earth: Array Analysis of Broadband Seismograms, edited by A. Levander and G. Nolet, pp81-98, *Geophysical Monograph* 157, AGU. Washington DC.

Griot, D.A., Montagner, J.P., 1998. Phase velocity structure from Rayleigh and Love waves in Tibet and its neighboring regions. *J. Geophys. Res.* 103, 21215–21232.

Hodges, K.V., Hurtado, J.M., and Whipple, K.X., 2001. Southward extrusion of Tibetan crust and its effect on Himalayan tectonics, *Tectonics*, 20(6), 799-809.

Holt, W.E., 2000. Correlated crust and mantle strain fields in Tibet, *Geology*, 28(1), 67-70.

Huang, J., Zhao, D., & Zheng, S., 2002. Lithospheric structure and its relationship to seismic and volcanic activity in southwest China, *J. Geophys. Res*, 107(B10), 2255, doi:10.1029/2000JB000137.

Huang, Z., W. Su, Y. Peng, Y. Zheng, and H. Li, 2003. Rayleigh wave tomography of China and adjacent regions, *J. Geophys. Res.*, 108(B2), 2073, doi:10.1029/2001 JB001696.

Lebedev, S. and Van der Hilst, R.D., 2008. Global upper-mantle tomography with the automated multi-mode surface and S waveforms, *Geophys. J. Int.,* 173, doi: 10.1111/ j.1365-246X.2008.03721.x

Lev, E., Long, M., van der Hilst, R.D., 2006. Seismic anisotropy in Eastern Tibet from Shear-wave splitting reveals changes in lithosphere deformation. *Earth Planet. Sci. Lett.* 251, 293 - 304.

Li, C., Van der Hilst, R.D. & Toksoz, M.N., 2006. Constraining P-wave velocity variations in upper mantle beneath Southeast Asia, *Phys. Earth Planet. Inter.,* 154, 180–195.

Li, C., Van der Hilst, R.D., Meltzer, A.S., Sun, R., and Engdahl, E.R., 2008. Subduction of the Indian lithosphere beneath the Tibetan Plateau and Burma, *Earth Planet. Sci. Lett,* 274, 157-168.

Liu QY, Li Y, Chen JH, 2009. Wenchuan M(S)8.0 earthquake: preliminary study of the S-wave velocity structure of the crust and upper mantle, *Chinese J. Geophys.* (in Chinese), 52 (2), 309-319.

Lobkis, O. I. and R. L., Weaver, 2001. On the emergence of the Green's function in the correlations of a diffusive field, *J. Acoust. Soc. Am.*, 110, 3011-3017.

Molnar, P. & Tapponnier, P., 1975. Cenozoic tectonics of Asia: Effects of a continental collision. *Science*, 189, 419-426.

Molnar, P., England, P. and Martinod, J., 1993. Mantle dynamics, uplift of the Tibetan Plateau, the Indian Monsoon, *Rev. Geophys.*, 31, 357-396.

Montagner, J.-P. & Nataf, H.-C., 1986. A simple method for inverting the azimuthal anisotropy of surface waves, *J. geophys. Res.,* 91, 511–520.

Montagner, J.-P. & Tanimoto, T., 1991. Global upper mantle tomography of seismic velocities and anisotropies, *J. geophys. Res.,* 96, 20337–20351.

Mooney, W.D., G. Laske and G. Masters, 1998. CRUST5.1: A global crustal model at 5°x5°, *J. Geophys. Res.*, 103, 727-747.

Ni, J.F., Guzman-Speziale, M., Bevis, M., Holt, W.E., Wallace, T.C., Seager, W., 1989. Accretionary tectonics of Burma and the three-dimensional geometry of the Burma subduction zone. *Geology*, 17, 68 - 71.

Passier, M. L., Van der Hilst, R. D., and Snieder, R. K., 1997. Surface wave waveform inversions for local shear-wave velocities under eastern Australia, *Geophys. Res. Lett.*, 24, 1291-1294.

Pedersen, H. A., Kr¨uger, F. and the SVEKALAPKO Seismic Tomography Working Group, 2007. Influence of the seismic noise characteristics on noise correlations in the Baltic shield, *Geophys. J. Int.*, 168, 197–210.

Ritzwoller, M., Levshin, A., 1998. Eurasian surface wave tomography: group velocities, *J. Geophys. Res.,* 103, 4839–4878.

Royden, L. H., Burchfiel, B. C., King, R. W., et al., 1997. Surface deformation and lower crustal flow in eastern Tibet, *Science,* 276, 788-790.

Royden, L.H., Burchfiel, B.K., and Van der Hilst, R.D., 2008. The geological evolution of the Tibetan Plateau, *Science*, 321, 1054-1058.

Rowley, D. B., 1996. Age of initiation of collision between India and Asia: A review of stratigraphic data, *Earth Planet. Sci. Lett.*, 145, 1-13.

Roux, P., Sabra, K. G., Kuperman, W. A. & Roux, A., 2005. Ambient noise cross correlation in free space: Theoretical approach, *J. Acoust. Soc. Am.*, 117(1), 79–84.

Sabra, K. G., P. Gerstoft, P. Roux, W. A. Kuperman, and M. C. Fehler, 2005a. Extracting time-domain Greens function estimates from ambient seismic noise, *Geophys. Res. Lett.*, 32, L03310, doi:10.1029/2004GL021862.

Sebai A, Stutzmann E, Montagner JP, Sicilia D, Beucler E, 2006. Anisotropic structure of the African upper mantle from Rayleigh and Love wave tomography, *Phys. Earth Planet. Inter.,* 155, 48-62.

Shapiro, N. M., Ritzwoller, M. H., Molnar, P. and Levin, V., 2004. Thinning and flow of Tibetan crust constrained by seismic anisotropy, *Science*, 305, 233-236.

Shapiro, N. M. and Campillo, M., 2004. Emergence of broadband Rayleigh waves from correlations of the ambient seismic noise, *Geophys. Res. Lett*, 31, L07614, doi:10.1029/ 2004GL019491.

Shapiro, N. M., Campillo, M., Stehly, L., and Ritzwoller, M. H., 2005. High-resolution surface wave tomography from ambient seismic noise, *Science*, 307, 1615-1618.

Simons, F.J., Zielhuis, A., and Van der Hilst, R.D., , 1999. The deep structure of the Australian continent inferred from surface wave tomography, *Lithos*, 48/1-4, 17-43.

Simons, F. J., van der Hilst, R. D., Montagner, J. P., and Zielhuis, A., 2002. Multimode Rayleigh wave inversion for heterogeneity and azimuthal anisotropy of the Australian upper mantle, *Geophys. J. Int.*, 151, 738-754

Snieder, R., 2004. Extracting the Green's function from the correlation of coda waves: A derivation based on stationary phase, *Phys. Rev. E*, 69, 046610.

Sol, S., Meltzer, A., Burgmann, R., Van der Hilst, R.D., et al., 2007. Geodynamics of southeastern Tibet from seismic anisotropy and geodesy, *Geology*, 35, 563-566, doi: 10.1130/G23408A.1.

Sun J., Jin, G.W., Bai, D.H., & Wang, L.F., 2003. Sounding of electrical structure of the crust and upper mantle along the eastern border of Qinghai-Tibet Plateau and its tectonic significance (in Chinese), *Sci. China Ser. D.*, 46, 243-+Suppl. S.

Unsworth, M. J., Jones, A. G., Wei, W., et al., 2005. Crustal rheology of the Himalaya and southern Tibet from magnetotelluric data, *Nature*, 438, 78-81.

Wang, C.-Y., Chan, W.W., & Mooney, W.D., 2003. Three-dimensional velocity structure of crust and upper mantle in southwestern China and its tectonic implications, *J. Geophys. Res*, 108(B9), 2442, doi:10.1029/2002JB001973.

Wang, C.-Y., Flesch, L.M., Silver, P.G., Chang, L.-J., and Chan, W.W., 2008. Evidence for mechanically coupled lithosphere in central Asia and resulting implication, *Geology*, 36, 363-366, doi:10.1130/G24450A.1

Wang, C.-Y., Lou, H., Silver, P.G., Zhu, L, and Chang, L.-J,, 2009. Crustal structure along 30° N in the eastern Tibetan Plateau and its tectonic implications, submitted to *Earth Planet. Sci. Lett.*

Wang, E. and Burchfiel, B.C., 2000. Late Cenozoic to Holocene deformation in southwestern Sichuan and adjacent Yunnan, China, and its role in formation of the southeastern part of the Tibetan Plateau, *GSA Bulletin*, 112(3), 413-423.

Weaver, R. L. and O. I., Lobkis, 2004. Diffuse fields in open systems and the emergence of the Green's function. *J. Acoust. Soc. Am.*, 116, 2731-2734

Xu, L., Rondenay, S., Van der Hilst, R.D., 2007. Structure of the crust beneath the Southeastern Tibetan Plateau from Teleseismic Receiver Functions, *Phys. Earth Planet. Int.*, 176-193, doi:10.1016/j.pepi.2007.09.002

Yao, H., G., Xu, L., Zhu, and X., Xiao, 2005. Mantle structure from inter-station Rayleigh wave dispersion and its tectonic implication in western China and neighboring regions, *Phys. Earth Planet. Inter.*, 148, 39-54.

Yao, H., Van der Hilst, R.D., & de Hoop, M.V., 2006. Surface-wave array tomography in SE Tibet from ambient seismic noise and two-station analysis – I. phase velocity maps, *Geophys. J. Int.*, 166, 732-744.

Yao, H., Beghein, C., and Van der Hist, R.D., 2008. Surface-wave array tomography in SE Tibet from ambient seismic noise and two-station analysis: II – Crustal and upper-mantle structure, *Geophys. J. Int.*, Vol. 163, 205-219, doi: 10.1111/j.1365-246X.2007.03696.x.

Yao, H., Campman, X., De Hoop, M.V., and Van der Hilst, R.D., 2009. Estimation of surface-wave Green's function from correlations of direct waves, coda waves, and ambient noise in SE Tibet, *Phys. Earth Planet. Inter.*, under review.

Yao, H. and Van der Hilst, R.D., 2009. Analysis of ambient noise energy distribution and phase velocity bias in ambient noise tomography, with application to SE Tibet, revised for publication in *Geophys. J. Int.*

Yi, G.-x., Yao, H., Zhu, J.-s, and Van der Hilst, R.D., Rayleigh wave phase velocity distribution in continental China and its adjacent regions, *Chinese J. Geophys.*, 51, 402-411.

Yin A. and Harrison, T.M., 2000. Geologic evolution of the Himalayan-Tibetan orogen, *Annu. Rev. Earth Planet. Sci.,* 28, 211-280.

Zhang P., Shen, Z., Wang, M., et al., 2004. Continuous deformation of the Tibetan Plateau from global positioning system data, *Geology*, 32(9), 809-812.

Zhao, W. & Morgan, W. J., 1987. Injection of Indian crust into Tibetan lower crust: A two dimensional finite element model study, *Tectonics*, 64, 489-504.

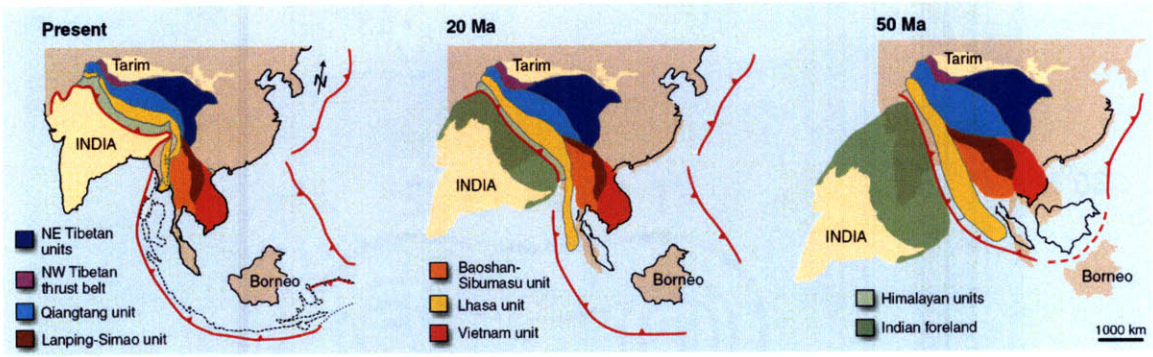

Figure 1-1. Tectonic reconstruction of collision between Indian subcontinent and Eurasia at 50 Ma, 20 Ma, and present time (from Fig. 3 by Royden et al., 2008). Major tectonic units of Tibet and Indochina are depicted by color and bold red lines are estimated positions of subduction zones.

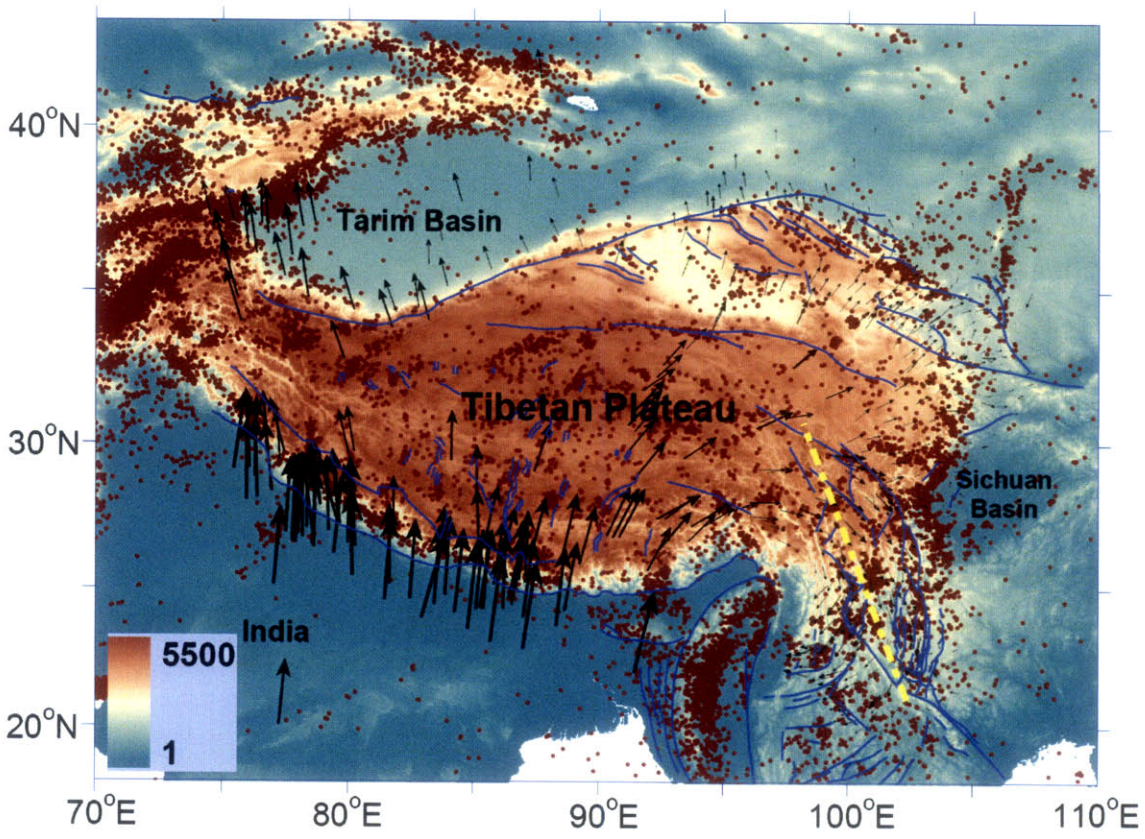

Figure 1-2. Topography, seismicity, and the surface velocity field of the Tibetan plateau and adjacent regions. The color bar in the left corner shows for surface elevation in m. The dots show the location of earthquakes between 1964-2007 from the EHB dataset (Engdahl et al., 1998). The black vectors show the GPS velocity vectors (Chen et al., 2000; Zhang et al., 2004; Sol et al., 2007). The blue lines show the location of major faults.

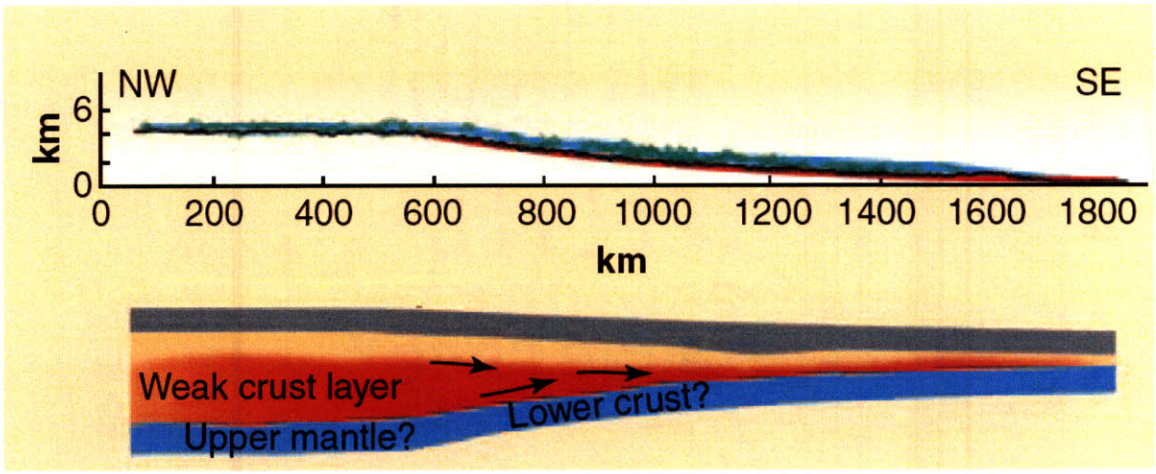

Figure 1-3. Illustration of lower crust flow model (modified from Fig. 5 by Royden et al., 2008). The top panel shows topography, and the lower panel shows the conceptual crustal model in southeastern Tibet and its margin along the profile shown as the yellow dashed line in Figure 1-2.

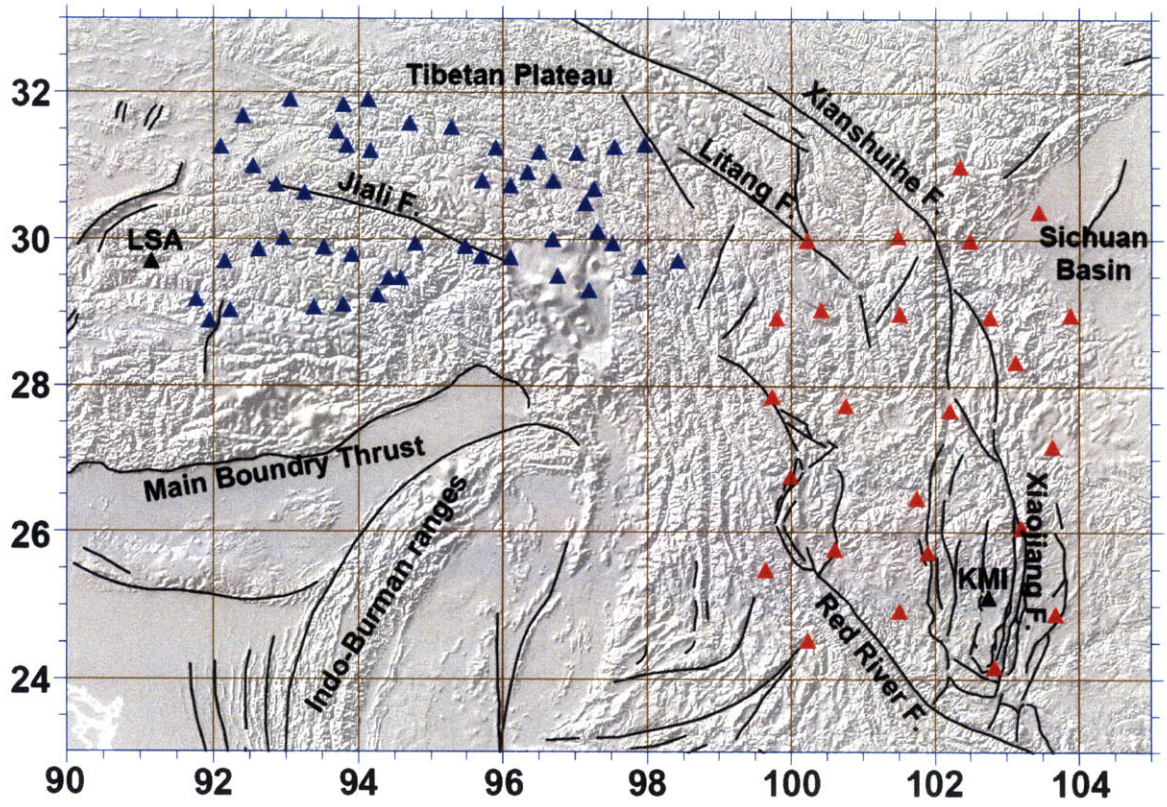

Figure 1-4. Seismograph stations deployed in SE Tibet used in this thesis study. Red triangles and blue triangles show for the temporary array stations deployed by MIT and Lehigh University, respectively. The two black triangles shows for the two permanent stations (LSA and KMI) deployed at Lhasa and Kunming in China, respectively. The total number of stations is 75. The black lines show for the location of major faults in SE Tibet and surrounding area. F. is the abbreviation for 'fault'.

Chapter 2

Surface-wave array tomography in SE Tibet from ambient seismic noise and two-station analysis: I - Phase velocity maps[1]

Abstract

Empirical Green's functions (EGFs) between pairs of seismographs can be estimated from the time-derivative of the long-time cross-correlation of ambient seismic noise. These EGFs reveal velocity dispersion at relatively short periods, which can be used to resolve structures in the crust and uppermost mantle better than with traditional surface wave tomography. We combine Rayleigh-wave dispersion estimates from EGFs and from traditional two-station analysis into a new approach to surface-wave array tomography with data from dense receiver arrays. We illustrate the methodology with continuous broad-band recordings from a temporary seismographic network on the southeastern part of the Tibetan plateau, in Sichuan and Yunnan provinces, SW China. The EGFs are robust under temporal changes in regional seismicity and the use of either ambient noise (approximated by records without signal from events with magnitude $m_b \geq$ 5 or 4) or surface wave coda produces similar results. The EGFs do not strongly depend on the presence of large earthquakes, but they are not reciprocal for stations aligned in the N-S. This directionality reflects the paucity of seismicity to the north of the array. Using a far-field representation of the surface-wave Green's function and an image transformation technique, we infer from the EGFs the Rayleigh-wave phase velocity dispersion in the period band from 10 – 30 s. A classical two-station approach is used to determine Rayleigh-wave phase velocity dispersion between 20 – 120 s. Together, they

[1] Published as: Yao H., Van der Hilst, R.D., and De Hoop, M.V., 2006. Surface-wave array tomography in SE Tibet from ambient seismic noise and two-station analysis: I - Phase velocity maps, *Geophys. J. Int.*, Vol. 166, 732-744, doi: 10.1111/j. 1365-246X.2006.03028.x.

constrain phase velocity variations for T = 10 – 120 s, which can be used to study the structure from the crust to the upper mantle. Beneath SE Tibet, short and intermediate period (10 – 80 s) phase velocities are prominently low, suggesting that the crust and upper mantle beneath SE Tibet is characterized by slow shear wave propagation.

2.1 Introduction

Surface-wave tomography based on ballistic waves propagating from a source to multiple receivers has provided important information about the 3-D shear wave velocity structure in the upper mantle both on a global (Trampert & Woodhouse, 1996; Shapiro & Ritzwoller, 2002, to name but a few) and regional (e.g., Zielhuis and Nolet, 1994; Simons *et al.*, 2002; Huang *et al.*, 2003) scale. In these studies, depth resolution is obtained from (fundamental and/or higher mode) group or phase velocity dispersion, with the low frequency component constraining deeper structures than the high frequency ones. Accurate imaging of the shallow part of the lithosphere, including the crust, is of particular interest for understanding the relationships between mantle dynamics and geologic processes at or near the surface. Unfortunately, if one considers surface wave dispersion along source-receiver paths, the resolution of structure in the relevant depth range is often limited by: (1) scattering at the short-period part (T < 30 s) of the waveforms; (2) inadequate path coverage due to the uneven distribution of seismic sources and receivers; (3) insufficient information about the seismic source, and (4) uncertainties about the spatial characteristics of the surface-wave sensitivity kernel (e.g., Yoshizawa & Kennett, 2002; Spetzler, *et al.*, 2002; Zhou *et al.*, 2004).

Recent studies show that surface-wave Green's function between two seismograph stations can be estimated from the long-time cross-correlation of coda waves (Campillo & Paul, 2003) and ambient seismic noise (Shapiro & Campillo, 2004; Shapiro *et al.*, 2005; Sabra *et al.*, 2005a). The surface wave periods considered in these studies are shorter than those that can (reliably) be used in traditional analyses of source-receiver propagation. Moreover, measurements can, in principle, be made for any pair of receivers within seismograph arrays, and the dense path coverage thus produced enables high resolution surface-wave tomography (Shapiro *et al.*, 2005; Sabra *et al.*, 2005b). Previous studies

used group velocity dispersion extracted from the noise cross-correlation function (Shapiro & Campillo, 2004; Shapiro *et al.*, 2005) – hereinafter referred to as NCF – or from its time-derivative, the empirical Green's function (Sabra *et al.*, 2005a, b) – hereinafter EGF. Theoretically, the time-derivative of the NCF is equivalent to the Green's function except for a frequency dependent amplitude factor (Lobkis & Weaver, 2001; Weaver and Lobkis, 2004; Roux *et al.*, 2005), but in contrast to the real Green's functions, which are by definition reciprocal and independent of the seismic source, the EGFs that are estimated from actual coda waves or ambient seismic noise may be time-asymmetrical due to the inhomogeneous distribution of noise sources and attenuation (Sabra *et al.*, 2005a; Paul *et al.*, 2005).

Group dispersion measurements rely on amplitude information and may, therefore, be affected by distortion of the amplitude spectrum of the EGF. The phase information in EGFs estimated from the NCF is, however, theoretically the same as that of the real Green's function. In this paper we demonstrate that accurate phase velocity dispersion measurements can be obtained from the EGF by using the far-field representation of the surface-wave Green's function and an image transformation technique.

Traditional global and regional surface wave tomography relies on relatively long period data and assumes integration over wave paths – or finite frequency kernels – between source and receivers that are often many thousands of kilometers apart. Such approaches cannot fully exploit the potential data redundancy (and resulting spatial resolution) provided by dense receiver arrays. In principle, better spatial localization can be obtained with the classical two-station method (Knopoff *et al.*, 1966), which measures phase-velocity dispersion between two stations in the intermediate and longer periods range using cross-correlation. For example, Passier *et al.* (1997) use the two-station approach to SKIPPY array data in Australia. Brisbourne and Stuart (1998) invert shear wave velocity structure beneath North Island, New Zealand, from Rayleigh-wave inter-station phase velocities. Recently, Yao et al. (2005) introduce an image transformation technique to measure inter-station phase velocity dispersion and presented Rayleigh-wave phase velocity maps from 15 to 120 s in western China and adjacent regions.

Here we explore how the Rayleigh-wave phase velocity dispersion data from the Green's function (GF) and the two-station (TS) methods can be integrated into a method for high-resolution surface wave array tomography of continental lithosphere. We show applications to data from a temporary array of 25 broad-band seismometers operated by MIT and CIGMR (Chengdu Institute of Geology and Mineral Resources) on the southeastern Tibetan plateau, in Sichuan and Yunnan provinces, SW China (Figure 2- 1). We carry out the analysis up to the construction of phase velocity maps for surface wave periods of 10 – 120 s. The inversion for and interpretation of shear heterogeneity in the crust and upper mantle beneath the study region will presented elsewhere (Yao *et al.*, 2008, see Chapter 3).

2.2 Empirical Green's function (EGF)

We calculate empirical Green's functions (EGFs) from continuous vertical component seismograms recorded from April to August 2004. The instrument response has been removed from all the data prior to cross-correlation. We conduct several experiments to test the robustness of the EGFs for temporal variations and directionality of the "noise" signals. First, we compare EGFs calculated for different time periods. Second, we compare the EGFs reconstructed from data in different frequency bands and discuss the effects of the spatial distribution of the "noise" sources. Third, we calculate EGFs from ambient seismic "noise" using records in which signal from known earthquakes (considering different magnitude cut-offs) is suppressed. Fourth, for comparison, we also calculate EGFs explicitly from the surface wave coda. In this paper we use the term "noise" rather loosely either for scattered waves or for the parts of the records that are not directly related to (known) large events. In the latter case, "noise" may contain signal from background seismicity, not just micro-seismic activity.

2.2.1 Noise correlation

Previous studies (Lobkis & Weaver, 2001; Weaver and Lobkis, 2004; Roux *et al.*, 2005; Sabra *et al.*, 2005a) have demonstrated that EGFs obtained from the noise cross-correlation function (NCF), by taking the time derivative, are equivalent to real Green's

function except for a frequency dependent amplitude correction. For hypothetical seismograph stations at position A and B, the relationship between the NCF, $C(t)$, the EGF, $\hat{G}(t)$, and the real (unknown) Green's function, $G(t)$, can be represented as

$$\frac{dC_{AB}(t)}{dt} = -\hat{G}_{AB}(t) + \hat{G}_{BA}(-t) \approx -G_{AB}(t) + G_{BA}(-t)\,. \qquad (2\text{-}1)$$

Here, the approximation indicates that the EGF, $\hat{G}(t)$, may differ from the exact Green's function, $G(t)$, because of effects of anelasticity and specific spatial distribution and spectral properties of the (ambient) noise (Roux *et al.*, 2005; Paul *et al.*, 2005). Later in this section we will illustrate some of these effects, but for notational simplicity we will drop the distinction of $\hat{G}$ and G. In equation (2-1), $G_{AB}(t)$ is the actual Green's function at receiver B for a fictitious (point) source located at A, and $G_{BA}(-t)$ is the time-reversed Green's function at A for a fictitious (point) source at B. In view of causality, $G_{AB}(t)$ contributes at $t \geq 0$ and $G_{BA}(-t)$ contributes at $t \leq 0$. Furthermore, $C_{AB}(t)$ is the approximate cross-correlation function between the two stations given by

$$C_{AB}(t) \approx \int_0^{t_C} v_A(\tau) v_B(t+\tau)\, d\tau\,, \qquad (2\text{-}2)$$

where $v_A(t)$ and $v_B(t)$ are the continuously recorded, but time-windowed broad-band data at stations A and B, respectively, and t_C is the total cross-correlation time (i.e., observation time).

The $\pi/2$ phase shift between EGF and NCF does not influence estimates of the group velocity between points A and B: indeed, some studies use NCFs (Shapiro & Campillo, 2004; Shapiro *et al.*, 2005), whereas others prefer to use EGFs because the time-derivation enhances the higher frequencies (Sabra *et al.*, 2005a, b). The change in amplitude spectrum may, however, affect the group velocity measurements. In contrast, phase velocities do not depend on the amplitude information, but ignoring the phase shift produces an error, which becomes significant if the inter-station distance AB is comparable to or less than the wavelengths considered. In this study, we compute the phase velocities from the EGFs.

2.2.2 Temporal variations from microseisms and scatter

To test the robustness of the EGFs we compute them for different time periods: for this purpose, we arbitrarily choose the months of April, May, June, and July of 2004. In a first set of experiments, we use a (generous) group-velocity window (2 – 10 km/s) to mute the wave trains from earthquakes with $m_b \geq 6$ (that is, in the corresponding group-velocity window we set the amplitude to zero) in order to approximate cross-correlations from ambient "noise" (which includes signal that is not directly related to large events). We follow Campillo & Paul (2003) and Shapiro & Campillo (2004) to compute for every possible station pair the NCF by one-bit cross-correlation of the vertical component seismograms which are both band-pass filtered in the period bands 10 – 60 s. We do this for each month separately. The time t in equation (2-2) is from $-t_m$ to t_m; $t_m = \Delta/v_m$, with Δ the inter-station distance and v_m the minimum group velocity, which is set to be 1.5 km/s. Figures 2-2a and 2-3 show, for different station pairs, that the EGFs constructed from recordings in the different months are similar to one another.

2.2.3 Directionality and amplitude spectrum

Theoretically, the Green's functions $G_{AB}(t)$ and $G_{BA}(-t)$ should be each others reciprocal. However, EGFs may become one-sided due to preferred directions to noise sources, e.g., the ocean microseisms in the study by Sabra *et al.* (2005a). For our study, Figures 2-2a and 2-3(a,c,d) reveal a clear directionality: the EGFs for station pairs lining up in N-S direction are one-sided whereas the stations lining up in E-W direction are much more symmetric (e.g., Figure 2- 3b).

In order to investigate if this difference depends on frequency, for station pair MC04-MC23 we compute EGFs in different period bands (10 – 20 s, 20 – 30 s, 30 – 40 s, and 40 – 60 s) (Figure 2-4). In the period bands 10 – 20 s (Figure 2-4a) and 20 – 30 s (Figure 2-4b) the EGFs are one-sided and stable over the four months. However, in the period bands 30 – 40 s (Figure 2-4c) and 40 – 60 s (Figure 2-4d) the EGFs do not show the one-sided feature and the different months yield different results. Similar frequency dependencies are observed for other station pairs.

The EGFs in the period bands 10 – 20 s (Figure 2-4a) are very similar to those for 10 – 60 s (Figure 2-2a). Amplitude spectra, shown in Figure 2-5 for April, reveal that the dominant frequency band of the EGFs is ~ 0.08 – 0.05 Hz (i.e., ~ 12 – 20 s) and that their energy is very low at frequencies less than 0.04 Hz (or periods larger than 25 s). The latter may explain the instability of the EGFs observed in Figures 2-4c and d; the low frequency waves do not create coherent waves between the station pair. It seems reasonable to assume that the one-sided feature (that is, the failure of reciprocity) in EGFs for the N-S directions is primarily due to the significant lack of seismicity north of the array (Figure 2-1, inset), in combination with inter-station scattering. However it is not obvious why the expression of this is so different in the intermediate or longer period bands (T > 30 s), and the part of the data that contributes to the EGFs at periods larger than 30 s should be investigated further.

2.2.4 Effects on EGFs of specific earthquakes and noise signals

By definition, a Green's function represents the solution due to a point source and is unrelated to the actual source. This is not, generally, true for EGFs. Indeed, because uneven regional distribution of background seismicity can produce directionality of the EGFs (see above), we should investigate if the presence of large earthquakes can produce bias. For that purpose, we compute EGFs, for T = 10 – 60 s, after muting signal related to (known) earthquakes with $m_b \geq 5$ (instead of the $m_b \geq 6$ used in the experiment described above). The results, shown (again) for station pair MC04-MC23 (Figure 2-2b), are almost the same as for input data void only of the signal due to larger earthquakes (Figure 2-2a). Tests with magnitude cut-off at 4 or 3 give similar results, which implies that the effect on EGFs from specific earthquakes is small compared to the contributions from micro-seismicity and ambient noise.

2.2.5 EGFs from surface-wave coda

It has been demonstrated that the diffusive character of coda waves due to multiple scattering in the lithosphere can be used to estimate the Green's functions between two seismic stations (Campillo & Paul, 2003; Paul *et al.*, 2005). Therefore, complementary to calculating EGFs from background seismic noise (approximated by the muting of signal

from large earthquakes), we calculate them (again with one-bit cross correlation) from the coda of the surface waves due to large earthquakes. For this purpose we mute much of the data and only keep the surface-wave coda (in the group velocity window 1.5 – 3 km/s) from larger earthquakes with $m_b \geq 5$. The EGFs estimated from the surface-wave coda (Figure 2-2c) are almost the same (in the surface-wave part) as the EGFs from ambient seismic noise (previous section), but they become increasingly unstable when the magnitude cut-off increases and when, as a consequence, the number of data decreases (Figure 2-2d). Similar to the EGFs from ambient seismic noise (Figure 2-2a, b), the EGFs from coda correlation (Figure 2-2c, d) also show time-asymmetry due to the predominant directions in the source distribution (Paul *et al.*, 2005).

2.3 Phase velocity dispersion from EGFs

Previous studies estimated group velocity dispersion from NCFs (Shapiro & Campillo, 2004; Shapiro *et al.*, 2005) or EGFs (Sabra *et al.*, 2005a, b). However, this relies on the amplitudes of the wave trains, which may be more prone to bias than information on the phase. Here we demonstrate that phase velocity dispersion can be calculated from the EGF through the use of a far-field representation of the surface-wave Green's function and an image transformation technique (Yao *et al.*, 2005). In the far-field, the time harmonic wave of the Green's function for the surface-wave fundamental mode at frequency ω is given by (Dahlen & Tromp, 1998)

$$\mathrm{Re}\{G_{AB}(\omega)\exp(-i\omega t)\} \approx (8\pi kS)^{-1/2}\cos(k_{AB}\Delta - \omega t + \frac{\pi}{4}), \qquad (2\text{-}3)$$

where $k_{AB} = \frac{1}{\Delta}\int_0^{\Delta} k d\Delta = \frac{\omega}{c_{AB}}$ is the average wavenumber between "source" A and receiver B, c_{AB} is the average phase velocity, Δ is the surface distance traversed by the arrival under consideration between "source" A and receiver B, S is the geometrical spreading for surface waves such that $S \rightarrow \sin(\Delta/R)$ (R is the radius of the Earth) towards the source, and $\frac{\pi}{4}$ is remnant of the asymptotic expansion of the Legendre function. We require Δ to be at least three wavelengths (λ) in order to satisfy the far-field approximation. When the phase travel time t satisfies

$$k_{AB}\Delta - \omega t + \frac{\pi}{4} = 0 \tag{2-4}$$

it will correspond to one peak in the harmonic wave of Green's function. At that point the average phase velocity c_{AB} at frequency ω can be calculated by

$$c_{AB}(T) = \frac{\Delta}{t - T/8}, \tag{2-5}$$

where $T = 2\pi/\omega$ is the corresponding period. With the far-field limitation, we require

$$c_{AB} \cdot T = \lambda \leq \Delta/3. \tag{2-6}$$

For each station pair, equation (2-6) determines the largest period to be considered; effectively it produces denser path coverage at shorter periods than at longer periods. For multi-resolution imaging this has the attractive property that path coverage will be densest for the shortest period waves considered.

We now illustrate how to extract the phase velocity dispersion curve from the EGF using the far-field approximation and an image transformation technique. First, we band-pass filter the EGFs at central periods from 10 to 60 s, with 1 s intervals and a pass-band width of 0.4 s. (We remark that for non-symmetric correlation functions the side with the larger amplitude is used as the EGF for subsequent analyses – e.g., the left side of Figure 2-2a.) Then, we construct a time-period (t-T) image (e.g., Figure 2-6a) for the surface-wave part (determined by a group-velocity window, e.g., 2.5 – 5 km/s). Each column of the t-T image represents an amplitude normalized EGF filtered at certain period T (the black trace in Figure 2-6a is for T = 20 s). On the t-T image the frequency dependence is readily observed; notice, for instance, the increase of the phase travel time with decreasing period (Figure 2-6a).

Each column of the t-T image (e.g., the black trace in Figure 2-6a) is then transformed to a velocity-coordinate waveform (black trace in Figure 2-6b) using equation (2-5) and a spline interpolation in order to get an evenly spaced velocity coordinate and to keep the amplitude information unchanged upon transformation. Thus, a peak point at the filtered EGF (e.g., P in Figure 2-6a) will have the same phase velocity as that of the corresponding peak at the transformed waveform (e.g., P* in Figure 2-6b). We use this

procedure to transform the *t-T* image to a velocity-period (*c-T*) image (Figure 2-6b). On the *c-T* image the dispersion curve can be easily identified and automatically picked, and the 2π ambiguity in phase velocity measurement is well resolved. This image transformation technique, introduced by Yao *et al.* (2005) to measure phase velocities for the two-station method, greatly enhances the efficiency and reliability of phase velocity measurements. Compared to the measurement of the group travel time (i.e., the time of the (broad) peak at the envelope) that is needed to determine the group velocities (e.g., Shapiro & Campillo, 2004; Sabra *et al.*, 2005a), the measurement of the peak travel time for the phase velocities appears to be more accurate.

We infer the Rayleigh-wave phase velocity dispersion (e.g., blue lines in Figure 2-7a, b, c) for $T = 10 - 50$ s from vertical component EGFs for all possible two-station paths for the four months considered. Recall that the maximum period for the phase velocity measurement of each station pair is set by equation (2-6) and, thus, the distance between the pair of receivers considered. For each path we calculate the average phase velocity and its standard error at each period. Finally, we obtain the average phase velocities for the array area (with the corresponding standard errors) by averaging the phase velocity (and its standard error) for all paths (Figure 2-7d). The standard errors are quite small (about 0.01 km/s at 10 – 20 s, 0.015 km/s at 25 s, and 0.024 km/s at 30 s), which shows that EGFs from one-bit cross-correlation of one month of ambient seismic noise can give precise phase velocity measurements at the relatively short periods considered here (i.e., 10 – 30 s). For the phase velocity maps presented here we do not use EGF-derived phase velocity measurements at the periods larger than 30 s because at longer periods the EGFs are less robust, in part because the far-field approximation (2-6) and the lateral extent of the array limit the number of data at those periods.

2.4 Phase velocity maps

2.4.1 Phase velocity maps from EGFs

We use the technique by Tarantola & Valette (1982) and Tarantola & Nercessian (1984) to invert the phase velocity dispersion measurements from EGFs to obtain the Rayleigh-

wave phase velocity variation at different periods. We first obtain the phase slowness (the inverse of the phase velocity) maps by minimization of the cost function

$$\Phi(\mathbf{s}) = (\mathbf{t}-\mathbf{t}_{obs})^{\mathrm{T}}\mathbf{C}_D^{-1}(\mathbf{t}-\mathbf{t}_{obs}) + (\mathbf{s}-\mathbf{s}_p)^{\mathrm{T}}\mathbf{C}_M^{-1}(\mathbf{s}-\mathbf{s}_p); \tag{2-7}$$

from this we calculate the phase velocity distribution. In equation (2-7), $\mathbf{s}$ is the 2-D phase slowness model, $\mathbf{s}_p$ is the *prior* 2-D phase slowness model, $\mathbf{t}_{obs}$ is the vector of observed phase travel times (the i^{th} component is given by $(\mathbf{t}_{obs})_i = \Delta_i / c_i$, i runs through all combinations AB, see equation (2-5)), $\mathbf{t}$ is the predicted phase travel time from the phase slowness model $\mathbf{s}$, $\mathbf{C}_D$ is the data covariance matrix describing the data uncertainties, and $\mathbf{C}_M$ is the *prior* model covariance function.

The predicted phase travel time for the ith path is determined by $t_i = \int_0^{\Delta_i} s d\Delta$, where the integral is along the great-circle path and Δ_i is the inter-station distance. The region under study is parameterized by means of $0.5° \times 0.5°$ grid points. The phase slowness s at any point in the inversion area is determined from the values at four surrounded grid points using bilinear interpolation. The *prior* model covariance function $\mathbf{C}_M(r_1, r_2)$ represents the covariance between model estimates at r_1 and r_2:

$$\mathbf{C}_M(r_1, r_2) = \sigma_s^2 \exp\left(-\frac{(r_1 - r_2)^2}{2L^2}\right), \tag{2-8}$$

where $\sigma_s = \sigma_c / c_0^2$ represents the *prior* slowness uncertainty, σ_c is the *prior* phase velocity uncertainty with respect to the homogenous starting model with phase slowness $1/c_0$, and L is the correlation length of the model. We set σ_c to 0.15 km/s, and c_0 is the average phase velocity (at a certain period) in the region. On the basis of results from resolution tests, we choose the correlation length L, which determines the smoothness of the phase slowness maps, to be 100 km.

In order to investigate whether the phase velocity measurements from different months influence the inversion results, we invert the phase velocities at T = 10 s of each of the four months under consideration to obtain the Rayleigh-wave phase velocity maps for the four separate months using a homogeneous starting model. The results (Figure 2-8) are

quite similar to one another, which confirms the stability of the EGFs with regard to temporal variations in regional (micro-)seismicity. Subsequently, we use the phase velocities for each path averaged over the four months to obtain the phase velocity maps at 10, 15, 20, 25, and 30 s. Figure 2-9(a-c) shows the path coverage for the averaged dispersion data at T = 10, 20, and 30 s. At 10 s the number of averaged phase velocity measurements is 267, which is close to the maximal number (300) of two-station measurements for a seismic array with 25 stations. A series of checkerboard resolution tests suggests that in much of the area under study the horizontal resolution of the phase velocity maps derived from the EGFs is ~ 100 km (Figure 2-10b). Figures 2-11(a-c) show examples of phase velocity maps at T = 10, 20, and 30 s.

We evaluated the reliability of the phase velocity measurements from EGFs by a comparison with group velocities. Ignoring the distortion of the amplitude spectrum, we use a frequency-time analysis to measure from EGFs the group velocities in the period band 10 – 30 s. Using $g = d\omega / dk = c + k \cdot dc / dk$, with c and g the phase and group velocities, respectively, we then predict c from the measured g. The average absolute discrepancy between c thus inferred and the phase velocities measured directly from EGFs gradually increases from ~ 0.01 km/s at T ~ 10 s to ~ 0.04 km/s at T ~ 30 s, which for our study region is about an order of magnitude smaller than the observed variation (~ 0.3 – 0.4 km/s, Figure 2-11(a-c)). Compared to the phase velocities inferred directly from EGFs, c derived from the group velocities are 0.01 – 0.02 km/s higher in the period band 20 – 30 s, which may indicate that at these periods the phase velocity measurements are slightly underestimated (by about ~ 0.3 – 0.6%). The discrepancy increase with increasing period, suggesting that phase velocity measurements at shorter periods (10 – 20 s) are more reliable than at relatively longer periods (T > 30 s), in accord with Figure 2-7d.

2.4.2 Phase velocity maps from two-station (TS) method

We use a two-station (TS) method (Yao *et al.*, 2005) to measure Rayleigh-wave fundamental-mode phase velocity dispersion in the period bands 20 – 120 s. We assume surface-wave propagation along a great-circle path between earthquake and station. For

each two-station dispersion measurement, in order to suppress the influence of the structure between the earthquake and the station nearest to it, we require that the earthquake and the station pair considered are (approximately) on the same great circle path, with the maximum two deviation angles (α and β in Figure 2-12a) each less than 3°. The average phase velocity of the two-station path is then approximated by

$$c(T) \approx \frac{\Delta_2 - \Delta_1}{\Delta t(T)}, \tag{2-9}$$

where $c(T)$ is the phase velocity at period T, $\Delta t(T)$ is the phase travel time at period T estimated from cross-correlation of narrow band-pass filtered waveforms at central period T at the two stations*, Δ_2 is the distance from the earthquake to the farthest station, and Δ_1 is the distance to the nearest station. For a small difference in propagation distance, a small error δt in the measurement of $\Delta t(T)$ will cause a considerable error in the phase velocity measurements, in particular at longer periods. For example, if Δ_2 - Δ_1 = 200 km, Δt = 60 s at T = 20 s (i.e., c ~ 3.33 km/s), Δt = 48 s at T = 100 s (i.e., c ~ 4.17 km/s), and δt = 1 s, the relatively error in the phase velocity measurement $\delta c/c = \delta t/\Delta t$ is ~ 1.7% at T = 20 s and ~ 2.1% at T = 100 s. In order to make reliable measurements at relatively longer periods, we require Δ_2 - Δ_1 to be at least half of the wavelength ($\lambda = c(T) \cdot T$); here we refer to this as the half-wavelength criterion. Consequently, the available phase velocity measurements decrease as the period increases (Figure 2-9(d-j)), which yields a relatively high path density at the shorter periods and lower path density at the longer periods. Note that this has an effect similar to the effect of the far-field approximation described above.

In this way, we obtain about 600 phase velocity dispersion curves for T = 20 – 120 s from about 160 earthquakes with $5.0 \leq M_w \leq 7.0$ and depth < 100 km from October 2003 to September 2004 (Figure 2-13). Figure 2-14 shows an example of phase velocity measurements using the image transformation technique. Red lines in Figure 2-7(a-c) show the extracted dispersion curves for three two-station paths from different earthquakes. Phase velocity dispersion measurements for the same two-station path are

* We note that, formally speaking, the measurement yielded by time domain cross correlation is not the travel time proper and should be interpreted with the appropriate finite frequency sensitivity kernel (see, e.g., Dahlen et al. (2000) and De Hoop and Van der Hilst (2005).

averaged to make 158 average dispersion curves within the period bands 20 – 120 s, and the standard errors of the phase velocities are calculated for paths with at least two measurements. The average phase velocities (red line in Figure 2-7d) and the corresponding standard errors (red error bars in Figure 2-7d) for T = 20 – 120 s are then obtained by averaging all the phase velocity measurements and the standard errors for each period. The standard error increases with increasing period mainly due to the decrease of the inter-station phase travel time $\Delta t(T)$. At the short and intermediate periods (20 – 80 s), the standard error is about 0.03 – 0.04 km/s. However, the standard error increases to ~ 0.05 km/s at 120 s. The standard error given here are lower estimates because we do not consider errors from other sources, e.g., scattering, off-great-circle propagation, etc.

The path coverage of the average phase velocity measurements at different periods, shown in Figure 2-9(d-j), is quite good at periods 20 – 80 s but only about 40 measurements could be made at longer periods (100 – 120 s) due, in part, to the half wavelength criteria and, in part, to the relatively poor data quality at these long periods. We use the same inversion scheme as described in Section 2.4 to produce phase velocity maps for T = 20 – 120 s, except that we set the correlation length L to 100 km at 20 – 60 s, to 150 km at 65 – 80 s, and to 200 km at 85 – 120 s in view of the fact that the physical resolution is limited by the predominant wavelengths considered. The phase velocity maps at 20, 30, 40, 60, 80, 100, and 120 s are shown in Figure 2-11(d-j). The lateral resolution of these maps is about 100 – 200 km at 20 – 60 s (Figure 2-10c, e) and 200 – 300 km at 65 – 120 s (Figure 2-10f).

2.4.3 Wavespeed variations beneath SE Tibet and SW China

In a separate study (Chapter 3) the phase velocity maps will be inverted for 3-D shear wave velocity structure of the crust and upper mantle. Here we merely make some first order observations. In the entire frequency band considered here, high phase velocities mark the (north)eastern part of the array area, close to the Sichuan Basin. In contrast, phase velocity maps at short and intermediate periods (T = 10 – 80 s), shown in Figure 2-11(a-h), exhibit a pronounced low-velocity structure in the northwestern part of the array

area (SE Tibet), which suggests a low shear wave velocity structure in the crust and upper mantle. At T = 100 – 120 s this low velocity anomaly is mapped further South (Figure 2-11i, j). These results are – at least qualitatively – consistent with the finding from travel time that P wave propagation is anomalously slow in the upper mantle beneath SE Tibet and the Red River area (Li *et al.*, 2006), which may be of relevance for geodynamical models of lower crustal flow as suggested by Royden *et al.* (1997) and, for instance, Beaumont *et al.* (2004).

2.5 Discussion: comparison of the EGF and TS results

Phase velocity dispersion measurements were obtained from the EGF and TS analysis in different period bands. The phase velocities at the relatively short period bands (20 – 30 s) are similar for both methods (Figure 2-7a, b, c), but the discrepancies become larger (> 2%) at periods larger than 30 s (e.g., Figure 2-7a). The average phase velocities from the EGF analysis are 0.046 km/s, 0.069 km/s, 0.080 km/s lower than the results from the TS method at 20, 25, and 30 s, respectively. Note that these differences exceed the uncertainties for either method which suggests that the discrepancy may be systematic. Comparison of the phase velocity maps at 20 s (Figure 2-11b, d) and 30 s (Figure 2-11c, e) shows that the overall low and high velocity features are quite similar but that the TS method gives phase velocities that are about 1 – 3% higher than the EGF results.

Several factors can contribute to this discrepancy. For the EGF analysis, in addition to the possibility of (slightly) underestimating the phase velocity measurements (see remarks at the end of Section 2.4.1), the error in the estimation of inter-station phase velocities mainly comes from: (1) incomplete recovery of the Green's function due to the inhomogeneous distribution of the noise sources; and (2) off-great-circle propagation due to inter-station velocity anomalies. The first effect is hard to quantify, but the observed stability of the EGFs between 10 – 30 s suggests that it is relatively small. The second will underestimate inter-station phase velocities because the length of off-great-circle paths is always larger than that of great-circle paths (Figure 2-12b).

For the TS method there are other sources of inaccuracy. The incoming surface-waves are approximated as plane waves. If surface-waves propagate along the great-circle path (solid parallel lines with arrow in Figure 2-12c), the inter-station phase velocity (c_{gc}) is estimated by $c_{gc} \approx (\Delta_2 - \Delta_1)/\Delta t \approx d_{A'B}/\Delta t$, where Δ_1, Δ_2, and Δt are the same as those defined in equation (2-9), and $d_{A'B}$, the difference in great-circle propagation distance between two stations, is the distance of the solid line A′B in Figure 2-12c. When the incoming surface-wave (dashed parallel lines with arrow in Figure 2-12c) deviates from the great-circle propagation path with angle θ (defined in Figure 2-12c), the inter-station phase velocity of this off-great-circle propagation (c_{ogc}) is estimated by $c_{ogc} \approx d_{A''B}/\Delta t$, where $d_{A''B}$, the difference in off-great-circle propagation distance between two stations, is the distance of the dashed line A″B in Figure 2-12c. Therefore, the ratio $c_{ogc}/c_{gc} = d_{A''B}/d_{A'B} = \cos(\beta + \theta)/\cos\beta$, where β is the deviation angle in Figure 2-12c which is same as that in Figure 2-12a. For a very small angle (in our study $\beta \leq 3°$), the ratio c_{ogc}/c_{gc} is less than 1 almost for all θ except in a very small range $-2\beta \leq \theta \leq 0°$ (Figure 2-15), which indicates that the inter-station phase velocity measurements based on the approximation of great-circle propagation will commonly give a higher estimation (e.g., if $\beta = 0°$, the phase velocity is ~ 1.5% higher estimated when $\theta = 10°$ as shown in Figure 2-15).

Other reasons for the frequency-dependent discrepancy of phase velocities between the two methods include the fact that the surface-wave sensitivity zone in the TS method is much larger than the zone of sensitivity to structure in the case of the EGF analysis as shown in Figure 2-12d, especially at longer periods (Yoshizawa & Kennett, 2002; Spetzler, *et al.*, 2002; Zhou *et al.*, 2004). In contrast, the measurements from the EGF analysis are only sensitive to heterogeneity in a very narrow zone between the two stations (Figure 2-12d), which provides a much higher resolution of the structure along the two-station path. Most earthquakes used for the TS analysis are located to the southeastern direction of the array (Figure 2-13); the broader sensitivity kernel for the TS method mainly samples areas with relatively high velocities (e.g., Sichuan basin), whereas wave speeds under the array are mainly slow. This would result in a higher estimation of phase velocities from the TS method than from EGF analysis. (NB this

effect is likely to be small for low frequency waves that are primarily sensitive to upper mantle structure.)

In combination, such physical, geometrical, and structural factors explain why, for our study region, the inter-station phase velocity measurement from the TS method tends to be higher than that from the EGF analysis because the latter tends to underestimate the average phase velocities while at short period the former may overestimate them.

The EGF analysis can provide more reliable phase velocity measurements at relatively short periods (10 – 30 s, in this study), but for array tomography studies it becomes less accurate at longer periods because of the use of the far field approximation. Furthermore, our analysis shows that, for our array, the dispersion measurements become unstable at periods larger than 30 s. In contrast, the TS method can be used to measure phase velocities to much longer periods (e.g., to about 100 s for a two-station path with distance 200 km with the TS method, compared to only ~ 20 s with the EGF analysis). However, the phase velocity measurements at 20 – 30 s from the TS method are less reliable mainly due to the effects of strong scattering on the shorter period part (T < 30 s) of the waveform, off-great-circle propagation and much broader sensitivity zone. To exploit the strengths of both methods, we combine the dispersion data from the EGF and TS analysis to construct phase velocity maps in the period bands from 10 – 120 s, which (in a separate study) we will invert for 3-D shear wave velocity structure of the crust and upper mantle.

2.6 Summary

We have determined empirical Green's functions (EGFs) from the cross-correlation of either (monthly) ambient seismic noise or surface-wave coda recorded at the MIT-CIGMR broad-band network (25 stations) on the southeastern Tibetan plateau in Sichuan and Yunnan provinces, SW China. We used an image transformation technique and a far-field approximation of the surface-wave Green's function to make accurate phase velocity dispersion measurements for relatively short period data (T = 10 – 30 s) for all possible two-station combinations in the array. We showed that noise correlations for

different months give consistent results, that the EGFs are not biased by individual earthquakes, and that the results from ambient noise or surface wave coda are very similar. However, the EGFs are time-asymmetric (one-sided) for stations aligned in the N-S direction, which we attribute to the paucity of seismicity north of the array. For longer periods we have measured inter-station phase velocities using classical two station analysis, and the combination of these methods provides dispersion curves and phase velocity maps over a very broad period range (T = 10 – 120 s), which can be used for high-resolution tomographic studies of the crust and upper mantle beneath this region.

Application of a far-field approximation (in the case of the Green's function analysis) or a half-wavelength criterion (for the two-station analysis) produces a situation that is attractive for multi-scale surface wave tomography: the density of path coverage is proportional to the periods under consideration decreases. Tests with synthetic data demonstrate that our array data should be able to resolve heterogeneity on length scales comparable to and larger than the inter-station spacing (~ 100 km and up, for our array). In future studies this will be exploited in multi-resolution tomography for isotropic and (azimuthally) anisotropic variations in shear wavespeed in the crust and upper mantle beneath SE Tibet.

Phase velocities at short and intermediate periods (T = 10 – 80 s) are prominently low in SE Tibet, suggesting that shear wave propagation may be slow in the shallow part of the lithosphere in SE Tibet. Moreover, phase velocities in the entire period band considered here (T = 10 – 120 s) are high in the vicinity of the Archean Sichuan craton.

Acknowledgements

This work was funded by NSF grant 6892042 of Collaborative Research in Eastern Tibet and AFRL grant FA8718-04-C-0018. We thank Kees Wapenaar (Technical University Delft, The Netherlands), an anonymous reviewer, and Xander Campman (MIT, Cambridge, USA) for their constructive comments, which helped us improve the manuscript.

References

Beaumont, C., R. A. Jamieson, M. H. Nguyen, and S. Medvedev (2004), Crustal channel flows: 1. Numerical models with applications to the tectonics of the Himalayan-Tibetan orogen, *J. Geophys. Res.*, 109, B06406, doi:10.1029/2003JB002809.

Brisbourne, A. and Stuart, G., 1998. Shear-wave velocity structure beneath North Island, New Zealand, from Rayleigh-wave interstation phase velocities, *Geophys. J. Int.*, 133, 175-184.

Campillo, M. and A. Paul, 2003. Long-Range correlations in the diffuse seismic coda, *Science*, 299, 547-549.

Dahlen, F. A. and Tromp, J., 1998. Theoretical Global Seismology, Princeton Univ. Press, Princeton, New Jersey.

Dahlen, F., Hung, S.-H. and Nolet, G., 2000. Fréchet kernels for finite-frequency traveltimes–I. Theory, *Geophys. J. Int.*, 141, 157-174.

De Hoop, M. V. and Van der Hilst, R. D., 2005. On sensitivity kernels for 'wave-equation' transmission tomography, *Geophys. J. Int.*, 160, 621-633.

Engdahl, E.R., Van der Hilst, R.D. & Buland, R.P., 1998. Global teleseismic earthquake relocation from improved travel times and procedures for depth determination, *Bull. seism. Soc. Am.*, 88, 722–743.

Huang, Z., W. Su, Y. Peng, Y. Zheng, and H. Li, 2003. Rayleigh wave tomography of China and adjacent regions, *J. Geophys. Res.*, 108(B2), 2073, doi:10.1029/ 2001JB001696.

Knopoff, L., Muller, S., Pilant,W.L., 1966. Structure of the crust and upper mantle in the Alps from the phase velocity of Rayleigh waves, *Bull. Seismol. Soc. Am.*, 56, 1009-1044.

Li, C., Van der Hilst, R. D., and Toksoz, M. N., 2006. Constraining P-wave velocity variations in upper mantle beneath Southeast Aisa, *Phys. Earth Planet. Inter.*,154, 180-195.

Lobkis, O. I. and R. L., Weaver, 2001. On the emergence of the Green's function in the correlations of a diffusive field, *J. Acoust. Soc. Am.*, 110, 3011-3017.

Passier, M. L., Van der Hilst, R. D., and Snieder, R. K., 1997. Surface wave waveform inversions for local shear-wave velocities under eastern Australia, *Geophys. Res. Lett.*, 24, 1291-1294.

Paul, A., M. Campillo, L. Margerin, E. Larose, and A. Derode, 2005. Empirical synthesis of time-asymmetrical Green functions from the correlation of coda waves, *J. Geophys. Res.*, 110, B08302, doi:10.1029/2004JB003521.

Roux, P., K. G., Sabra, W. A., Kuperman, and A. Roux, 2005. Ambient noise cross correlation in free space: Theoretical approach, 2005, *J. Acoust. Soc. Am.*, 117, 79-84.

Royden, L.H., Burchfiel, B.C., King, R.W., Wang, E., Chen, Z., Shen, F. and Yuping, L., 1997. Surface deformation and lower crustal flow in eastern Tibet, *Science,* 276, 788–790.

Sabra, K. G., P. Gerstoft, P. Roux, W. A. Kuperman, and M. C. Fehler, 2005a. Extracting time-domain Greens function estimates from ambient seismic noise, *Geophys. Res. Lett.*, 32, L03310, doi:10.1029/2004GL021862.

Sabra, K. G., P. Gerstoft, P. Roux, and W. A. Kuperman, 2005b. Surface wave tomography from microseisms in Southern California, *Geophys. Res. Lett.*, 32, L14311, doi:10.1029/2005GL023155.

Shapiro, N. M. and Ritzwoller, M. H., 2002. Monte-Carlo inversion for a global shear-velocity model of the crust and upper mantle, *Geophys. J. Int.*, 151, 88-105.

Shapiro, N. M. and Campillo, M., 2004. Emergence of broadband Rayleigh waves from correlations of the ambient seismic noise, *Geophys. Res. Lett*, 31,L07614, doi:10.1029/ 2004GL019491.

Shapiro, N. M., Campillo, M., Stehly, L., and Ritzwoller, M. H., 2005. High-resolution surface wave tomography from ambient seismic noise, *Science*, 307, 1615-1618.

Simons, F. J., van der Hilst, R. D., Montagner, J. P., and Zielhuis, A., 2002. Multimode Rayleigh wave inversion for heterogeneity and azimuthal anisotropy of the Australian upper mantle, *Geophys. J. Int.*, 151, 738-754.

Spetzler, J., Trampert, J., Snieder, R., 2002. The effect of scattering in surface wave tomography, *Geophys. J. Int.*, 149, 755-767.

Tarantola, A., and B., Valette, 1982. Generalized nonlinear inverse problem solved using the least squares criterion, *Rev. Geophys. Space Phys.*, 20(2), 219-232.

Tarantola, A., and Nercessian, A., 1984. Three-dimensional inversion with blocks, *Geophys. J. R. Astron. Soc.* 76, 299-306.

Trampert, J. and Woodhouse, J., 1996. High resolution global phase velocity distributions. *Geophys. Res. Lett.*, 23, 21–24.

Weaver, R. L. and O. I., Lobkis, 2004. Diffuse fields in open systems and the emergence of the Green's function. *J. Acoust. Soc. Am.*, 116, 2731-2734

Yao, H., G., Xu, L., Zhu, and X., Xiao, 2005. Mantle structure from inter-station Rayleigh wave dispersion and its tectonic implication in western China and neighboring regions, *Phys. Earth Planet. Inter.*, 148, 39-54.

Yao, H., Beghein, C., and Van der Hilst, R.D., 2008, Surface-wave array tomography in SE Tibet from ambient seismic noise and two-station analysis: II – Crustal and upper mantle structure, *Geophys. J. Int.*, 173, 205-219.

Yoshizawa, K. and Kennett, B.L.N., 2002. Determination of the influence zone for surface wave paths, *Geophys. J. Int.*, 149, 441-454.

Zielhuis, A. and Nolet, G., 1994. Deep seismic expression of an ancient plate boundary in Europe, *Science*, 265, 79-81.

Zhou Y., Dahlen, F. A., and Nolet, G., 2004. Three-dimensional sensitivity kernels for surface wave observables, *Geophys. J. Int.*, 158, 142-168.

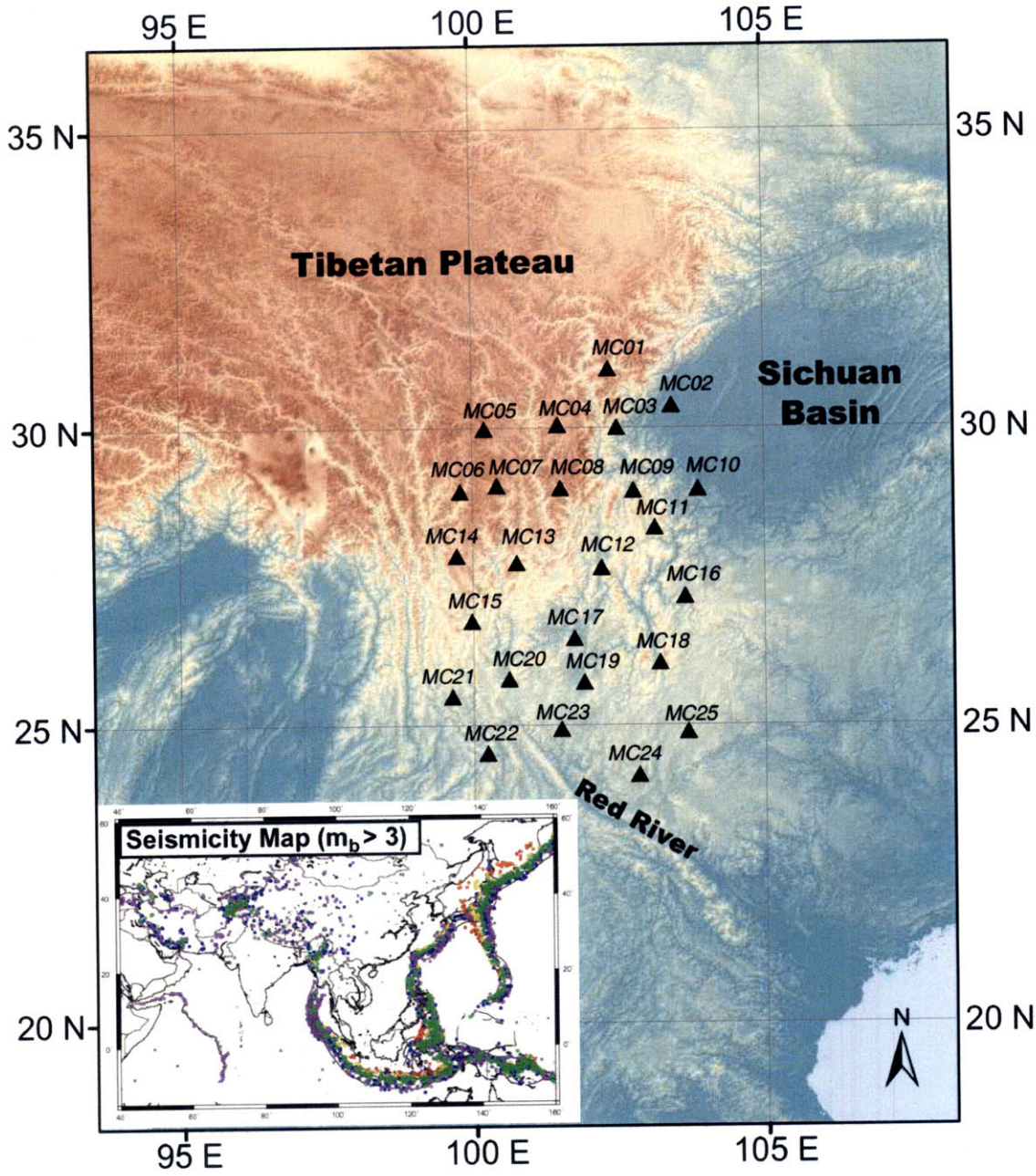

Figure 2-1. The location of 25 stations of the MIT - CIGMR array. The inset (lower left): epicenter of earthquakes with $m_b > 3$ that occurred in 2004 (according to Engdahl et al., 1998).

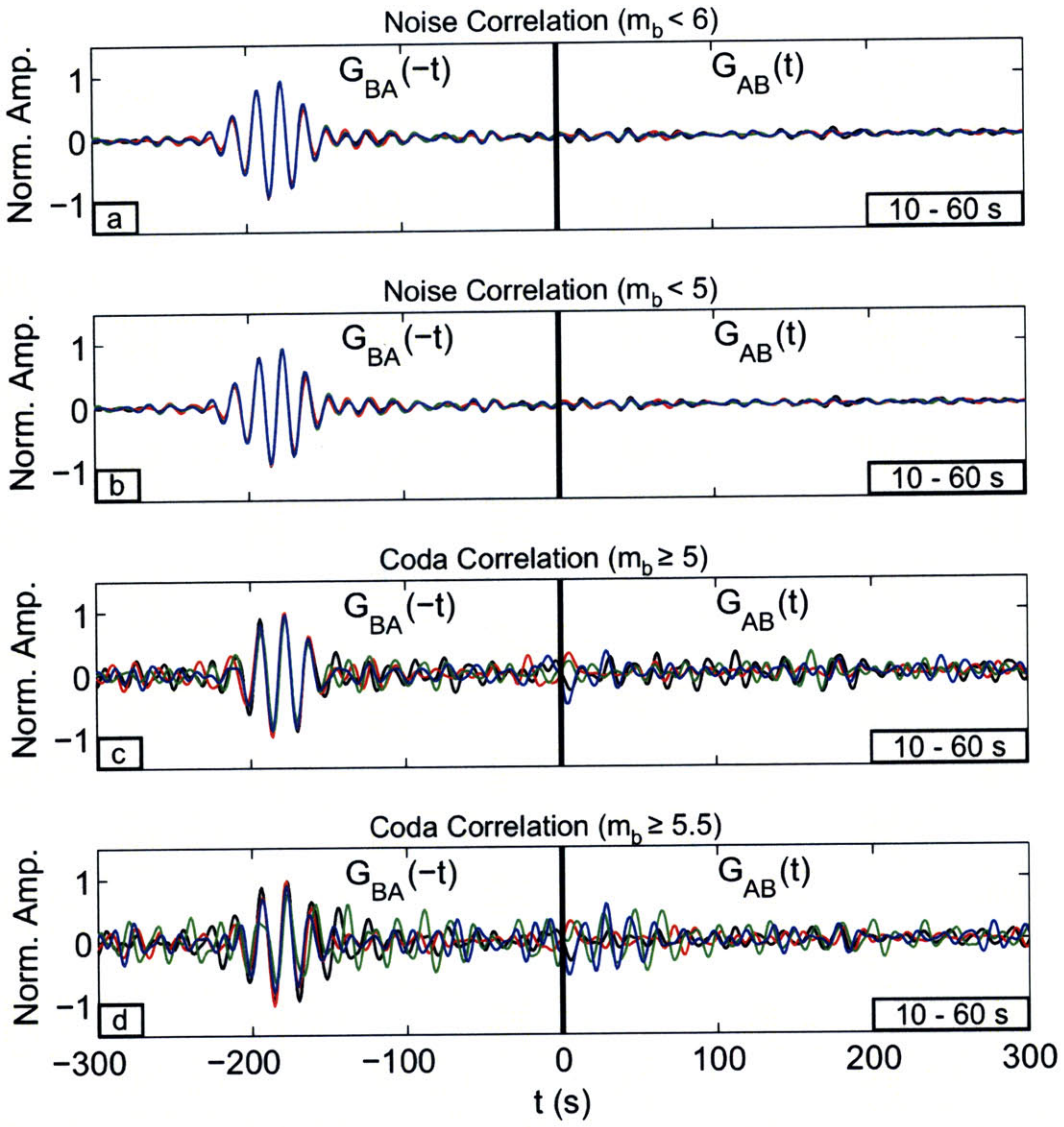

Figure 2-2. EGFs in the period bands 10 – 60 s from one-bit cross-correlation of vertical component ambient seismic noise (a, b) and surface-wave coda (c, d) of the two-station pair MC04-MC23 for four months in 2004 (black - April, red - May, green - June and blue - July). The right half ($t > 0$) and the left half ($t < 0$) of each plot represent the EGF from MC04 (source) to MC23 (receiver) and the EGF from MC23 to MC04, respectively. For (a), using a group-velocity window, wave trains from earthquakes with $m_b \geq 6.0$ are muted for both stations before the correlation, and the same for (b) but with $m_b \geq 5.0$. For (c) only surface-wave coda from earthquakes with $m_b \geq 5.0$ are kept for the cross-correlation and the same for (d) but with $m_b \geq 5.5$. "Norm. Amp." on the vertical axis means "normalized amplitude".

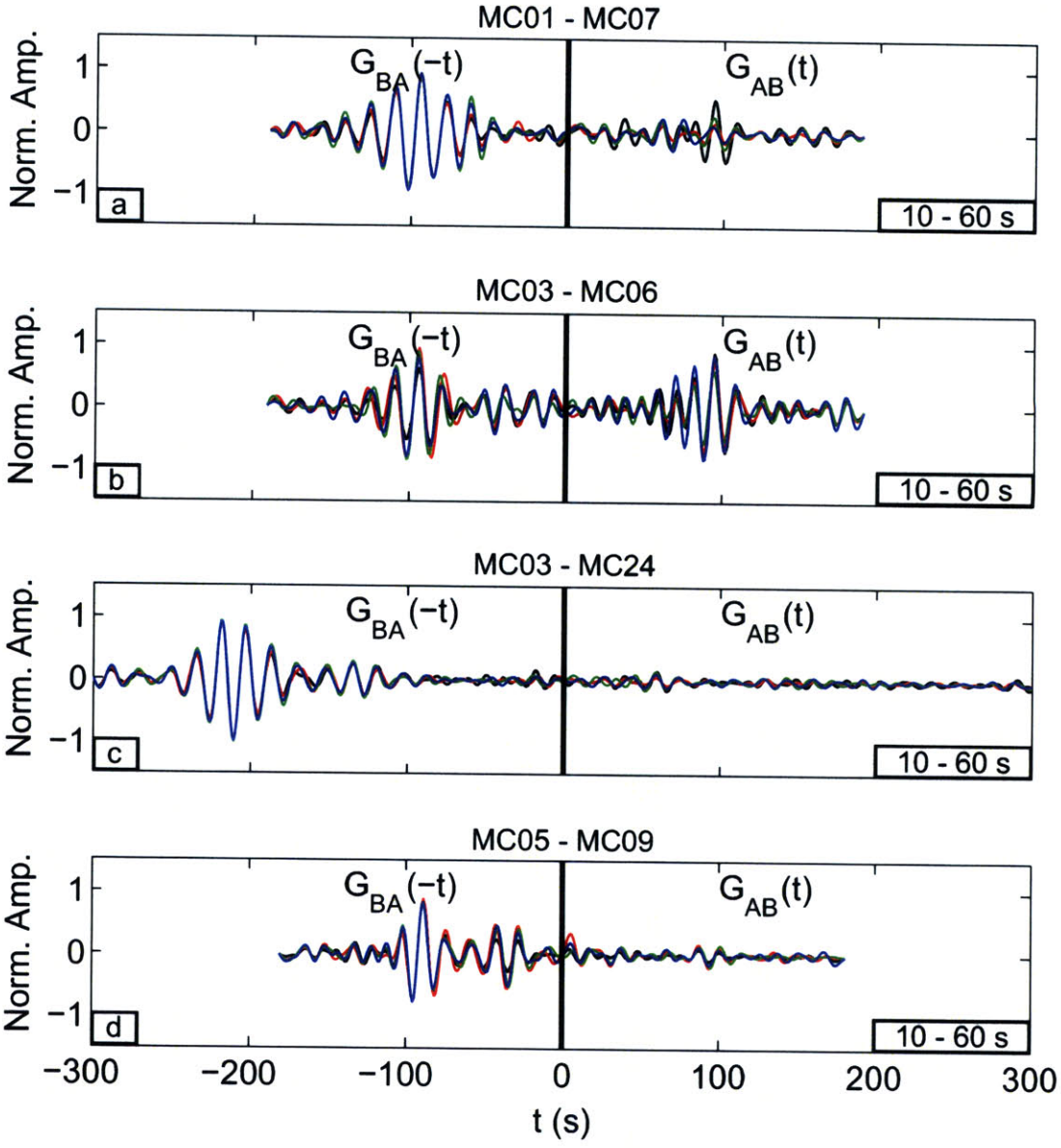

Figure 2-3. EGFs (normalized amplitude) from the cross-correlation of ambient seismic noise of different station pairs in the period bands 10 – 60 s for four months in 2004 as in Figure 2-2(a).

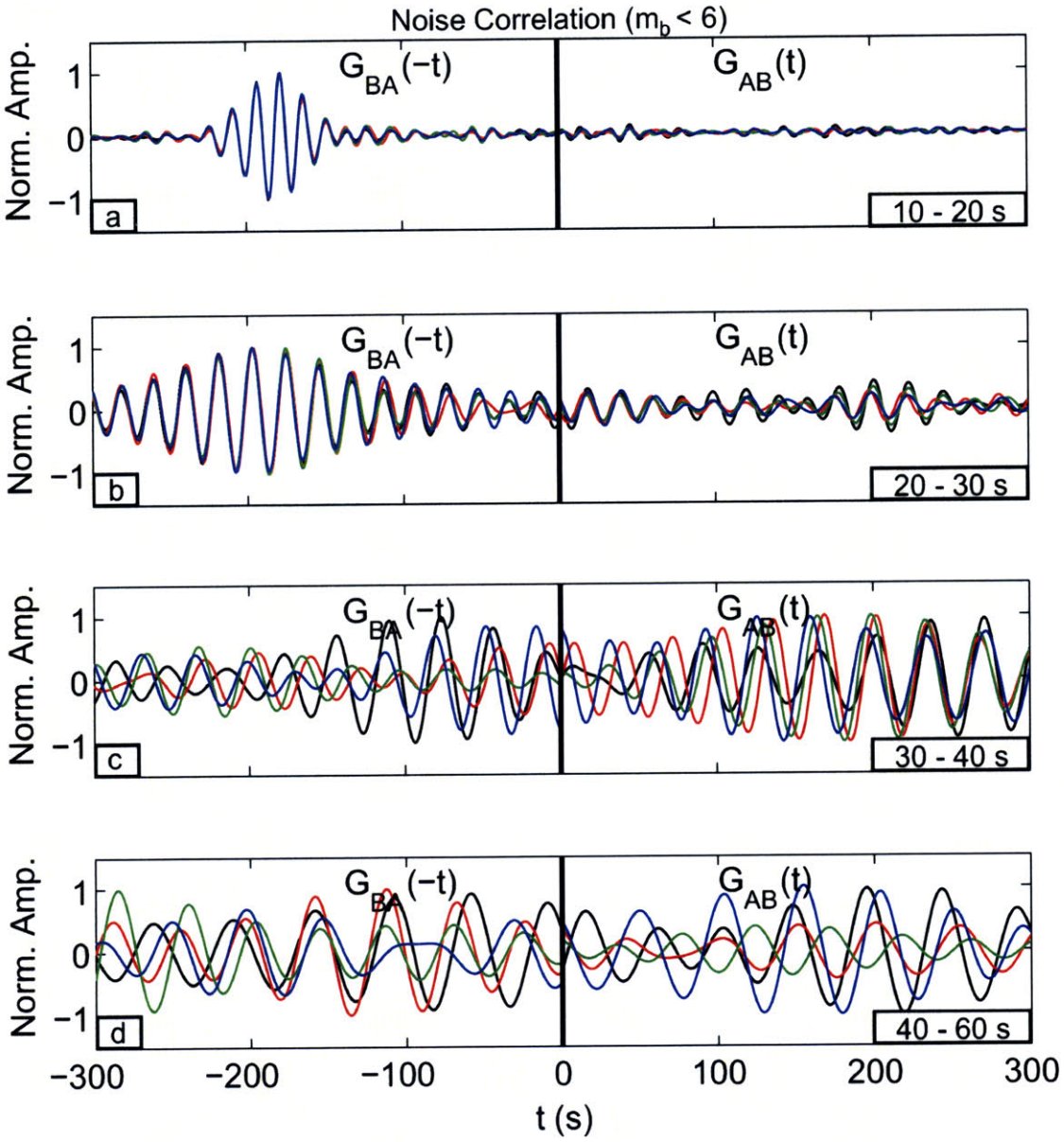

Figure 2-4. EGFs (normalized amplitude) from the cross-correlation of ambient seismic noise of the two-station pair MC04-MC23 for four months in 2004 as in Figure 2- 2(a) but in different period bands: (a) 10 – 20 s; (b) 20 – 30 s; (c) 30 – 40 s; and (d) 40 – 60 s.

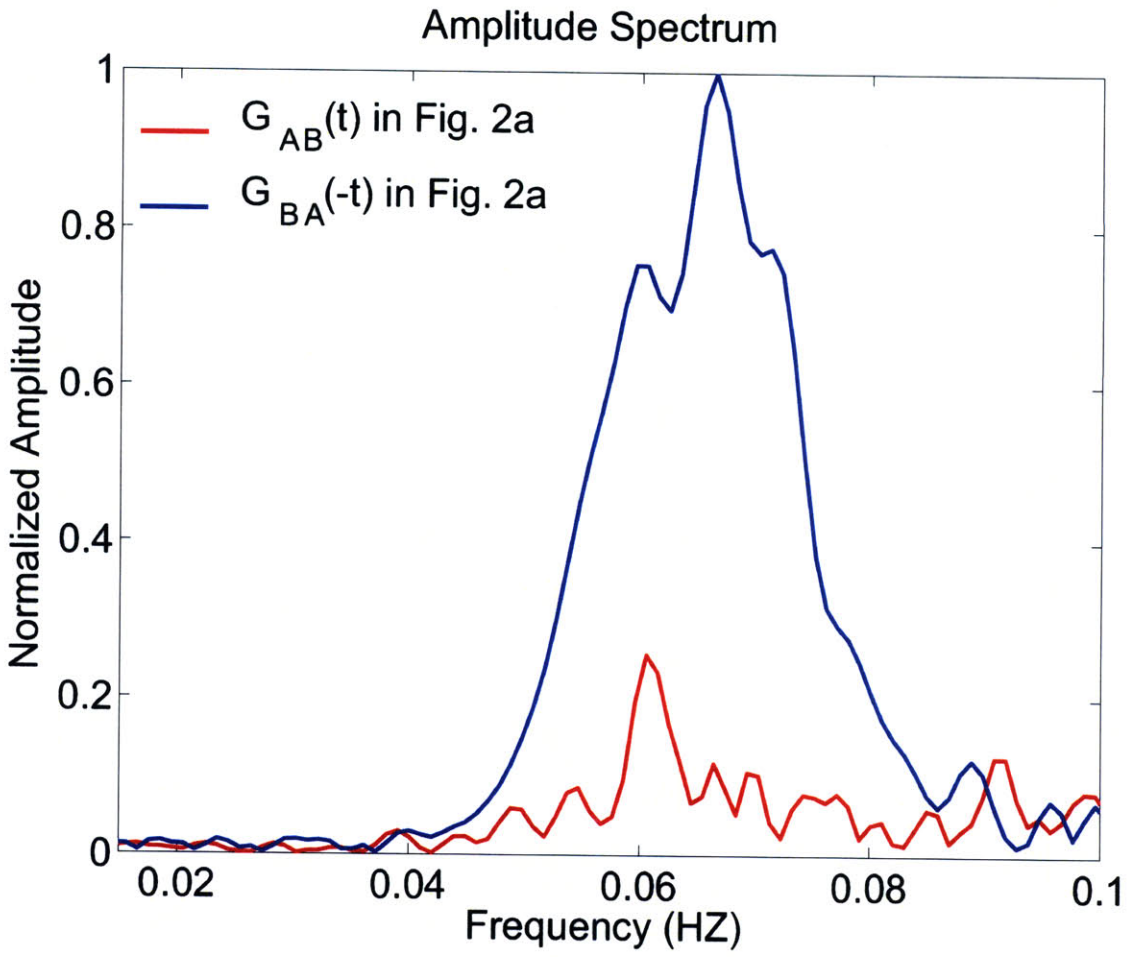

Figure 2-5. Amplitude spectrum of the EGF of the two-station pair MC04-MC23 for April in 2004 (black waveform in Figure 2-2a): blue line for the left part of the EGF and red line for the right part of the EGF.

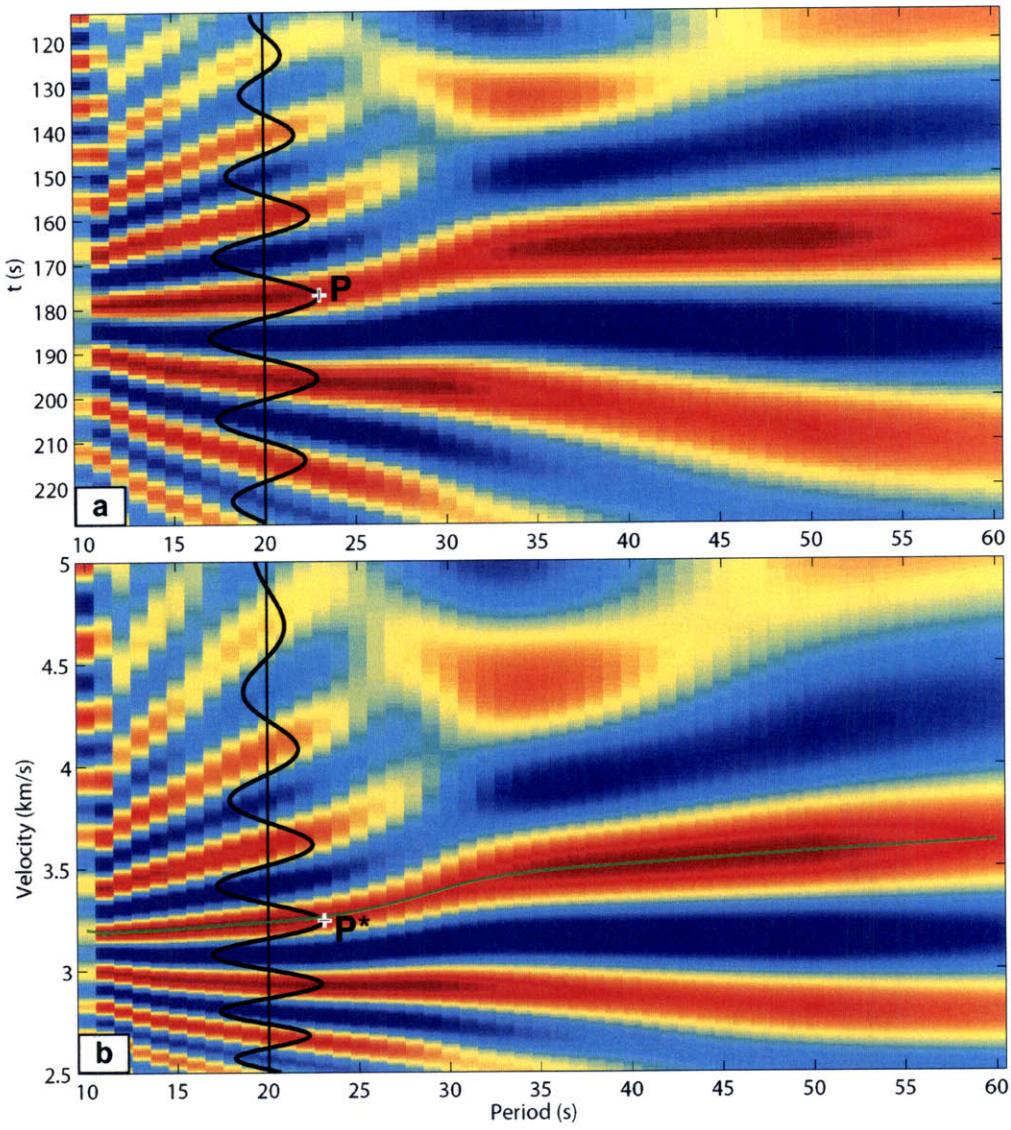

Figure 2-6. Phase velocity dispersion measurements from the EGF of MC23-MC04 in April 2004: (a) time-period (t-T) image by narrow band-pass filtering the EGF; the black waveform is the normalized EGF filtered at the central period T = 20 s, which corresponds to the column at the T = 20 s on the t-T image; (b) velocity-period (c-T) image and phase velocity dispersion measurements (solid green line); the black waveform, which corresponds to the column at the T = 20 s on the c-T image, is the transformed velocity coordinate waveform from the waveform in (a) using equation (2-5) and a spline interpolation. Red and blue on (a) and (b) represent the peak and trough of the wave trains, respectively. The peak point P at the waveform in (a) is transformed to the peak point P* at the waveform in (b).

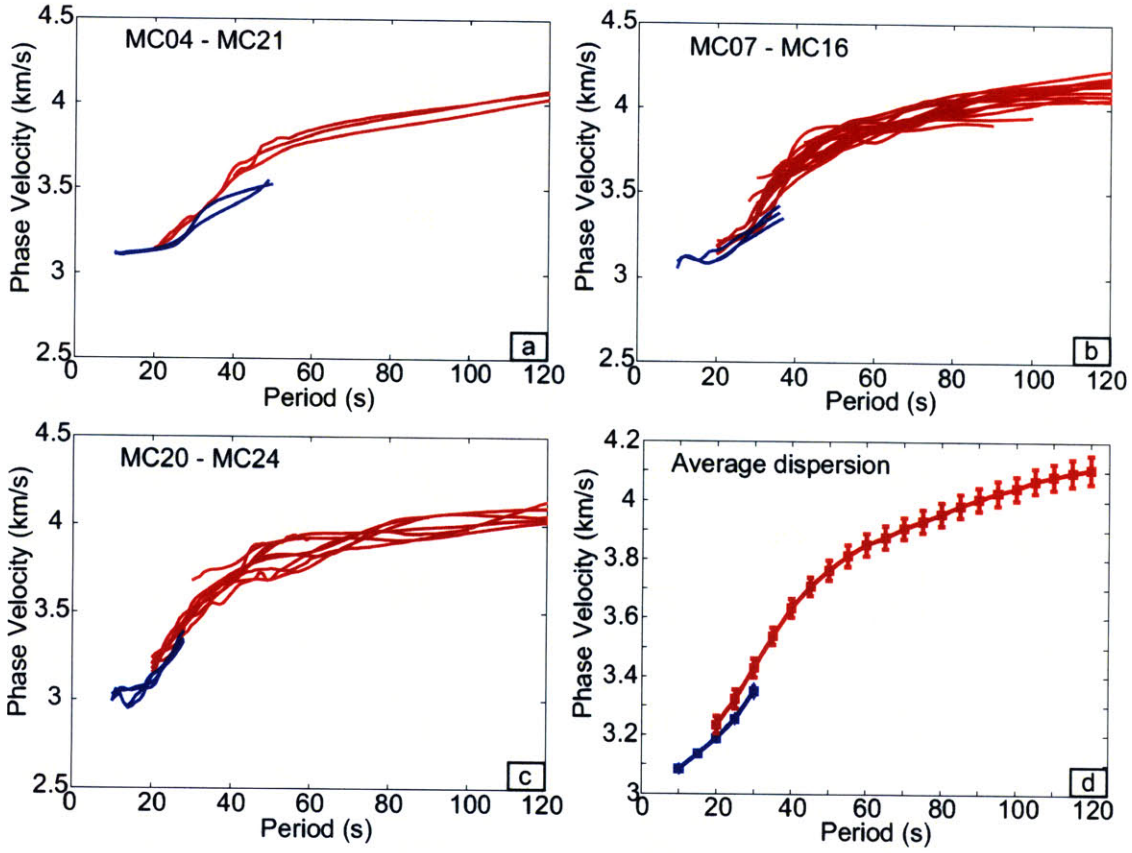

Figure 2-7. Rayleigh-wave phase velocity dispersion measurements from the EGF and TS analysis: (a-c) Rayleigh-wave phase velocity dispersion curves of different two-station paths from the EGF analysis for different months (blue lines) and from the TS analysis for different earthquakes (red lines); (d) average Rayleigh-wave phase velocity dispersion curve and the average standard errors for the studied area from the EGF analysis (blue line and error bars in the period bands 10 – 30 s) and from the TS method (red line and error bars in the period bands 20 – 120 s).

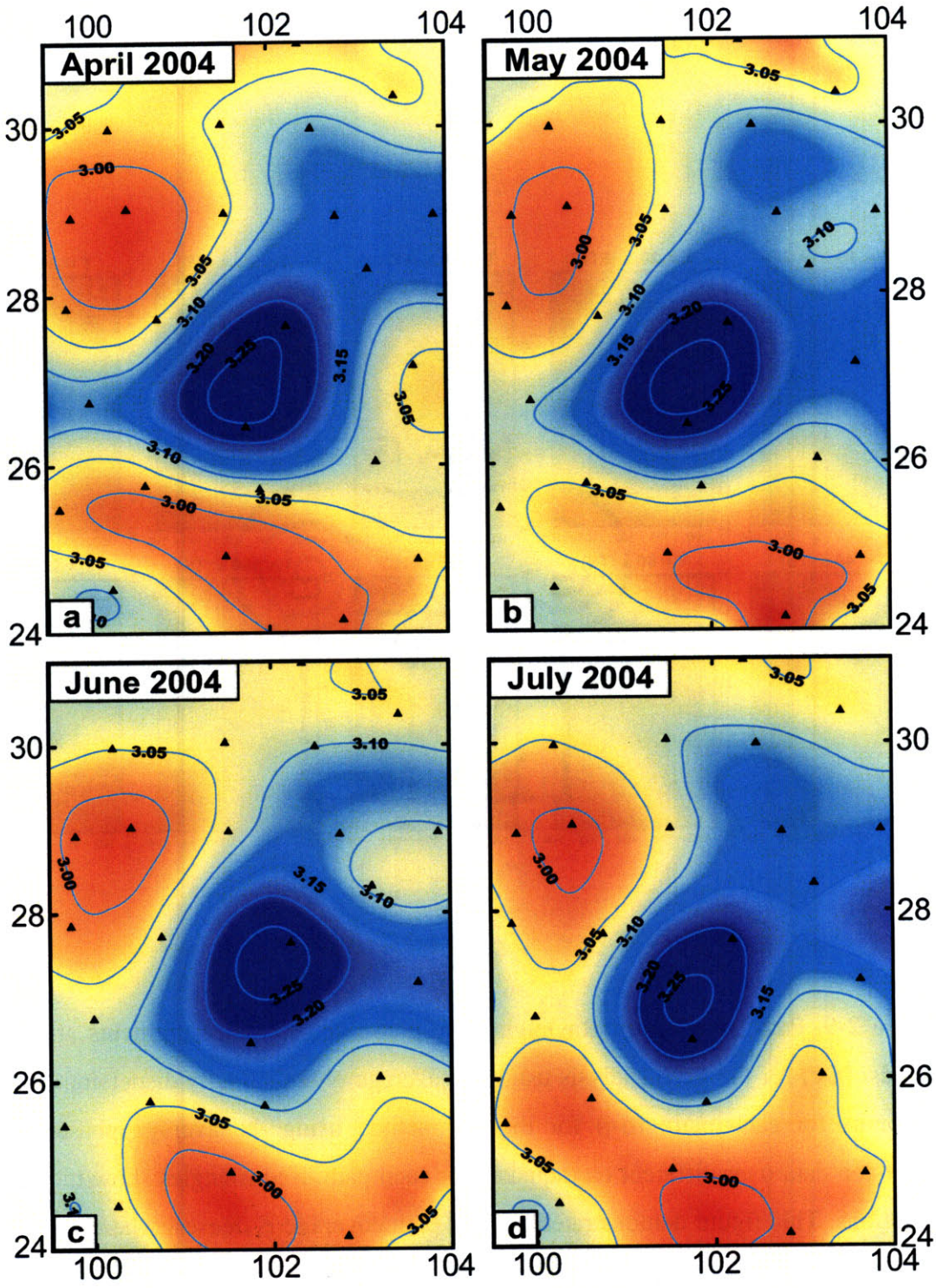

Figure 2-8. Comparison of inverted phase velocity maps at period T = 10 s for four different months from the EGF analysis. The contour values are Rayleigh-wave phase velocities (km/s). Red and blue represents lower and higher velocity, respectively.

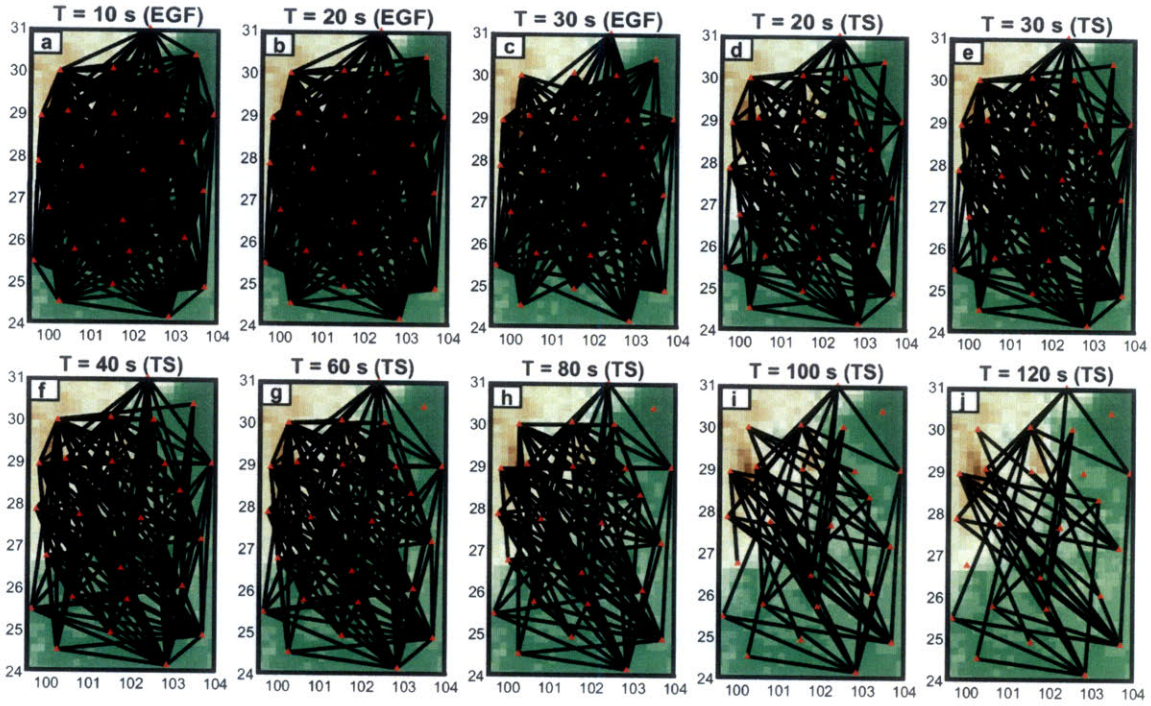

Figure 2-9. Path coverage of Rayleigh-wave phase velocity measurements at different periods: (a-c) for the EGF analysis using the average phase velocity dispersion data over 4 months for each path; (d-j) for the TS method using the average phase velocity dispersion data over different earthquakes for each path. Red triangles show the location of stations. This figure demonstrates that the path coverage is densest where it is needed most, namely, at short-periods, whereas the coverage for lower frequency data (which constrain the longer wavelength structures) is much sparser.

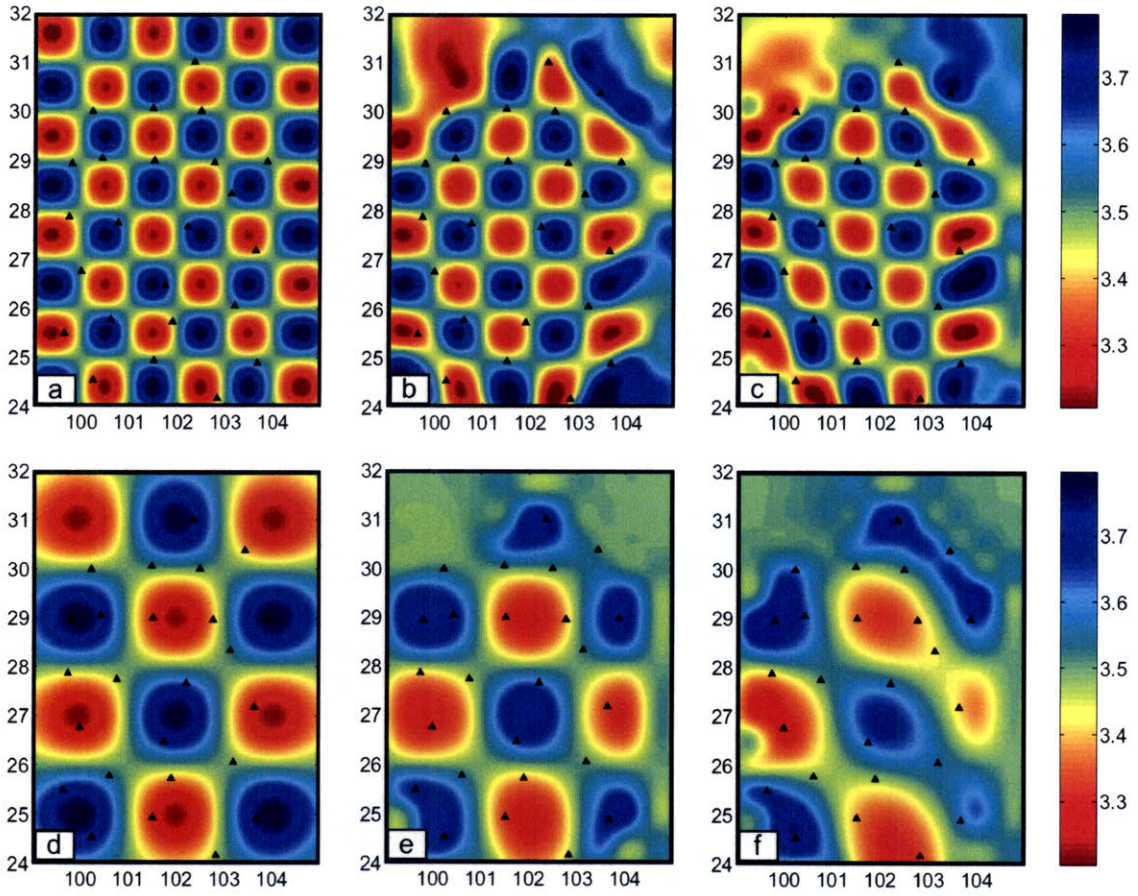

Figure 2-10. Resolution tests: (a) input 1°×1° model; (b) recovery of 1°×1° model for the path coverage at T = 10 s (EGF) shown as Figure 2-9a; (c) recovery of 1°×1° model for the path coverage at T = 40 s (TS) shown as Figure 2-9f; (d) input 2°×2° model; (e) recovery of 2°×2° model for the path coverage at T = 60 s (TS) shown as Figure 2-9g; (f) recovery of 2°×2° model for the path coverage at T = 80 s (TS) shown as Figure 2-9h. Black triangles show the location of stations. The values of the color bar are Rayleigh-wave phase velocities (km/s).

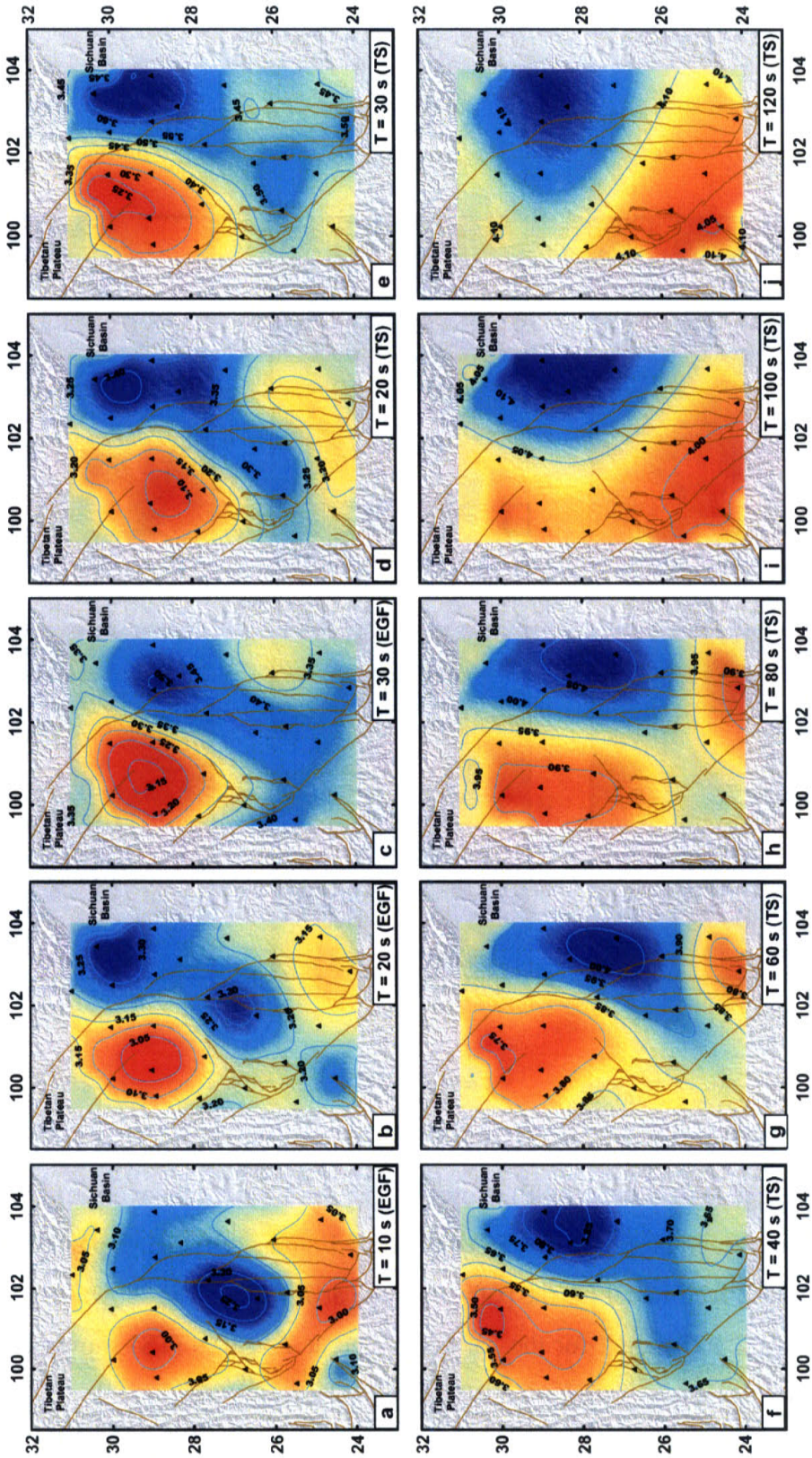

Figure 2-11. Rayleigh-wave phase velocity maps at different periods (10 – 120 s): (a-c) are the inversion results (10 – 30 s) from the EGF analysis using the average phase

velocity dispersion data over four months for each path; (d-j) are the inversion results (20 – 120 s) from the TS method. Black triangles show station locations. The corresponding path coverage maps are shown in Figure 2-9. The contour values are Rayleigh-wave phase velocities (km/s). Red and blue represents lower and higher velocity, respectively. Brown lines depict the major faults in the study area.

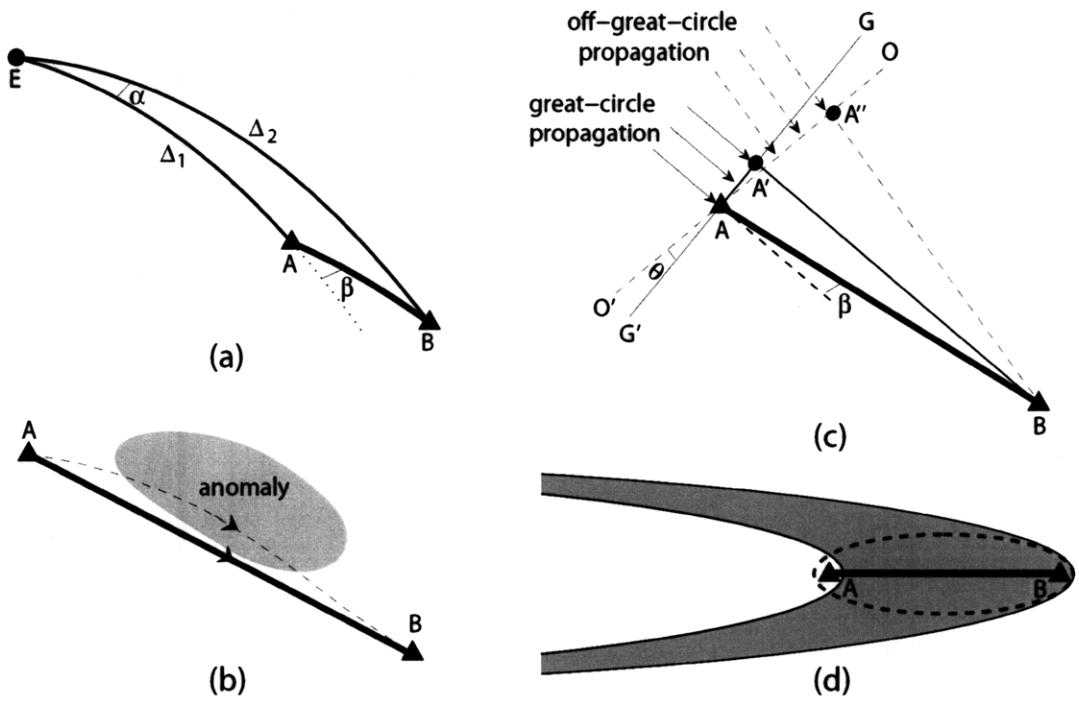

Figure 2-12. (a) Illustration of two deviation angles α and β defined in the TS method: α is the azimuthal difference of the earthquake (E) to the two stations (A and B, with A nearest to the earthquake); β is the azimuthal difference between the earthquake (E) to the station A and the station A to the station B. The solid lines are all great-circle paths and the dashed line is the extended great-circle path from E to A. Δ_1 is the great-circle distance between E and A and Δ_2 is the great-circle distance between E and B. (b) Illustration of off-great-circle propagation of surface-waves between source A and receiver B for the EGF analysis. The solid line represents the path of great-circle propagation between two stations A and B; the dashed line is the path of off-great-circle propagation due to the influence of the velocity anomaly region (shaded area). The distance of off-great-circle path (dashed line) is always larger than that of the great-circle path (solid line), which results in a lower estimation of the average phase velocity between two stations because the estimated phase travel time from the EGF is the same. (c) Illustration of great-circle propagation (solid parallel lines with arrow) and off-great-circle propagation (dashed parallel lines with arrow) of surface-waves for the array TS analysis, where the solid triangles A and B are the two stations, the solid line GG′ is the wave front of great-circle propagating surface waves and is perpendicular to the solid line

A′B with distance (approximately) equal to $\Delta_2 - \Delta_1$ in (a), the dashed line OO′ is the wave front of off-great-circle propagating surface waves and is perpendicular to the dashed line A″B, the deviation angle β is the same as that defined in (a), and the off-great-circle angle θ is defined as the angle from GG′ to OO′ (clockwise is defined to be positive here). (d) Illustration of surface-wave sensitivity zones for the EGF analysis and the TS method. The shaded area is the sensitivity zone for the TS method, which is much broader than the sensitivity zone (the area inside the dashed ellipse) for the EGF analysis. The solid triangles A and B are the two stations. The solid line is the great circle path between the two stations.

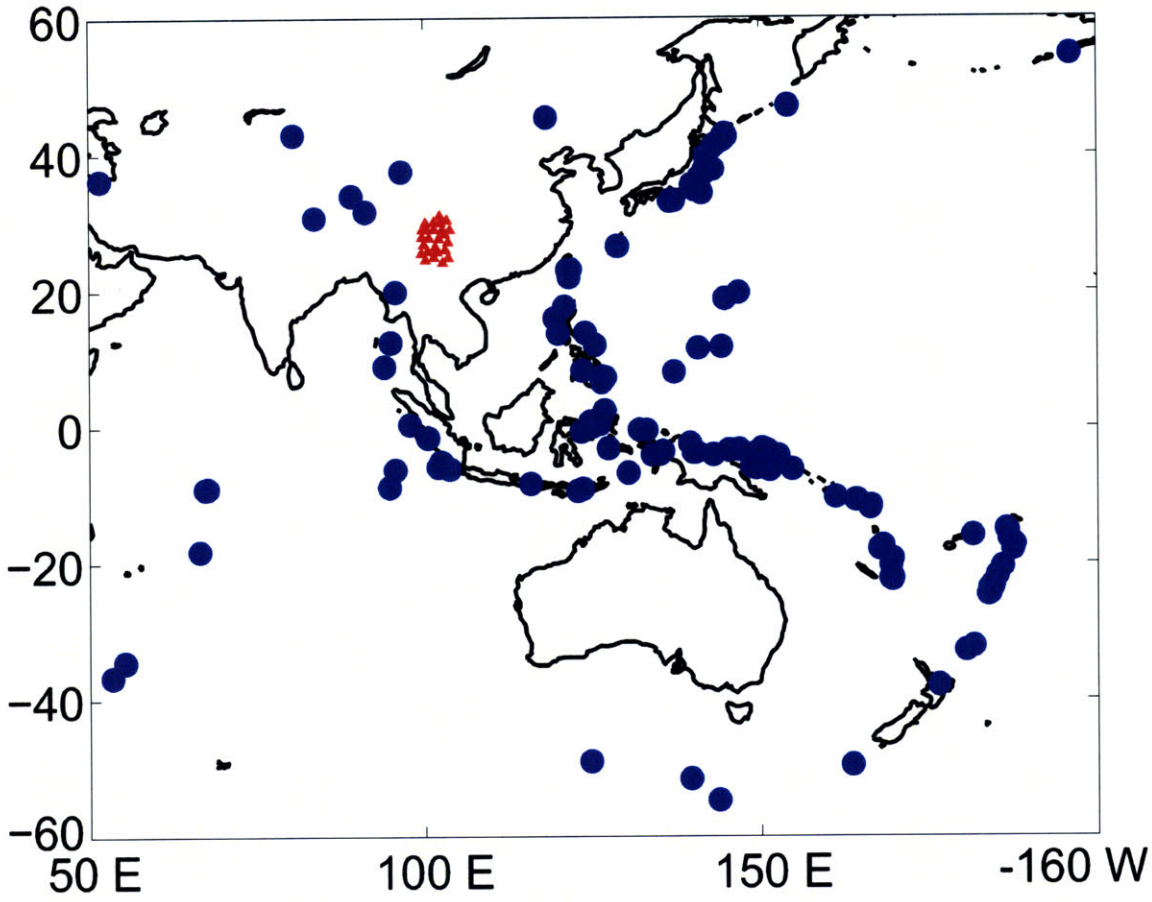

Figure 2-13. The location of earthquakes (blue solid circles) used in the TS method. The red solid triangles show the location of array stations.

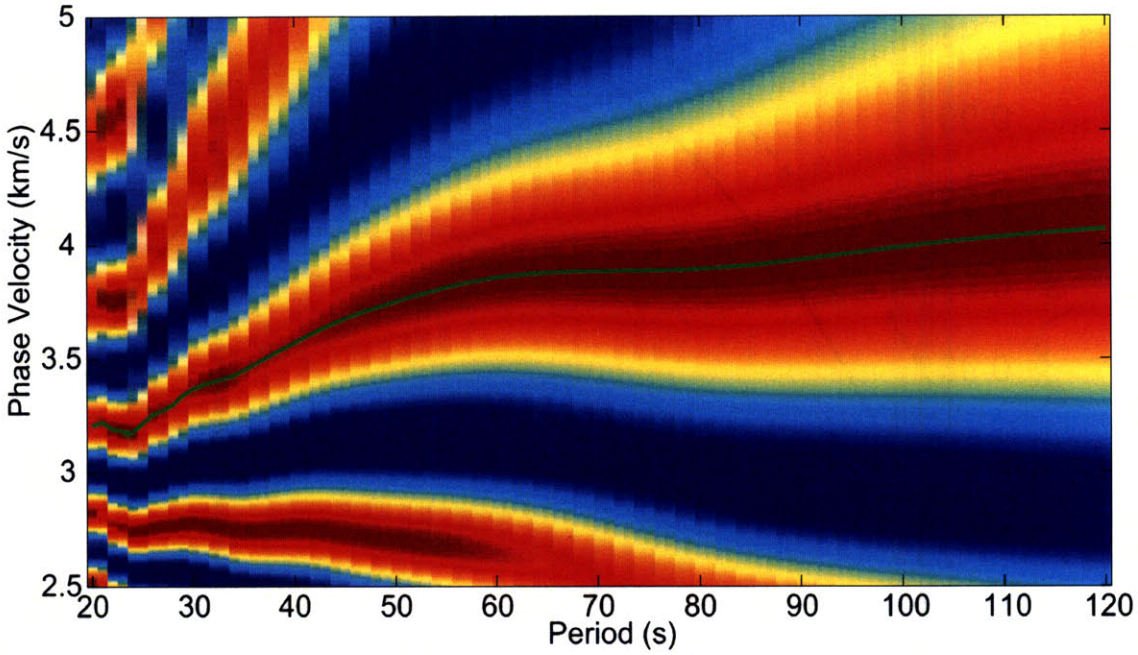

Figure 2-14. Example of extracted dispersion curve (green curve on the *c-T* image) for the station pair MC20 – MC05 using the TS method based on the image transformation technique. The earthquake locates at (-5.8010°, 102.0280°) with M_w = 5.5, depth = 10.0, and source time = 2003/12/24, 11:33:04.36.

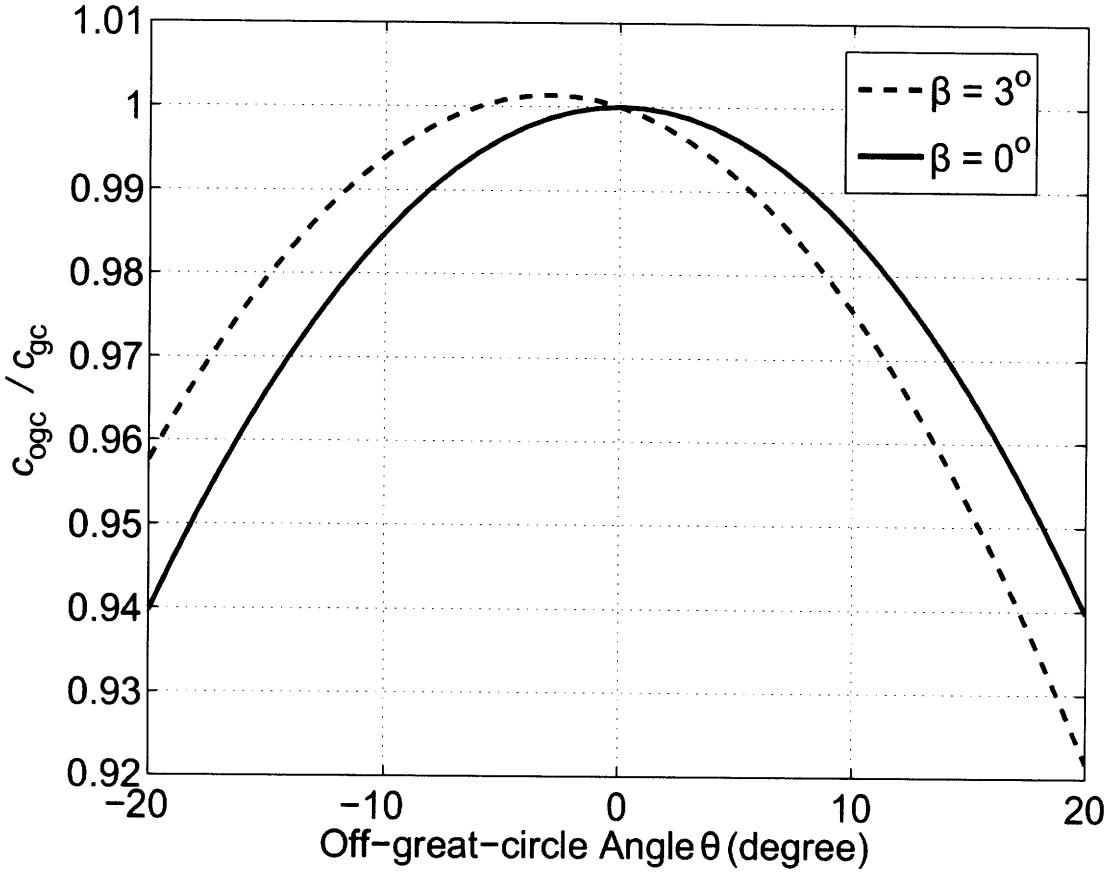

Figure 2-15. The ratio of the inter-station phase velocity estimated from off-great-circle propagation (c_{ogc}) to the inter-station phase velocity estimated from great-circle propagation (c_{gc}) at given off-great-circle angle θ with the deviation angle β = 0° (solid curve) and β = 3° (dashed curve) as illustrated in Figure 2-12d.

Chapter 3

Surface-wave array tomography in SE Tibet from ambient seismic noise and two-station analysis: II – Crustal and upper mantle structure[2]

Abstract

We determine the 3-D shear wavespeed variations in the crust and upper mantle in the southeastern borderland of the Tibetan Plateau, SW China, with data from 25 temporary broadband stations and one permanent station. Inter-station Rayleigh wave (phase velocity) dispersion curves were obtained at periods from 10-50 s from empirical Green's function (EGF) derived from (ambient noise) interferometry and from 20-150 s from traditional two-station (TS) analysis. Here, we use these measurements to construct phase velocity maps (from 10-150 s, using the average inter-station dispersion from the EGF and TS methods between 20-50 s) and estimate from them (with the Neighborhood Algorithm) the 3-D wavespeed variations and their uncertainty. The crustal structure, parameterized in three layers, can be well resolved with a horizontal resolution about 100 km or less. Because of the possible effect of mechanically weak layers on regional deformation, of particular interest is the existence and geometry of low (shear) velocity layers (LVLs). In some regions prominent LVLs occur in the middle crust, in others they may appear in the lower crust. In some cases the lateral transition of shear wavespeed coincides with major fault zones. The spatial variation in strength and depth of crustal LVLs suggests that the 3-D geometry of weak layers is complex and that unhindered

[2] Published as: Yao, H., Beghein, C., and Van der Hist, R.D., 2008. Surface-wave array tomography in SE Tibet from ambient seismic noise and two-station analysis: II – Crustal and upper-mantle structure, *Geophys. J. Int.*, Vol. 163, 205-219, doi: 10.1111/j.1365-246X.2007.03696.x.

crustal flow over large regions may not occur. Consideration of such complexity may be the key to a better understanding of relative block motion and patterns of seismicity.

3.1 Introduction

The Tibetan Plateau is the result of the collision of the Indian and Eurasian plates during the Cenozoic, which began some 50 million years ago (Molnar & Tapponnier, 1975; Rowley, 1996). Different from the central collision zone, the southeast borderland of the Tibetan Plateau (from western Sichuan to central Yunnan in southwest China, Figure 3-1a) is characterized by a gentle slope, lack of large-scale young crustal shortening, and a predominance of N-S-trending strike slip faults (Royden et al., 1997) . These deformation characteristics have been attributed to ductile channel flow in a weak lower crust (Royden et al., 1997; Clark & Royden, 2000; Shen et al., 2001), but many first-order questions remain about the presumed weak zones. Using high resolution surface wave (array) tomography, in this paper we seek to establish the existence of weak crustal flow channels, map out their lateral extent, and determine which part of the crust is actually involved. Research targets of particular interest are crustal zones of low shear wave speed and/or low electric resistivity, since they are often considered as diagnostic for low strength, or the presence of partial melt.

The study region represents the eastern part of the Lhasa block and comprises three major active fault systems (Figure 3-1b): the left-lateral Xianshuihe-Xiaojiang fault system, the right-lateral Red River fault system, and the left-lateral Dali fault systems, among which the Xianshuihe-Xiaojiang fault system is the most active (Wang et al., 1998; Wang & Burchfiel, 2000). The diamond-shaped crustal fragment bounded by these fault systems is usually interpreted as a tectonic terrain, called the Chuan-Dian Fragment (Figure 3-1b; Kan, 1977; Wang et al., 1998). The crustal motion of this fragment is dominated by a clockwise rotation around the eastern Himalayan Syntaxis (EHS), as revealed by geodetic measurements (King et al., 1997; Chen et al., 2000; Zhang et al., 2004; Shen et al., 2005) and geological studies (Wang et al., 1998; Wang & Burchfiel, 2000), which suggests an eastward or southeastward extrusion of crustal material from the central and eastern part of the plateau.

Regional travel-time tomography studies (Huang et al., 2002; Wang et al., 2003; Li et al., 2006, 2008) have revealed large velocity variations in the lithosphere of southwest China, including prominent low velocity anomalies in the crust and upper mantle in western Sichuan and in the Tengchong volcanic area. Receiver function analyses (Hu et al., 2005a; Xu et al., 2007) have shown that in SW China low velocity layers exist not only between 10 – 15 km depth (in sedimentary basins), but also between 30 – 40 km depth (that is, the middle to lower crust) and that the Poisson's ratio in this region is generally high. Joint inversion of surface wave and receiver function data (Hu et al., 2005b) revealed low-velocity layers in the upper mantle beneath areas in central Yunnan and Yunnan-Myanmar-Thailand that are also characterized by high heat flow (Hu et al., 2000) and major earthquakes (Huang et al., 2002). In this region, wide-angle seismic profiles in western Yunnan show that seismic reflections from the middle-lower crust are weak (Zhang et al., 2005). Furthermore, shear-wave splitting studies have revealed a complex pattern of anisotropy, with a dramatic change in fast polarization direction across the Chuan-Dian Fragment. Mantle anisotropy occurs at large angles with structural trends at the surface, which is consistent with (but does by itself not require) weak crust-mantle coupling (Lev et al., 2006; Sol et al., 2007).

Magnetotelluric (MT) sounding has revealed a large-scale low resistivity layer at more than ten kilometers depth beneath northern part of the Chuan-Dian fragment (Sun et al., 2003). Bai et al. (2006) provided evidence for low resistivity in the middle/lower crust between the Jinsha River suture zone and the Xianshuihe fault along latitude ~30°, and also between the Red-River fault and the Xiaojiang fault along latitude ~25°.

Collectively, the seismological and magnetotelluric evidence is consistent with the view that the southeastern margin of the Tibetan plateau is underlain by a weak middle-lower crust. However, due to the specific resolution limitations of each of these methods, the vertical and horizontal extent of the low velocity (or resistivity) zones has remained enigmatic, and the level of inter-connectedness between the different low velocity zones is not known. Body wave travel time tomography usually does not have good depth

resolution, especially in the crust part. For MT studies, the upper boundary of the low resistivity layer can be well resolved but the lower boundary is usually unconstrained. Receiver functions resolve interfaces with large velocity contrast quite well, but are less sensitive to absolute wavespeed values. Moreover, interpolation between stations may not be justified across major fault systems.

The dispersion of short period surface waves is more sensitive to shallow heterogeneity than phase arrival times of steeply incident body waves, and it provides more accurate constraints on shear wave speeds than receiver functions. Traditional dispersion analysis, however, does not yield reliable estimates of the structure in the shallow crust because of strong scattering at short-periods ($T < 30$ s). Recent advances in surface-wave ambient noise tomography (e.g., Shapiro et al., 2005; Sabra et al., 2005; Yao et al., 2006; Yang et al., 2007; Lin et al., 2007) greatly enhance our ability to resolve the shallow crustal structure. This approach involves measuring the dispersion of empirical Green's functions (EGFs) obtained from cross-correlation of time series containing ambient noise.

Yao et al. (2006, Chapter 2 in this thesis), hereinafter referred to as Paper I, introduced a method for multi-scale surface-wave array tomography that combines Rayleigh wave phase velocity measurements from the traditional two-station (TS) analysis and the empirical Green's function (EGF) estimated from (ambient noise) interferometry. In this paper we improve the dispersion measurements (both for the EGF and the TS analysis), construct phase velocity maps in the period band 10 – 150 s, and invert them for 3-D shear wavespeed variations in the crust and upper mantle beneath the southeastern borderland of the Tibetan Plateau using the Neighborhood Algorithm (NA) (Sambridge, 1999a, b). NA is an inversion approach, based on forward modeling, that searches the entire model space and identifies all models that fit the observations (here, the dispersion data) and produces quantitative measures of parameter trade-offs and uncertainties. NA differs from direct search techniques, such as LSQR (Nolet, 1985), which select a single model (subject to a particular, often subjective regularization) that optimizes a cost function. NA has previously been used for P and S tomography using normal-mode and surface wave data (Beghein, et al., 2002), non-linear waveform inversion (Yoshizawa &

Kennett, 2002), and S-wave velocity structure inversion from surface-wave data (Snoke & Sambridge, 2002).

We present the tomography model (that is, 3-D shear wavespeeds and their uncertainty) of the crust and upper mantle beneath the southeastern borderland of the Tibetan Plateau, SW China, with special emphasis on intra-crustal low velocity zones and their implications for our understanding of the present-day seismo-tectonic setting of the region and the dynamic evolution of the Tibetan Plateau.

3.2 Data

From 09/2003 to 10/2004 MIT and the Chengdu Institute of Geology and Mineral Resources (CIGMR) operated an array of 25 three-component, broad band seismometers in the Sichuan and Yunnan provinces, SW China (Figure 3-1a) to investigate the structure and geological evolution of the eastern Tibetan Plateau. Seismograms from this array have been used for travel time tomography (Li et al., 2006, 2008), receiver function analysis (Xu et al., 2007), and shear wave splitting (Lev et al., 2006; Sol et al., 2007).

3.2.1 Phase velocities from EGF analysis

In Paper I we present a method for measuring Rayleigh wave phase velocity dispersion from empirical Green's functions (EGF) and two-station (TS) analysis. In that paper we obtained EGFs from four months of data (April 2004 – July 2007) and then measured phase velocities between the MIT-CIGMR array stations. Here we redo the analysis and construct vertical component EGFs from 10 months long (continuous) records, and in addition to the MIT-CIGMR array we used data from KMI, a permanent (Global Seismograph Network) station in Kunming,Yunnan (Figure 3-1a). The use of the longer records increased the signal to noise ratio (in the EGFs) and resulted in better path coverage. Due to the uneven distribution of noise sources, the positive time and negative time parts of EGFs are, in general, not time-symmetrical. For each inter-station path, we average the causal and acausal parts of the EGF to produce the symmetrical component (Yang et al., 2007) and enhance the signal to noise ratio. From the symmetrical component of EGFs we then measure Rayleigh wave phase velocity dispersion within the

period band 10 – 50 s. The green line in Figure 3-2a shows the number of measurements (or paths) at each period, which decreases as the period increases due to the far field approximation for surface waves representation (Paper I). The average dispersion curve in the period band 10 – 50 s from EGF analysis is shown as the green line in Figure 3-2b.

3.2.2 Phase velocities from TS analysis

To obtain phase velocity dispersion at larger periods we follow the procedures outlined in Paper I and measure the dispersion from 20 to 150 s using the two-station (TS) analysis. For the MIT-CIGMR array and KMI we obtained about 1700 inter-station dispersion curves from about 200 earthquakes at teleseismic distances (and for deviation angles α and β – defined in Paper I – less than 3° and 7°, respectively). For each station pair we average the dispersion curves from different events to obtain the input for the phase velocity and standard error calculations. The total number of paths at each period is shown in Figure 3-2a (black line). The regional average dispersion curve from TS analysis is shown Figure 3-2b. The relative standard error (Figure 3-2b) is about 1 – 1.5% for the periods considered here.

3.2.3 Phase velocities from EGF+TS averaging

For periods between 20 and 50 s the average phase velocities from the TS and EGF analysis are similar. Indeed, the discrepancy is generally less than 1%, which is smaller than the standard errors of either method and much smaller than the difference with the reference values according to *ak135*. Compared to Paper I, we note a substantial increase in quality of the phase velocity measurements, which we attribute to the use of longer time windows for the EGF measurement and the larger number of TS measurements. In Figure 3-3 we compare (for the period band they have in common) the TS and EGF measurements for the same two-station pairs. The average phase velocities from TS analysis can be up to 1% higher than those from the EGF analysis. This difference can be due to differences in sensitivity to structure (Paper I) and to imperfect recovery of the surface wave Green's functions due to the unknown but certainly inhomogeneous distribution of noise sources (Yao et al., in preparation). However, within reasonable uncertainty, the EGF and TS methods appear to yield similar results.

The input inter-station dispersion data for the calculation of phase velocity maps between 10 and 150 s is obtained as follows. For periods smaller than 20 s we use the results of interferometry (i.e., the EGFs) and for periods between 50 and 150 s we use the TS results. For periods between 20 and 50 s we take the mean of the phase velocity from the EGF analysis (C_{EGF}) and the TS analysis (C_{TS}) if $|C_{EGF} - C_{TS}| \leq 0.1$ km/s, C_{TS} if $|C_{EGF} - C_{TS}| > 0.1$ km/s (and if either at least five measurements from TS analysis have been made for that period or the standard error of phase velocity measurement at that period is less than 0.04 km/s), or C_{EGF} in all other cases. The number of (average) phase velocity measurements (or paths) at each period is shown as the red dot in Figure 3-2a. As expected, the number of paths for the overlapping periods after averaging the TS and EGF measurements is larger than that from either method alone. This averaging scheme mitigates the problem that the number of EGFs measurements decreases sharply as the period increases (Figure 3-2a) and greatly enhances the path coverage and the reliability of measurements for the TS analysis at shorter periods.

3.3 Phase velocity maps

Following Paper I, we construct 2-D phase velocity maps from 10 s to 150 s. The path distributions for six different periods (10, 30, 60, 90, 120, 150 s) are shown in Figure 3-4. At each period the data coverage is denser than in Paper I, especially at the longer periods. The corresponding phase velocity maps are shown in Figure 3-5. The lateral resolution in these maps is generally of the order of (or less than) the inter-station distance (~100 km). From the maps, we infer the phase velocity as a function of frequency at each point of the $0.5° \times 0.5°$ grid that is used to parameterize the study region.

3.4 Structure inversion using Neighborhood Algorithm (NA)

3.4.1 NA optimization

The NA involves two stages (Sambridge, 1999a, b). The first stage consists of a model space search to identify the "good" data fitting regions. It employs a geometrical construct – the Voronoi cells – to drive the search towards the best data-fitting regions while continuing to sample a relatively wide variety of different models. The use of these

cells makes this algorithm self-adaptive because, with a good choice of some tuning parameters, one can explore the complete model space with the possibility to jump out of a local minimum. It also has the advantage of being able to sample several promising regions simultaneously. During this search, the sampling density increases in the surroundings of the good models without losing information on the models previously generated (even the "bad" ones). The first stage results in a distribution of misfits, which serves to approximate the posterior probability density function (PPDF).

In the second stage of NA, a sampling of this distribution generates a "resampled ensemble" that follows the PPDF. This resampled ensemble is then integrated numerically to compute the likelihood associated with each model parameter, also called 1-D marginal PPDFs (or 1-D marginals), the correlation matrix, and 2-D marginal PPDFs (or 2-D marginals). The departure of these 1-D marginals from a Gaussian distribution can be used as a diagnostic of the degree of ill-posedness of the problem. In addition, their width can be seen as a more realistic measure of model uncertainty than one we obtain from traditional inversion techniques. The 2-D marginals quantify the trade-offs between two variables. (NB the same information can be deduced from the correlation matrix if a Gaussian approximation of the model space could be made.) Since they characterize the entire ensemble of models compatible with the data, the 1-D and 2-D marginals are powerful instruments for estimating true resolution and uncertainty of model parameters.

3.4.2 Model space parameterization and misfit function

From the phase velocity as function of period we estimate with NA the shear wavespeed as a function of depth at all grid points in the study area. At each location, we parameterize the inversion problem using 9 parameters: these are Moho depth and the shear wavespeeds in 8 (non-overlapping) depth intervals in the crust and upper mantle. The detail of the parameters as well as their perturbation range with respect to the reference model is shown in Table 1. The mantle part of the reference model follows the global *ak135* model (Kennett et al., 1995). The crust part of the model is parameterized by means of three layers (upper, middle, and lower crust); for each grid point, the Moho

depth inferred from receiver functions (Xu et al., 2007) represents the reference value for total crustal thickness, and the upper, middle, and lower crust are set to about 1/3 of the total crustal thickness. We allow the Moho depth to vary within 5 km above or below the reference Moho depth, and the thickness of the lower crustal and uppermost mantle layer will change accordingly.

Because of the evanescent character of the surface waves, the sensitivity of the data to changes in wavespeed decreases with increasing depths, and for depth larger than 280 km we simply adopt Vp, Vs and ρ from the *ak135* model. Because short period (e.g., $T < 40$ s) Rayleigh waves are also sensitive to Vp and ρ in the shallow crust (Mooney, et al., 1998; Simons & van der Hilst, 2003), we also account for the sensitivity of Rayleigh wave phase velocity to perturbations in Vp and ρ. In the first stage of the NA, for each layer in the crust, once Vs is given, Vp and ρ in that corresponding layer are calculated from Vs using the empirical relations between elastic wavespeeds and density in the Earth's crust (Brocher, 2005). In each of the five upper mantle layers, the perturbation in shear wavespeed is ± 0.6 km/s with respect to the reference value from the value of *ak135* at pertinent depths. The reference values of Vp and ρ in each upper mantle layer are also taken directly from the *ak135*. (We remark that we do not apply the empirical relationships by Brocher (2005) for the lithospheric mantle because they are only valid for crustal rocks). For each upper mantle layer, when a perturbation ΔVs is produced with respect to the reference Vs, the perturbations of P-wave speed (ΔVp) and density ($\Delta\rho$) with respect to the *ak135* values for that layer are also obtained using the following relations (Masters et al., 2000):

$$\frac{d\ln V_p}{d\ln V_s} = 0.6, \qquad \frac{d\ln \rho}{d\ln V_s} = 0.4 . \tag{3-1}$$

Through the use of relationships among Vs, Vp and ρ for the crustal and mantle layers, we thus incorporate the influence of Vp and ρ on the phase velocities in NA.

For every model generated in the NA model space search, Rayleigh wave phase velocities are calculated in the period band 10 – 150 s. To calculate misfit we use the L_2-norm to represent the distance between the predicted and the observed dispersion data

$$\Phi = \sqrt{\frac{1}{N}\sum_{i=1}^{N}\left(\frac{c_i^{pred} - c_i^{obs}}{\sigma_i}\right)^2} \quad , \tag{3-2}$$

where N is the total number of periods at which the phase velocity is measured; c_i^{pred} and c_i^{obs} is the predicted and observed phase velocity at the i^{th} period, respectively; σ_i is the estimated standard error of the observed phase velocity at the i^{th} period. In this study, N = 25, and σ_i is set to be $0.01\, c_i^{obs}$ because the standard error of inter-station phase velocity measurements is about 1% (Yao et al., 2006).

Each stage of the NA requires the tuning of parameters whose optimum values have to be found by trial and error. Several authors have described the influence of these parameters on the survey of the model space and on the Bayesian interpretation of the results (e.g. Sambridge, 1999 a,b; Resovsky & Trampert, 2002). To broaden the survey in the model space and to consider the speed of convergence of the algorithm, the total number of new models generated at each iteration step, n_s, is set to 100, and the number of best data-fitting cells in which the new models are created, n_r, is set to 50 after a set of stability and convergence tests.

3.4.3 Example of NA optimization

We use the dispersion data, the solid dots with error bars in Figure 3-6a, at the grid point at (101° E, 29° N) to illustrate the performance of NA. Note that the observed phase velocities in the short and intermediate period range (10 – 80 s) are much lower than those predicted from the reference model (dashed line in Figure 3-6a), which indicates a possible reduction in seismic wavespeeds at the crustal and uppermost mantle depth. A total of 35,200 models were generated during the first stage of the NA to ensure the convergence of the search. During the second stage, these models and their misfits were used to produce 1-D and 2-D marginals (Figures 3-7 and 3-8, respectively). The 1-D marginals are used to determine the posterior mean value and the corresponding standard error of each model parameter. A most likely (best fitting) model can be obtained from the peak of the 1-D marginal distributions. The posterior mean model is shown as the

solid line in Figure 3-6b and the corresponding predicted dispersion curve is shown as the solid line in Figure 3-6a, which falls within data uncertainties.

The width of the 1-D marginal distributions shown in Figure 3-7 demonstrates that *Vs* is better constrained in the three crustal layers than in the upper mantle layers. The standard errors of *Vs* associated with the posterior mean model parameters are also shown as the grey area in Figure 3-6b. The shallow crust can be constrained better than the lower crust because short period (dispersion) data has a narrower depth sensitivity kernel and, in particular, because the wavespeed estimates for the lower crust structure trade-off strongly with the Moho depth. For this grid point the Moho depth is poorly constrained. The posterior mean Moho depth is 57.8 km with a standard error about 3 km. The posterior mean shear wavespeeds (solid lines in Figure 3-7) of the three crustal layers are very close to the most likely model, the peak of the corresponding 1-D marginals with approximate Gaussian distributions. For the five upper mantle layers, the posterior mean shear wavespeeds are also close to the most likely model, but generally with larger standard errors than those of the crustal layers, indicating that the long-period surface data which sample this depth range have relatively poorer depth resolution. The *Vs* of uppermost mantle layer (Moho – 90 km) has the largest standard error (0.29 km/s), implying a large trade-off between Moho depth and the shear wavespeed. The posterior mean shear wavespeeds of both the middle crust and the lower crust are much lower than the *Vs* in the reference model (Figure 3-6b, 7). Relatively low shear wavespeed also persists in one of the upper mantle layer (90 – 130 km). However, from 130 km to 280 km, the posterior mean *Vs* is higher than that of *ak135*.

The 2-D marginals (Figure 3-8) illustrate the trade-off between different model parameters. The *Vs* in nearby layers shows apparent negative correlations. The trade-off between *Vs* of adjacent layers in the crust is smaller compared to trade-offs between *Vs* in nearby upper mantle layers. This is a reflection of the fact that depth resolution is better for shorter than for longer period dispersion data. The Moho depth shows large trade-off (positive correlation) with the *Vs* in the lower crust and that in the uppermost mantle (Moho – 90 km) (Figure 3-8). Indeed, Moho depth cannot be constrained well with

dispersion data alone because of the trade-off between the Moho depth and the wavespeeds in the lower crust and uppermost mantle (Figure 3-8). We recall, however, that we use the Moho depths from receiver function studies (Xu et al., 2007) as reference values in the NA search, which results in better estimations of the Moho depth than from dispersion data alone.

3.5 Crustal and upper mantle structure

From the 1-D posterior mean model and standard error inferred from the NA at each grid point, we infer 3-D wavespeed variations, and their uncertainty, beneath the array. We will now present the inferred variation in Moho depth and images of *Vs* variations at different depths and along different vertical profiles.

3.5.1 Variation of Moho depth

In map view, the lateral variation in Moho depth beneath the array area is presented in Figure 3-9. These results are, by design, consistent with the estimates by Xu et al. (2007). From west to east across the array the Moho depth decreases rather abruptly from 55-63 km in southwest Sichuan (i.e., the northwestern part of the array) to 37-45 km beneath the western margin of Sichuan basin. Southeastward the Moho depth (and crustal thickness) decreases more gradually to ~40 km beneath central Yunnan. The 1-D marginals suggest that the standard error in Moho depth is 2-3 km.

3.5.2 3-D variation in shear wavespeed

The lateral variation of *Vs* at 10, 25, 50, 75, 100, and 200 km depth is depicted in Figure 3-10, with the uncertainties displayed in Figure 3-11. Figure 3-12 shows *Vs* heterogeneity along five vertical profiles from the surface to 250 km depth, with the uncertainties shown in Figure 3-13.

In the Chuan-Dian Fragment (Figure 3-1b, the magenta shaded area) the wavespeed patterns vary significantly from the upper crust to the upper mantle. In the upper crust, high wavespeed appears in the central and eastern part of this tectonic unit, while low wavespeed mainly appears in the southern and western parts (Figure 3-10a). The region

northeast of the Red River fault (only the northern part is sampled in this study) shows prominent low wavespeed in the upper crust (Figure 3-10a), but this feature seems to disappear at larger depths. At the mid crustal depth range, the northern Chuan-Dian Fragment is marked by a low velocity layer (LVL), bounded to the south approximately by the Lijiang and Muli faults (Figure 3-10b). Another prominent mid crustal LVL appears in the southeastern part of Chuan-Dian Fragment, around the Luzhijiang-Xiaojiang fault zone (Figure 3-10b; profiles CC' and DD' in Figure 3-12). In the lower crust, a LVL appears in the central part of Chuan-Dian Fragment, and in contrast to the middle crust the lower crust beneath northern portion is not anomalously slow (Figure 3-10c; profiles AA', BB', and EE' in Figure 3-12). We notice also that the LVL detected at mid-crustal depth beneath the northern Chuan-Dian Fragment (Figure 3-10b) does not extend northeastward across the Xianshuihe fault (XSHF); in fact, normal shear wavespeeds are observed northeast of this fault (profile AA' in Figure 3-12).

In the uppermost mantle (Figure 3-10d), the eastern Chuan-Dian Fragment mainly appears slow while relatively high wavespeeds prevail in part of the central fragment north of Lijiang fault. At 100 km depth (Figure 3-10e), the northern Chuan-Dian Fragment is marked by low wavespeeds while southern Chuan-Dian Fragment is relatively fast. The wavespeed pattern at 200 km depth beneath the Chuan-Dian Fragment (Figure 3-10f) seems to be quite different from that at 100 km depth, with low wavespeed anomaly in the south fragment but high velocity anomaly in the northern fragment.

At very shallow depths, shear wavespeed is slow in the western margin of Sichuan basin (Figure 3-10a), probably due to presence of the thick sedimentary layers, but wavespeed is high in the middle crust (Figure 3-10b). The upper mantle structure below the western margin of the Sichuan basin may be not reliable because the path coverage at intermediate and longer periods is poor (Figure 3-4). Southwest of the Zhongdian-Dali-Red River fault the uppermost mantle (Moho – 130 km) is relatively slow (Figure 3-10d,e), while at 200 km depth it changes to fast structure (Figure 3-10f).

The average wavespeeds in each layer of the study region are shown in Table 1. With respect to the reference value, we observe relatively low wavespeeds in the three crustal layers and two uppermost mantle layers (Moho – 90 km, 90 – 130 km) and higher wavespeeds in other three deeper upper mantle layers (130 – 170 km, 170 – 220 km, 220 – 280 km). The average crustal velocity is about 3.47 km/s, which is about 4.3% lower than that (~3.63 km/s) of the global *ak135* (continental) crustal model.

3.6 Discussion

The variation of the 3-D shear wavespeed structure in the crust and upper mantle beneath the array area (up to about ±8% variation with respect to the average value) is much larger than suggested by traditional (larger scale, but lower resolution) surface wave tomography. The inferred heterogeneity reflects a complicated (tectonic) transition from the Tibetan Plateau (Lhasa block, Qiangtang block, and Songpan-Ganze Fold Belt) to the South China Block and Indo-China Block. Our results suggest that boundaries between major tectonic units identified at the surface appear to involve much – if not all – of the crust, and in some cases the uppermost mantle as well.

3.6.1 Uncertainties of the shear wavespeeds from NA

Figure 3-11 shows the standard errors (or uncertainties) of shear wavespeeds for horizontal profiles at different depths in Figure 3-10, and Figure 3-13 shows the standard errors of shear wavespeeds for vertical profiles in Figure 3-12. The standard errors in the shear wavespeed estimates are relatively small (~ 0.15 – 0.2 km/s) at upper and middle crustal depth but larger (~0.2 – 0.3 km/s) in the lower crust and the upper mantle layers (Figures 3-11, 3-13). This is due to the trade-offs with Moho depth and to the evanescent properties of surface waves at different periods: shorter period surface waves have a better depth sensitivity in the shallow crust, whereas longer period surface waves sample the upper mantle structure with a much broader depth sensitivity kernel which results in a relatively poor depth resolution in the upper mantle.

At a given depth, the standard errors vary laterally (Figures 3-11, 3-13) because of the lateral variability in model parameterization of the crust and upper mantle layers (section

3.4.2) and lateral variations in standard error of phase velocity. Estimating the uncertainties on the 2D phase velocity maps directly from the uncertainties on the inter-station measurements is still difficult at this stage. This is why we made a rough estimate using 1% of the phase velocity determined at every period for each grid point.

The wavespeed error is generally inversely proportional to layer thickness. For example, in the uppermost mantle layer (Moho-90 km) the largest uncertainties occur in regions where the Moho is deepest and, hence, the layer thinnest (i.e., in the northwestern part of the study region (Figures 3-9, 3-11d)). Setting the thickness of the upper and middle crust layer both about 1/3 of the total crustal thickness prevents any of these layers to become arbitrarily thin. The wavespeed uncertainty is generally larger in the lower crust than in the upper and middle crust (Figures 3-11, 3-13) because of the reduced sensitivity of the data and also because of the trade-off between Moho depth and the wavespeed of the lower crust.

The uncertainty maps suggest that the LVLs in the middle crust, e.g., in the northern Chuan-Dian Fragment and the Luzhijiang-Xiaojiang fault zone, are robust. Also the LVL in the lower crust beneath the central Chuan-Dian Fragment seems to be well resolved (Figure 3-13b,c,e). Some of the structures in the upper mantle have larger uncertainties. Because we performed a model space search that provided PPDFs for each model parameter, we have an overview of all the models compatible with the data. We did not choose a particular model based on regularization, as we would with a more traditional inverse method. In addition, because we carefully sampled the model space (with appropriate choice of the tuning parameters to make a broad sampling), we are confident that the models we obtained are not associated with local minima of the misfit function.

3.6.2 Heterogeneity of Chuan-Dian Fragment

The Chuan-Dian Fragment is usually regarded as a unique tectonic terrain and is thought to play an important role in the dynamics and tectonics of the eastern part of the Tibetan Plateau. According to recent GPS studies (King et al., 1997; Chen et al., 2000; Zhang et al., 2004; Shen et al., 2005) this block is moving southeastward at a rate larger than

adjacent crust, which indicates that the crustal material is transported from the central part of the Tibetan Plateau to SW China and Burma around the eastern Himalayan syntaxis by clockwise rotation. However, the Chuan-Dian Fragment is not tectonically uniform, and on the basis of geological and geodetic studies one can identify different tectonic units (Wang et al., 1998; Wang & Burchfiel, 2000; Shen et al., 2005).

Our results confirm that the crust and upper mantle beneath the Chuan-Dian Fragment are highly heterogeneous. At the surface, the Xianshuihe-Xiaojiang left-lateral fault system acts as the boundary between the Chuan-Dian Fragment and the South China block (which comprises the Yangtze Craton and the South China Fold Belt). In the northern part of the study region, we observe large wavespeed contrasts across the Xianshuihe fault at the mid crustal depth (Figure 3-10b). Further south, and at larger depths, the Xiaojiang fault is not evident in the images. Further study must establish if this is a resolution issue or if it reflects spatial variations in character of and elastic properties across the fault. The data also reveal substantial contrasts across the Lijiang-Muli fault system (Figure 3-10), which suggests that it is a main boundary within the Chuan-Dian Fragment. This inference is consistent with results from (surface) block modeling using GPS data (Shen et al., 2005), which identifies a northern block (including the Yajiang and Shangrilla subblocks) and a southern block (the Central Yunnan subblocks), separated by the Lijiang-Muli fault. The Lijiang-Muli fault is also part of the boundary between the Songpan-Ganza Fold Belt and the Yangtze Craton (Figure 3-1b).

3.6.3 Crustal weak zones and the importance of faults

The tomographic images of the continental lithosphere demonstrate that low velocity layers (LVLs) are ubiquitous in the middle/lower crust and upper mantle beneath the southeastern borderland of the Tibetan Plateau. This is consistent with previous results (e.g., Huang et al., 2002; Wang et al., 2003; Hu et al., 2005a,b; Xu et al., 2007), but because of superior depth resolution we can determine, more confidently, the depth and lateral continuity of these LVLs.

High regional surface heat flow values (Hu et al., 2000) indicate steep geothermal gradients. The high geothermal gradient can reduce the shear wave speed and may cause partial melt in the crust. Partial melt of the crustal material in the Tibetan Plateau has been suggested by other studies, e.g., partially molten in the middle crust beneath southern Tibet (Nelson et al., 1996; Unsworth et al., 2005), and in the mid-lower crust and upper mantle beneath northern Tibet (Meissner et al., 2004; Wei et al., 2001). It thus seems reasonable to attribute the large (>10%), local reductions in shear wavespeed to a reduction in rigidity due to elevated temperatures and, perhaps, partial melt in the middle or lower crust. Even small melt fractions would reduce the strength of the lithosphere (Kohlstedt & Zimmerman, 1996) and facilitate intra-crustal (plastic) flow due to external tectonic forces. From analysis of seismic anisotropy, Shapiro et al. (2004) and Ozacar & Zandt (2004) argued that channel flow is likely within the middle or middle-to-lower crust beneath the central parts of the plateau. The argument of crustal channel flow is further supported by the very low equivalent elastic thickness ($0< T_e<20$ km) beneath the Tibetan Plateau and SW China (Jordan & Watts, 2005), and by the detection of zones of high (electric) conductivity in the crust of our study region (Sun et al. 2003; Bai et al. 2006).

The presence (or absence) of weak zones is important for our understanding of the geological development of the Tibetan plateau. Indeed, geodynamical modeling involving gravity and/or thermal driven lateral flow within a weak middle/lower crust channel has been used to explain the tectonics in the Himalayan-Tibetan orogen (e.g., Beaumont et al., 2004) and eastern Tibet (e.g., Royden et al., 1997; Clark & Royden, 2000; Shen et al., 2001). But many first-order issues about such weak layers have remained unresolved. The (geographical and depth) distribution of and interconnectivity between LVLs – and, by implication, the 3-D geometry of the presumed channel flow – are not well known. Can flow occur freely over large regions or are there local structures (such as faults) that interrupt or deflect flow? And what is effect of the asthenospheric upper mantle on crustal channel flow? Answering these questions will be of key importance for understanding the (tectonic) block motions inferred from GPS data and – indeed – regional seismicity.

In northern Tibet, the possible weak channel due to partial melt is likely to exist from the middle crust to upper mantle (Meissner et al., 2004; Wei et al., 2001). In southern Tibet, beneath the Himalayan orogen, many geophysical observations (e.g., Nelson et al., 1996; Unsworth et al., 2005) suggest that the partial melt and the consequent weaker channel probably dominate in the middle crust. In southeastern Tibet, lower crustal flow models (e.g., Royden et al., 1997) explain many geologic aspects, such as the lack of young crustal shortening and the gentle topographic slope.

Our high-resolution surface wave array tomography reveals considerable regional variations in the strength and depth range of LVLs. In the northern part of the Chuan-Dian fragment and the Luzhijiang-Xiaojiang fault zone, the images reveal a mid-crustal LVL with a (horizontal) E-W extent of 150 – 200 km. In the central Chuan-Dian Fragment, the data require LVL in the lower crust. The high-resolution (3-D) images are beginning to suggest that some major fault zones in this area (e.g., Xianshuihe fault, Litang fault, Luzhijiang fault) mark lateral transitions in the mid- or lower crustal LVZs. This crustal heterogeneity implies that the flow pattern is more complicated and, in particular, that some of the major faults seem to play a more important role than assumed in the current generation of middle or lower crustal flow models. A better understanding of these structural relationships requires even higher resolution images of the crust beneath this region. This can be achieved through a combination of denser array deployments and the use of more powerful inverse scattering or (full wave) inversion approaches (e.g., De Hoop et al., 2006)

3.7 Summary

We have used dispersion data from empirical Green's function and two-station analysis to construct high-resolution Rayleigh wave phase velocity maps in the period band 10 – 150 s in the southeastern borderland of the Tibetan Plateau. These phase velocity maps were then inverted for 3-D shear wavespeed variations in the study region using the Neighborhood Algorithm (NA). With NA, a global optimization method, we estimated parameter trade-offs and uncertainties. Because of the large trade-off between the Moho

depth and the shear wavespeed in the lower crust and uppermost mantle, we constrain the Moho depth using results from receiver function studies (Xu et al., 2007). The 15% peak-to-peak variation of shear wavespeed implies a complicated tectonic make up of the southeastern borderland of the Tibetan Plateau. The shear wavespeed in the shallow crust beneath Chuan-Dian Fragment is characterized by regions with high and low velocity anomaly separated by some of the major faults, which is consistent with the tectonic and GPS studies and implies that Chuan-Dian Fragment is not a uniformly rigid block. Prominent low velocity layers have been found in the middle crust beneath the northern Chuan-Dian Fragment and the Luzhijiang-Xiaojiang fault zone and in the lower crust beneath the central Chuan-Dian Fragment.

The high resolution images are beginning to reveal relationships between major faults in the area and the occurrence and lateral extent of crustal low velocity layers. The heterogeneous spatial distribution of the low velocity layers in the middle or lower crust in the southeastern borderland of the Tibetan Plateau and the possible interaction of the major faults with deep crustal structure suggest that the pattern of the possible crustal channel flow is complicated and may involve both middle and lower crustal flow. Establishing the relationship between major fault systems and the spatial distribution of crustal weak zones is of key importance for our understanding of the regional block motion (as inferred from GPS) and seismicity. These structural relationships are not yet fully resolved with the data coverage and inversion techniques used here, but we anticipate that new array deployments and the use of more powerful combinations of interferometry and full wave inversion methods will change this situation in the not too distant future.

Acknowledgments

We thank two anonymous reviewers for their constructive comments, which helped us improve the manuscript. We also thank Dr. Malcolm Sambridge for providing us the source code of the Neighborhood Algorithm, Prof. Denghai Bai at the Institute of Geology and Geophysics Chinese Academy of Science and Jiangning Lü at MIT for

sharing their results for comparison, Prof. Qiyuan Liu at Chinese Earthquake Administration for helpful discussions, and Dr. Yaoqiang Wu and his research staff at Sichuan Earthquake Administration, China for their discussions and hospitality during our visit to Chengdu, China. This work was supported by the Continental Dynamics Program of the US National Science Foundation under grant 6892042.

References

Bai, D., Meju, M., Arora, B., Ma, X., Jiang, C., Zhou, Z., Zhao, C., and Wang, L., 2006. Large crustal-mantle channel flow in central Tibet and eastern Himalaya inferred from magnetotelluric models, *Eos Trans. AGU*, 87(36), West. Pac. Geophys. Meet. Suppl., Abstract S45A-07.

Beaumont, C., Jamieson, R. A., Nguyen, M. H. and Medvedev, S., 2004. Crustal channel flow: 1. Numerical models with applications to the tectonics of the Himalayan-Tibetan orogen, *J. Geophys. Res.*, 109, B06406, doi:10.1029 /2003JB002809.

Beghein, C., Resovsky, J. S., and Trampert, J., 2002. P and S tomography using normal-mode and surface wave data with a neighbourhood algorithm, *Geophys. J. Int.*, 149, 646-658.

Brocher, T. M., 2005. Empirical relations between elastic wavespeeds and density in the Earth's Crust, *Bull. Seism. Soc. Am.*, 95(6), 2081-2092.

Chen, Z., Burchfiel, B.C., Liu., Y., King, R.W., Royden, L.H., Tang, W., Wang, E., Zhao, J., Zhang, X., 2000. Global positioning system measurements from eastern Tibet and their implications for India/Eurasia intercontinental deformation, *J. Geophys. Res*, 105, 16215-16227.

Clark, M. & Royden, L. H., 2000. Topographic ooze: building the eastern margin of Tibet by lower crustal flow, *Geology*, 28(8), 703-706.

De Hoop, M.V., van der Hilst, R.D., Shen, P., 2006. Wave-equation reflection tomography: annihilators and sensitivity kernels, *Geophys. J. Int.*, 167, 1211-1214.

Hu, S., He, L., & Wang, J., 2000. Heat flow in the continental area of China: a new data set, *Earth Planet. Sci. Lett.*, 179, 407-419.

Hu, J.F., Su, Y.J., Zhu, X.G., & Chen, Y., 2005a. S-wave velocity and Poisson's ratio structure of crust in Yunnan and its application (in Chinese), *Sci. China Ser. D.*, 48(2), 210-218.

Hu, J.F., Chu, X.G., Xia, J.Y., & Chen, Y., 2005b. Using surface wave and receiver function to jointly inverse the crust-mantle velocity structure in the West Yunnan area (in Chinese), *Chinese J. Geophys.*, 2005, 48(5), 1069-1076.

Huang, J., Zhao, D., & Zheng, S., 2002. Lithospheric structure and its relationship to seismic and volcanic activity in southwest China, *J. Geophys. Res*, 107(B10), 2255, doi:10.1029/2000JB000137.

Jordan, T. A., and Watts, A. B., 2005. Gravity anomalies, flexure and the elastic thickness structure of the India-Eurasia collisional system, *Earth Planet. Sci. Lett.*, 236, 732-750.

Kan, R., 1977. Study on the current tectonic stress field and the characteristics of current tectonics activity in southwest China (in Chinese), *Chinese J. Geophys.*, 20(2), 96-107.

Kennett, B. L. N., Engdahl, E. R. & Buland, R., 1995. Constraints on the velocity structure in the earth from travel times, *Geophys. J. Int.*, 122, 108–124.

King, R.W., Shen, F., Burchfiel, B.C., Royden, L.H., Wang, E., Chen, Z., Liu, Y., Zhang, X., Zhao, J., Li, Y., 1997. Geodetic measurement of crustal motion in southwest China, *Geology*, 25, 179-182.

Kohlstedt, D.L., & Zimmerman, M.E., 1996. Rheology of partially molten mantle rocks. *Annu. Rev.Earth Planet. Sci.*, 24, 41-62.

Lev, E., Long, M.D., Van der Hilst, R.D., 2006. Seismic anisotropy in eastern Tibet from shear wave splitting reveals changes in lithospheric deformation, *Earth Planet. Sci. Lett.*, 251, 293-304.

Li, C., Van der Hilst, R.D. & Toksoz, M.N., 2006. Constraining P-wave velocity variations in upper mantle beneath Southeast Asia, *Phys. Earth Planet. Inter.*, 154, 180–195.

Li, C., Van der Hilst, R.D., Meltzer, A.S., Sun, R., and Engdahl, E.R., 2008. Subduction of the Indian lithosphere beneath the Tibetan Plateau and Burma, *Earth Planet. Sci. Lett.*, under review.

Li, Z.X., 1998. Tectonic history of the major East Asian lithosphere blocks since the mid-Proterozoic. in *Mantle Dynamics and Plate Interactions in East Asia*, pp. 211–243, ed. Flower, M.F.J., Chung, S.-L., Lo, C.-H., and Lee, T.-Y., *Geodyn. Ser.*, 27.

Lin, F.-C., Ritzwoller, M.H., Townend, J., Bannister, S., and Savage, M.K., 2007 Ambient noise Rayleigh wave tomography of New Zealand, *Geophys. J. Int.*, 170 (2), 649–666. doi:10.1111/j.1365-246X.2007.03414.x

Masters, G., Laske, G., Bolton, H., & Dziewonski, A., 2000. The relative behavior of shear velocity, bulk sound speed, and compressional velocity in the mantle: Implication for chemical and thermal structure, *Geophysical Monograph Series*, 117, 63-87.

Meissner, R., Tilmann, F. and Haines, S., 2004. About the lithospheric structure of central Tibet, based on seismic data from the INDEPTH III profile, *Tectonophysics*, 380, 1-25.

Molnar, P. & Tapponnier, P., 1975. Cenozoic tectonics of Asia: Effects of a continental collision, *Science*, 189, 419-426.

Mooney, W.D., G. Laske and G. Masters, 1998. CRUST5.1: A global crustal model at 5°x5°, *J. Geophys. Res.*, 103, 727-747.

Nelson, K.D., Zhao, W.J., Brown, L.D., Kuo, J., Che, J., Liu, X., Klemperer, S.L., Makovsky, Y., et al., 1996. Partially molten middle crust beneath Southern Tibet: Synthesis of Project INDEPTH results, *Science*, 294, 1684-1688.

Nolet, G., 1985. Solving or resolving inadequate and noisy tomographic systems, *J. Comput. Phys.*, 61, 463–482.

Ozacar, A., and Zandt, G., 2004. Crustal seismic anisotropy in central Tibet: Implications for deformational style and flow in the crust, *Geophys. Res. Lett.*, 31, L23601, doi:10.1029/2004GL021096.

Resovsky, J.S. & Trampert, J., 2002. Reliable mantle density error bars: an application of the neighbourhood algorithm to normal-mode and surface wave data, *Geophys. J. Int.*, 150, 665-672.

Rowley, D. B., 1996. Age of initiation of collision between India and Asia: A review of stratigraphic data, *Earth Planet. Sci. Lett.*, 145, 1-13.

Royden, L. H., Burchfiel, B. C., King, R. W., Wang, E., Chen, Z., Shen, F., Liu, Y., 1997. Surface deformation and lower crustal flow in eastern Tibet, *Science*, 276, 788-790.

Sabra, K.G., Gerstoft, P., Roux, P. & Kuperman, W.A., 2005b. Surface wave tomography from microseisms in Southern California, *Geophys. Res. Lett.*, 32, L14311, doi:10.1029/2005GL023155.

Sambridge, M., 1999a. Geophysical inversion with a neighbourhood algorithm - I. Searching a parameter space, *Geophys. J. Int.*, 138, 479-494.

Sambridge, M., 1999b. Geophysical inversion with a neighbourhood algorithm - II. Appraising the ensemble, *Geophys. J. Int.*, 138, 727-746.

Shen, F., Royden, L. H. and Burchfiel, B. C., 2001. Large-scale crustal deformation of the Tibetan Plateau, *J. Geophys. Res.*, 106(B4), 6793-6816.

Shapiro, N. M., Campillo, M., Stehly, L., and Ritzwoller, M. H., 2005. High-resolution surface wave tomography from ambient seismic noise, *Science*, 307, 1615-1618.

Shen, Z.-K., Lü, J., Wang, M., & Bürgmann, R., 2005. Contemporary crustal deformation around the southeast borderland of the Tibetan Plateau, *J. Geophys. Res*, 110, B11409, doi:10.1029/2004JB003421.

Simons, F. J., & Van der Hilst, R.D., 2003. Structure and deformation of the Australian lithosphere, *Earth Planet. Sci. Lett.*, 211, 271-286.

Snoke, J. A., and Sambridge, M., 2002. Constraints on the S-wave velocity structure in a continental shield from surface-wave data: comparing linearized least-squares inversion and the direct-search neighbourhood algorithm, *J. Geophys. Res.*, 107(B5), 2094, 10.1029/2001JB000498.

Sol, S., Meltzer, A., Bürgmann, R., Van der Hilst, R.D., King, R., Chen, Z., Koons, P.O., Lev, E., et al., 2007. Geodynamics of southeastern Tibet from seismic anisotropy and geodesy, *Geology*, 35, 563-566, doi: 10.1130/G23408A.1.

Sun, J., Jin, G.W., Bai, D.H., and Wang, L.F., 2003, Electrical structure of the crust and upper mantle and tectonics sense on the edge of the East Tibet. *Science in China* (Series D) (in Chinese), 33(Suppl.), pp.173-180.

Tapponnier, P., Xu, Z., Roger, F., Meyer, B., Arnaud, N., Wittlinger, G., Yang, J., 2001. Oblique stepwise rise and growth of the Tibet Plateau. *Science*, 294, 1671–1677.

Unsworth, M. J., Jones, A. G., Wei, W., Marquis, G., Gokarn, S.G., Spratt, J.E., 2005. Crustal rheology of the Himalaya and southern Tibet from magnetotelluric data, *Nature*, 438, 78-81.

Wang, C.-Y., Chan, W.W., & Mooney, W.D., 2003. Three-dimensional velocity structure of crust and upper mantle in southwestern China and its tectonic implications, *J. Geophys. Res*, 108(B9), 2442, doi:10.1029/2002JB001973.

Wang, E., Burchfiel, B.C., Royden, L.H., Chen, L., Chen, J., Li, W., Chen, Z., 1998. Late Cenozoic Xianshuihe-Xiaojiang, Red River and Dali fault systems of southwestern Sichuan and central Yunnan, China. *Spec. Pap. Geol. Soc. Am.*, 327, 1-108.

Wang, E. & Burchfiel, B.C., 2000. Late Cenozoic to Holocene deformation in southwestern Sichuan and adjacent Yunnan, China, and its role in formation of the southeastern part of the Tibetan Plateau, *Geol. Soc. Am. Bull*, 112, 413-423.

Wei, W., Unsworth, M., Jones, A., Booker, J., Tan, H., Nelson, D., Chen, L., Li, S., et al., 2001. Detection of widespread fluids in the Tibetan crust by magnetotelluric studies, *Science*, 292, 716-718.

Xu, L., Rondenay, S., Van der Hilst, R.D., 2007. Structure of the crust beneath the Southeastern Tibetan Plateau from Teleseismic Receiver Functions, *Phys. Earth Planet. Int.*, 176-193, doi:10.1016/j.pepi.2007.09.002

Yang, Y., Ritzwoller, M.H., Levshin, A.L., & Shapiro, N.M., 2007. Ambient noise Rayleigh wave tomography across Europe, *Geophys. J. Int.*, 168, 259-274.

Yao, H., Van der Hilst, R.D., & de Hoop, M.V., 2006. Surface-wave array tomography in SE Tibet from ambient seismic noise and two-station analysis – I. phase velocity maps, *Geophys. J. Int.*, 166, 732-744.

Yoshizawa, K., and Kennett, B. L. N., 2002. Non-linear waveform inversion for surface waves with a neighbourhood algorithm - Application to multimode dispersion measurements, *Geophys. J. Int.*, 149, 118-133.

Zhang P., Shen, Z., Wang, M., Gan, W., Bürgmann, R., Molnar, P., Wang, Q., Niu, Z., et al., 2004. Continuous deformation of the Tibetan Plateau from global positioning system data, *Geology*, 32(9), 809-812.

Zhang, Z., Bai, Z., Wang, C., Teng, J., Lu, Q., Li, J., Sun, S., Wang, Z., 2005. Crustal structure of Gondwana- and Yangtze-typed blocks: An example by wide-angle seismic profile from Menglian to Malong in western Yunnan, *Science in China* (Series D) (in Chinese), 48(11), 1826-183.

Table 1. Model parameters in NA , their perturbation range, and average perturbation

Name of Model Parameter	Reference Value of Parameter	Perturbation with respect to the reference value	Average Perturbation
Moho depth	*H* (km)	[–5 5] km	–0.32 km
Vs in the upper crust	3.4 km/s	[–0.8 0.4] km/s	–0.069 km/s
Vs in the middle crust	3.6 km/s	[–0.8 0.4] km/s	–0.192 km/s
Vs in the lower crust	3.8 km/s	[–0.8 0.4] km/s	–0.120 km/s
Vs in Moho – 90 km	*Vs* from *ak135* (km/s)	[–0.6 0.6] km/s	–0.197 km/s
Vs in 90 – 130 km	*Vs* from *ak135* (km/s)	[–0.6 0.6] km/s	–0.053 km/s
Vs in 130 – 170 km	*Vs* from *ak135* (km/s)	[–0.6 0.6] km/s	0.102 km/s
Vs in 170 – 220 km	*Vs* from *ak135* (km/s)	[–0.6 0.6] km/s	0.130 km/s
Vs in 220 – 280 km	*Vs* from *ak135* (km/s)	[–0.6 0.6] km/s	0.058 km/s

H denotes the reference Moho depth from teleseismic receiver functions (Xu et al., 2007) and *Vs* is shear wavespeed (km/s). 'Average Perturbation' in the fourth column means the average perturbation of the model parameters for all grid points in the study region. The average Moho depth is 49.87 km from receiver functions (Xu et al., 2007) and 49.55 km after NA.

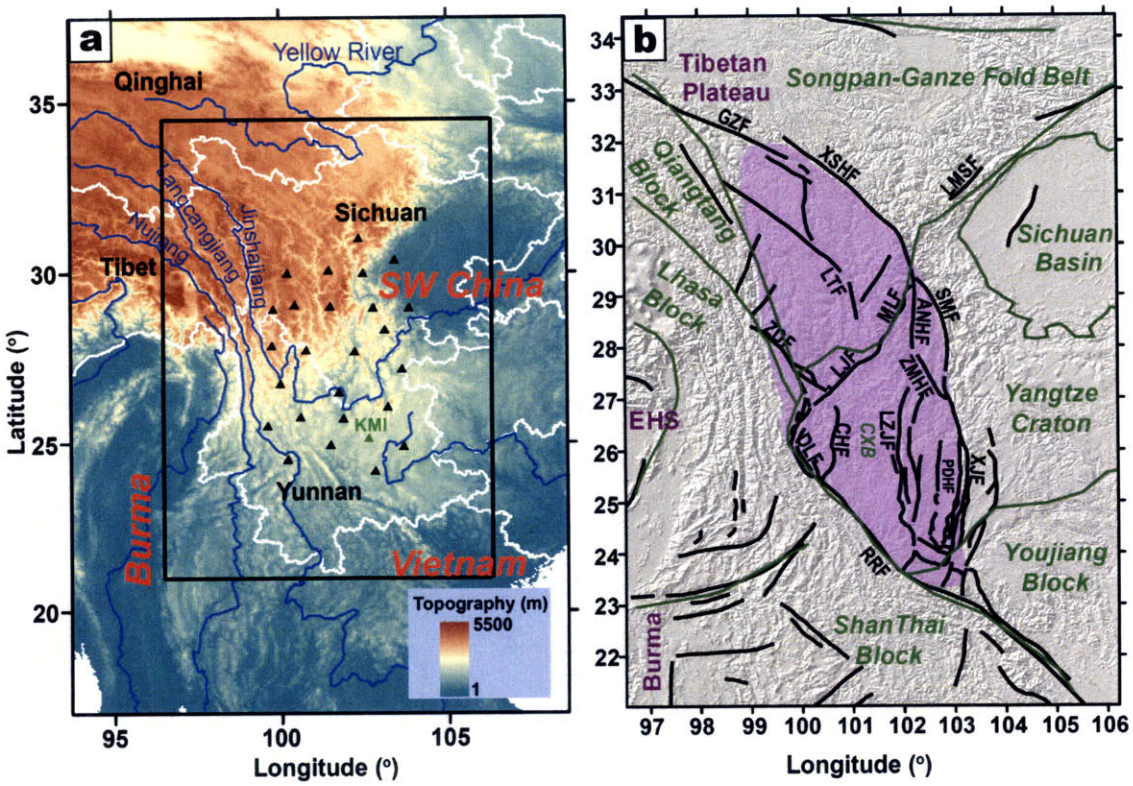

Figure 3-1. (a) Geographic map of SW China and adjacent areas. White lines show provincial boundaries in China; blue lines depict major rivers. The MIT-CIGMR array stations are depicted as black triangles and the permanent station KMI is shown as the green triangle. The black box outlines the study region shown in (b). (b) Tectonic elements and fault systems in the southeastern borderland of the Tibetan Plateau. Tectonic boundaries (modified from Li, 1998 and Tapponnier et al., 2001) are shown as dark green lines. The magenta shaded area shows the approximate region of the Chuan-Dian Fragment. The major faults are depicted with black lines (after Wang et al., 1998; Wang & Burchfiel, 2000; Shen et al, 2005). Abbreviations are: GZF – Ganzi Fault, LMSF – Longmenshan Fault, XSHF – Xianshuihe Fault, LTF – Litang Fault, ANHF – Anninghe Fault, SMF – Shimian Fault, ZMHF – Zemuhe Fault, ZDF – Zhongdian Fault, LJF – Lijiang Fault, MLF – Muli Fault, DLF – Dali Fault, CHF – Chenghai Fault, LZJF – Luzhijiang Fault, PDHF – Pudude Fault, XJF – Xiaojiang Fault, RRF – Red River Fault, CXB – Chuxiong Basin, and EHS – Eastern Himalaya Syntaxis.

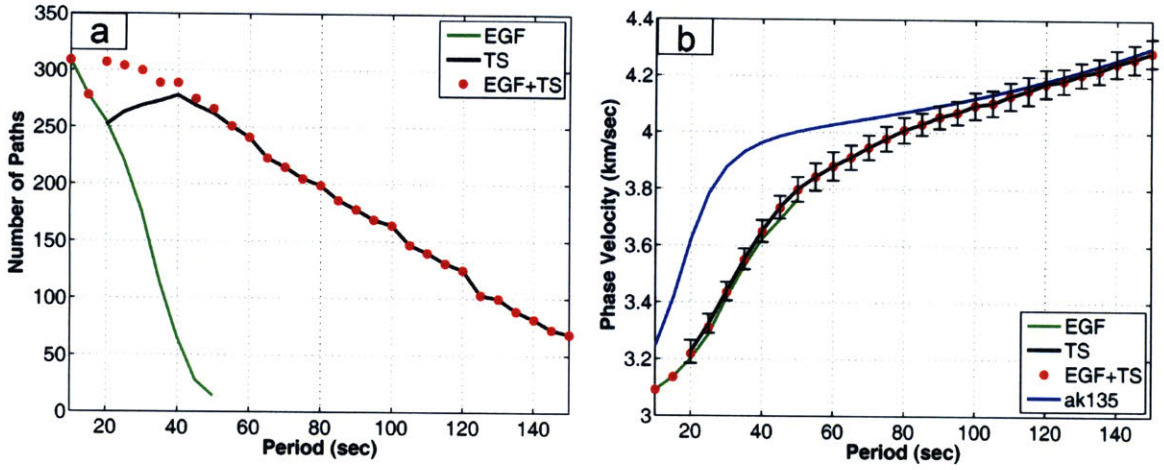

Figure 3-2. (a) Number of inter-station paths at different periods from the EGF analysis (green line), TS analysis (black line), and EGF+TS averaging (red dots); (b) the average dispersion curve for the array area from the EGF analysis (green line), TS analysis (black line), and EGF+TS averaging (red dots). The black error bars in (b) are the average standard errors for the average dispersion curve from the TS analysis. The blue line in (b) is the Rayleigh wave phase velocity dispersion curve (fundamental mode) predicted from the global *ak135* (continental) model (Kennett et al., 1995).

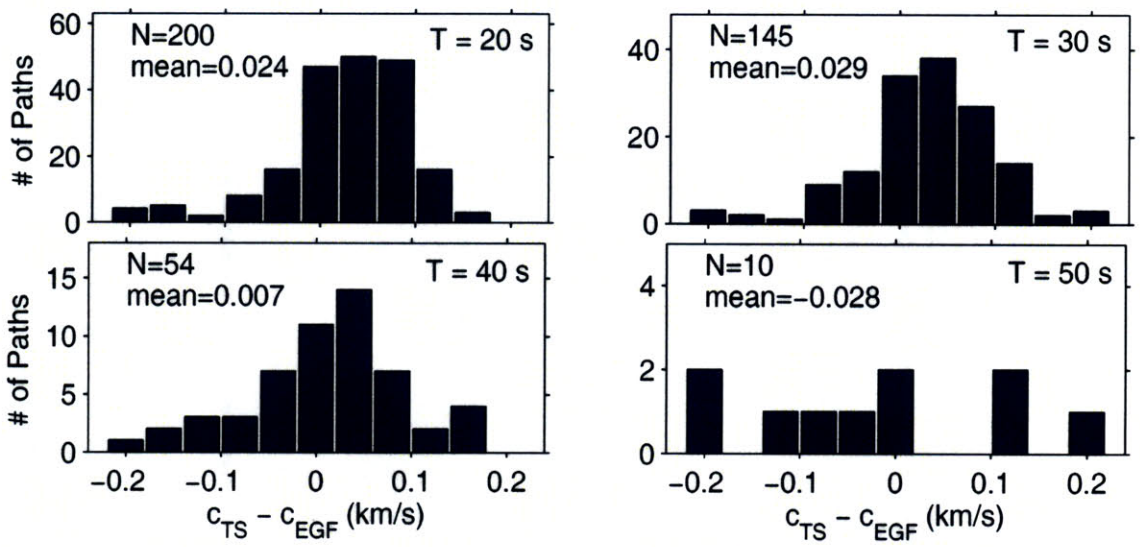

Figure 3-3. Histogram to show the comparison of inter-station Rayleigh wave phase velocity measurements from the TS and EGF analysis at overlapping periods (20 – 50 s). The horizontal axis show the difference between the phase velocity from the TS analysis (C_{TS}) and that from the EGF analysis (C_{EGF}), i.e., $C_{TS} - C_{EGF}$, while the vertical axis shows the number of inter-station paths which falls in the different $C_{TS} - C_{EGF}$ interval each with a width of 0.04 km/s. In each plot, 'N' is the total number of paths for comparison and 'mean' is the average difference (km/s) of $C_{TS} - C_{EGF}$ for all paths at that period.

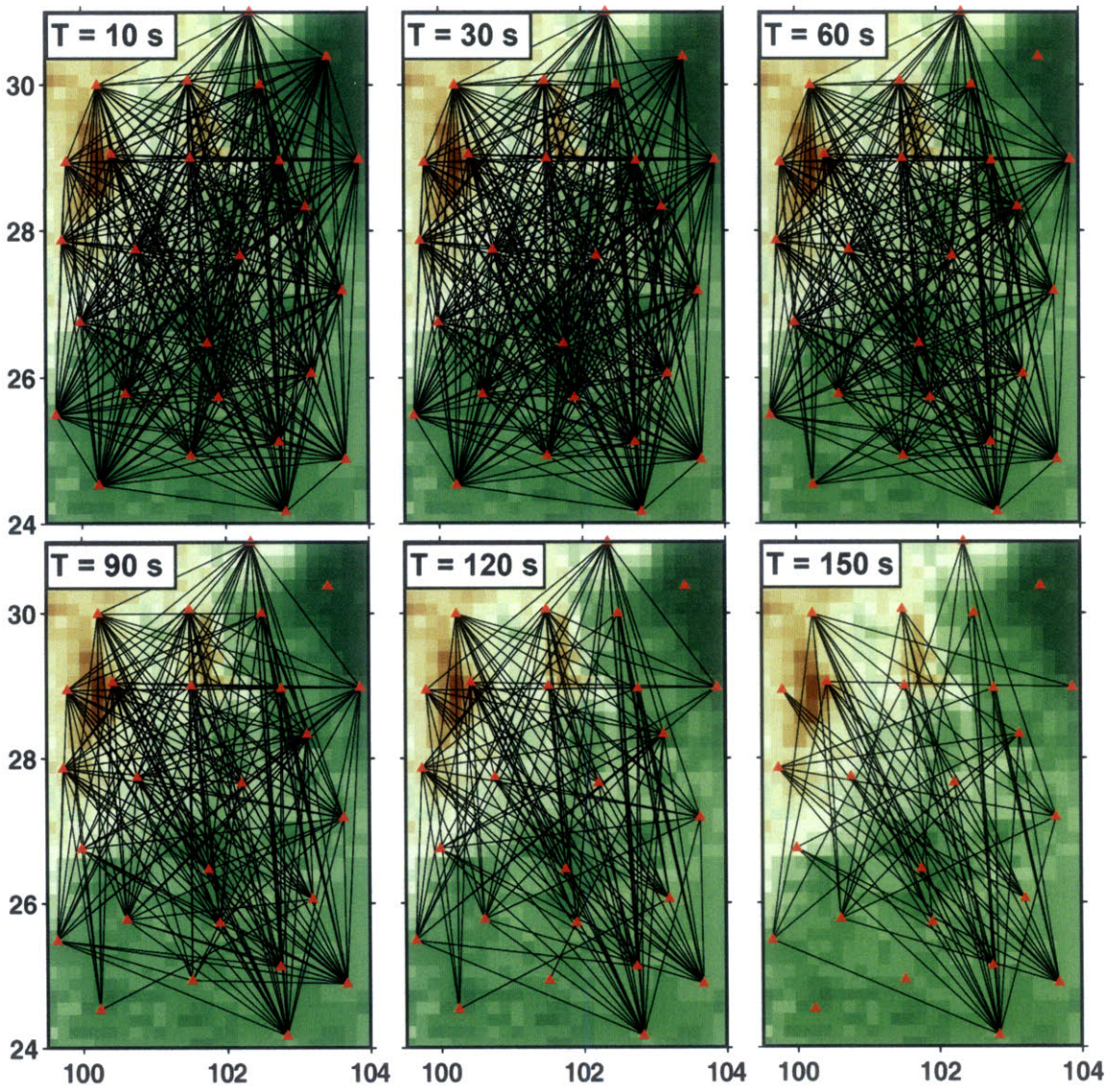

Figure 3-4. Inter-station ray path distribution for phase velocity measurements after EGF+TS averaging for 6 different periods (10, 30, 60, 90, 120, 150 s). The stations are shown as red triangles.

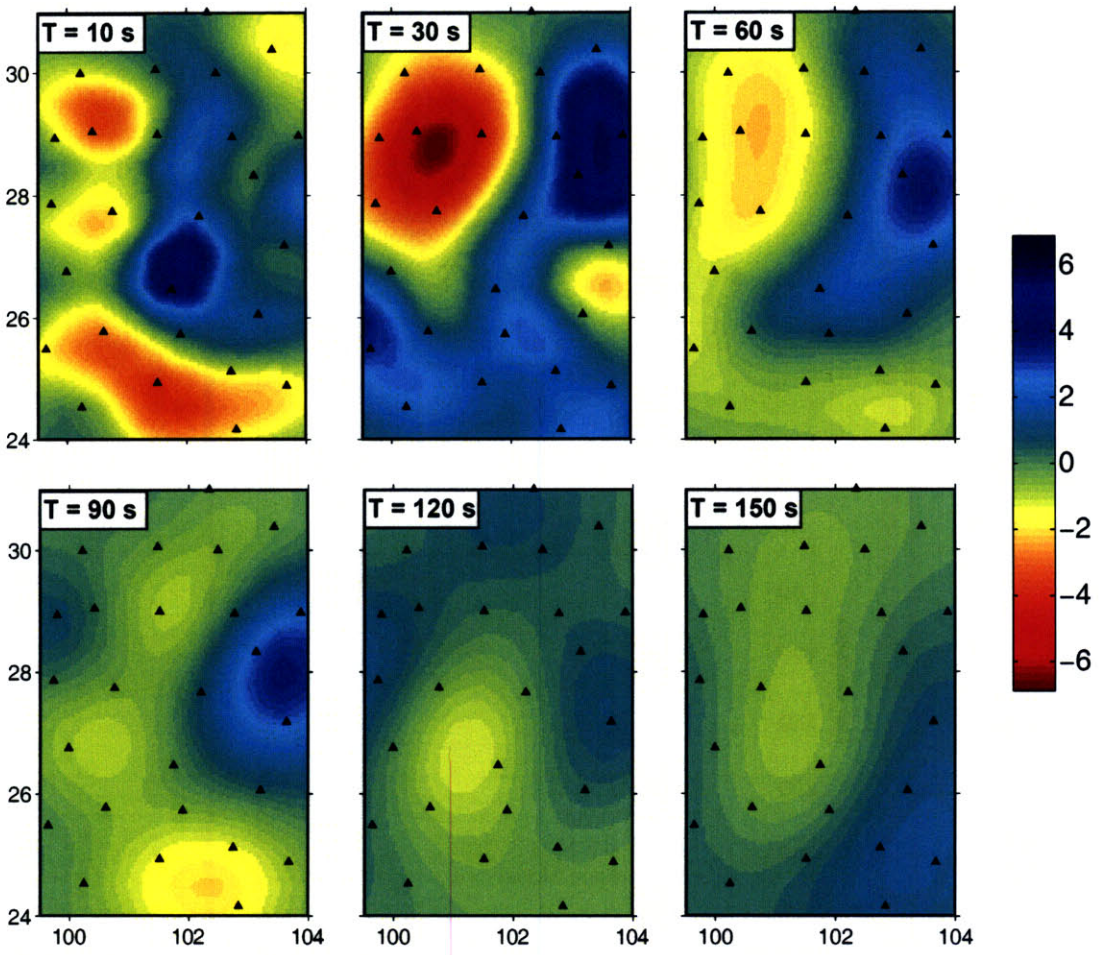

Figure 3-5. Perturbation (in percentage) of 2-D phase velocity maps at 6 different periods (10, 30, 60, 90, 120, 150 s) with respect to the average phase velocities (red dots in Figure 3-2b) constructed from the dispersion data after EGF+TS averaging. The corresponding ray path distribution map at each period is shown in Figure 3-4. The stations are shown as black triangles.

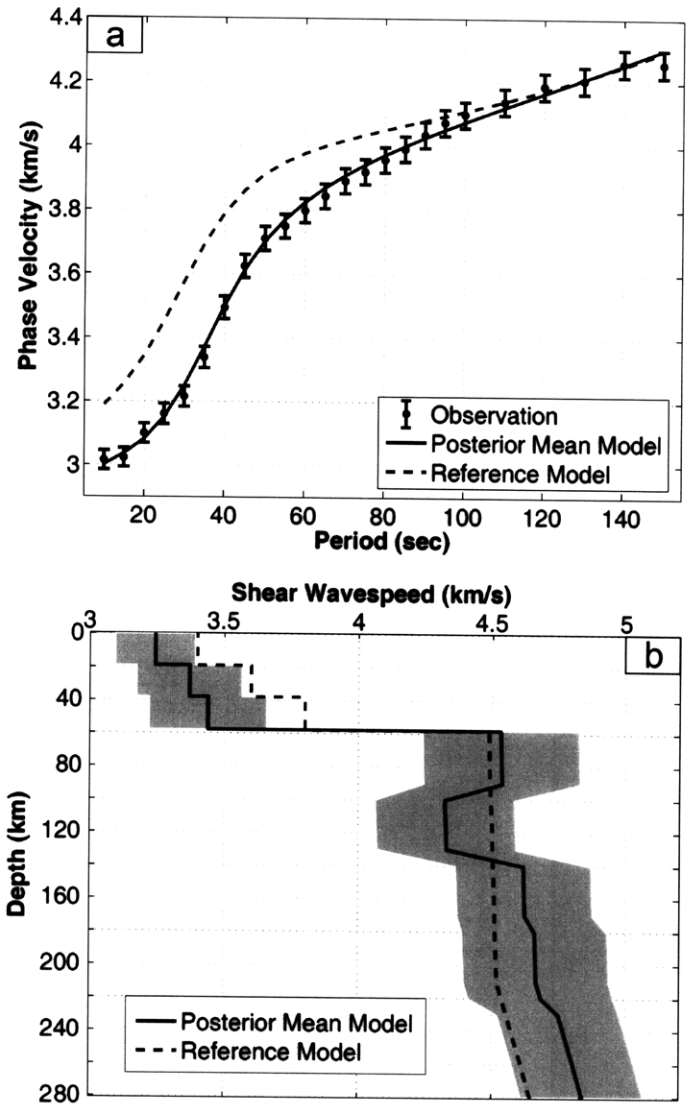

Figure 3-6. Rayleigh-wave phase velocity dispersion curves (a) and shear wavespeed model (b) for the grid point at (101°E, 29°N) obtained from the NA. The observed dispersion data at the grid point are shown as the black dots in (a). The error bar on the observed dispersion point shows the standard error (1% of the observed phase velocity) of the dispersion measurement at each period. The solid line in (b) shows the posterior mean *Vs* model and the predicted dispersion curve from this model is shown as the solid line in (a). The dashed line in (a) shows the predicted dispersion curve of the reference model (the dashed line in (b)), which consists of three crustal layers and mantle structure from the global *ak135* model (Table 1). The width of the shaded area shows the standard error of the posterior mean *Vs* in each layer.

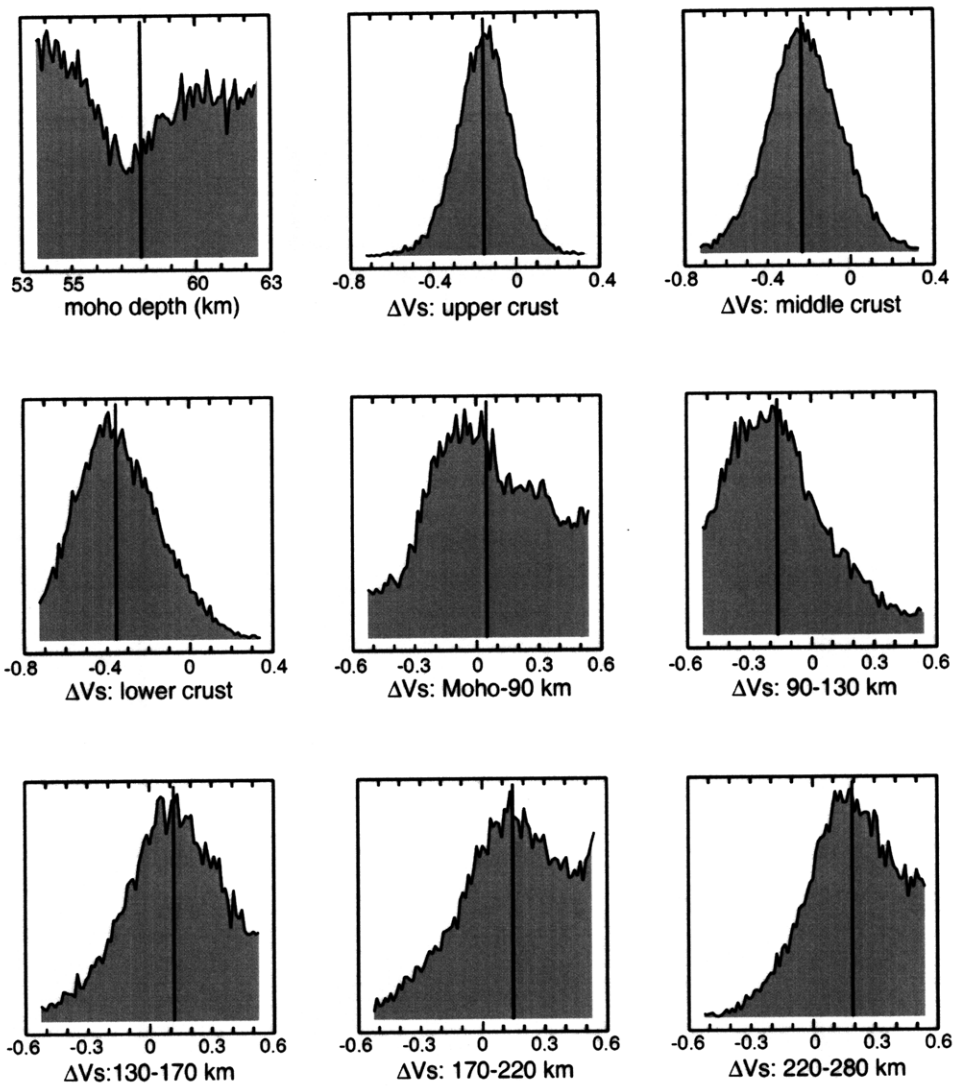

Figure 3-7. 1-D marginal posterior probability density functions (PPDFs) of the 9 model parameters at (101°E, 29°N). The horizontal axis shows the variation range of Moho depth (km) or the perturbation range of ΔVs (km/s) for each layer as shown in Table 1 and the vertical axis is the normalized posterior probability density. In each plot, the solid line shows the parameter value of the posterior mean model. The reference Moho depth for this grid point is 58 km, and the posterior mean value from of the Moho depth from the 1-D marginal is 57.8 km with a standard error about 3 km. The almost flat 1-D marginal PPDF of the Moho depth implies the Moho depth is not well constrained at this grid point. Notice that the posterior mean ΔVs of each crustal layer is very close to the value of the most likely model, which corresponds to the peak of each 1-D marginal PPDF with almost Gaussian distribution.

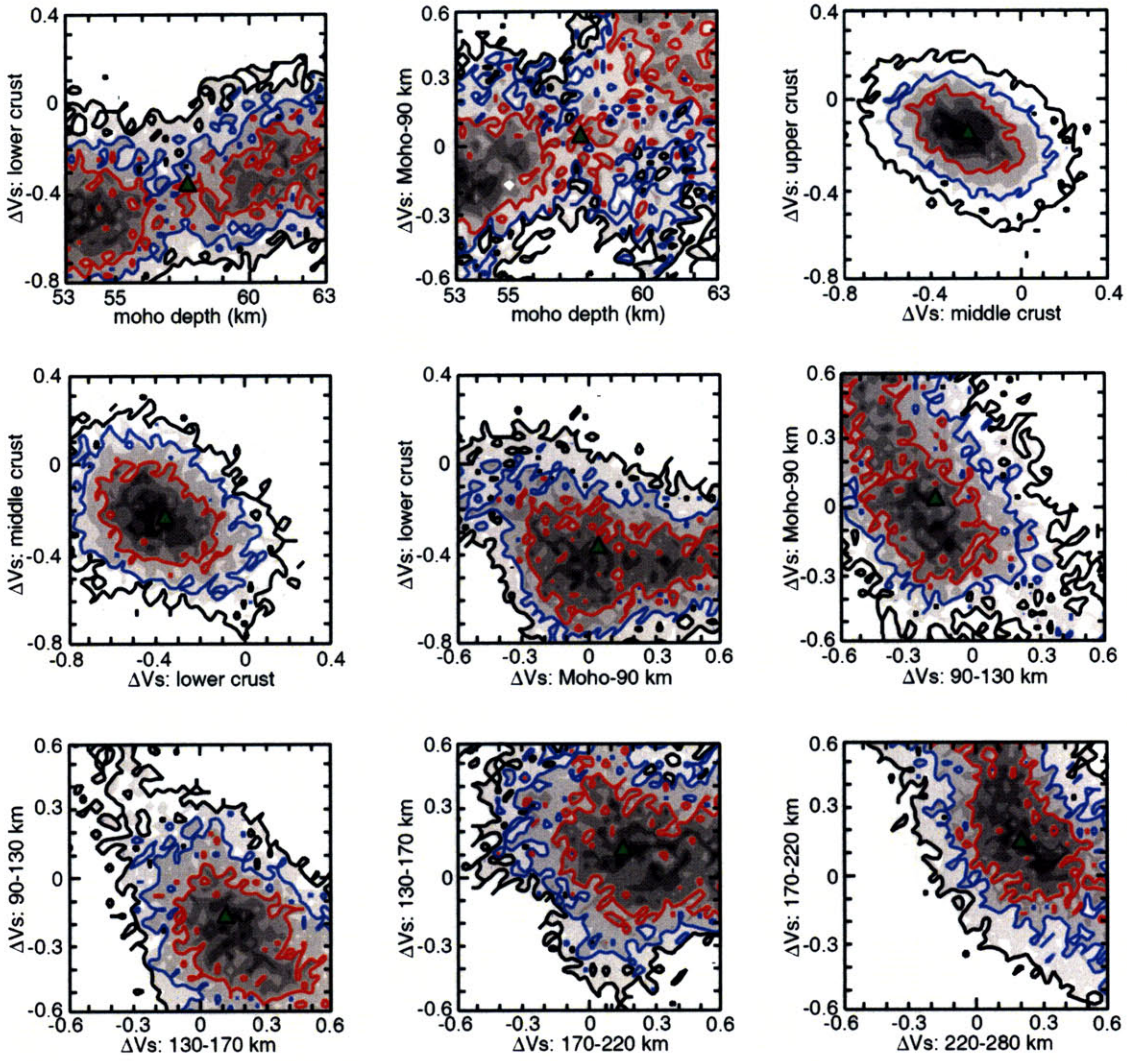

Figure 3-8. Examples of 2-D marginal PPDFs of the 9 model parameters at (101°E, 29°N). In each panel, the values for the horizontal and vertical axis show the perturbation range of ΔVs (km/s) for each layer or the variation range of Moho depth (km). Black, blue, and red lines are the contours to show 60%, 90%, and 99% confidence level. The more circular and narrower the contour is, the smaller the trade-off between the two model parameters is. The posterior mean model is shown as a green triangle in each plot.

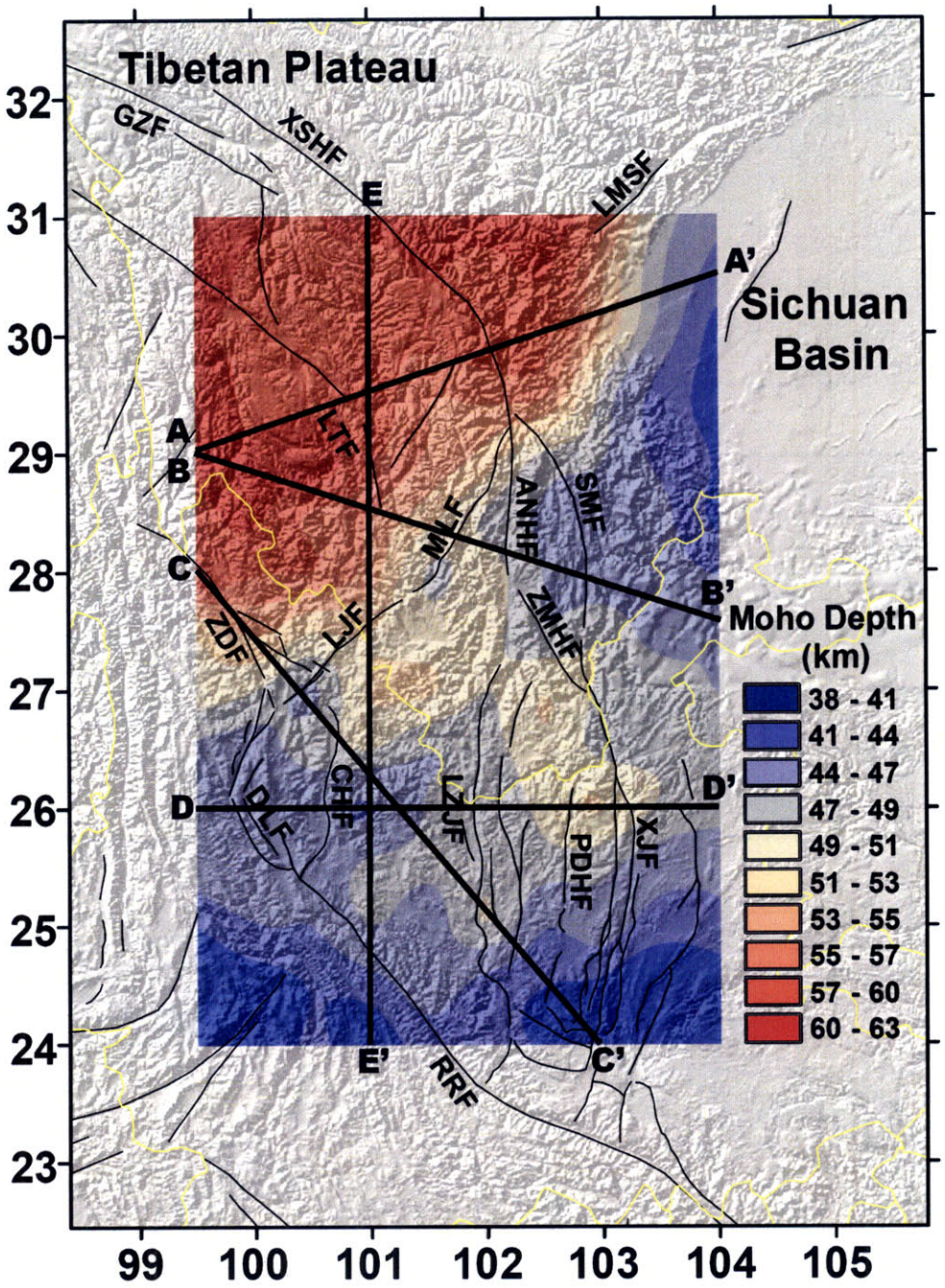

Figure 3-9. Variation of the Moho depth as inferred from the posterior mean model using the NA at each grid point in the studied area. The color bar in the right corner shows the value of Moho depth. The black thick lines are the section lines of the vertical profiles (AA', BB', CC', DD', and EE') shown in Figure 3-12.

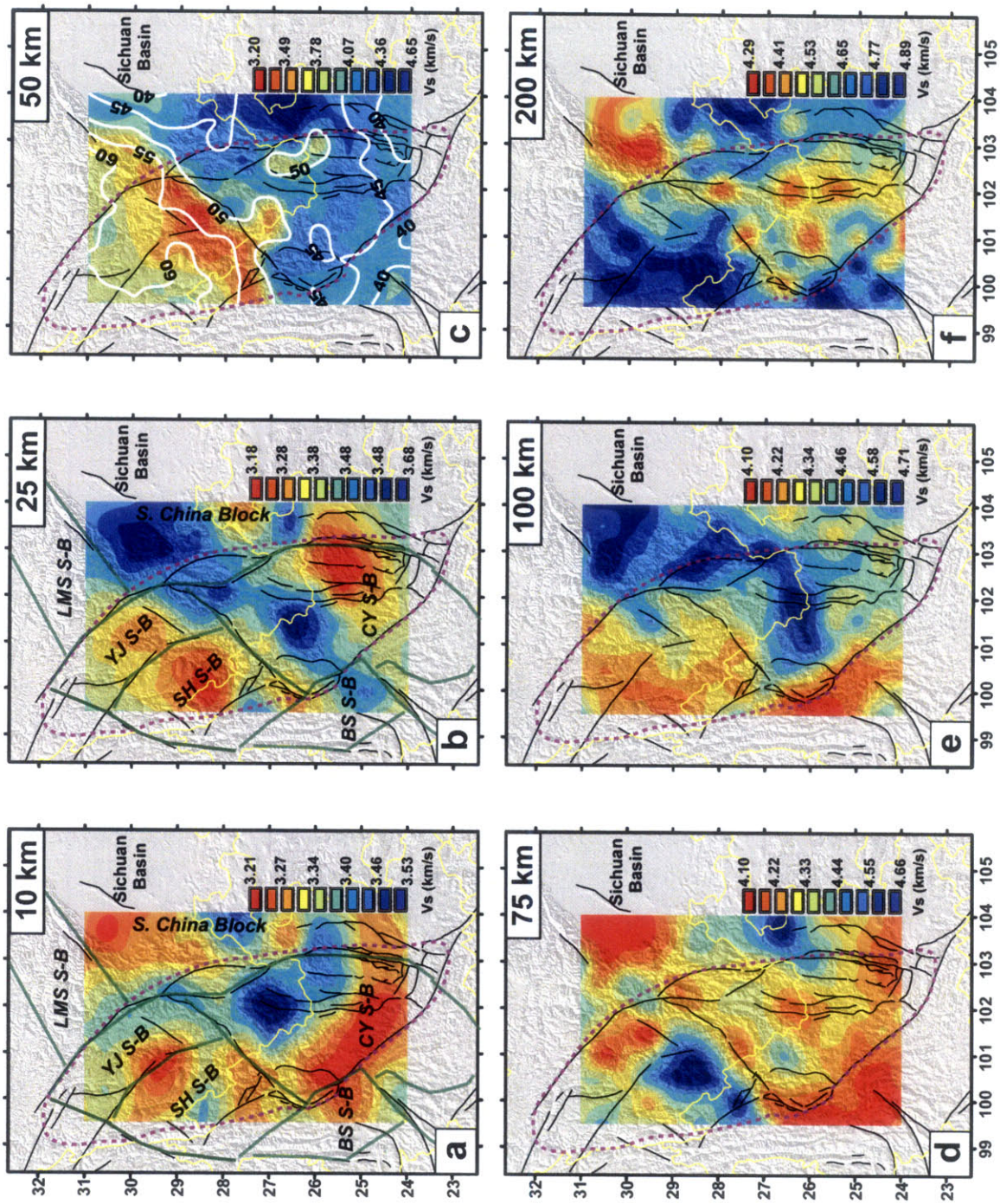

Figure 3-10. Variation in shear wavespeed relative to the posterior mean model inferred from the NA: (a) 10 km; (b) 25 km; (c) 50 km; (d) 75 km; (e) 100 km; and (f) 200 km. The major faults are depicted as thin black lines - for abbreviations see Figure 3-1b. The thick dark green lines are the block boundaries from the surface GPS data modeling (Shen et al., 2005). The abbreviations for subblocks are YJ (Yajiang), SH (Shangrilla),

CY (Central Yunnan), LMS (Longmenshan), and BS (Baoshan) subblock (S-B). The white lines in (c) are the contour lines of Moho depth and the values are shown as the black numbers on them. The color bar in the right corner of each plot shows the value of shear wavespeed (km/s).

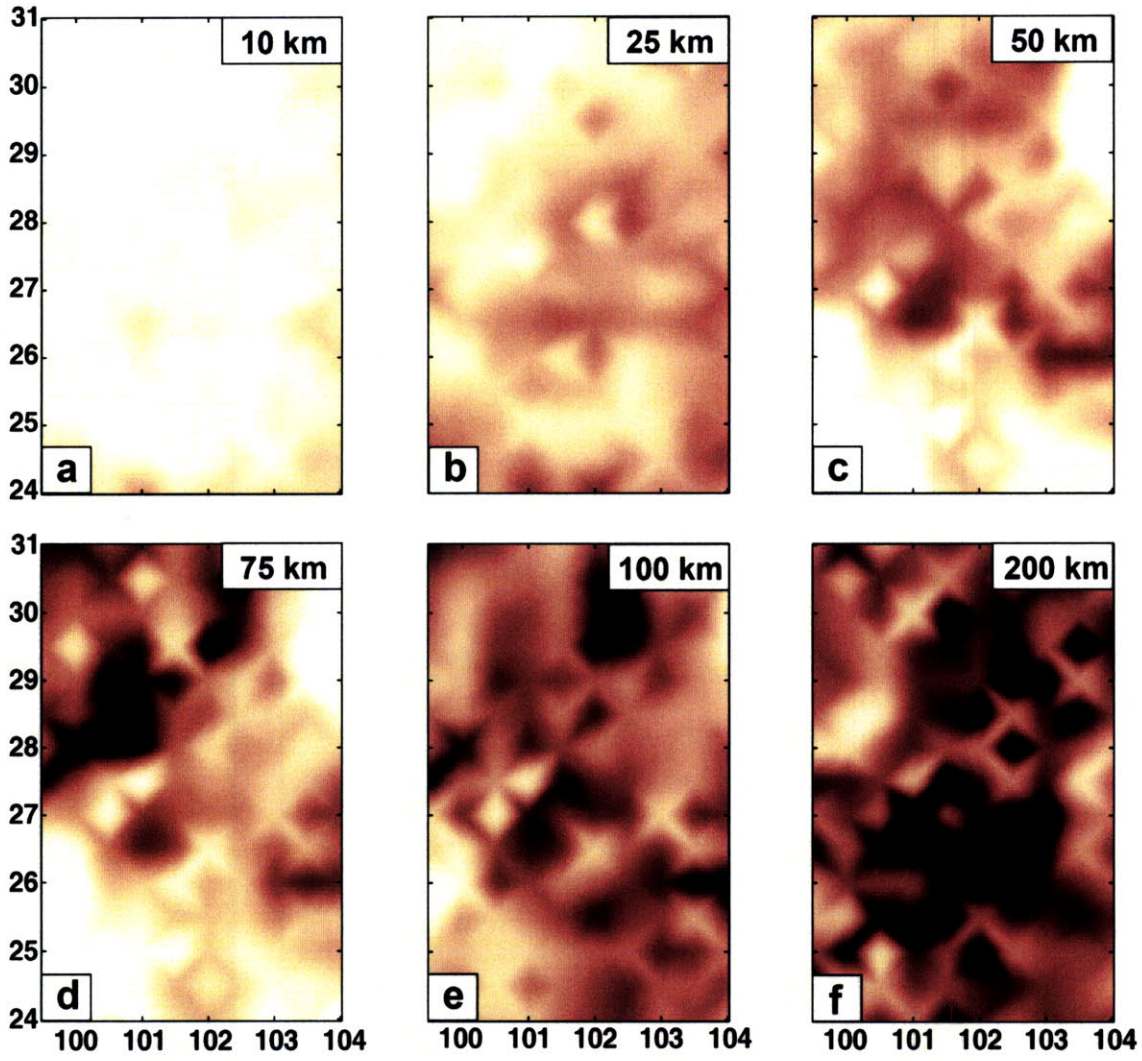

Figure 3-11. Standard error (σ_v) of the shear wavespeed at different depths shown in Figure 3-10. The color bar in the right shows the value of σ_v (km/s).

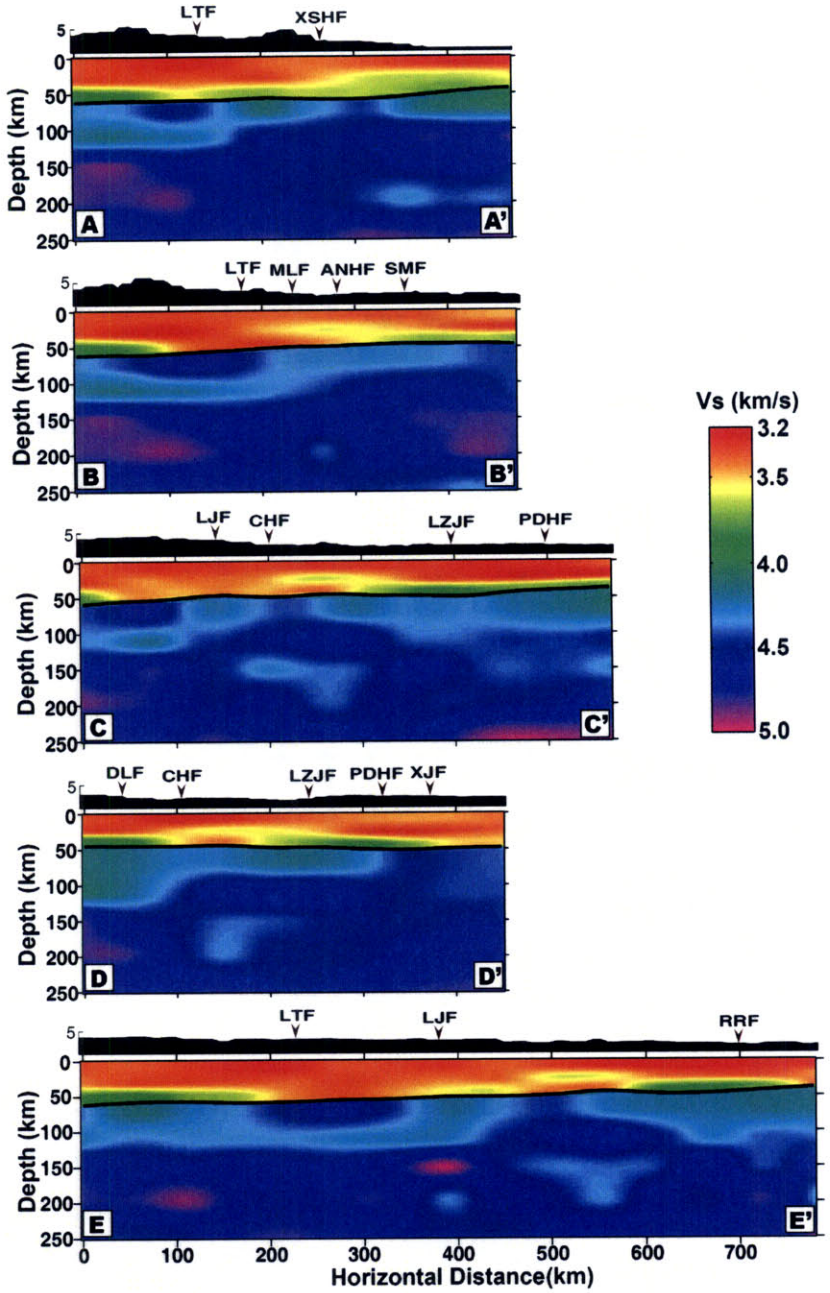

Figure 3-12. Shear wavespeed variation relative to the posterior mean model inferred from the NA along five vertical profiles (AA', BB', CC', DD', and EE' shown in the bottom of each plot; for location, see Figure 3-9). The wavespeed (km/s) color scale is shown in the right. Topography is depicted above each profile (black area) and the arrows above it mark the location of major faults along each profile. The abbreviations for fault names are the same as in Figure 3-1b. The black line (around 50 km depth) on each color profile indicates the Moho discontinuity.

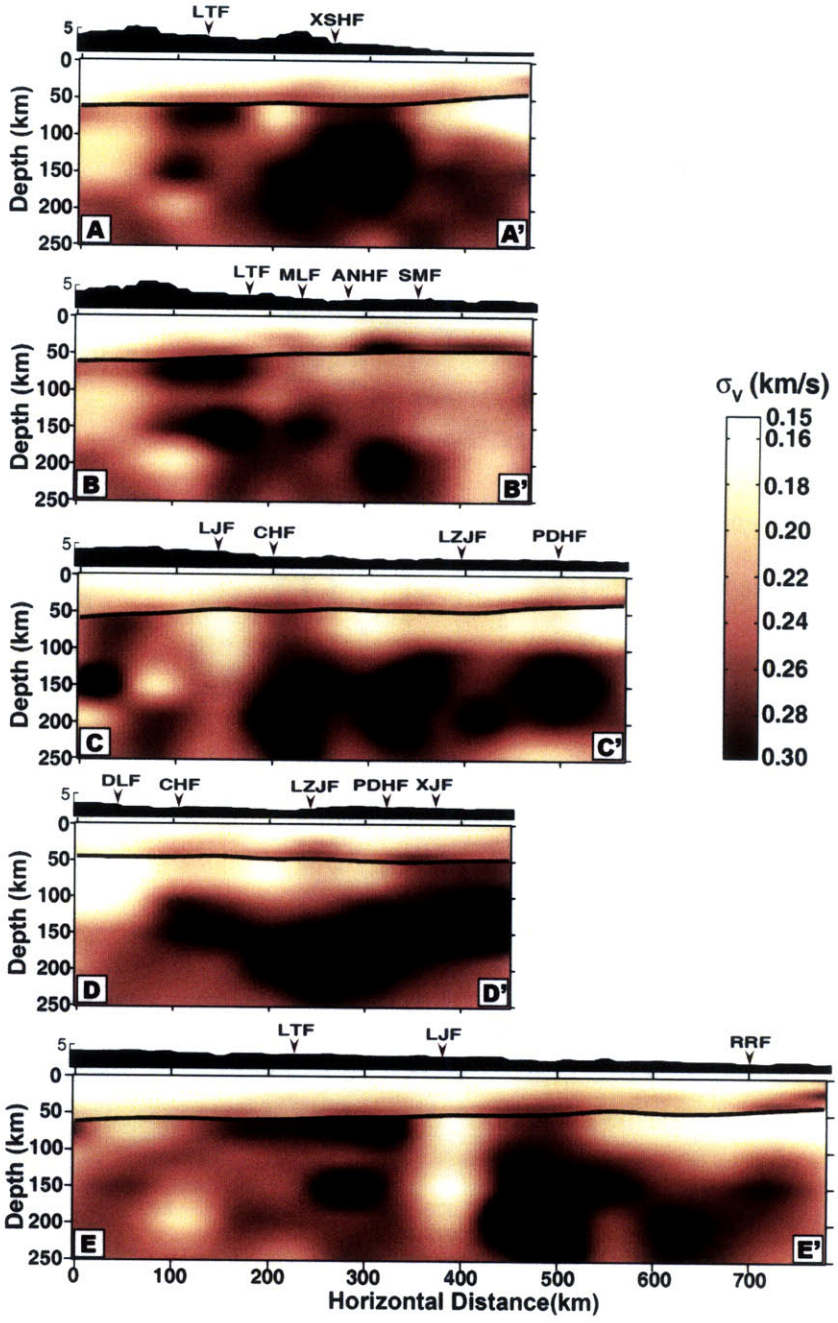

Figure 3-13. Standard error (σ_v) of the shear wavespeed along five vertical profiles shown in Figure 3-12. The color bar in the right shows the value of σ_v (km/s).

Chapter 4

Estimation of surface-wave Green's functions from correlation of direct waves, coda waves, and ambient noise in SE Tibet[3]

Abstract

Empirical Green's functions (EGFs) between receivers can be obtained from seismic interferometry through cross-correlation of pairs of ground motion records. Full reconstruction of the Green's function requires diffuse wavefields or a uniform distribution of (noise) sources. In practice, EGFs differ from actual Green's functions because wavefields are not diffuse and the source-distribution not uniform. This difference, which may depend on medium heterogeneity, complicates (stochastic) medium characterization as well as imaging and tomographic velocity analysis with EGFs. We investigate how source distribution and scale lengths of medium heterogeneity influence Green's function reconstruction in the period band of primary microseisms (T = 10-20 s). With data from a broad-band seismograph array in SE Tibet we analyze the symmetry and travel-time properties of surface-wave EGFs from correlation of data in different windows: ambient noise, direct surface waves, and surface wave coda. The EGFs from these different windows show similar dispersion characteristics, which demonstrates that the Green's function can be recovered from direct wavefields (e.g., ambient noise or earthquakes) or from wavefields scattered by heterogeneity on a regional scale. Directional bias and signal-to-noise ratio of EGFs can be understood better with (plane wave) beamforming of the energy contributing to EGF construction.

[3] Under review as: Yao, H., Campman, X., De Hoop, M.V., and Van der Hilst, R.D., 2009. Estimation of surface-wave Green's function from correlations of direct waves, coda waves, and ambient noise in SE Tibet, submitted to *Phys. Earth Planet. Inter.*

Beamforming also demonstrates that seasonal variations in cross-correlation functions correlate with changes in ocean activity.

4.1 Introduction

Traditional seismic imaging and tomographic velocity analysis of Earth's interior relies on data associated with ballistic (source-receiver) wave propagation. However, over the past few years one has also started to use information contained in seismic coda waves and ambient noise to image the Earth's structure from regional scale to continental scale (Campillo & Paul, 2003, Shapiro & Campillo, 2004; Shapiro et al., 2005; Bakulin & Calvert, 2006; Willis et al., 2006, Yao et al, 2006, 2008; Yang et al., 2007). Modal representation of diffuse wavefields, elastodynamic representation theorems, and stationary phase arguments (Weaver & Lobkis, 2004; Wapenaar, 2004; Snieder , 2004; Paul et al., 2005; Roux et al., 2005; Nakahara, 2006) have been used to argue that the Green's function between the two stations can be estimated from the summation of cross correlations of continuous records of ground motion at these stations. These studies make different assumptions about noise characteristics and (stochastic) properties of the medium. The results of ambient noise cross correlation are analyzed by Colin de Verdière (2006a, 2006b), Bardos et al. (2008), and De Hoop and Solna (2008).

Continuous records of ground motion typically contain seismic energy in several regimes. For example, earthquakes generate deterministic, transient energy that can be registered as distinct phase arrivals by seismometers. Non-smooth medium heterogeneity can, however, complicate waveforms in such a way that they can no longer be described deterministically. After multiple scattering the wave field may become diffuse. This regime is often called the seismic coda, mostly arriving after the ballistic waves (see, for instance, Sato and Fehler, 1998). Outside the time windows containing direct and coda waves from earthquakes continuous records contain energy that is mainly due to continuous processes near and below Earth's surface. This regime is often referred to as ambient seismic noise. In theory, the cross-correlation-and-summation approach can be applied to each of these regimes to obtain an empirical Green's function (EGF), as long

as energy arrives at the two seismic stations from all directions and in all possible modes (assuming equipartitioning).

For simple media cross correlation of the ballistic responses due to sources surrounding two receivers gives the exact Green's function between the receivers (De Hoop & De Hoop, 2000; Wapenaar, 2004). In practice, seismic energy is neither uniformly distributed nor equipartitioned (Malcolm et al., 2004; Sánchez-Sesma et al., 2008; Paul et al., 2005). In field experiments, equipartitioning is generally not achieved because the mode structure of the wave field depends on the mechanism and the location of the noise sources. Moreover, equipartitioned waves are weak and their contribution to the wavefield can easily be overwhelmed by (directional) waves and noise, as shown below. As a consequence, Green's functions are not fully reconstructed, and the accuracy of reconstruction is generally unknown. How well the Green's function is estimated depends on the mechanism and spatial distribution of the noise sources as well as the properties of the medium beneath the receiver arrays. On the positive side, one could exploit this dependence to constrain (stochastic) medium properties (e.g., Scales et al., 2004) if the effects of noise distribution can be accounted for. In this context, the length scale of heterogeneity, the frequency content of the wave fields, and the spatial and temporal spectra of noise sources are all important (De Hoop and Solna, 2008). On the negative side, the (unknown) uncertainty in Green's function construction complicates imaging and, in particular, multi-scale (tomographic) velocity analysis with EGFs.

The problem of incomplete Green's function reconstruction has been recognized before – see, for instance, Yao et al. (2006) for cases of incomplete reconstruction of EGFs for Rayleigh wave propagation) – and practical solutions have been proposed. For active source applications of seismic interferometry, source distributions can be designed with the objective to optimize the retrieval of the Green's function (Metha et al., 2008). In earthquake seismology, where the source configuration cannot be manipulated, one can enhance the illumination of receiver arrays by ballistic waves either by waiting long enough for contributions from a large range of source areas to accumulate or one can make better use of the (continuously) recorded wavefield.

To improve the inference of medium properties from EGFs or the imaging or velocity analysis of complex media with EGFs we need a more comprehensive understanding of the relationships between EGFs and medium heterogeneity and properties of noise sources. De Hoop & Solna (2008) present a theoretical framework for the estimation of Green's functions in medium with random fluctuations; and show that EGFs are related to the actual Green's function through a convolution with a statistically stable filter that depends on the medium fluctuations.

Using field observations (from an array in SW China) we investigate here the different contributions of the wavefield to the construction of EGFs through cross correlation. For this purpose we analyze EGFs obtained from windows of ambient noise, direct surface waves, or surface-wave coda. Cross correlation of (direct) surface windows yield EGFs (only) for direct surface wave propagation, but by changing the data window we can manipulate the parts of the wavefield that contribute to the construction of the EGF. Cross correlation of coda waves should yield EGFs that include scattered waves. The latter can also be obtained by correlation of long records of ambient noise. In principle, coda wave and (pure) ambient noise correlation should produce similar EGFs and differences between them can give information about the energy distribution and heterogeneity under and near the array. We complement our analysis with plane-wave beam forming (in the frequency-wavenumber domain), which quantifies the directional energy distribution of the signals that contribute to the EGF. This beamforming analysis reveals (temporal) variations in source regions of ambient noise, which – in turn – help understand the (changes in) symmetry and signal-to-noise ratio (SNR) of the EGFs.

4.2 Data and processing

We use 10 months (November 2003 to August 2004) of continuously recorded, vertical component broadband data from a temporary seismograph array in southeastern (SE) Tibet (see Figure 4-1). The 25 station array, with average station spacing ~100 km, was deployed by MIT and the Chengdu Institute of Geology and Mineral Resources (CIGMR). For more detailed descriptions of the array data and the preliminary results from surface

wave array tomography (ambient noise and traditional two-station analysis), which reveal strong heterogeneity in the crust, we refer to Yao et al. (2006, 2008).

Basic data pre-processing includes the removal of the mean and compensation for the instrument response. For the analyses presented here we first band-pass the data between periods of 10-20 s. Next, we select particular parts of the data (direct surface waves, surface wave coda, and ambient noise) from the continuous recordings, as shown in Figure 4-2. Consider seismic waves released by an earthquake with source time, at t_s, recorded by a seismograph station at epicentral distance Δ (km). For any time t after t_s (i.e., $t > t_s$) the corresponding average group velocity (or horizontal propagation speed) for 2-D surface waves $v_g = \Delta/(t-t_s)$, as shown in Figure 4-2. The example shows a main surface wave within window v_g = (2.5 - 5.0) km/s. By muting (setting the amplitude of the seismic trace to zero) outside or inside a specific time window (e.g., Figure 4-2), we select specific data windows associated with (known) earthquakes (e.g., Figure 4-3) or (unknown) ambient noise. The detailed time window partitioning is given in Section 4.3.

We apply one-bit or normalized cross correlation to the data band-pass-filtered in these data windows to obtain the cross correlation function. EGFs are then obtained from the time-derivative of the cross correlation function by $-\hat{G}_{AB}(t)+\hat{G}_{BA}(-t)=\frac{dC_{AB}(t)}{dt}$, where $\hat{G}_{AB}(t)$ ($t\geq 0$) is the causal part EGF at station B for a fictitious (point) source located at A, $\hat{G}_{BA}(-t)$ ($t\leq 0$) is the anti-causal part EGF at A for a fictitious (point) source at B, and $C_{AB}(t)$ is the one-bit cross correlation function between the two stations (Yao et al., 2006). Since for this analysis we use vertical component data we recover predominantly the Green's function for (fundamental mode) Rayleigh wave propagation. Similarly, Love waves can be recovered from transverse component data (Campillo & Paul, 2003; Paul et al., 2005; Lin et al., 2008).

4.3 EGFs from different data windows

In a heterogeneous medium, the Green's function for wave propagation between two points contains contributions from scattering anywhere in the medium – not just from

structure located between these points. EGFs are estimates of the Green function obtained from correlation and summation of the diffuse wavefields recorded at two receivers. How well the EGF reconstructs the actual Green function strongly depends on the characteristics of the energy in the wavefields used. EGFs from cross correlation of field data usually show a strong dependence on (non uniform) energy distribution (Yao et al., 2006; Yao and Van der Hilst, 2009).

In this section we evaluate EGFs extracted from cross correlation of data in different time windows. From the continuous records, we extract data associated with ambient noise, direct surface waves, and surface wave coda. We illustrate our analysis with data from two station pairs (Figure 4-1): MC04-MC23 (a N-S (north-south) pair with inter-station distance ~570 km) and MC06-MC10 (a W-E (west-east) pair with distance ~400 km).

4.3.1 EGFs from all continuous data

For reference, we first calculate EGFs for the two station pairs from one-bit cross correlation of the entire 10-month record, shown as the red trace in Figures 4-4a,b for MC04-MC23 and MC06-MC10, respectively. Like other normalized cross correlation methods (e.g., Bensen et al., 2007) one-bit cross correlation normalizes the energy of all sources contributing to the construction of the EGF, so that the average energy flux is an indicator of the number (or normalized strength) of these sources, not their real magnitude. For both station pairs, the EGFs reveal Rayleigh wave arrivals with group speed around 3 km/s. Neither EGF is time-symmetrical, however, and the amplitude (or SNR) in the anti-causal part is much larger than in the causal part. For MC04-MC23 the 10-month average energy flux seems much higher from S to N (which contributes to the recovery of the anti-causal part of the EGF) than from N to S (the causal part). For MC06-MC10 the average energy flux in the 10 months is larger from E to W than from W to E.

4.3.2 EGFs from ambient noise

In the previous section we used continuous 10-month records. In this section and the next, we partition the data in specific energy propagation regimes (ambient noise, direct

surface waves, and surface wave coda). The group velocity window procedure described above allows us to obtain EGFs (mostly) from ambient noise by suppressing signals associated with large earthquakes (see also Yao et al., 2006). Most direct body waves and surface waves, as well as their coda, appear in the group-velocity window 2 -10 km/s (see Figure 4-2). Using earthquake origin times t_s from the EHB catalog by Engdahl et al., (1998) we suppress the amplitude of signal within the 2-10 km/s group velocity windows for earthquakes larger than certain magnitude. One-bit cross-correlation to the remaining signals is then used to extract EGFs (approximately) from ambient noise.

Note that ambient noise is here defined as all seismic energy unrelated to earthquakes with magnitude larger than the cut-off magnitude. Thus defined, ambient noise contains contributions from small earthquakes, but the smaller the cut-off magnitude the closer the remaining seismograms are to ambient seismic noise proper. The energy from such a source distribution approximately corresponds to the diffuse wave field theoretically required for accurate Green's function construction. In this study we set the smallest cut-off magnitude to $m_b = 4$, because many earthquakes smaller than $m_b = 4$ are not listed in the EHB catalogue and recorded signals from those small earthquakes are usually below the ambient noise level due to the attenuation and geometrical spreading over a few thousand kilometers.

EGFs obtained from 10-month records of ambient noise, as defined above, are shown as the black traces in Figure 4-4 for two cut-off magnitudes $m_b = 5$ and $m_b = 4$. The distribution of earthquakes with $m_b \geq 4$ and $m_b \geq 5$ is shown as in Figures 4-3a and 4-3b, respectively. These EGFs are almost identical to the EGFs from the continuous 10-month records (red traces in Figure 4-4). This implies that in the period band considered (10-20 s) the contributions from large earthquakes is small compared to that from ambient noise, as expected from one-bit cross correlation (see also Yao et al., 2006). This also implies that the asymmetry of the EGFs is not caused by non-uniform distribution of large earthquakes but (for the time period considered) by ambient noise directionality, with most noise sources to the south and east of the array. Furthermore, tests (not shown here) with 1-month records showed that variations of EGFs over time are not related to the

temporal variations in earthquake activity. In fact, (plane wave) beam forming with the EGFs (see Section 4.4 below) demonstrates that the temporal changes in EGF symmetry and amplitude are related to seasonal variations of ocean microseisms (see also Stehly et al. 2006, Pedersen et al., 2007). Together, these results suggest that for T = 10-20 s ambient noise is dominated by primary microseisms, which are usually attributed to coupling of oceanic wave energy into seismic energy in the Earth in shallow waters (Cessaro, 1994; Bromirski et al., 2005).

4.3.3 EGFs from direct surface waves

Earthquakes are distributed along plate boundaries (Figure 4-3a) and because of this uneven geographical distribution Green's function reconstruction from direct surface waves is often incomplete. To study the EGFs from surface waves the data selection is almost the opposite of what we did in the previous section; we keep only the the data inside the 2.5-5 km/s group velocity window (calculated for earthquakes with $m_b \geq 5$, Figure 4-3b). This window contains mainly the (dispersive) fundamental surface wave mode (Figure 4-2). From stationary phase analysis it is easily understood that the strongest contribution for a particular station pair comes mainly from sources located on or near the line connecting the stations (Snieder, 2004). For a given seismic station pair we can, therefore, choose the direction from which we want contributions. For this purpose we divide the earthquake source regions into E, S, W and N quadrants (Figure 4-3b). As before, one-bit normalization is used to the records before cross correlations.

For both station pairs, the EGFs from all earthquake data (Figure 4-5, black traces labeled as 'ESWN') show a similar time-asymmetry as EGFs from the 10-month continuous data (Figures 4-4, red trace). For MC04-MC23 the anti-causal part of the EGF from earthquake data in each quadrant is similar to the anti-causal part from all data (Figure 4-4a). However, the causal part (that is, surface waves propagating from N to S) can only be recovered from the earthquakes in the N quadrant (yellow circles in Figure 4-3b). Seismicity in the north is relatively low and the earthquakes used are mostly far away from the array. We still observe a causal phase around the same time as the reference phase (Figure 4-5a, blue trace), but it is much noisier than the anti-causal part. For the E-

W station pair we can make similar observations (Figure 4-5b). The anti-causal EGF from earthquakes in the E, S, and N quadrants are, again, similar to that from all data. Data from events in the W quadrant produce both a causal and anti-causal part (Figure 4-5b, black trace labeled as 'W'), but the latter is substantially weaker. This demonstrates that we can indeed recover the (anti-) causal parts of the surface wave Green's function by using earthquake data from a specific direction.

The fact that for both the N-S and E-W station pairs we can recover anti-causal surface wave EGFs for all seismicity quadrants is surprising. In principle, energy from directions perpendicular to the geographical orientation of the receiver pair contributes little to the Green's function of (surface) wave propagation between them. We speculate that the successful recovery of anti-causal EGFs is due to presence of ambient noise energy in the 2.5-5 km/s group velocity window.

To suppress this contamination by ambient noise energy we define a more rigorous direct surface wave window (Figure 4-2), which centers at the maximum energy arrival within the group velocity window 2.5-4 km/s in the period band 10-20s calculated for each earthquake with $m_b \geq 5$ (Figure 4-3b). This new window is only 200 s long and contains only the most energetic part of the direct surface waves from large earthquakes. Instead of applying one-bit normalization to the records, which tends to enhance ambient noise energy, we normalize the records in this direct surface wave window by dividing by the maximum amplitude in that window before cross correlations. Figure 4-6 shows the EGFs from the correlation of recordings in this new direct surface wave window.

For the S-N station pair MC04-MC23, the EGF constructed from direct surface waves from all earthquakes in Figure 4-3b shows quite symmetric surface wave arrival around 178 s (the trace labeled as 'ESWN' in Figure 4-6a), although spurious earlier arrivals appear in both the causal and anti-causal parts. These early arrivals are probably due to surface wave energy coming from earthquakes in subduction zones along Japan, Kuril trench, and Aleutian trench, the eastern Pacific coastline (contributing to the early arrival in the causal part EGF), and earthquakes around the Philippine, New Guinea, Solomon

Islands, and Tonga trenches (contributing to the early arrival in the anti-causal part EGF). Unlike the results shown in Figure 4-5a, in which the anti-causal part EGF seems to be recovered due to the presence of ambient noise energy, the anti-causal part EGF in Figure 4-6a (the black trace labeled as 'S') is recovered only from direct surface waves propagating from S to N from the earthquakes in the S quadrant (Figure 4-3b). Similarly, the causal part EGF in Figure 4-6a (the black trace labeled as 'N') is recovered by the earthquake data in the N quadrant (Figure 4-3b) and has much lower SNR than that of anti-causal EGF recovered from the earthquake data in the S quadrant. This is probably due to the larger epicentral distances in the N quadrant. Earthquakes along the Kuril and Aleutian trenches and the eastern Pacific coastline, with back azimuths ~45° off the inter-station direction, tend to produce (spurious) early arrivals in the causal part EGF.

For the E-W station pair MC06-MC10 the recovery of EGFs using the new surface wave window (Figure 4-6b) is also quite different from that using the 2.5-5 km/s group velocity window (Figure 4-5b). This reflects the uneven distribution of earthquakes (Figure 4-3b), not ambient noise energy. Dominant early arrivals appear in the anti-causal EGFs inferred both from all earthquakes in Figure 4-3b and for earthquakes restricted to the N, E, or S quadrants. This reflects the fact that a large number of earthquakes exist with large angles (about 45°) off the E-W inter-station direction in the subduction zones along the western Pacific Ocean (Figure 4-3b). The causal EGF (the black trace labeled as 'W' in Figure 4-6b) from earthquakes in the W quadrant is very well recovered and the anti-causal part EGF almost disappears, which implies that the contamination of ambient noise energy in this new surface wave window is very small.

Stationary phase analysis implies that only sources locating along or near the line connecting the stations contribute to the reconstruction of the Green's function of that station pair (Snieder, 2004; Yao & Van der Hilst, 2009). Sources within the first Fresnel zone of interferometry constructively contribute to the recovery of the Green's function and the width of the first Fresnel zone depends on the inter-station distance and the frequency of waves considered (Yao & Van der Hilst, 2009). Sources far away from the inter-station line either interfere destructively (for even source distribution) or produce

spurious early arrivals (for uneven source distribution), as shown in Figure 4-6b. Therefore, through careful selection of earthquakes along the inter-station line, we can recover the Green's function and suppress (spurious) early arrivals. For example, for the S-N station pair MC04-MC23 we only select earthquakes near the S-N direction (less than 22.5° deviation); similarly, for the E-W station pair MC06-MC10 only earthquakes near the E-W direction (less than 22.5° deviation) are used (Figure 4-3c). For the S-N station pair MC04-MC23 the re-selected earthquakes in the N (or S) quadrant recover the causal (or anti-causal) part EGF (the green dashed trace labeled as 'N' (or 'S') in Figure 4-6a). Similarly, for the E-W station pair MC06-MC10 the re-selected earthquakes in the E or W quadrant recover the anti-causal or causal part EGF (the green dashed trace labeled as 'E' or 'W' in Figure 4-6b). In particular, the anti-causal part EGF is very well recovered and the early arrivals almost disappear. For the estimation of Green's function between two stations, this "steered" seismic interferometry with direct waves from selected earthquakes provides an alternative to ambient noise interferometry.

4.3.4 EGFs from coda waves

Independent of the source distribution, one can improve conditions for Green's function construction by exploiting wavefield scattering due to medium heterogeneity (Campillo & Paul; 2003Paul et al., 2005). Coda waves are due to (multiple) scattering in the shallow subsurface (Sato & Fehler, 1998) and can be divided into two regimes (Malcolm et al., 2004): an earlier diffusion regime and a later equipartitioning regime. The equipartitioning regime is theoretically the optimal regime for interferometric Green's function reconstruction because no preferred direction and mode of propagation exists (Van Tiggelen, 2004).

For surface wave applications in solid Earth seismology the diffusion regime is usually found in the (late) coda of direct S (Campillo & Paul, 2003; Paul et al., 2005) or Rayleigh waves (Langston, 1989). Equipartitioning has indeed been observed in late coda waves from short-period S waves (Hennino et al., 2001), but the associated energy usually falls below the ambient noise level because it arrives many mean-free times after the direct

waves. As a consequence, EGFs from late coda often show the same directional bias as EGFs from ambient noise (e.g., Paul et al., 2005).

Using the S-N station pair MC04-MC23 as an example, we investigate the correlations of coda from the selected earthquakes (Figure 4-3d) in two 800 s long coda windows (AB and BC in Figure 4-2). For each selected earthquake we require that (1) the root-mean-square (RMS) amplitude of surface wave coda in the first 2000 s window shows clear pattern of exponential decay (Figure 4-2b), (2) the SNR of the direct surface wave arrival has to be larger than 1000, and (3) the minimum SNR within each 800 s coda window is larger than 50. The reason for these strong requirements is to suppress the effect of ambient noise energy in coda waves on the reconstruction. Finally, the surface wave coda from 24 large earthquakes (Figure 4-3d) is used for the retrieval of Green's functions. Before cross-correlating coda waves we normalize their amplitudes by dividing by the RMS amplitude (the red dashed line in Figure 4-2a).

The recovered EGFs from the earlier coda window (AB) and the later coda window (BC) are shown in Figure 4-7, which seem to have much lower SNR compared to EGFs inferred from all 10 months of data. In contrast to the (reference) arrival from ambient noise (blue trace in Figure 4-7) the causal EGF from the earlier coda (the trace labeled as 'AB') does not show apparent surface wave arrival around 178. The anti-causal EGF from the earlier coda results in surface wave arrivals similar to that of the reference arrival (red trace in Figure 4-7), but appears to be too noisy. However, the recovery from the later coda is much improved. Both the causal and anti-causal part EGF from the later coda (the trace labeled as 'BC') show surface wave arrivals that are similar (also in amplited) to the reference arrival from ambient noise. This indicates that the later coda (in the second 800 s coda window) is sufficiently diffuse to construct both the causal and anti-causal part EGFs, while the scattered energy in the earlier coda (in the first 800 s coda window) may be still dominated in some specific directions related to the direction of incoming energy and local heterogeneities. For both coda windows the SNR of coda to ambient noise is sufficiently large (at least 50), and the contribution from ambient noise energy appears to be negligible.

4.4 Seasonal variability and origin of ambient noise energy

The energy density and distribution of ambient noise – and as a consequence, the reliability of EGFs from wavefield cross-correlation – varies with frequency and time. In this section we investigate the temporal changes in the directional distribution and origin of ambient noise energy (in the period band 10-20 s) with respect to the MIT-CIGMR array in SE Tibet. We first analyze the variations of the amplitude of one-bit cross-correlation functions (CFs) over time (Figures 4-8 and 4-9). Subsequently we perform a (frequency-wavenumber) beamforming analysis in order to constrain the temporal variations in the geographical origin of the ambient noise energy (Figure 4-10).

As in Stehly et al. (2006), we analyze the symmetry and amplitude of CFs using data band-passed between 10-20 s (the frequency band of the primary microseisms) during different seasons. We correlate one month of continuous records during the northern hemisphere summer (July 2004) and northern hemisphere winter (January 2004) for station pairs directed roughly from north to south and east to west (with 15° deviation). In the winter, the CFs for the E-W station pairs are dominated by energy traveling from the east, as is evident from the one-sided CFs (Figure 4-8a). For the E-W station pairs, the summer CFs (Figure 4-8b) have lower SNR than in the winter but not seem to have a preferred direction, and (weak) very early arrivals become apparent. The CFs calculated for the N-S station pairs show fairly good symmetry in winter (see Figure 4-8c) indicating a similar energy flux into the array from the south or north. In summer time (Figure 4-8d). The apparent asymmetry of the CFs indicates that energy coming from the south is much larger than from the north.

The traces in Figure 4-8 correspond to E-W and N-S station pair orientations, but pie charts illustrate the azimuthal dependence of the normalized amplitude of the CFs (or ambient noise energy flux) for all station pairs, both for winter (Figure 4-9a) and summer (Figure 4-9b). The background image in Figure 4-9 shows the distribution of the normalized global ocean wave height, modified after Stehly et al. (2006). The pie charts show that the ambient noise energy in the winter (Figure 4-9a) is more uniformly distributed than in the summer (Figure 4-9b). In the winter, noise energy is dominant in

the east and north-east directions (possibly related to enhanced wave power in the Northern Pacific) and also from the south (Indian Ocean) and the north (Northern Atlantic). In the summer, the main direction of the ambient noise energy is from the south-south west, pointing to an origin in the Indian Ocean. These results are consistent with the observations of Stehly et al. (2006) and Yang & Ritzwoller (2008).

To confirm, quantify, and interpret the above illustration of seasonal CF amplitude variations, we perform a wavenumber-frequency analysis of the same data. Wavenumber-frequency analysis of random noise fields decomposes the wave field into plane waves, which allows one to characterize the noise wave field – or the wavenumber-frequency power-spectral density – by an azimuth and apparent slowness (or velocity) (Lacoss et al. 1969, Aki & Richards, 1980, Johnson & Dudgeon, 1993). We divide approximately one month of data (January 2004 or July 2004) into 512 s windows with an overlap of 100 s. Using the algorithm due to Lacoss et al., 1969) we beamform the data in these windows for 20 central periods between 10 and 20 s using a narrow band-pass filter of about 0.002 s. The angle resolution is 2 degrees, while the velocity resolution is 20 m/s. The beamforming results in all time windows and frequency bands are then normalized and stacked to produce the final images of the power of the noise wave field in the period band 10-20 s in terms of velocity in m/s along the radial axis and azimuth in degrees, along the angle, shown in Figure 4-10.

Figures 4-10a and 4-10b show the noise power during January 2004 and July 2004, respectively. The wave field is dominated by energy coming from the south-south west during the July 2004 (Figure 4-10b), in excellent agreement with results of the above analysis of CF amplitudes (Figure 4-9b). The apparent velocity is around 3200 m/s, which agrees very well with the velocities obtained from dispersion analysis (see Figure 4-11b and 4-12b). The noise power during January 2004 has less obvious directionality (Figures 4-10a). The same direction in the south-south east causes arrivals with velocities around 3200 m/s, but significant energy also arrives from the north and east with approximately equal amounts and much weaker energy flux from the west. This is also

similar to the result from the above CF analysis (Figure 4-9a). Overall, the noise power in the January is less than during July.

The above observations that the CFs for E-W station pairs have a lower SNR in the summer (Figure 4-8b) than in the winter (Figure 4-8a) and that early arrivals appear in the summer time CFs may both be explained by the overall dominance of energy from the south in the summer, as established by the beamforming. If plane waves arrive from the south-south west at an E-W station pair, the result will be an arrival with very high apparent velocity (and thus early arrival time).

4.5 Discussion

In Section 4.3 we evaluated the recovery of (surface wave) Green's functions from ambient noise, direct surface waves, and surface wave coda (for $T = 10 - 20$ s). Figure 4-11a shows the EGFs recovered from different data windows for the S-N station pair MC04-MC23. The EGFs from the different data windows give similar surface wave arrival times (around 178 s). However, the arrival time of the EGF (labeled as 'S–' in Figure 4-11a) recovered from direct surface waves using the earthquakes in the S quadrant (see Figure 4-3c) appears several seconds later than the reference travel time of the EGF from ambient noise. The arrival time of the EGF (labeled as 'N+' in Figure 4-11a) using earthquakes in the N quadrant appears a few seconds earlier. Dispersion analysis for the various EGFs in Figure 4-11a shows differences among the phase velocities (Figure 4-11b) with a standard deviation about 1-2% of the average phase velocities. Indeed, the phase velocities of the 'N+' EGF (Figure 4-11a) are about 1-1.5% higher than the average and for the 'S–' EGF (Figure 4-11a) the phase velocities are 0.5 – 1.5% lower. This difference reflects the difference of source distribution (Figure 4-3c) for the construction of surface wave Green's function through cross correlation. The phase velocities of the causal and anti-causal EGFs from coda waves also show up to 1.5% difference, implying the difference of (scattered) energy for the Green's function retrieval. If the scattered wavefield in the late coda is isotropic and well above the ambient noise level, we would expect the same dispersion characteristics for the causal and anti-causal

part EGFs. However, in reality, attenuation and existence of ambient noise energy usually result in some predominant directions of energy propagation in the late coda.

In theory the causal and anti-causal part of the Green's function are the same. However, in practice, the recovered EGFs from cross correlation of different data windows may be different (Figures 4-4, 4-5, 4-6, and 4-7) indicating non-isotropic energy propagation. To improve the quality of dispersion analysis of the EGFs from seismic interferometry, one usually stacks the causal and anti-causal part EGFs to enhance the SNR and suppress the effect of uneven source distribution or energy propagation (e.g., Yang et al., 2007; Yao et al., 2008). Here we stack the causal and anti-causal part EGFs from ambient noise, direct surface waves, or surface wave coda, as shown in Figure 4-12a. The stacked EGFs from different data windows have very similar arrival times (the difference is less than 1 s, Figure 4-12a) and the SNR is also improved, especially for the stacked EGF using coda waves. The phase velocity dispersion curves between the stacked EGFs from ambient noise and surface wave coda are very similar with less than 1% difference (Figure 4-12b). The phase velocities around 14 s of the stacked EGF from direct surface waves are about 1.5% higher than from ambient noise or surface wave coda, but at other periods their differences are quite small (less than 0.5%). This suggests that stacking the causal and anti-causal parts of the EGFs does, indeed, improve the quality of dispersion analysis.

By using different data windows we effectively manipulate the character of seismic energy that contributes to the construction of the EGF. This, in turn, also alters the type of information that can be retrieved about the medium. As we demonstrated in Figure 4-11 or 4-12, EGFs can be retrieved successfully from continuous ambient noise, direct surface waves, or surface wave coda. The surface waves recovered from 10 months of ambient noise have higher SNR than those recovered from ground motion due to large earthquakes (with much shorter time length for cross correlation). The SNR of the recovered surface waves from direct surface waves is also high (Figure 4-11a). However, it is sometimes necessary to select the earthquakes (with back azimuths near the orientation of the two-station pair) to avoid the generation of spurious early arrivals (due to incomplete reconstruction) or bias from earthquakes with energy propagating

perpendicular or at large angle from the station pair (Figures 4-6 and 4-7). In practice, one can steer the known sources (e.g., larger earthquakes) within the regime of constructive interference to improve the recovery of the Green's function. The steering process may include both the selection of sources and compensation of source energy to enable the perfect recovery.

The SNR of the recovered surface waves from the later surface wave coda seems to be poor. However, the phase information can be well recovered (Figure 4-11) and the causal and anti-causal parts are nearly symmetric. The early coda is expected to be dominated by single scattering, whereas in the late coda, multiple scattering contributes to the diffusion of energy. In theory a diffuse wavefield produces a more symmetric EGF (S'anchez-Sesma et al., 2008, Malcolm et al, 2004) and this is clearly observed here (Figure 4-7). However, since multiply scattered energy decays faster and can quickly fall below the noise level, especially for the range of interstation distances considered in our study, this really limits our selection of coda waves for the Green's function retrieval. The poor SNR of the EGF from coda waves is probably due to the very limited data we can use for the recovery (Figure 4-3d) in order to minimize the contamination of ocean microseism in the period band 10-20 s. Therefore, the EGFs recovered from coda waves seem less well suited for using in ambient noise tomography.

Our study illustrates that the comparison of EGFs extracted from different regimes in the seismic trace is complicated by various factors. Much depends on the frequency band one uses for the correlations. For periods between 10 and 20 s ambient noise is dominated by the primary microseism and effects of scattering are relatively weak. For shorter periods, scattering is stronger (due to the shorter wavelength compared to heterogeneity) and ocean generated ambient noise may be weaker if the array is far from the coastline. For shorter periods we may, therefore, expect to retrieve more symmetric EGFs with higher SNR from late coda data for station pairs with shorter distance considering high attenuation at shorter periods. At longer periods, say, from 20 to 120 s, the effect of scattering is less (Langston, 1989) and ambient noise energy generally shows weak

(Yang & Ritzwoller, 2008) or no directionality (Pederson et al, 2007). Therefore, in this period band one can use direct waves and noise to retrieve Green's functions.

4.6 Conclusions

We demonstrated that the surface wave empirical Green's function can be retrieved from cross-correlation of different data windows (ambient noise, direct surface waves, or surface wave coda) using array data from SE Tibet. Phase velocity dispersion also reveals similar dispersion characteristics of these empirical Green's functions. The directionality of ambient noise energy distribution may have a large effect on the recovery of the Green's function when one tries to use direct surface waves or coda waves due to large earthquakes. Therefore, proper windowing of earthquake data in different regimes is necessary for the Green's function recovery. By examining the symmetry and amplitude of the cross-correlation functions and performing a frequency-wavenumber beamforming analysis, we conclude that the dominant ambient noise field in the period band 10-20 s is from the ocean activities and shows clear seasonal dependence. The average phase velocity between 10-20 s of the study area from beamforming analysis is very similar to what we obtained from dispersion analysis. Wavenumber-frequency beamforming analysis of the noise wave-field helps in interpreting the empirical Green's function obtained from cross-correlation and provides important knowledge of the directionality of ambient noise energy.

Acknowledgments

We thank three anonymous reviewers for their constructive comments, which helped us improve the manuscript. We also thank Dr. Pierre Gouedard at MIT for helpful discussion on coda wave analysis.

References

Aki, K. & Richards, P.G., 1980. Quantitative Seismology, Theory and methods. Vol.1, W.H. Freeman. San Francisco, CA.

Bakulin, A., & Calvert, R., 2006. The virtual source method: theory and case study, *Geophys.*, 71(4), SI139–SI150.

Bardos, C., Garnier, J. & Papanicolaou, G., 2008. Identification of Green's's functions singularities by cross correlation of noisy signals, *Inverse Problems*, 24, 015011.

Bensen, G. D., Ritzwoller, M. H., Barmin, M. P., Levshin, A. L., Lin, F., Moschetti, M. P., Shapiro, N. M., Yang, Y., 2007. Processing seismic ambient noise data to obtain reliable broad-band surface wave dispersion measurements, *Geophys. J. Int.*, 169, 1239–1260.

Bromirski, P. D., Duennebier, F. K. & Stephen, R. A., 2005. Mid-ocean microseisms, *Geochem. Geophys. Geosys.*, 6, Q04009, doi:10.1029/2004GC000768

Colin de Verdière, Y., 2006a. Mathematical models for passive imaging I: general background. URL http://fr.arxiv.org/abs/math-ph/0610043/.

Colin de Verdière, Y., 2006b. Mathematical models for passive imaging II: effective Hamiltonians associated to surface waves. URL http://fr.arxiv.org/abs/math-ph/0610044/.

Campillo, M., Paul, A., 2003. Long-Range correlations in the diffuse seismic coda, *Science*, 299, 547–549.

Cessaro, R. K., 1994. Sources of primary and secondary microseisms, *Bull. Seism. Soc. Am.*, 84, 142–148.

Correig, A. M. & Urquizú, M., 2002. Some dynamical characteristics of microseismic time-series, *Geophys. J. Int.*, 149, 589–598.

De Hoop, M.V. & De Hoop, A.T., 2000. Wave-field reciprocity and optimization in remoting sensing, *Proc. R. Soc. Lond. A* (Mathematical, Physical and Engineering Sciences), 456, 641-682

De Hoop, M. V. & Solna, K., 2008. Estimating a Green's function from field-field correlations in a random medium, *SIAM J. Appl. Math.*, 69(4), 909-932.

Engdahl, E.R., Van der Hilst, R.D. & Buland, R.P., 1998. Global teleseismic earthquake relocation from improved travel times and procedures for depth determination, *Bull. Seism. Soc. Am.*, 88, 722–743.

Gu, Y. J., Dublanko, C., Lerner-Lam, A., Brzak, K. & Steckler, M.2007. Probing the sources of ambient seismic noise noise near the coasts of Southern Italy, *Geophys. Res. Lett.*, 34, L22315,doi:10.1029/2007GL031967.

Hennino, R., Trégourès, N., Shapiro, N., Margerin, L., Campillo, M., Van Tiggelen, B. & Weaver, R. L., 2001, Observation of equipartition of seismic waves in Mexico, *Phys. Rev. Lett.*, 86, 3447-3450.

Langston, C. A., 1989. Scattering of long-period Rayleigh waves in Western North America and the interpretation of coda Q measurements, *Bull.Seism.Soc.Am.*, 793, 774–789.

Levshin, A. L., Barmin, M. P., Ritzwoller, M. H., Trampert, J., 2005. Minor-arc and major-arc global surface wave diffraction tomography, *Geophys. J. Int.*, 149, 205–223.

Lin, F.-C., M.P. Moschetti, and M.H. Ritzwoller, 2008. Surface wave tomography of the western United States from ambient seismic noise: Rayleigh and Love wave phase velocity maps, *Geophys. J. Int.*, doi:10.1111/j1365-246X.2008.03720.x.

Malcolm, A. E., Scales, J. A. & Van Tiggelen, B. A., 2004. Extracting the Green's function from diffuse, equipartitioned waves, *Phys. Rev. E*, 70, 015601.

Margerin, L., Campillo, M. & Van Tiggelen, B. A., 2001. Coherent backscattering of acoustic waves in the near-field, *Geophys. J. Int.*, 145, 593–603.

McNamara, N.M. & Buland, R. P., 2004. Ambient noise levels in the Continental United States, *Bull. Seism.Soc.Am.*, 94, 1517–1527.

Metha, K, Snieder, R., Calvert, R. & Sheiman, J. 2008. Acquisition geometry requirements for generating virtual-source data, *The Leading Edge*, 27, 620–629.

Nakahara, H., 2006. A systematic study of theoretical relations between spatial correlation and Green's function in one-, two- and three-dimensional random scalar wavefields, *Geophys. J. Int.*, 167, 1097-1105.

Pedersen, H. A., Kr¨uger, F. and the SVEKALAPKO Seismic Tomography Working Group, 2007. Influence of the seismic noise characteristics on noise correlations in the Baltic shield, *Geophys. J. Int.*, 168, 197–210.

Paul, A., Campillo, M., Margerin, L., Larose, E., Derode, A., 2005. Empirical synthesis of time-asymmetrical Green's functions from the correlation of coda waves, *J. Geophys. Res.*, 110, B08302, doi:10.1029/2004JB003521.

Roux, P., Sabra, K. G., Kuperman, W. A. & Roux, A., 2005. Ambient noise cross correlation in free space: Theoretical approach, *J. Acoust. Soc. Am.*, 117(1), 79–84.

Pollitz, F., 1999. Regional velocity structure in northern California from inversion of scattered seismic surface waves, *J. Geophys. Res.*, 104, 15043–15072.

S'anchez-Sesma, F. J., P'erez-Ruiz, J. A., Luz'on, F., Campillo, M., Rodr'.guez-Castellanos, A., 2008. Diffuse fields in dynamic elasticity, *Wave Motion*, 45(5), 641-654.

Sato, H., and M. Fehler, 1998. Seismic Wave Propagation and Scattering in the Heterogeneous Earth, American Institute of Physics Press.

Scales, J. A., Malcolm, A. E. & Van Tiggelen, B. A., 2004. Estimating scattering strength from the transition to equipartitioning, *AGU Fall Meeting Abstracts*, B1053.

Shapiro, N. M., Campillo, M. Stehly, L. & Ritzwoller, M. H., 2005. High-Resolution Surface-Wave Tomography from Ambient Seismic Noise, *Science*, 307, (5715), 1615-1618.

Shapiro, N. M., Campillo, 2004. Emergence of broadband Rayleigh waves from correlations of the ambient seismic noise, *Geophys. Res. Lett.*, 31, L07614, doi:10.1029/2004GL019491.

Snieder, R., 1986. The influence of topography on the propagation and scattering of surface waves, *Phys. Earth Planet. Inter.*, 44, 226–241.

Snieder, R., 2004. Extracting the Green's's function from the correlation of coda waves: A derivation based on stationary phase, *Phys. Rev. E*, 69, 046610.

Stehly, L., Campillo, M., Shapiro, N. M., 2006. A study of the seismic noise from its long-range correlation properties, *J. Geophys. Res.*, 111, B10306, doi:10.1029/2005JB004237.

Tr'egour`es, N., Hennino, R., Lacombe, C., Shapiro, N. M., Margerin, L., Campillo, M. & Van Tiggelen, B. A., 2002. Multiple scattering of seismic waves, *Ultrasonics*, 40, 269–274.

Van Tiggelen, B. A., 2003. Green's function retrieval and time-reversal in a disordered world, *Phys. Rev. Lett.*, 91, 243904.

Wapenaar, K., 2004. Retrieving the elastodynamic Green's's function of an arbitrary inhomogeneous medium by cross correlation, *Phys. Rev. Lett.*, 93, 254301.

Wapenaar, C.P.A., Fokkema, J. T. & Snieder, R. , 2005. Retrieving the Green's function in an open system by crosscorrelation: a comparison of approaches, *J. Acoust. Soc. Am.*, 118, 2783–2786.

Wapenaar, K., 2006. Green's function retrieval by cross-correlation in case of one-sided illumination, *Geophys. Res. Lett.*, 33, L19304, doi:10.1029/2006GL027747.

Weaver, R. & Lobkis, O., I., 2004. Diffuse fields in open systems and the emergence of the Green's function, *J. Acoust. Soc. Am.*, 116, 2731–2734.

Weaver, R. & Lobkis, O., I., 2005. Fluctuations in diffuse field-field correlations and the emergence of the Green's's function in open systems, *J. Acoust. Soc. Am.*, 117(6), 3432– 3439.

Willis, M. E., Lu, R., Campman, X., Toksöz, M. N., Zhang, Y. & De Hoop, M., 2006. A novel application of time reverse acoustics: salt dome flank imaging using walk away VSP surveys, *Geophys.*, 71(2), A7–A11.

Yang, Y., Ritzwoller, M.H., Levshin, A.L., & Shapiro, N.M., 2007. Ambient noise Rayleigh wave tomography across Europe, *Geophys. J. Int.*, 168, 259-274.

Yang, Y. and Ritzwoller, M.H., 2008. Characteristics of ambient seismic noise as a source for surface wave tomography, *Geochem. Geophys. Geosyst.*, 9, doi10.1029/2007GC001814.

Yao, H., Van der Hilst, R. D.,De Hoop, M. V., 2006. Surface-wave array tomography in SE Tibet from ambient seismic noise and two-station analysis – I Phase velocity maps, *Geophys. J. Int.*, 166, 732–744.

Yao, H., Beghein, C., Van der Hilst, R. D., 2008. Surface-wave array tomography in SE Tibet from ambient seismic noise and two-station analysis – II Crustal and upper mantle structure, *Geophys. J. Int.*, 173, 205–219.

Yao, H. and Van der Hilst, R.D., 2009. Analysis of ambient noise energy distribution and phase velocity bias in ambient noise tomography, with application to SE Tibet, *Geophys. J. Int.*, under review.

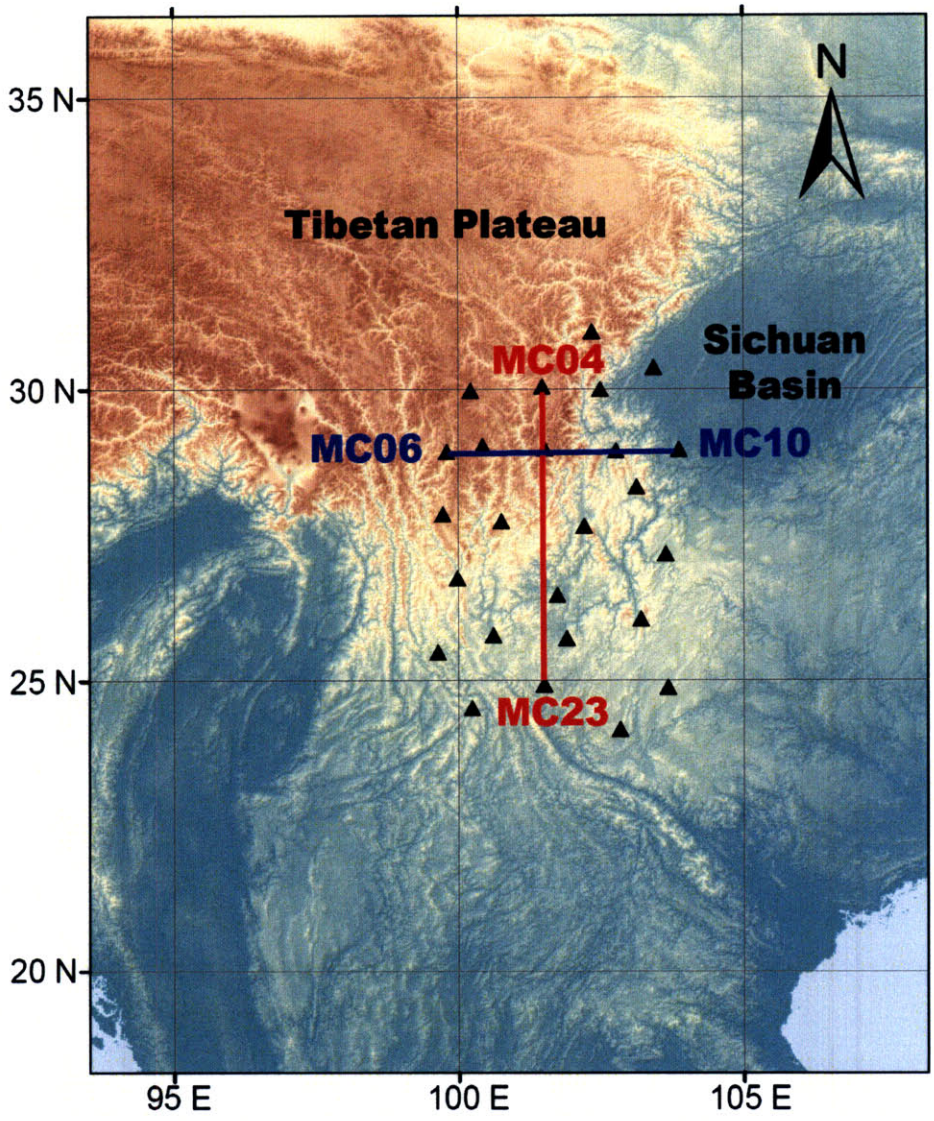

Figure 4-1. The location of 25 stations (black triangles) of the MIT- CIGMR array in SE Tibet. The red line and the blue line show the two-station paths for the S-N directional station pair MC04-MC23 and the E-W directional station pair MC06-MC10, respectively.

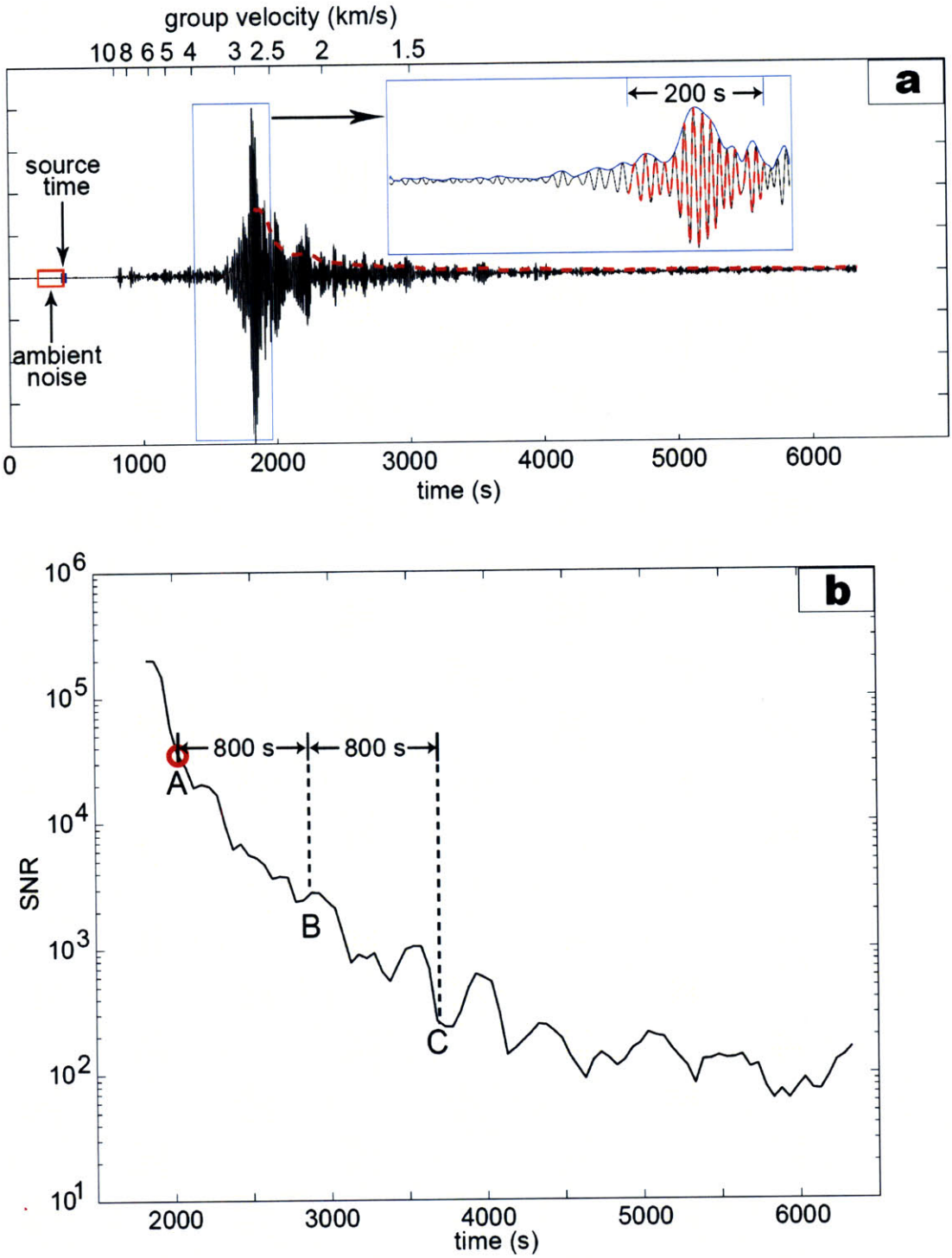

Figure 4-2. Illustration of time windows used for the EGF retrieval. The seismogram in (a), band-pass filtered in the period band 10-20s, is recorded by the station MC04 shown in Figure 4-1 and the earthquake is located at (37.74°N, 143.08°E) with the magnitude m_b

= 5.9. The epicentral distance is 3900 km. The bottom and top horizontal axes in (a) show the recording time and the corresponding group velocity (or horizontal propagation speed) of the records, respectively. The earthquake started at t = 400 s on the records. The seismogram in the inset figure of (a) shows the recordings in the 2.5 – 4 km/s group velocity window, which includes mainly direct surface waves, and the blue curve shows the envelope of the windowed recordings. The red dashed trace (200 s in length) in the inset figure, which centers at the point P corresponding to the maximum amplitude of the envelope, is selected as the direct surface waves for the retrieval of the Green's function. The red dashed curve in (a) is the root-mean-square (RMS) amplitude (using a 200 s running window) of the recordings after the maximum energy arrival point P. Here we define the surface wave coda starts at the point A, which is 200 s after P. The signal to noise ratio (SNR) of the coda is shown in (b), which shows apparent exponential decay of coda energy. The (ambient) noise window is defined as the 200 s window before the source time at 400 s, shown as the recordings in the red box in (a). For the retrieval of Green's function using surface wave coda, we select two time windows: the first and second 800 s window after A (the recordings within the window AB and BC, respectively).

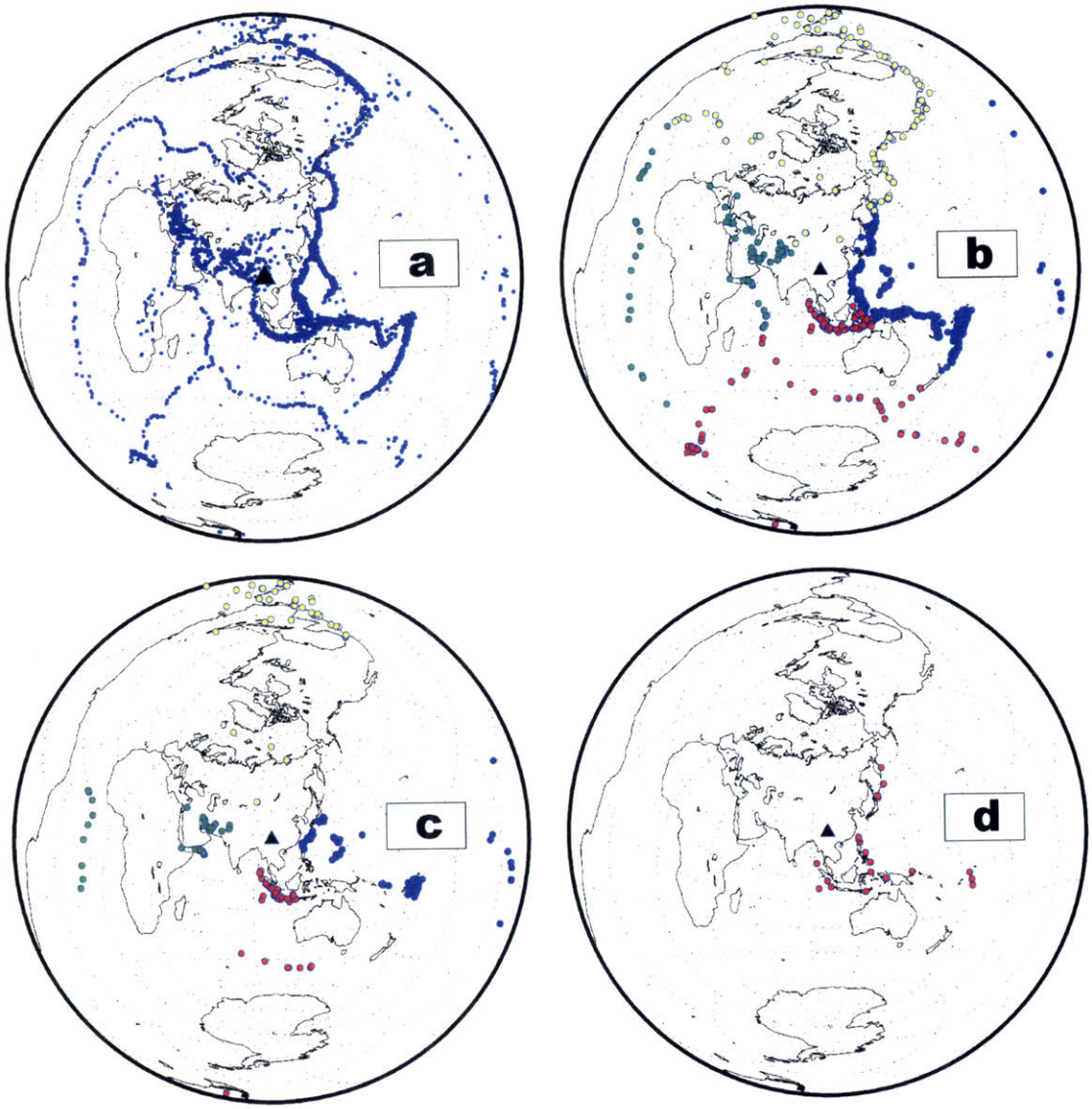

Figure 4-3. (a) Epicenters of earthquakes with $m_b \geq 4$ (blue dots) that occurred in the 10 months from November 2003 to August 2004 (from EHB catalogue by Engdahl et al., 1998). The total number of earthquakes is about 7250. (b) Same as in (a) but for earthquakes with $m_b \geq 5$ and at least 2000 km away for the center of the array. The azimuth angle θ of the earthquake with respect to the center of the array satisfies $-45^\circ \leq \theta \leq 45^\circ$, $45^\circ \leq \theta \leq 135^\circ$, $135^\circ \leq \theta \leq 225^\circ$, and $225^\circ \leq \theta \leq 315^\circ$, for the earthquakes in the N, E, S, and W quadrants, shown as yellow, blue, red, and green dots, respectively. The total number of earthquakes in (b) is about 1000 and the number in the N, E, S, and W

quadrants is 149, 577, 158, and 133, respectively. (c) Same as in (b) but only for the earthquakes near S-N or E-W direction (with respect to the array) with a maximum deviation angle of 22.5°. The number of earthquakes in the N, E, S, and W quadrants in (c) is 49, 120, 55, and 49, respectively. (d) Epicenters of 24 earthquakes ($m_b \geq 5$) for the retrieval of Green's function using surface wave coda (Section 4.3.4). The black triangle shows the location of the array.

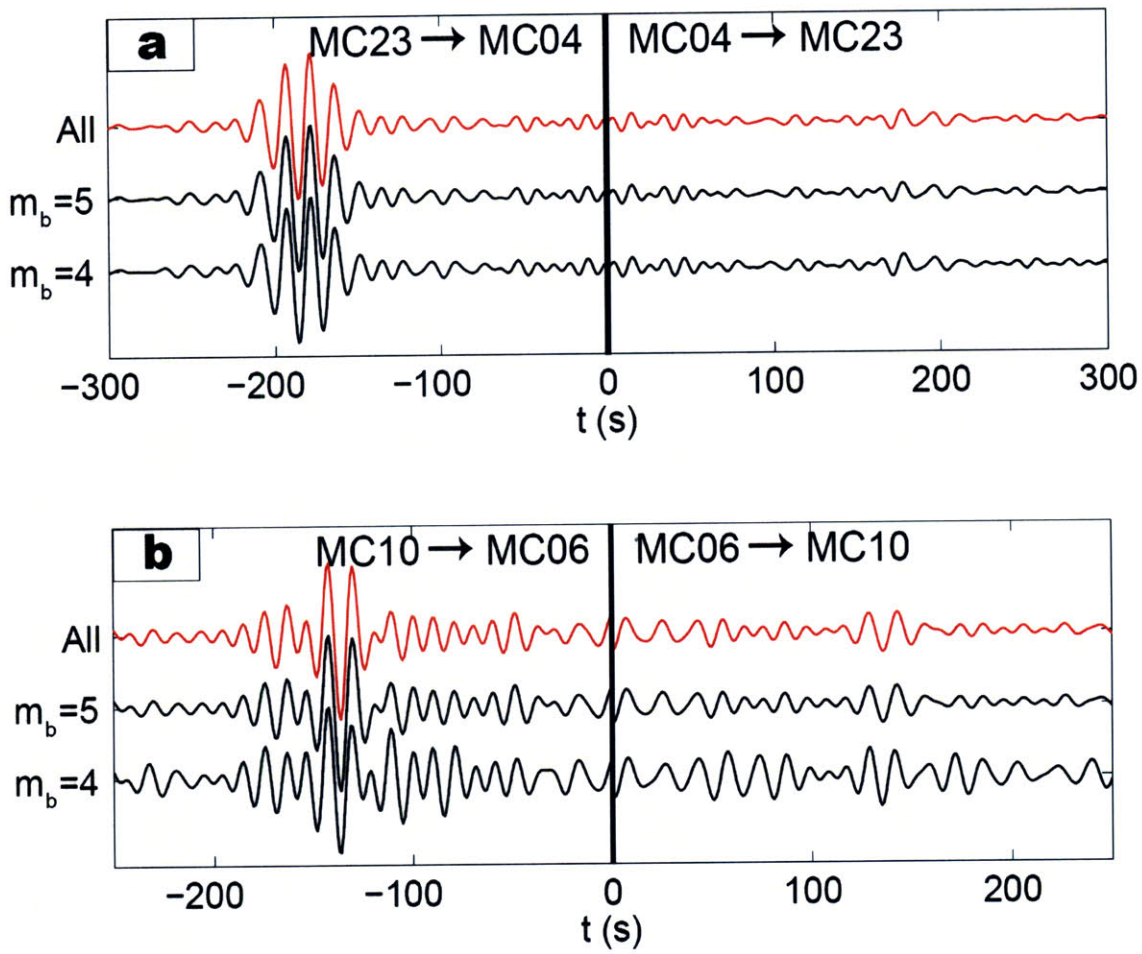

Figure 4-4. EGFs (black traces) for the station pair (a) MC04-MC23 and (b) MC06-MC10 in the period band 10-20 s from approximately ambient noise after muting the wave trains in the 2-10 km/s group velocity window from earthquakes larger than the cut-off magnitude (m_b = 5 or 4, shown at the left side of each black trace) for all the 10 months data. The location of earthquakes is shown in Figure 4-3a and b. The red traces in (a) and (b) are the EGFs from all the 10 months continuous data. The causal part shows for the EGF recorded at the station MC23 (or MC10) generated by a fictitious source at the station MC04 (or MC06) while the anti-causal part for recordings at MC04 (or MC06) with the source at MC23 (or MC10), same as shown in Figures 4-5, 4-6, and 4-7.

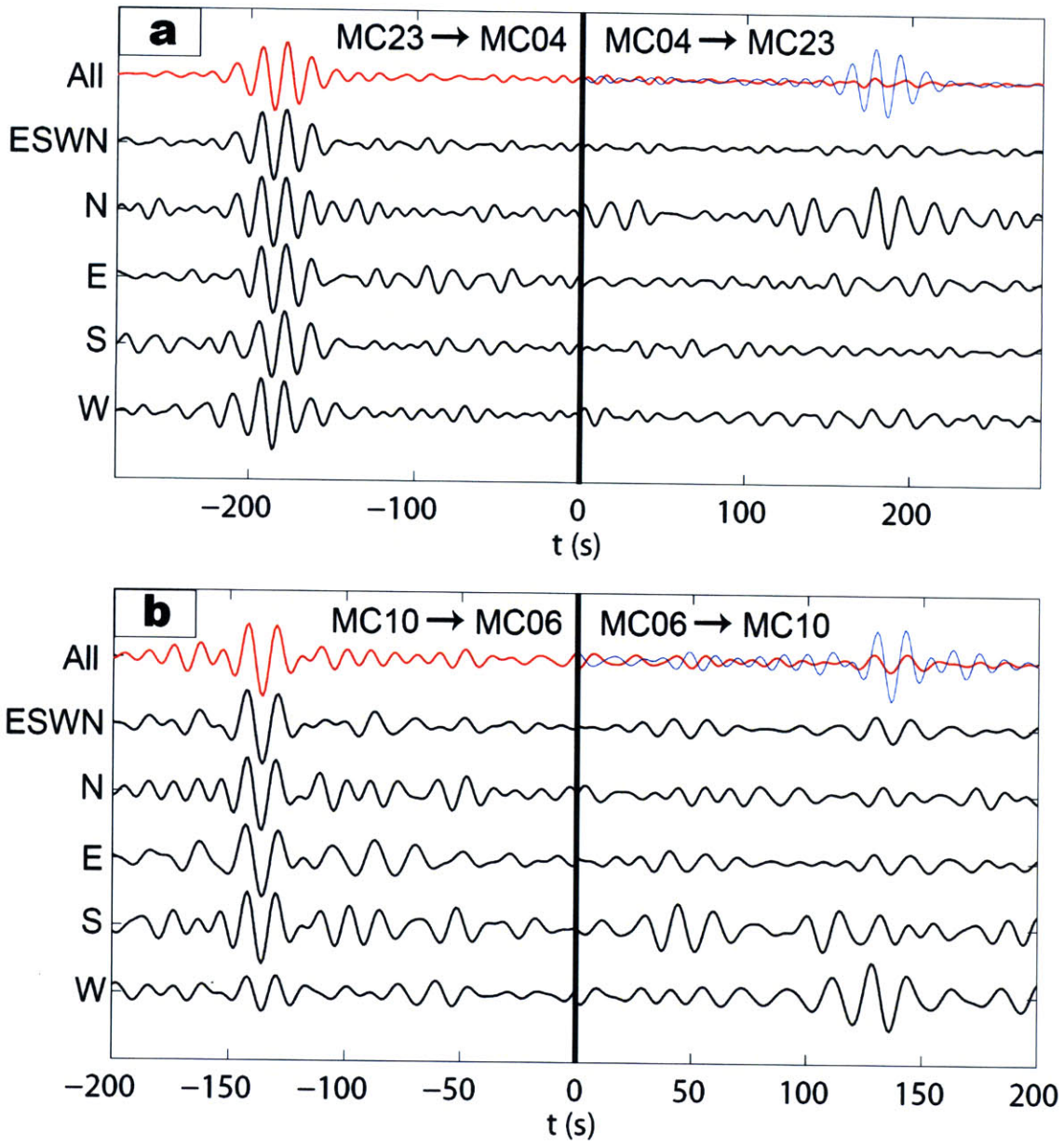

Figure 4-5. EGFs (black traces) in the period band 10-20s for the station pair (a) MC04-MC23 and (b) MC06-MC10 only from direct (minor-arc) surface waves in the 2.5-5 km/s group velocity window from the earthquakes with $m_b \geq 5$ in the 10 months in the world (labeled as 'ESWN' at the left side), and from four different quadrants (labeled as 'N', 'E', 'S', and 'W' at the left side; for location of earthquakes in each quadrant, see Figure 4-3b). The red trace in (a) and (b) is the same as that shown in Figures 4-4a and b, respectively. The blue trace in (a) and (b) is the time reversal of the anti-causal EGF of the red trace, shown as the reference for the causal part EGF.

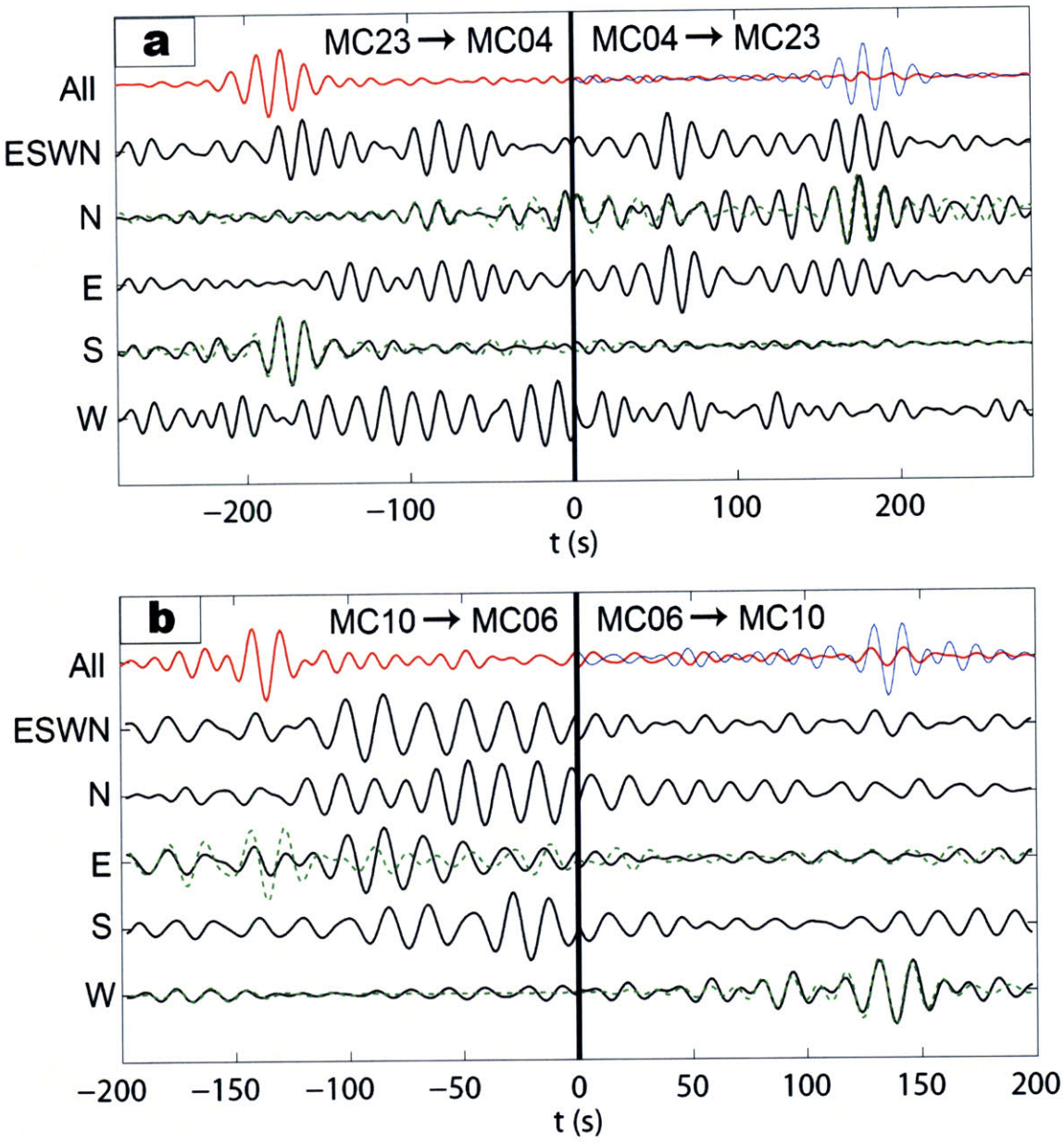

Figure 4-6. Similar as shown in Figure 4-5, but for EGFs (black traces) recovered from direct surface waves in a more rigorously defined window from large earthquakes (see Figure 4-2a and Section 4.3.3). The green dashed trace labeled as 'N' (or 'S') in (a) is the EGF for MC04-MC23 from earthquakes in the N (or S) quadrant only near the S-N direction within 22.5° deviation (red or yellow dots in Figure 4-3c). The green dashed trace labeled as 'E' (or 'W') in (b) is the EGF for MC06-MC10 only using earthquakes in the E (or W) quadrant near the E-W direction (blue or green dots in Figure 4-3c). The top red and blue traces are the same as shown in Figure 4-5.

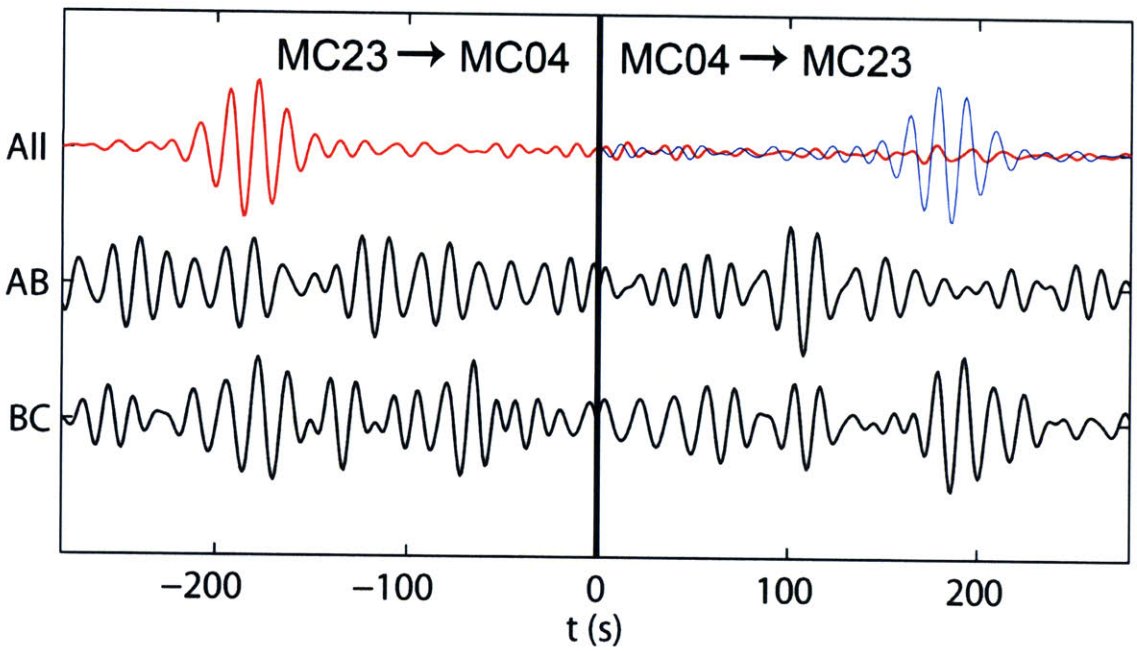

Figure 4-7. EGFs (black traces) in the period band 10-20 s for MC04-MC23 from surface wave coda of the large earthquakes ($m_b \geq 5$, red dots in Figure 4-3d) in two different time windows (AB and BC, each with 800 s length) shown at the left side of each black trace. The detailed definition of these two coda windows is given in Figure 4-2 and Section 4.3.4. The coda in the window AB and BC is the earlier and later part of surface wave coda, respectively.

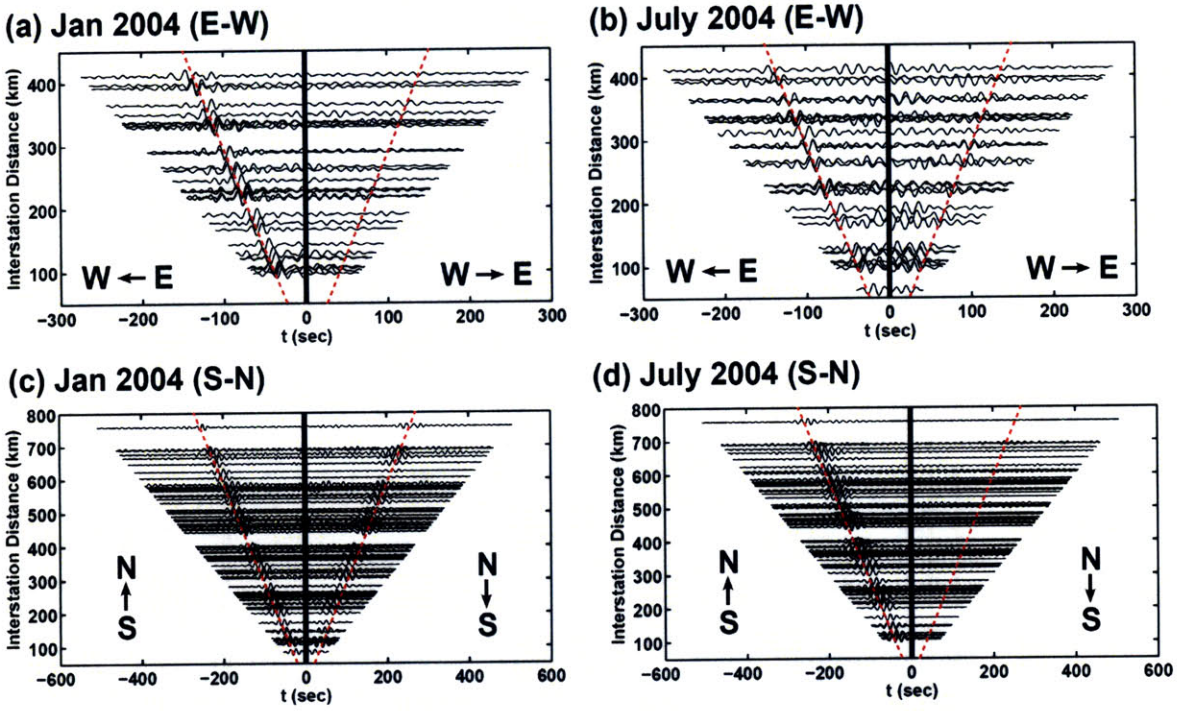

Figure 4-8. Comparison of cross correlation functions in the period band 10-20 s from one month data of (a) January 2004 for E-W two-station pairs, (b) July 2004 for E-W two-station pairs, (c) January 2004 for S-N two-station pairs, and (d) July 2004 for S-N two-station pairs. Here the E-W or S-N two-station pairs are station pairs directed roughly from E to W or N to S with a maximum of 15° deviation. 'E→W' means the fictitious noise sources approximately to the E of the array generate waves propagating to the W for the retrieval of the anti-causal EGF as shown in (a) or (b), similarly for 'W→E' but for the retrieval of the causal EGF in (a) and (b), 'S→N' for the anti-causal EGF in (c) and (d), and 'N→S' for the causal EGF in (c) and (d).

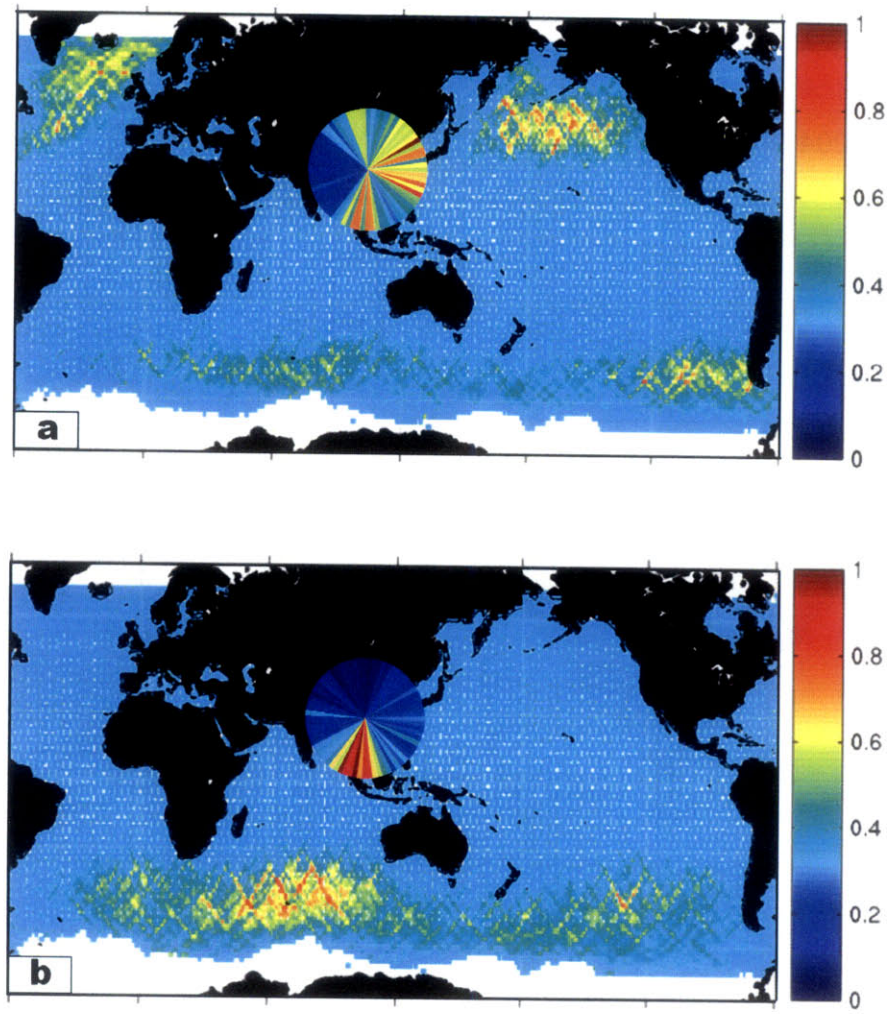

Figure 4-9. Seasonal variation of the azimuthal dependence of the normalized amplitude of the cross correlation functions (shown as the pie chart) for all possible MIT-CIGMR array station pairs: (a) in northern hemisphere winter time (January 2004) and (b) in northern hemisphere summer time (July 2007). The pie charts are constructed using the procedure from Stehly et al. (2006) by averaging the amplitude of all CFs in each azimuthal sector (5° width here) with a geometrical spreading amplitude correction considering the difference in interstation distance. The background image shows the distribution of the normalized global ocean wave height in winter time (a) and in summer time (b) (modified after Stehly et al., 2006). The color bar in the right gives the value of normalized amplitude for both cross correlation functions and the ocean wave heights. In the pie chart, the red sector at certain azimuth angle approximately implies that more energy is coming from that azimuth angle and propagating into the array (center of the pie chart).

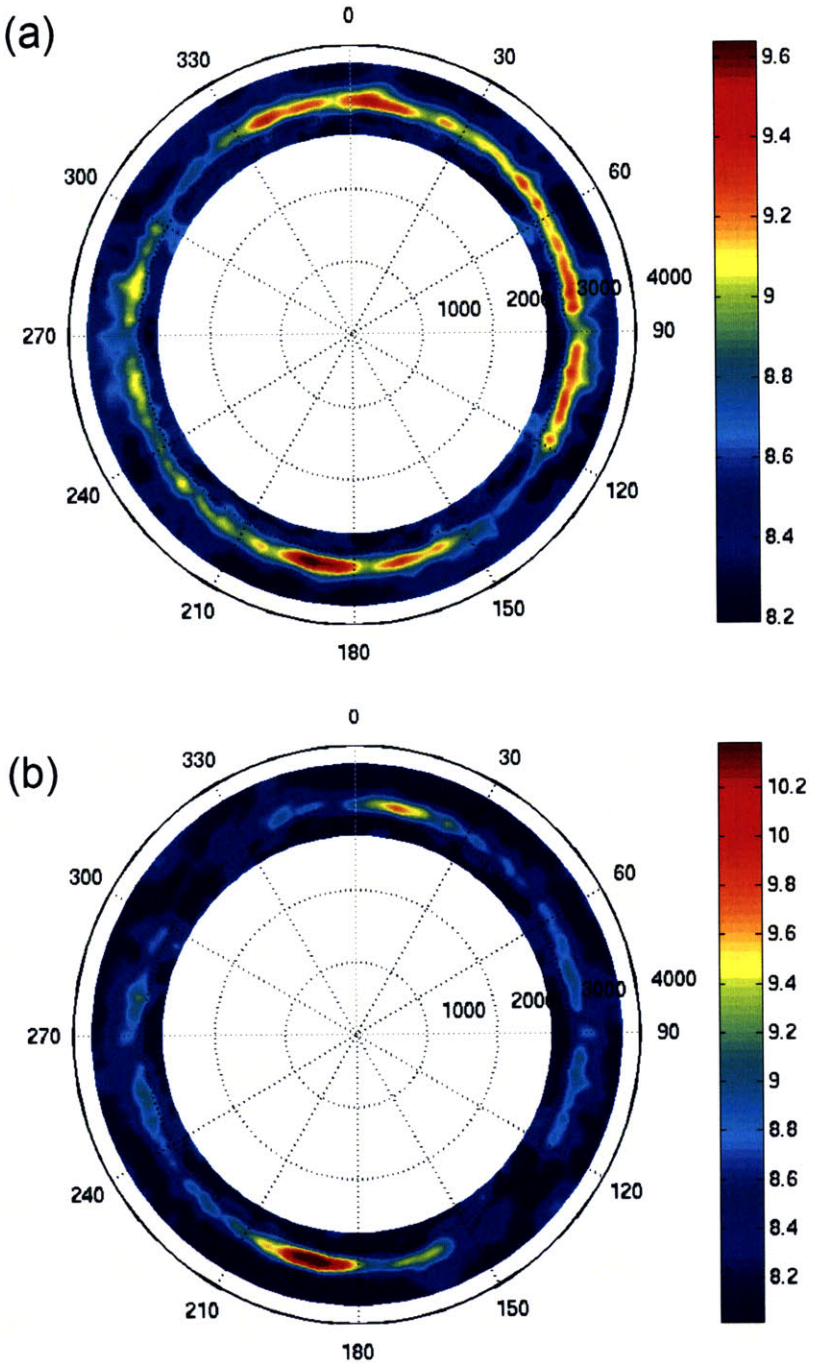

Figure 4-10. (a) Noise power from beamforming analysis in January 2004, for the period band 10-20 s. The noise mainly arrives from the south-southwest and from between the north-northwest and east-southeast. The apparent velocity is around 3200 m/s. b) Noise power from beamforming analysis in July 2004, for the period band 10-20 s. The noise mainly arrives from the south-southwest. The apparent velocity is around 3200 m/s.

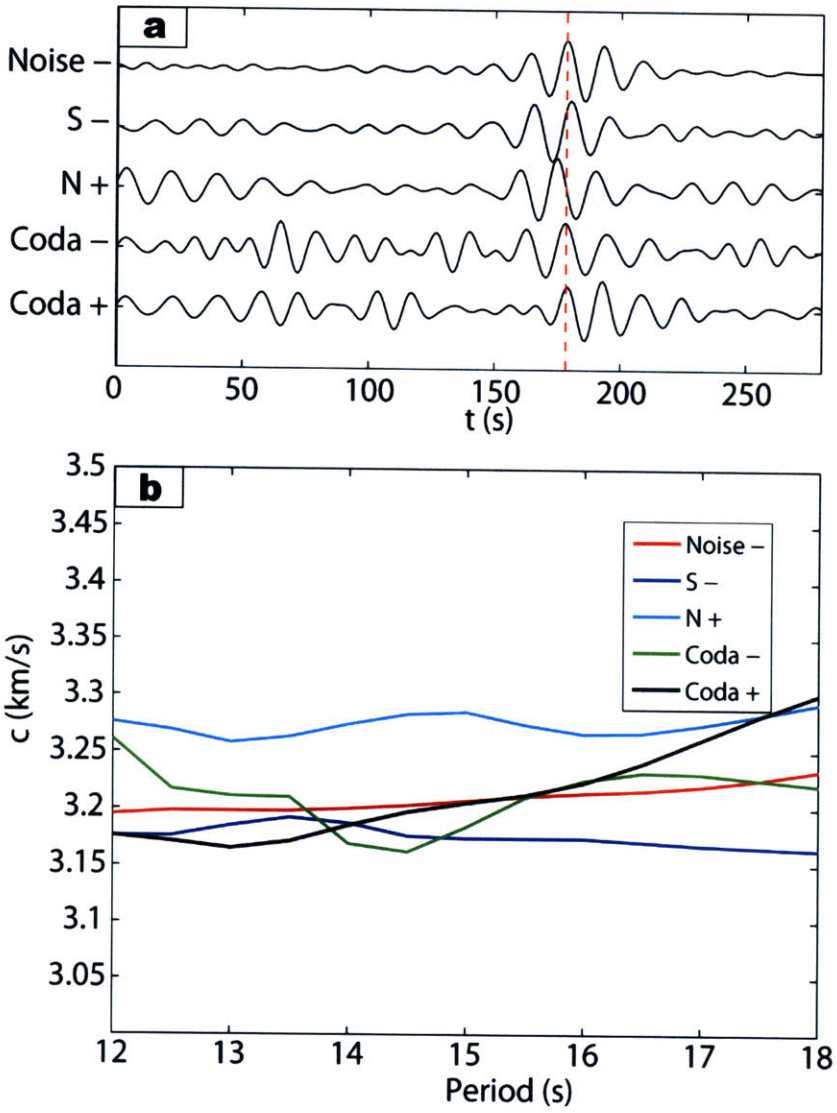

Figure 4-12. (a) Comparison of the EGFs of MC04-MC23 constructed from cross correlations of different data windows: 'Noise –' for the anti-causal part EGF labeled as '$m_b = 4$' in Figure 4-4a, 'S–' for the anti-causal part EGF (green dashed trace) labeled as 'S' in Figure 4-6a, 'N–' for the causal part EGF (green dashed trace) labeled as 'N' in Figure 4-6a, 'Coda–' for the anti-causal part EGF labeled as 'BC' in Figure 4-7, and 'Coda–' for the causal part EGF labeled as 'BC' in Figure 4-7. (b) Phase velocity dispersion curves in the period band 12 – 18 s for the EGFs in (a). The red dashed line in (a) shows the reference travel time (at 178 s) corresponding to the point with the maximum amplitude of the EGF labeled as 'Noise –'.

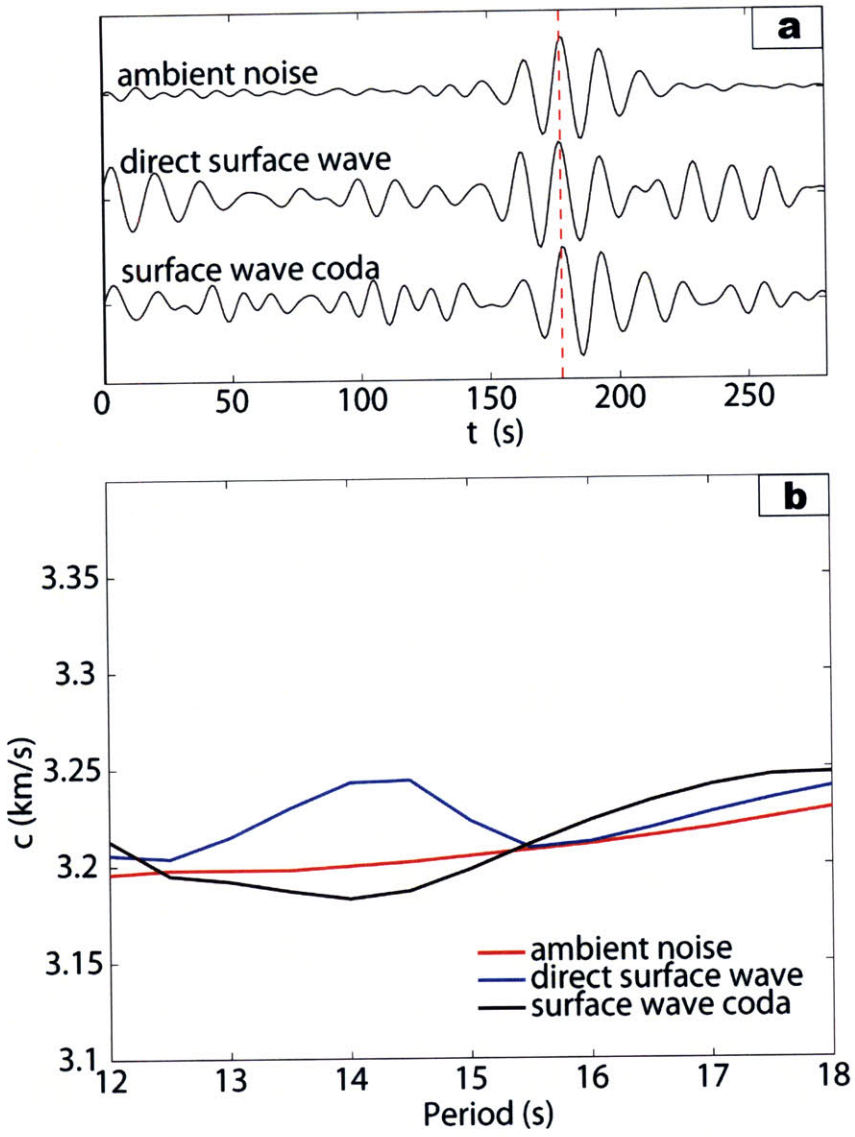

Figure 4-12. (a) Comparison of the stacked EGFs of MC04-MC23 constructed from three different data windows, i.e., ambient noise (top trace, stack of the causal and anti-causal parts of the bottom trace in Figure 4-4a labeled as 'm_b = 4'), direct surface wave (middle trace, stack of the two traces labeled as 'S–' and 'N+' in Figure 4-11a), and surface wave coda (bottom trace, stack of the two traces labeled as 'Coda–' and 'Coda+' in Figure 4-11a). (b) Comparison of phase velocity dispersion in the period band 12-18 s of the stacked EGFs in (a). The red dashed line in (a) shows the reference travel time (at 178 s) corresponding to the point with the maximum amplitude of the stacked EGF labeled as 'ambient noise'.

Chapter 5

Analysis of ambient noise energy distribution and phase velocity bias in ambient noise tomography, with application to SE Tibet[4]

Abstract

Green's functions of surface wave propagation between two receivers can be estimated from the cross correlation of ambient noise under the assumption of diffuse wavefields or energy equipartitioning. Interferometric Green's function reconstruction is generally incomplete, however, because the distribution of noise sources is neither isotropic nor stationary and the wave fields considered in the cross-correlation are generally non-diffuse. Furthermore, medium complexity can affect the empirical Green's function (EGF) if noise sources are all far away (i.e., approximately plane-wave sources), which makes the problem non-linear. We analyze the effect of uneven ambient noise distribution and medium heterogeneity and azimuthal anisotropy on phase velocities measured from EGFs with an asymptotic plane wave (far-field) approximation (which underlies most constructions of phase velocity maps). Phase velocity bias due to uneven noise distribution can be determined (and corrected) if the noise energy distribution is known. We estimate the (normalized) azimuthal distribution of ambient noise energy directly from the cross correlation functions obtained through ambient noise interferometry. The (smaller, second order) bias due to non-linearity can be reduced iteratively, for instance by using the tomographic model that results from the inversion of uncorrected data. We illustrate our method for noise energy estimation, phase velocity bias suppression, and

[4] Under review as: Yao, H. and Van der Hilst, R.D., 2009. Analysis of ambient noise energy distribution and phase velocity bias in ambient noise tomography, with application to SE Tibet, submitted to *Geophys. J. Int.*

ambient noise tomography (including azimuthal anisotropy) with data from a seismic array (26 stations) in SE Tibet. We show that the phase velocity bias due to uneven noise energy distribution (and medium complexity) in SE Tibet has a small effect (<1%) on the isotropic part phase velocities (for T=10-30 s) and the azimuthal anisotropy obtained before and after bias correction shows very similar pattern and magnitude.

5.1 Introduction

Traditional surface wave tomography, based on ballistic source-receiver propagation, has produced important constraints on the long wavelength structure of Earth's upper mantle, both on global and regional scale. With this approach to (linearized) tomographic velocity analysis, however, the (uneven) source-receiver distribution controls (and restricts) the geographical regions that can be studied at high-resolution, and scattering from local heterogeneity and topography along the long wave paths can prevent accurate inversion for shallow structures, such as in Earth's crust. Instead of relying on source-receiver wave propagation, theoretical, experimental, and observational studies in ultrasonics, acoustics, and seismology have shown that the Green's function for wave propagation between two receivers can be recovered from cross correlation of ambient wave fields (e.g., Lobkis & Weaver, 2001; Campillo & Paul, 2003; Malcolm et al., 2004; Weaver & Lobkis, 2004; Shapiro & Campillo, 2004; Snieder et al., 2004; Wapenaar, 2004; Roux et al., 2005; Wapenaar et al., 2006; Nakahara, 2006). Indeed, surface wave array tomography from ambient noise interferometry (e.g., Shapiro et al., 2005; Sabra et al., 2005; Kang & Shin, 2006; Yao et al., 2006, 2008; Lin et al., 2007, 2008; Moschetti et al., 2007; Yang et al., 2007, 2008; Liang & Langston, 2008; Zheng et al., 2008) has greatly improved our ability to resolve the shallow crust structure by extracting short periods group or phase velocity dispersion measurements from the recovered empirical Green's function (EGF).

Inferring the (empirical) Green's function (EGF) from time domain cross-correlations is conceptually simple, but in general the EGF differs from the exact Green's function and this (unknown) difference is becoming more important when applications are pushed to higher accuracy or medium complexity (e.g., anisotropy). Correct reconstruction of the

Green's function requires diffuse fields (Lobkis & Weaver, 2001), isotropic ambient noise distribution (e.g., Snieder, 2004; Roux et al., 2005), or isotropic incidence of wavefields (Nakahara, 2006), in the dimensions relevant for application at hand (e.g., 2-D for surface wave Green's functions). Recent surface wave studies show that the actual distribution of ambient noise energy is, in general, neither isotropic nor stationary but reveals directional and temporal variations (Stehly et al., 2006; Yang & Ritzwoller, 2008a; Yao et al., 2009). As a consequence, the EGF is generally an incomplete reconstruction of the true GF, which can be manifest, for instance, in a lack of reciprocity of the EGFs between two receivers (e.g., Yao et al., 2006).

The uneven distribution of noise sources can produce a bias in the surface wave group or phase velocities measured from the EGFs. Furthermore, if the predominant noise sources are all far away so that wave energy propagating across the receiver array can be approximated as plane waves (e.g., Yang & Ritzwoller, 2008b), the (unknown) medium heterogeneity can also produce travel time bias from the EGFs even for an isotropic distribution of noise energy (e.g., Tsai, 2009). However, in case of spatially homogeneous distribution of noise sources or diffuse wave fields, we would expect accurate travel time measurements from the EGFs regardless of any medium complexity. Comparisons of phase velocities from ambient noise interferometry and traditional two-station analysis (Yao et al., 2008) and of phase velocity maps from ambient noise tomography and teleseismic surface wave tomography (Yang & Ritzwoller, 2008b) as well as numerical simulations for certain types of noise distribution (Yang & Ritzwoller, 2008a; Lin et al., 2008) indicate that the bias is, indeed, small for the types of study done so far. It appears that the use of long time windows for cross-correlation (e.g., 1 year) and temporal and spectral normalization before cross correlation, e.g., one-bit (Shapiro & Campillo, 2004) or running-absolute-mean normalization and whitening (Bensen et al., 2007), are efficient in making the distribution of ambient noise sources more isotropic. Any remaining non-isotropic component of the ambient noise distribution will, however, result in an azimuth-dependence of bias of the phase or group velocity measurements from EGFs, and these discrepancies may be significant for high resolution studies or for determination of azimuthal and radial anisotropy.

De Hoop and Solna (2008) present a multi-scale analysis of Green's functions estimated from 'field-field' correlations in a random medium. Closer to the problem of interest here, Tsai (2009) corrects phase or group velocity bias using estimated travel times between two stations for given distribution of (ambient noise) source intensity. With synthetic data he shows that both the azimuthally uneven distribution of source intensity and the heterogeneity of the medium can produce bias in surface wave dispersion measurements. Stehly et al. (2006) and Yang & Ritzwoller (2008a) investigated the azimuth-dependence of ambient noise energy but do not provide a quantitative measure of this distribution, which is needed to actually correct the bias.

We describe here an approach to estimate the energy distribution of ambient noise and to correct the phase velocity bias for ambient noise surface wave array tomography. We illustrate the problems – and solutions – with data from a seismograph array in SW China (Yao at el., 2006, 2008). The accuracy of Green's function reconstruction from ambient noise interferometry depends on (i) the azimuthal distribution of noise energy (even vs. uneven), (ii) the type of medium (homogeneous vs. heterogeneous; isotropic vs. anisotropic) in case of plane-wave source distribution, and (iii) the scales in the data (frequency) and medium (structural length scales). It is impractical to explore all possible cases but the examples shown here give insight in the type and magnitude of the problem and the promise of the solution. In Section 5.2 of this paper we analyze cross correlations (and associated EGFs) through stationary phase and Fresnel zone arguments and present our approach to bias estimation through (asymptotic) plane-wave modeling. Section 5.3 investigates phase velocity bias for different types of noise distribution and medium. Section 5.4 presents a damped least-squares inversion that can be used to estimate the azimuthal variations of ambient noise energy from the (given) correlation functions. In Section 5.5, we apply the proposed method for noise energy estimation and phase velocity bias correction to array data in SE Tibet with an iterative approach. Finally we discuss the importance of analysis of phase velocity bias and noise energy estimation for isotropic and anisotropic ambient noise tomography.

5.2 Plane-wave modeling and interferometry

We investigate the surface wave part from ambient noise interferometry and ignore other types of waves generated by the noise sources. If the aperture of an array is small compared to the distance to the main noise sources – many ambient noise tomography studies concern arrays a few hundred kilometers across (e.g., SE Tibet, by Yao et al., 2006, 2008; New Zealand, by Lin et al., 2007; South Korea, by Cho et al., 2006) – we can approximate the energy from ambient noise sources as plane waves. We represent the noise energy as $E_P(\omega,\theta)$, with ω the angular frequency and θ the azimuth angle of the incoming plane wave passing across the array. Local scattering due to heterogeneity of the medium within or close to the array is not considered but their contribution is probably small compared to that from direct waves (like ocean- or earthquake-generated surface waves). Note that $E_P(\omega,\theta)$ represents the total energy of the plane waves with azimuth θ propagating across the array, which may be have contributions from many ambient noise sources. We use "plane wave energy" $E_P(\omega,\theta)$ and "ambient noise energy" as synonymous throughout this paper. For simplicity we assume straight rays but there is no obstruction for expanding the method to include ray bending or finite frequency sensitivities.

We consider seismograph stations at locations A and B in a 2-D elastic medium (Figure 5-1). The incoming plane wave with azimuth angle θ and energy $E_P(\omega,\theta)$ is assumed to be recorded at both stations with an equal amplitude – one-bit cross correlation (e.g., Yao et al., 2006) or normalized cross correlation (Bensen et al., 2007) removes the effect of geometrical spreading and attenuation. The phase travel time difference δt (or phase delay $\delta\phi = \omega\delta t$) of the plane wave between the two stations will result in a peak in the cross correlation function. The summation of cross correlation functions from all plane waves with azimuth angle from 0 to 2π produces the final cross correlation function, $C_{AB}(\omega,t)$, between stations A and B:

$$C_{AB}(\omega,t) = \int_0^{2\pi} E_P(\omega,\theta)\cos\left[\omega(t-\delta t)\right]H(t,\delta t)d\theta, \qquad (5\text{-}1)$$

where t is time and $H(t,\delta t)$ a time domain taper for the cross correlation function $E_P(\omega,\theta)\cos[\omega(t-\delta t)]$, which is infinite in time (blue sinusoid trace in Figure 5-2a). We use for $H(t,\delta t)$ a simple cosine taper function with peak centered at δt (dashed trace, Figure 5-2a):

$$H(t,\delta t)=\begin{cases}0.5\{1+\cos[2\pi(t-\delta t)/T^*]\} & t\in[\delta t-T^*/2,\delta t+T^*/2]\\ 0 & elsewhere\end{cases}, \tag{5-2}$$

where T^* is the (time) width of $H(t,\delta t)$. Here we choose $T^*=5T$, with $T=2\pi/\omega$ the period of the sinusoid wave. The integrant in equation (5-1) denotes the individual cross correlation function of the incoming plane wave with azimuth angle θ.

For homogeneous and isotropic medium with phase velocity c, the phase delay of the plane wave (with azimuthal angle θ) between stations A and B is

$$\delta\phi=k\Delta_{AB}\cos(\theta-\varphi)=\omega\Delta_{AB}\cos(\theta-\varphi)/c, \tag{5-3}$$

where $k=\omega/c$ is the wavenumber, Δ_{AB} is the interstation distance, and φ is the azimuth angle from station A to station B measured from north.

For a homogeneous but azimuthally anisotropic medium, Rayleigh wave phase velocity c can be approximated by $c=c_0\{1+A_c\cos 2(\theta-\psi)\}$ (Smith & Dahlen, 1973), where c_0 is the transversely isotropic part of the phase velocity, A_c is the amplitude of the azimuthal anisotropy, and ψ is the fast direction of the medium. For general heterogeneous and azimuthally anisotropic medium (Figure 5-1), the phase delay $\delta\phi$ between two stations is

$$\delta\phi=\int_{B'}^{B}\frac{\omega}{c(\omega,\mathbf{x})}dl-\int_{A'}^{A}\frac{\omega}{c(\omega,\mathbf{x})}dl, \tag{5-4}$$

where $\mathbf{x}$ is the spatial coordinate and the integration is along the ray path B'B and A'A as shown in Figure 5-1.

The time derivative of the ambient noise cross correlation function $C_{AB}(\omega,t)$ yields the empirical Green's functions (EGF) $\tilde{G}_{AB}(\omega,t)$ and $\tilde{G}_{BA}(\omega,t)$:

$$\frac{dC_{AB}(\omega,t)}{dt} = -\tilde{G}_{AB}(\omega,t) + \tilde{G}_{BA}(\omega,-t)$$
$$\tilde{G}_{AB}(\omega,t) = -\frac{dC_{AB}(\omega,t)}{dt} \qquad t \geq 0 \qquad . \qquad (5\text{-}5)$$
$$\tilde{G}_{BA}(\omega,t) = -\frac{dC_{AB}(\omega,-t)}{dt} \qquad t \leq 0$$

Under the assumption of isotropic wavefields or homogeneous distribution of noise sources, theoretical studies (e.g., Weaver & Lobkis, 2004; Snieder, 2004; Roux et al., 2005) have demonstrated that the EGF $\tilde{G}_{AB}(\omega,t)$ (or $\tilde{G}_{BA}(\omega,t)$) is equivalent to the real Green's function $G_{AB}(\omega,t)$ (or $G_{BA}(\omega,t)$), that is the Green's function (GF) that would have been recorded at station at B for a point source at A (or GF recorded at station A for a point source at B), except for a frequency-dependent amplitude correction. The phase of EGF is the same as that of GF.

In the far field (loosely, at least three wavelengths apart) the time-domain windowed Green's function for the surface wave fundamental mode centered at frequency ω can be approximated by (e.g., Dahlen & Tromp, 1998):

$$G_{AB}(\omega,t) = A\cos(\bar{k}_{AB}\Delta_{AB} - \omega t + \pi/4)H(t,t_{AB}), \qquad (5\text{-}6)$$

where A is the amplitude of surface-wave Green's function, $\bar{k}_{AB} = \frac{1}{\Delta_{AB}}\int_A^B k(\omega,\mathbf{x})dl$ the path average wavenumber between A and B, $H(t,t_{AB})$ the taper defined as equation (5-2), and $t_{AB} = (\bar{k}_{AB}\Delta_{AB} + \pi/4)/\omega$ the phase travel time of surface-wave fundamental mode at frequency ω. In the context of phase velocity maps, which is an asymptotic concept, we assume great circle propagation of surface waves between A and B.

In order to compare the $\tilde{G}_{AB}(\omega,t)$ and $G_{AB}(\omega,t)$ in the same time window, we define a surface wave window function (black trace, Figure 5-2b)

$$W(t,\Delta_{AB}) = \begin{cases} 1 & t \in [t_L,t_U] = [\Delta_{AB}/v_{\max}, \Delta_{AB}/v_{\min}] \\ 0.5\{1+\cos[\pi(t-t_U)/T]\} & t \in (t_U, t_U + T/2] \\ 0.5\{1+\cos[\pi(t_L-t)/T]\} & t \in [t_L - T/2, t_L) \\ 0 & elsewhere \end{cases}, \qquad (5\text{-}7)$$

where $v_{\min}$ and $v_{\max}$ are the minimum and the maximum group velocities to define the main surface wave window, respectively. $W(t,\Delta_{AB})$ can be frequency-dependent. For typical regional ambient noise surface wave tomography in the period band 10 – 50 s, $v_{\min} \approx 2$ km/s and $v_{\max} \approx 5$ km/s. For very short periods (e.g., several seconds), the group velocities that define the surface wave window will depend on the wavespeeds at shallow depth (e.g., top few kilometers).

Inside $W(t,\Delta_{AB})$ we measure the phase difference ($\delta\phi_{AB}$) between the EGF, $\tilde{G}_{AB}(\omega,t)$, and the theoretical GF, $G_{AB}(\omega,t)$, at frequency ω:

$$\delta\phi_{AB}(\omega) = \Theta(\tilde{G}_{AB}(\omega,t)W(t,\Delta_{AB})) - \Theta(G_{AB}(\omega,t)W(t,\Delta_{AB})), \tag{5-8}$$

where Θ is the operator to obtain the phase angle of a trace at frequency ω (for example, one can take the Fourier transform of the trace and calculate the phase from the real and imaginary part of spectrum at frequency ω). The travel time difference between EGF and GF is then given by $\delta t_{AB} = \delta\phi_{AB}(\omega)/\omega$. If $\delta\phi_{AB} > 0$, the surface wave EGF has a phase shift away from zero time with respect to the theoretical surface wave GF; in other words, the phase travel time of the empirical surface wave recovered from noise correlation is larger than that of theoretical surface wave. In this case the apparent phase velocity obtained from the EGF is slower than that from the theoretical GF. For $\delta\phi_{AB}$ or δt_{AB} less than zero, we would expect a higher phase velocity from the EGF than that from the theoretical GF. The relative phase velocity bias (μ) between the EGF and GF can then be expressed as

$$\mu = \frac{\tilde{c}_{AB} - c_{AB}}{c_{AB}} \approx -\frac{\delta t_{AB}}{t_{AB}} = -\frac{\delta\phi_{AB}(\omega)}{\omega t_{AB}}, \tag{5-9}$$

where $\tilde{c}_{AB}$ and c_{AB} are the surface wave phase velocities of the EGF and GF, respectively.

5.3 Azimuth dependent phase velocity bias

As shown above, with plane-wave modeling we can estimate the bias, that is, the relative difference between (fundamental mode) surface wave phase velocities measured from EGF and GF for a known ambient noise energy distribution $E_P(\omega,\theta)$ and medium. We

illustrate this with an isotropic and a realistic azimuth dependent ambient noise energy distribution and with simple models for structural heterogeneity and anisotropy. The geometry of the experiments is given in Figure 5-1, with φ the azimuth from A to B measured from north. Unless otherwise mentioned, the period of the plane wave $T = 30$ s, the distance between the stations $l_{AB} = 480$ km with central point fixed at O, and the background phase velocity $c_0 = 4$ km/s. In all examples we consider – for equation (5-1) – incoming plane waves with θ from 0-360° in intervals $d\theta = 0.5°$.

5.3.1 Homogeneous and isotropic medium

5.3.1.1 Isotropic energy distribution

For an isotropic distribution of ambient noise energy, that is, $\partial E_P(\omega,\theta)/\partial\theta = 0$, and station pair AB in S-N direction (that is, φ = 0°), Figure 5-3a shows cross correlation functions for plane waves arriving from 0° to 360°. The maximum plane wave travel time difference between A and B is δt_{max} = 120 s for a northward propagating plane wave (θ = 0° or 360°), and δt_{min} = -120 s for a southward propagating plane wave (θ = 180°). For waves perpendicular to A-B (θ = 90° or 270°), δt = 0 s. Following (5-1), the sum of individual cross correlations gives the cross correlation function $C_{AB}(\omega,t)$ for stations A and B (blue line, Figure 5-3b). The time derivative of $C_{AB}(\omega,t)$ then yields the EGF (red dashed line, Figure 5-3b).

The appearance of two arrivals in $C_{AB}(\omega,t)$ (and EGF) can be understood both with stationary phase (e.g., Snieder, 2004) and Fresnel zone analysis. The individual cross correlation functions from plane waves propagating near the azimuth of the two-station pair, that is, small $|\theta-\varphi|$, interfere (stack) constructively (near δt = +/-120 s), whereas waves with larger $|\theta-\varphi|$ interfere destructively and do not contribute to $C_{AB}(\omega,t)$. With λ the wave length, constructive interference occurs if

$$\left|\Delta_{AB}\cos(\theta-\varphi)-\Delta_{AB}\right| < \lambda/2 \ , \qquad (5\text{-}10)$$

which defines the first Fresnel for a homogeneous and isotropic medium, or

$$\left|\Delta\phi(\theta)\right| = \left| \left\{ \int_{B'}^{B} \frac{\omega}{c(\omega,\mathbf{x})} dl(\theta) - \int_{A'}^{A} \frac{\omega}{c(\omega,\mathbf{x})} dl(\theta) \right\} - \int_{A}^{B} \frac{\omega}{c(\omega,\mathbf{x})} dl(\varphi) \right| < \pi \qquad (5\text{-}11)$$

for a general heterogeneous medium. In (5-11), $\Delta\phi(\theta)$ is the phase difference between the individual cross correlation function from the incoming plane wave with azimuth θ and ray path $l(\theta)$ and the individual cross correlation function from the plane wave propagating along the inter-station ray path $l(\varphi)$ from A to B. Plane waves within the first Fresnel zone, that is, with θ satisfying (5-10) or (5-11), contribute most to the construction of the Green's function. Plane waves outside the first Fresnel zone either cancel out through destructive interference (as in the example shown) or give spurious arrivals if destructive interference is incomplete owing to, for instance, uneven distribution of ambient noise energy. For the parameters given, the first Fresnel zone consists of two parts: $0^\circ \le \theta \le 28.9^\circ$ and $331.1^\circ \le \theta \le 360^\circ$ (yellow boxes, Figure 5-3a) for the construction of $G_{AB}(\omega,t)$ and $|\theta\text{-}180^\circ| < 28.9^\circ$ (red box, Figure 5-3a) for the construction of $G_{BA}(\omega,t)$. Here, the EGF (red dashed line, Figure 5-3b) is nearly identical to the real GF (black line), with zero phase shift for both the causal (positive-time) and acausal (negative-time) part, as expected from theory (e.g., Weaver & Lobkis, 2004; Roux et al., 2005; Nakahara, 2006).

5.3.1.2 Uneven energy distribution

For uneven distribution of plane-wave sources we consider two cases. In the first, ambient noise generated plane waves only propagate along the direction of the two-station path, that is, $E_P(\omega,\theta)>0$ for $\theta = \varphi$ or $\theta = \pi+\varphi$ and $E_P(\omega,\theta) = 0$ elsewhere. The cross correlation function obtained (blue line, Figure 5-3c) is the same as in traditional two-station analysis (e.g, Yao et al., 2006) but has a $\pi/4$ phase advance compared to the GF (black lines, Figure 5-3b and c). Since the EGF (red dashed lines, Figure 5-3c) is $\pi/2$ phase delayed (away from zero time) with respect to $C_{AB}(\omega,t)$, as expected from the time derivative, there is a $\pi/4$ phase shift between EGF and GF.

For the second case we consider a more realistic, azimuth-dependent (normalized) ambient noise energy distribution (black curve, Figure 5-4a), inferred from our study in

SW China (Yao et al., 2006, 2008). The azimuth dependence of the (normalized) amplitude of the cross correlation functions, $C_{AB}(\omega,t)$, blue curve in Figure 5-4a, differs from that of the ambient noise energy (black curve), indicating that $C_{AB}(\omega,t)$ cannot be used as a proxy for $E_P(\omega,\theta)$. As a consequence, the phase velocity bias between EGF and GF (blue line, Figure 5-4b) depends on azimuth: that is, $\mu = \mu(\theta)$. The largest phase velocity biases occur where $E_P(\omega,\theta)$ changes most rapidly with azimuth (for instance, between 0-90° and between 180-270°, Figure 5-4a), with up to 3% bias for some station pairs (e.g., $\varphi \sim 20°$ or 70°). For relatively smooth azimuthal variation of ambient noise energy (e.g., 90°-135° or 270°-315°) the phase velocity bias is small (< 1%).

As discussed above, energy within the first Fresnel zone controls the recovery of the GF of the phase of interest. One would expect that the better the distribution of noise sources within the Fresnel zone the smaller the bias in phase velocity. Figure 5-4b shows, however, that bias can vanish (e.g., at $\varphi \sim 32°$ and 58°) even if the ambient noise energy distribution within the Fresnel zone is heterogeneous. In a homogeneous and isotropic medium, plane waves with azimuth $\theta=\varphi-\Delta\theta$ and $\theta=\varphi+\Delta\theta$ contribute equally to the recovery of $G_{AB}(\omega,t)$ at station pair with angle φ, so that adequate distribution in half of the Fresnel zone is generally sufficient to prevent bias.

5.3.2 Homogeneous and azimuthally anisotropic medium

In the previous section we considered only the effect of uneven ambient noise energy distribution. Here we use similar experiments to assess the effect of noise energy distribution on phase velocity bias in the presence of azimuthal anisotropy. We recall that the Green's functions (GFs) used here are evaluated with a ray theoretical approximation. In heterogeneous media the full wave Green's function may be different, but the (scale dependent) difference is expected to be small.

5.3.2.1 Isotropic energy distribution

Under the plane wave approximation, azimuthal anisotropy can cause phase shifts between EGF and GF, even for an isotropic energy distribution. The effect is small,

however. For a homogeneous, 5% azimuthally anisotropic medium (with fast axis at ψ = 45°, along the NE-SW direction) the phase velocity bias $\mu(\theta)$ is generally less than 0.5% (Figure 5-5c). The bias vanishes for station pairs in the direction of zero phase velocity gradient (in the first Fresnel zone), e.g., φ = 45°, 135°, 225°, and 315° (Figures 5-5b,c) and is largest for the station pairs with the largest velocity gradient with respect to azimuth, e.g., φ = 0°, 90°, 180°, and 270° (Figures 5-5b, c).

5.3.2.2 Uneven energy distribution

To assess the effect of medium anisotropy on Green's function reconstruction and phase velocity bias in the presence of uneven energy distribution we use the same $E_P(\omega,\theta)$ as in Section 5.3.1.2 (black line, Figure 5-4a). The variations with azimuth of (normalized) amplitude of the cross correlations and bias μ (red lines in Figures 5-4a,b) are virtually the same as in the isotropic case (blue lines, Figures 5-4a,b), with large biases occurring near azimuths where ambient noise energy changes rapidly with respect to station pair azimuth φ. From tests like this we conclude that the bias in phase velocity (from EGFs) due to (weak) azimuthal anisotropy is much smaller than that of uneven distribution of ambient noise energy.

5.3.3 Heterogeneous and anisotropic medium

Finally, we examine the effect of ambient noise energy distribution on phase velocity bias $\mu(\theta)$ in the presence of both azimuthal anisotropy and (2-D) medium heterogeneity.

5.3.3.1 Isotropic energy distribution

Much like azimuthal anisotropy (previous section), medium heterogeneity can bias phase velocities measured from EGFs even for an isotropic energy distribution due to the assumption of distant (plane-wave) sources. In a first experiment we consider a Gaussian anomaly – centered on O between A and B (Figure 5-6) – expressed as $c(x,y) = c_0 + \Delta c.\exp\{-0.5(x^2 + y^2)/r^2\}$, where c_0 = 4.0 km/s is the background wavespeed, Δc (0.5 km/s for case 1 and -0.5 km/s for case 2) the magnitude of the anomaly, x and y spatial coordinates, and R the characteristic length (in km) of the anomaly. Since the velocity distribution is rotationally symmetric the average phase velocity for any station pair

azimuth φ will be equal; for the following calculation we take the station pair with $\varphi = 0°$ (Figure 5-6).

To investigate the dependence of bias on spatial scale (of medium heterogeneity), we fix the period of incoming plane waves T at 30 s and let r increase from 2 to 150 km (Figure 5-7a). For case 1, that is Δc = 0.5 km/s, the resulting phase travel time difference δt_{AB} between EGF and the theoretical GF is close to zero for r less than several kilometers or larger than ~100 km, but δt_{AB} will be as much as 1 s for r around 35 km. The latter would correspond to a phase velocity measured from EGF that is ~1% slower than from GF. In case 1, $\delta t_{AB} \geq 0$ for all r, which implies that phase velocities estimated from EGFs are always less than the theoretical phase velocities. Likewise, for case 2 (Δc = - 0.5 km/s), $\delta t_{AB} \leq 0$ for any r, indicating that the phase velocity will be overestimated.

This can, again, be understood with a simple Fresnel zone analysis. For the geometry given (Figure 5-6), the average velocity will (for case 1) be largest between the two stations. Plane waves propagating off the two-station path but within the first Fresnel zone (and thus relevant for the construction of the EGF) will sense lower average velocities and thus render a larger travel difference δt_{AB} than in a homogeneous, isotropic medium. This results in a lower phase velocity, that is, a phase velocity bias $\mu < 0$. Similarly, $\Delta c < 0$ leads to $\mu > 0$. For small r the average phase velocity between A-B is close to c_0 and for very large scale anomalies (here, r > 100 km) plane waves within the first Fresnel zone all propagate with speeds similar to the interstation average. For both cases, δt_{AB} (within the first Fresnel zone) will be very similar to that in a homogeneous and isotropic medium, and therefore the final phase velocity estimation from the EGF will be very close to that from the theoretical GF, that is, $\mu \sim 0$.

To investigate the dependence on spectral scale (in the data), we fix r at 50 km and let period T increase from 5 to 70 s (Figure 5-7b). We set c_0 at 4 km/s for all periods. For homogeneous and isotropic media (that is $\Delta c = 0$) δt_{AB} is close to zero from T = 5 to 55 s (as expected); the negative values for T > 55 s reflect the breakdown of far field

approximation for surface wave propagation (Yao et al., 2006) and, thus, the accuracy of (5-6). For $\Delta c > 0$ (case 1) δt_{AB} is positive (and $\mu < 0$) and increases as T increases. For $\Delta c < 0$ (case 2) δt_{AB} is negative (and $\mu > 0$) and the magnitudes of the travel time and phase velocity biases ($|\delta t_{AB}|$ and $|\mu|$, respectively) increase with increasing T.

Since the velocity distribution $c(x,y)$ is the same for each period T, the width of the first Fresnel zone increases with increasing T (or wavelength λ) according to (5-11). The half width of the first Fresnel zone with respect to the two-station path is about 17°, 29°, and 38° for T = 10, 30, and 50 s, respectively (Figure 5-6.) Narrower widths of the first Fresnel zone generally produce smaller bias δt_{AB} and μ between stations A and B, whereas, longer period (longer wavelength) data produces larger differences between EGF and the theoretical GF, which confirms results by Tsai (2009).

In a second experiment we investigate a heterogeneous model (Figure 5-8) with positive and negative anomalies centered around (0, -100) and (100, 50), respectively. The geometry of the station pair AB is as before, and the ambient noise energy is initially azimuthally isotropic (black line, Figure 5-9a). For this model, the relative phase velocity bias at T = 30 s reaches -2% for φ = 0° and 1% for station pairs with azimuth angle φ° ~50° (Figure 5-9c). In general, phase velocities are underestimated for station pairs with high average interstation phase velocities, whereas phase velocities from EGF are overestimated for low velocities (Figures 5-9b, c). In summary, for isotropic energy distribution, and with asymptotic theory, the strength of phase velocity anomalies (with respect to a constant background) obtained from EGFs is usually underestimated.

5.3.3.2 Uneven energy distribution

The velocity bias $\mu(\theta)$ produced by uneven energy distribution (black line, Figures 5-4a, 5-10a) in the presence of 2-D heterogeneity with and without 5% azimuthal anisotropy (case 1 and 2 in Figure 5-8) is presented in Figure 5-10b (blue line for isotropic medium; red line for 5% anisotropy). For comparison, the green dotted curve shows the velocity bias for the heterogeneous medium but isotropic plane-wave distribution (section 5.3.3.1) and the brown curve shows the bias for the homogeneous medium but uneven plane-

wave energy distribution (black line, Figure 5-10a). The velocity bias for the heterogeneous (isotropic or anisotropic) medium with uneven plane-wave energy distribution consists of two parts (which are not entirely independent of each other): bias for homogeneous medium with uneven plane-wave energy distribution (brown dashed line, Figure 5-10b) and bias for heterogeneous (isotropic or anisotropic) medium with isotropic plane-wave energy distribution (green dashed line, Figure 5-10b). Our tests suggest, as before, that the former is generally (much) larger than the latter.

5.4 Recovery of ambient noise energy

5.4.1 Methodology

In the previous section we have shown that uneven distribution of ambient noise (plane wave) energy can produce a substantial bias in phase velocities measured from ambient noise interferometry (that is, from EGFs). So far, we have assumed a particular noise energy distribution (e.g., black curve in Figures 5-4a and 5-10a). In general, however, we do not know $E_P(\omega,\theta)$ *a priori.* But we do know the interstation cross correlation functions $C_{AB}(\omega,t)$, or the EGFs inferred from them (e.g., red or blue curves in Figures 5-4a and 5-10a). The relationship between the amplitudes of $C_{AB}(\omega,t)$ and $E_P(\omega,\theta)$ is nonlinear – as shown in (5-1) and, for instance, Figure 5-4a – and the former cannot be used as a proxy for the latter. We will show, however, that $E_P(\omega,\theta)$ can be estimated from $C_{AB}(\omega,t)$ and that the bias in phase velocity measurement from ambient noise interferometry can be quantified and reduced. This involves an inversion, which is here formulated in the context of the plane-wave modeling described in Section 5.2.

After discretization, equation (5-1) in the main surface wave window can be rewritten as

$$C_n(\omega,t,\varphi_n)W_n(t,\Delta_n)=\sum_{m=1}^{M}\mathbf{E}_m(\theta_m)\cos\left[\omega(t-\delta t_{nm})\right]H_{nm}(t,\delta t_{nm})W_n(t,\Delta_n), \qquad (5\text{-}12)$$

where $C_n(\omega,t,\varphi_n)$ is the cross correlation function for the n^{th} (n = 1, 2, …, N) two-station pair with azimuth angle φ_n and interstation distance Δ_n, $W_n(t,\Delta_n)$ the surface wave window function for the n^{th} two-station pair (equation(7)), $\mathbf{E}_m(\theta_m)$ the plane wave

energy at the m^{th} azimuth θ_m ($m = 1, 2, \ldots, M$), and δt_{nm} and $H_{nm}(t, \delta t_{nm})$ the phase travel time difference and cosine taper window function of the n^{th} two-station pair for the m^{th} incoming plane wave, respectively. Taking the Fourier transform $\mathbb{F}$ for both sides of (5-12) gives

$$\mathbb{F}\{C_n(\omega,t,\varphi_n)W_n(t,\Delta_n)\} = \sum_{m=1}^{M} \mathbf{E}_m(\theta_m)\mathbb{F}\{\cos[\omega(t-\delta t_{nm})]H_{nm}(t,\delta t_{nm})W_n(t,\Delta_n)\}. \quad (5\text{-}13)$$

Separation of the real and imagery part (at frequency ω) gives the following matrix equation:

$$\mathbf{A}_R + j\mathbf{A}_S = (\mathbf{R} + j\mathbf{S})\mathbf{E}, \quad (5\text{-}14)$$

where j is the imaginary unit, $\mathbf{A}_R$ and $\mathbf{A}_S$ $N\times 1$ dimensional vectors, $\mathbf{R}$ and $\mathbf{S}$ $N\times M$ dimension matrices, and $\mathbf{E}$ an $M\times 1$ dimension vector:

$$\begin{aligned}
(\mathbf{A}_R)_n &= \mathrm{Re}\left(\mathbb{F}\{C_n(\omega,t,\varphi_n)W_n(t,\Delta_n)\}\right)\Big|_\omega \\
(\mathbf{A}_S)_n &= \mathrm{Im}\left(\mathbb{F}\{C_n(\omega,t,\varphi_n)W_n(t,\Delta_n)\}\right)\Big|_\omega \\
\mathbf{R}_{nm} &= \mathrm{Re}\left(\mathbb{F}\{\cos[\omega(t-\delta t_{nm})]H_{nm}(t,\delta t_{nm})W_n(t,\Delta_n)\}\right)\Big|_\omega, \\
\mathbf{S}_{nm} &= \mathrm{Im}\left(\mathbb{F}\{\cos[\omega(t-\delta t_{nm})]H_{nm}(t,\delta t_{nm})W_n(t,\Delta_n)\}\right)\Big|_\omega \\
\mathbf{E}_m &= \mathbf{E}_m(\theta_m)
\end{aligned} \quad (5\text{-}15)$$

with $\mathrm{Re}(\cdots)\big|_\omega$ and $\mathrm{Im}(\cdots)\big|_\omega$ operators that take the real and imaginary part at frequency ω.

We notice that equation (5-14) is linear between data ($\mathbf{A}_R$ and $\mathbf{A}_S$) and model parameters $\mathbf{E}$ because of the linear property of the Fourier transform. Therefore $\mathbf{E}$ can be solved from $\mathbf{A}_R$ and $\mathbf{A}_S$ through a least-squares inversion scheme. However, the energy or amplitude of the windowed cross correlation function is nonlinearly dependent on $\mathbf{E}$ as inferred from (5-13) and (5-14). To obtain, by inversion, the ambient noise energy vector $\mathbf{E}$ we define the penalty function $\chi(\mathbf{E})$

$$\chi(\mathbf{E}) = (\mathbf{RE}-\mathbf{A}_R)^T(\mathbf{RE}-\mathbf{A}_R) + (\mathbf{SE}-\mathbf{A}_S)^T(\mathbf{SE}-\mathbf{A}_S) + \lambda_D(\mathbf{DE})^T(\mathbf{DE}), \quad (5\text{-}16)$$

where the superscript ^{T} denotes the transpose of a matrix, λ_D a damping parameter, and $\mathbf{D}$ an $M\times(M\text{-}1)$ dimension smoothing operator (first finite difference matrix) defined as

$$\mathbf{D}=\begin{bmatrix} -1 & 1 & 0 & \dots & \dots & 0 \\ 0 & -1 & 1 & \dots & \dots & 0 \\ & & \dots & \dots & & \\ & & & \dots & \dots & \\ 0 & \dots & \dots & -1 & 1 & 0 \\ 0 & \dots & \dots & 0 & -1 & 1 \end{bmatrix}.$$

On the right hand side of (5-16) the first and second terms give the data misfit for the real and imaginary part as shown in (5-14) respectively, and the third term denotes model roughness. Optimization of this equation, that is, solving for $\partial\chi(\mathbf{E})/\partial\mathbf{E}=0$, gives the solution

$$\mathbf{E}=(\mathbf{R}^T\mathbf{R}+\mathbf{S}^T\mathbf{S}+\lambda_D\mathbf{D}^T\mathbf{D})^{-1}(\mathbf{R}^T\mathbf{A}_R+\mathbf{S}^T\mathbf{A}_S). \tag{5-17}$$

Equation (5-17) shows how the distribution of ambient noise energy can be estimated from the real and imaginary part of the Fourier transformed cross correlation functions.

5.4.2 Proof of concept

To illustrate the inversion for ambient noise energy **E** we use the same station geometry as before, with station azimuth φ (from A to B) varying from 0° to 358° with $\mathrm{d}\varphi=2°$ so that the number of data (cross correlations) N = 180. For the discretization in (5-12) we use $\mathrm{d}\theta$ = 0.5° to ensure enough sampling of plane waves for the Green's function recovery. Inverting for **E** at $\mathrm{d}\theta$= 0.5° intervals would imply 720 unknowns ($M>>N$). In order to reduce the number of unknowns (to K = 90), however, we invert for $\tilde{\mathbf{E}}$ at 4° interval (that is, $\tilde{\theta}_k$= 0°, 4°, …, 356°). For any incoming plane wave with azimuth θ_m ($0\le\theta_m<360°$), there exists a number k such that $\tilde{\theta}_k\le\theta_m<\tilde{\theta}_{k+1}$ and the energy $\mathbf{E}_m$ is linearly interpolated between $\left(\tilde{\mathbf{E}}\right)_k$ and $\left(\tilde{\mathbf{E}}\right)_{k+1}$ as

$$\begin{aligned} \mathbf{E}_m &= \beta_{mk}\left(\tilde{\mathbf{E}}\right)_k+\beta_{m(k+1)}\left(\tilde{\mathbf{E}}\right)_{k+1} \\ \beta_{mk} &= \left(\theta_m-\tilde{\theta}_k\right)\Big/\left(\tilde{\theta}_{k+1}-\tilde{\theta}_k\right) \quad , \\ \beta_{m(k+1)} &= (1-\beta_{mk}) \end{aligned} \tag{5-18}$$

or in a matrix form as

$$\mathbf{E} = \boldsymbol{\beta}\tilde{\mathbf{E}}, \tag{5-19}$$

with $\boldsymbol{\beta}$ an $M\times K$ matrix with elements β_{mk}; if $\theta_m \geq \tilde{\theta}_K = 356°$, $\tilde{\theta}_{K+1} = 360°$ and $\left(\tilde{\mathbf{E}}\right)_{K+1} = \left(\tilde{\mathbf{E}}\right)_1$. Substituting (5-18) into (5-14) and reformatting it, we obtain $\mathbf{A}_R + j\mathbf{A}_S = (\tilde{\mathbf{R}} + j\tilde{\mathbf{S}})\tilde{\mathbf{E}}$, with $\tilde{\mathbf{R}}$ and $\tilde{\mathbf{S}}$ $N\times K$ dimensional matrices defined as:

$$\begin{aligned} \tilde{\mathbf{R}} &= \mathbf{R}\boldsymbol{\beta} \\ \tilde{\mathbf{S}} &= \mathbf{S}\boldsymbol{\beta} \end{aligned}. \tag{5-20}$$

Therefore, the solution sought is

$$\tilde{\mathbf{E}} = (\tilde{\mathbf{R}}^T\tilde{\mathbf{R}} + \tilde{\mathbf{S}}^T\tilde{\mathbf{S}} + \lambda_D\mathbf{D}^T\mathbf{D})^{-1}(\tilde{\mathbf{R}}^T\mathbf{A}_R + \tilde{\mathbf{S}}^T\mathbf{A}_S). \tag{5-21}$$

We test this inversion scheme with the same noise energy distribution as before (black lines in Figure 5-4a). We calculate the N=180 cross correlation functions using (5-1) and take the real and imaginary parts, i.e., $\mathbf{A}_R$ and $\mathbf{A}_S$, as in (5-15). With $\delta t_{nm} = \omega\delta\phi_{nm}$, where $\delta\phi_{nm}$ is the phase delay in (5-4), we obtain $\tilde{\mathbf{R}}$ and $\tilde{\mathbf{S}}$ from (5-15) and (5-20). Finally, we obtain estimates of the azimuthal distribution of ambient noise energy $\tilde{\mathbf{E}}$ from (5-21) for different damping parameters λ_D.

For a homogeneous and isotropic medium (as in section 5.3.1) we can recover the ambient noise energy (magenta circles, Figure 5-11a) without damping, i.e., λ_D=0. For a heterogeneous, isotropic medium (Figure 5-8, case 1) the undamped solution (magenta circles, Figure 5-11b) is unstable, but $\tilde{\mathbf{E}}$ is identical to distribution $\mathbf{E}$ for λ_D=100 (blue circles, Figure 5-11b). If the medium is azimuthally anisotropic (we added 5% anisotropy, as in Figure 5-8, case 2) $\mathbf{E}$ can still be recovered but stronger damping is needed to stabilize the solution (Figure 5-11c).

The above examples demonstrate that ambient noise energy $E_P(\omega,\theta)$ can be recovered from data, that is the cross correlations. We have, however, used the same model in the forward problem as in the inversion, whereas in practice the input model, e.g., phase velocity maps (Yao et al., 2006), will be an estimate of the true model. We recall that measurements (EGFs) are influenced by a combination of uneven ambient noise energy

distribution and medium complexity (heterogeneity and anisotropy). The influence from medium complexity is a consequence of our assumption of plane-wave sources, and is generally smaller than that from noise energy distribution (Section 5.3). To assess the recovery of $E_P(\omega,\theta)$ when the input model for inversion is different from (but close to) the true model we calculate cross correlation functions from one model (Figure 5-8, case 2) and perform the inversion with another (Figure 5-12a). The fact that recovery (blue circles, Figure 5-12b) is satisfactory motivates the following three-step approach: First, we use the phase velocity maps obtained by inversion of the original (uncorrected) data (e.g., Yao et al., 2006) to estimate the spatial distribution of ambient noise energy. Second, we use this estimate of the noise energy distribution to calculate (and remove) the bias in phase velocities. Third, we use the corrected phase velocities for final unbiased inversion. (This loop can be repeated, but our simulations suggest that a single iteration is sufficient.)

5.5 Application in SE Tibet and azimuthal anisotropy

We use one month of vertical component data from the seismograph array in SE Tibet (Figure 5-13a) to illustrate the process of recovery of ambient noise, estimation of phase velocity bias, and inversion for velocity model using an iterative procedure. We show the difference of the isotropic phase velocity map and azimuthal anisotropy before and after the correction of phase velocity bias.

5.5.1 Iterative procedure

We obtain $C_{AB}(\omega,t)$ for all possible two-station pairs (Figure 5-13c) by one-bit cross correlation of vertical component data recorded at A and B in the period band 10 – 30 s – see Yao et al. (2008) for details about data processing. To obtain more symmetric (reciprocal) EGFs from the cross-correlation functions $C_{AB}(\omega,t)$ we use equation (5-5) and stack, for each station pair, the causal and anti-causal parts of the EGFs. We refer to this stack as the symmetric component. From the resulting EGF we measure the phase velocities $\tilde{c}_{AB}$ using the method by Yao et al. (2006). This assumes perfect recovery of GF in a far field, but – as discussed in section 5.3 – the obtained dispersion data may be

biased due to uneven noise distribution and structure complexity. We use the following iterative procedure to estimate the ambient noise energy distribution, phase velocity bias, and 2-D phase velocity distribution at certain period T:

Step 1: Invert for 2-D phase velocity map (isotropic or azimuthally anisotropic) using interstation phase velocity measurements $c^{(k)}$ (k = 1, 2, ...; k = 1 for the original measurements $\tilde{c}_{AB}$ from symmetric component EGFs, and $k > 1$ for updated phase velocities in Step 3 after bias correction in each iteration)

Step 2: Estimate ambient noise (plane-wave) energy distribution $\tilde{\mathbf{E}}^{(k)}$ by means of plane-wave modeling (Section 5.4). As point of departure for the modeling we use the 2-D phase velocity maps from Step 1, and we use both the causal and anti-causal part of the cross correlation functions to obtain the data $\mathbf{A}_R$ and $\mathbf{A}_S$ in (5-15), with the requirement that the interstation distance is at least 2 wavelengths.

Step 3: Estimate the relative phase velocity bias $\mu^{(k)}$ between the EGF and theoretical GF defined in (5-9) and update the phase velocity measurements with

$$c^{(k+1)} = \tilde{c}_{AB}/(1+\mu^{(k)}). \tag{5-22}$$

Since we use the symmetric component EGFs for dispersion analysis, the phase delay between the EGF and GF expressed as equation (5-8) can be modified as

$$\delta\phi_{AB}(\omega) = \Theta(\left[\tilde{G}_{AB}(\omega,t)+\tilde{G}_{BA}(\omega,t)\right]W(t,\Delta_{AB})) - \Theta(G_{AB}(\omega,t)W(t,\Delta_{AB})). \tag{5-23}$$

Note that we still use the 2-D phase velocity map from Step 1 for plane-wave modeling and for calculating the EGF and theoretical GF.

Step 4: If $c^{(k+1)}$ or $\tilde{\mathbf{E}}^{(k)}$ converges, stop iteration; otherwise go back to Step 1.

We emphasize that the obtained ambient noise energy distribution $\tilde{\mathbf{E}}^{(k)}$ depends on the normalization involved in cross-correlation (here we use one-bit cross-correlation). In view of the relationship between the cross-correlation function and ambient noise energy (equations (5-1) and (5-13)), $\tilde{\mathbf{E}}^{(k)}(\theta)$ measures the overall normalized energy of the

incoming plane waves at azimuth θ in the entire period of cross-correlation, which, in our example, is one month. This linearity also implies that the overall noise energy in a longer time window can be obtained through summation of noise energy in shorter time windows.

The convergence depends on the quality of the first preliminary phase velocity map from ambient noise tomography. If it is close to the real model, we may expect convergence after one or two iterations. During the iterative process we can simultaneously invert for azimuthal anisotropy and the isotropic part of phase velocity maps. In the examples shown below we consider isotropy for the first two iterations (i.e., k = 1, 2) and subsequently (k = 3, 4, ...) invert for azimuthally anisotropic phase velocity at the period T = 25 s. The corresponding ray path coverage at T = 25 s is shown as Figure 5-13b.

5.5.2 Results

In Figure 5-14, we show the estimated ambient noise (plane-wave) energy distribution $\tilde{\mathbf{E}}^{(k)}$ for the first four iterations. The first two iterations, based on the isotropic phase velocity maps, yield similar values of $\tilde{\mathbf{E}}^{(k)}$ almost at all azimuth angles. Similar results are obtained for the 3rd and 4th iterations, which are based on azimuthally anisotropic phase velocity maps. The incorporation of azimuthal anisotropy yields slight differences in $\tilde{\mathbf{E}}^{(k)}$ at some azimuth angles. This result suggests that one iteration is enough to obtain stable estimation of ambient noise energy both for isotropic and azimuthally anisotropic media. During the inversion for $\tilde{\mathbf{E}}^{(k)}$, an appropriate value of the damping parameter λ_D need to be set. Using an automated scheme, we determine λ_D from the tradeoff curve (e.g., upper left inset figure in Figure 5-14) between the data misfit ($d_{misfit} = (\tilde{\mathbf{R}}\tilde{\mathbf{E}} - \mathbf{A}_R)^T(\tilde{\mathbf{R}}\tilde{\mathbf{E}} - \mathbf{A}_R) + (\tilde{\mathbf{S}}\tilde{\mathbf{E}} - \mathbf{A}_S)^T(\tilde{\mathbf{S}}\tilde{\mathbf{E}} - \mathbf{A}_S)$, modified from the first two terms of (5-16)) and the model roughness ($m_{rough} = (\mathbf{D}\tilde{\mathbf{E}})^T(\mathbf{D}\tilde{\mathbf{E}})$, modified from the third term of (5-16)). We try a broad range of values for λ_D from 0 to $\mathbf{A}_R{}^T\mathbf{A}_R + \mathbf{A}_S{}^T\mathbf{A}_S$ (open circles in the inset figure of Figure 5-14) to obtain the tradeoff curve by interpolation. On the tradeoff curve we find λ_1 such that $d_{misfit}(\lambda_1) = 0.15\max(d_{misfit})$ and λ_2 such that

$m_{rough}(\lambda_2) = 0.15 \max(m_{rough})$. The value of λ_D for the final inversion of $\tilde{\mathbf{E}}$ is set, empirically, to $\lambda_D = 10^{0.5(\log_{10}\lambda_1 + \log_{10}\lambda_2)}$. The λ_D selected this way yields a smooth $\tilde{\mathbf{E}}$ and also a small data misfit from our tests.

Figure 5-15 shows the relative interstation phase velocity bias $\mu^{(k)}$ from EGFs for two periods T = 10 s (Figures 5-15 a-d) and T = 25 s (Figures 5-15 e-h) as a function of interstation distance (left column) or azimuth (right column) for the isotropic or azimuthally anisotropic case. As expected, the bias $\mu^{(k)}$ depends on azimuth (Figures 5-15 b, d, f, h). For example, the systematic bias $\mu^{(k)}$ for the paths with azimuth angles 90°-135° (Figures 5-15 f & h) is mainly due to the large variation of ambient noise energy propagating into the array with the azimuth angle between 270°-315° (Figure 5-14), which is originated to the east of the array, probably from oceans. The obtained azimuthal distribution of ambient noise energy from inversion is also confirmed through analysis of azimuthal distribution of the normalized amplitudes of cross correlation functions (e.g., Stehly et al., 2006; Yao et al., 2009). For most paths the bias is less than 1%, probably because we use the symmetric component of EGFs which creates a more isotropic noise distribution. The magnitude of the bias decreases with increasing interstation distance (Figures 5-15 a, c, e, g). This is mainly because that the width of the first Fresnel zone for interferometry decreases as the interstation distance increases. As a consequence, the final construction of GF will be less sensitive to the (relatively long wavelength) variation of ambient noise energy and medium heterogeneity. This effect is similar to the decrease in phase velocity bias due to a decrease in wavelength (and, thus, Fresnel zone width) discussed in Section 5.3.3.1. Indeed, the bias at T=10 s (Figures 5-15 a & c) is smaller than at T = 25 s (Figures 5-15 e & g). Consistent with the outcome of the modeling experiments (Section 5.3), the incorporation of (weak) azimuthal anisotropy has only a small effect on the estimation of bias for most paths (e.g., comparing results between Figures 5-15 b & d, or Figures 5-15 f & h) .

Figure 5-16 shows the phase velocity maps at T = 25 s obtained from the original, uncorrected phase velocity measurements $\tilde{c}_{AB}$ and from the corrected measurements $c^{(k)}$.

Using $\tilde{c}_{AB}$, we first perform inversions for isotropic and anisotropic phase velocity maps (Figure 5-16a,b) using the regionalization due to Montagner (1986). For the anisotropy inversion, the phase velocity at each grid point (x, y) is expressed as $c(x,y) = c_0(x,y)\cdot\{1 + A(x,y)\cos(2\psi) + B(x,y)\sin(2\psi)\}$, where $c_0(x, y)$ is the transversely isotropic part of the phase velocity, $A(x, y)$ and $B(x, y)$ are the azimuthally anisotropic terms, and ψ is the azimuth of the ray path through (x, y). The isotropic part of the inversion that also allows for azimuthal anisotropy (Figure 5-16b) is very similar to the map from the inversion that considers only isotropy (Figure 5-16a), which implies that the tradeoff between isotropic phase velocities $c_0(x, y)$ and azimuthally anisotropic terms $A(x, y)$ and $B(x, y)$ is small (see also Simons et al., 2002). In Figure 5-16c, we show the azimuthally anisotropic phase velocity map using the corrected interstation phase velocities $c^{(k)}$ after 4 iterations as given above, which is generally similar to the results using the uncorrected measurements $\tilde{c}_{AB}$ (Figure 5-16b). The largest difference in isotropic phase velocity before and after bias correction is about 1%, which is much smaller than the variation of phase velocity map at this period (>10%). The pattern and magnitude of the azimuthal anisotropy are also similar and the difference is probably less than the uncertainty in the inversion results. Inversions for other periods yield similar results. In particular, the pattern and magnitude of azimuthal anisotropy at 10s are almost the same before and after bias correction.

5.6 Discussions

Ambient noise tomography has become an important tool for investigations of the structure of the crust and shallow mantle lithosphere using data from seismograph array stations. However, the surface wave Green's functions are generally not fully reconstructed due to uneven distribution of ambient noise sources. This raises the concern that dispersion measurements from such empirical Green's functions are biased, which can degrade the accuracy of ambient noise tomography, especially for anisotropic structure.

We have investigated this problem under the assumption of plane wave propagation (that is, asymptotic theory). In particular, the theoretical Green's functions (GFs) used here are evaluated with a ray theoretical approximation. The approach presented here is based on plane-wave modeling and is generally applicable for ambient noise array tomography if (1) the waves generated from distant noise sources can be approximated as plane waves propagating across the array (that is, the horizontal scale of the study region must be relatively small compared to the distance to the main noise sources – e.g., ocean microseisms – and the energy of local scattered surface waves must be much weaker than that of faraway sources); (2) there is good azimuth coverage of two-station paths; and (3) an adequate initial model for plane wave modeling is available.

The first requirement is generally satisfied for most regional ambient noise array tomographic studies, e.g., in SE Tibet (Yao et al., 2006, 2008), New Zealand (Lin et al., 2007), South Korea (Kang & Shin, 2006), and southern California (Shapiro et al., 2005). For ambient noise tomography, the period range is typically within 10 – 40 s, for which the ambient noise is generated mainly through ocean wave activities (e.g., storms) generated in the northern oceans during the northern hemisphere winter and in the southern oceans during the northern summer (e.g., Stehly et al., 2006; Rhie & Romanowicz, 2006). It is still under debate whether the seismic noise for periods larger than 10 s is related to ocean wave activity in deep water (Stehly et al., 2006) or generated by the nonlinear interaction of ocean waves with seafloor near coastlines (Yang & Ritzwoller, 2008). Such nearby noise sources may invalidate plane wave modeling, especially at short periods (<10 s) and for near-coastal arrays, unless they can be accounted for by adding extra terms to (5-1) and (5-12). Plane-wave beamforming analysis (Yao et al., 2009) demonstrates that ambient noise energy in the primary microseism band (10 – 20 s) propagating into the array in SE Tibet correlates well with distant ocean wave activity with seasonal variations. Since the array in SE Tibet is at least about one thousand kilometers away from the coastline, even if there exist near coastal sources, plane wave approximation is still a good approximation to represent energy propagation through this small array. The requirement that local scattering is small compared to the energy from distant noise sources is not easily verified. For the array in

SE Tibet, however, the dominant sources are ocean microseisms and distant earthquakes, with much weaker contributions from local scattering (Yao et al., 2009).

The second and third requirements are needed to ensure robust estimation of the azimuthal distribution of ambient noise energy. For seismic arrays with good spatial and azimuthal interstation path coverage, such as the MIT array in SE Tibet (Yao et al., 2008), we can usually estimate noise energy at azimuth intervals of several degree. However, for seismic arrays with narrow azimuthal path coverage, such as a 2-D array with a large aspect ratio, the estimation of azimuthal energy distribution will be less reliable. As input velocity model for the plane wave modeling one can use the isotropic phase velocity maps from ambient noise tomography without bias correction or from earthquake-based surface wave tomography.

We note that in heterogeneous media the true (full wave) Green's function may be slightly different, with the difference expected to be dependent on the scale of the medium. The simplified approach presented here is relevant, however, because most current ambient noise (surface wave) tomography studies similarly rely on asymptotic theory (e.g., ray paths, phase velocity maps). There is no fundamental obstruction to extend the same concept to full wave theory, with the use of full wave sensitivity kernels, but that would only be useful if the entire tomographic inversion is posed as a full wave, multi-scale problem (with model parameters inferred directly from broad-band data and not from phase or group velocity maps).

Our analysis suggests that ambient noise tomography for isotropic wavespeed variations is likely to be robust (that is, it is relatively insensitive to bias due to incomplete GF reconstruction) if one uses long time windows (e.g., several months or even one year) for cross correlation and the symmetric component of the EGF (the sum of the causal and anti-causal part of EGF) for dispersion analysis (e.g., Yang et al., 2008; Yao et al., 2008). For the MIT array in SE Tibet the phase velocity bias is generally less than 1%, which is small compared to the inferred wavespeed variations and which causes a very small effect on the isotropic phase velocity maps in the wave period of interest (T=10-30s).

The azimuthal dependence of phase velocity bias is a bigger concern for inversions for (azimuthally) anisotropic structure. Our example in SE Tibet shows, however, that this effect is generally small, and the (spatial) smoothing employed in surface wave tomography further suppresses any effects of azimuth-dependent bias.

Even if the effect is small for our array in SE Tibet, we recommend that inversions for azimuthal anisotropy are subjected to bias analysis if the EGFs indicate that the distribution of ambient noise energy varies rapidly with azimuth. The azimuth dependence can be quantified by means of beam forming (Yao et al., 2009). Similar in concept to other differential methods, if ambient noise sources generate both Love and Rayleigh waves, radial anisotropy inferred from the discrepancy between Love and Rayleigh wave Green's functions is less sensitive to the actual distribution of ambient noise energy. If Love and Rayleigh waves are excited by different source distributions, however, careful analysis of phase velocity bias for both Love and Rayleigh dispersion is necessary to constrain radial anisotropy.

We note that our plane-wave modeling approach assumes a lossless medium; that is, it ignores the effect of attenuation on the amplitude of waves. We emphasize, however, that even without attenuation there will be an apparent decay of amplitude of EGFs due to the fact that the width of the first Fresnel zone for constructive interference decreases as the increase of inter-station distance (see also Harmon et al., 2007). Recent studies (Prieto & Beroza, 2008; Prieto, 2009) show that it is possible to extract anelastic (attenuation) structure from ambient noise interferometry, provided that the noise energy distribution is isotropic. Since the noise energy distribution is generally not isotropic, our inversion approach for estimating the ambient noise energy distribution could help interferometric quantification of medium attenuation.

5.7 Summary

We have presented a method for estimating the distribution of ambient noise energy and the bias in phase velocities from ambient noise interferometry under the assumption of plane wave propagation. Through an iterative approach we correct the phase velocity

measurements from EGFs and estimate the azimuthal anisotropy of surface wave propagation with more confidence. Our method can be applied to small-scale arrays with good spatial and azimuthal path coverage and which are located far from the dominant noise sources. With real application to SE Tibet, we find the azimuthal variation of ambient noise energy has very small effect on the isotropic and azimuthally anisotropic phase velocities in SE Tibet.

Acknowledgments

We thank Jean-Paul Montagner at IPG Paris for providing the code for inversion of surface wave azimuthal anisotropy, Jeannot Trampert, the editor of GJI, and an anonymous reviewer for their constructive comments, which helped us improve the manuscript. We also thank Victor Tsai at Harvard University for helpful discussions.

References

Bensen, G.D., Ritzwoller, M.H., Barmin, M.P., Levshin, A.L., Lin, F., Moschetti, M.P., Shapiro, N.M. & Yang, Y., 2007. Processing seismic ambient noise data to obtain reliable broad-band surface wave dispersion measurements, *Geophys. J. Int.*, 169, 1239-1260.

Campillo, M. and A. Paul, 2003. Long-range correlations in the diffuse seismic coda, *Science*, 299, 547-549.

Cho, K.H., Herrmann, R.B., Ammon, C.J., and Lee, K., 2007. Imaging the upper crust of the Korean Peninsula by surface-wave tomography, *Bull. Seismol. Soc. Am.*, 97, 198-207.

Dahlen, F. A. and Tromp, J., 1998. Theoretical Global Seismology, Princeton Univ. Press, Princeton, New Jersey.

Harmon, N., Forsyth, D., and Webb, S., 2007. Using ambient noise to determine short-period phase velocities and shallow shear velocities in young oceanic lithosphere, *Bull. Seismol. Soc. Am.*, 97, 2009-2023.

Kang, T.S. & Shin, J.S., 2006. Surface-wave tomography from ambient seismic noise of accelerograph networks in southern Korea, *Geophys. Res. Lett.*, 33, L17303.

Liang, C. & Langston, C.A., 2008. Ambient seismic noise tomography and structure of east North America, *J. Geophys.Res.*, 113, B3, B03309.

Lin, F.-C., Ritzwoller, M.H., Townend, J., Bannister, S., and Savage, M.K., 2007 Ambient noise Rayleigh wave tomography of New Zealand, *Geophys. J. Int.*, 170 (2), 649–666. doi:10.1111/j.1365-246X.2007.03414.x

Lin, F.-C., M.P. Moschetti, and M.H. Ritzwoller, 2008. Surface wave tomography of the western United States from ambient seismic noise: Rayleigh and Love wave phase velocity maps, *Geophys. J. Int.*, doi:10.1111/j1365-246X.2008.03720.x.

Lobkis, O. I. and R. L., Weaver, 2001. On the emergence of the Green's function in the correlations of a diffusive field, *J. Acoust. Soc. Am.*, 110, 3011-3017.

Malcolm, A.E., Scales, J.A., & van Tiggelen, B.A., 2004. Extracting the Green's function from diffuse, equipartitioned waves, *Phys. Rev. E*, 70, 015601.

Montagner, J.-P, 1986. Regional three-dimensional structures using long-period surface waves. *Annales Geophysicae*, 4, 283-294.

Moschetti, M.P., Ritzwoller, M.H., & Shapiro, N.M., 2007. Surface wave tomography of western United States from ambient seismic noise: Rayleigh wave group velocity maps, *Geochem., Geophys., Geosys.*, 8, Q080101, doi:10.1029/2007GC001655.

Nakahara, H., 2006. A systematic study of theoretical relations between spatial correlation and Green's function in one-, two- and three-dimensional random scalar wavefields, *Geophys. J. Int.*, 167, 1097-1105.

Prieto, G. A. and Beroza, G. C., 2008. Earthquake ground motion prediction using the ambient seismic field, *Geophys. Res. Lett.,* 35, L14304, doi:10.1029/2008GL034428.

Prieto, G.A., Lawrence, J.F., Beroza, G.C., 2009. Anelastic Earth structure from the coherence of the ambient seismic field, *J. Geophys. Res.*, in press.

Rhie, J. & Romanowicz, B., 2006. A study of the relation between ocean storms and the Earth's hum, *Geochem. Geophys. Geosyst.*, 7(10), doi:10.1029/2006GC001274

Roux, P., Sabra, K.G., Kuperman, W. A., and Roux, A., 2005. Ambient noise cross correlation in free space: Theoretical approach, 2005, *J. Acoust. Soc. Am.*, 117, 79-84.

Sabra, K.G., Gerstoft, P., Roux, P. & Kuperman, W.A., 2005. Surface wave tomography from microseisms in Southern California, *Geophys. Res. Lett.,* 32, L14311, doi:10.1029/2005GL023155.

Shapiro, N. M. and Campillo, M., 2004. Emergence of broadband Rayleigh waves from correlations of the ambient seismic noise, *Geophys. Res. Lett*, 31, L07614, doi:10.1029/2004GL019491.

Shapiro, N. M., Campillo, M., Stehly, L., and Ritzwoller, M. H., 2005. High-resolution surface wave tomography from ambient seismic noise, *Science*, 307, 1615-1618.

Simons, F.J., Van der Hilst, R.D., Montagner, J.-P., and Zielhuis, A., 2002. Multimode Rayleigh wave inversion for heterogeneity and azimuthal anisotropy of the Australian upper mantle, *Geophys. J. Int.*. 151, 738-755.

Smith, M.L. & Dahlen, F.A., 1973. Azimuthal dependence of Love and Rayleigh-wave propagation in a slightly anisotropic medium, *J. Geophys. Res.*, 78, 3321-3333.

Snieder, R., 2004. Extracting the Green's function from the correlation of coda waves: A derivation based on stationary phase, *Phys. Rev. E*, 69, 046610.

Stehly, L., Campillo, M., & Shapiro, N.M., 2006. A study of the seismic noise from its long range correlation properties, *J. Geophys. Res.*, 111, B10306, doi:10.1029/2005JB00237.

Tsai, V.C., 2009. On establishing the accuracy of noise tomography travel-time measurements in a realistic medium, *Geophys. J. Int.*, in press

Wapenaar, K., 2004. Retrieving the elastodynamic Green's function of an arbitrary inhomogeneous medium by cross correlation, *Phys. Rev. Lett.*, 93, 254301.

Wapenaar, K., Slob, E., & Snieder, R., 2006. Unified Green's function retrieval by cross correlation, *Phys. Rev. Lett.*, 97, doi:10.1103/PhysRevLett.97.234301.

Weaver, R. L. and O. I., Lobkis, 2004. Diffuse fields in open systems and the emergence of the Green's function. *J. Acoust. Soc. Am.*, 116, 2731-2734

Yang, Y., Ritzwoller, M.H., Levshin, A.L., & Shapiro, N.M., 2007. Ambient noise Rayleigh wave tomography across Europe, *Geophys. J. Int.*, 168, 259-274.

Yang, Y., Li, A., & Ritzwoller, M.H., 2008. Crustal and uppermost mantle structure in southern Africa revealed from ambient noise and teleseismic tomography, *Geophys. J. Int.*, 174, 235-248, 10.1111/j.1365-246X.2008.03779.x.

Yang, Y. and Ritzwoller, M.H., 2008a. Characteristics of ambient seismic noise as a source for surface wave tomography, *Geochem. Geophys. Geosyst.*, 9, doi10.1029/2007GC001814.

Yang, Y. and Ritzwoller, M.H., 2008b. Teleseismic surface wave tomography in the western US using the Transportable Array component of USArray, *Geophys. Res. Lett.*, 35, L04308.

Yao, H., Van der Hilst, R.D., & de Hoop, M.V., 2006. Surface-wave array tomography in SE Tibet from ambient seismic noise and two-station analysis – I. phase velocity maps, *Geophys. J. Int.*, 166, 732-744.

Yao, H., Beghein C., and van der Hilst, R.D., 2008. Surface wave array tomography in SE Tibet from ambient seismic noise and two-station analysis - II. Crustal and upper-mantle structure, *Geophys. J. Int.*, 173, 205-219.

Yao, H., Campman, X., de Hoop, M.V., and Van der Hilst, R.D., 2009. Construction of empirical Green's function from direct waves, coda waves, and ambient noise in SE Tibet, *Phys. Earth Planet. Inter.*, under review.

Zheng, S., X. Sun, X. Song, Y. Yang, and M. H. Ritzwoller, 2008. Surface wave tomography of China from ambient seismic noise correlation, *Geochem. Geophys. Geosyst.*, 9, Q0502, doi:10.1029/2008GC001981.

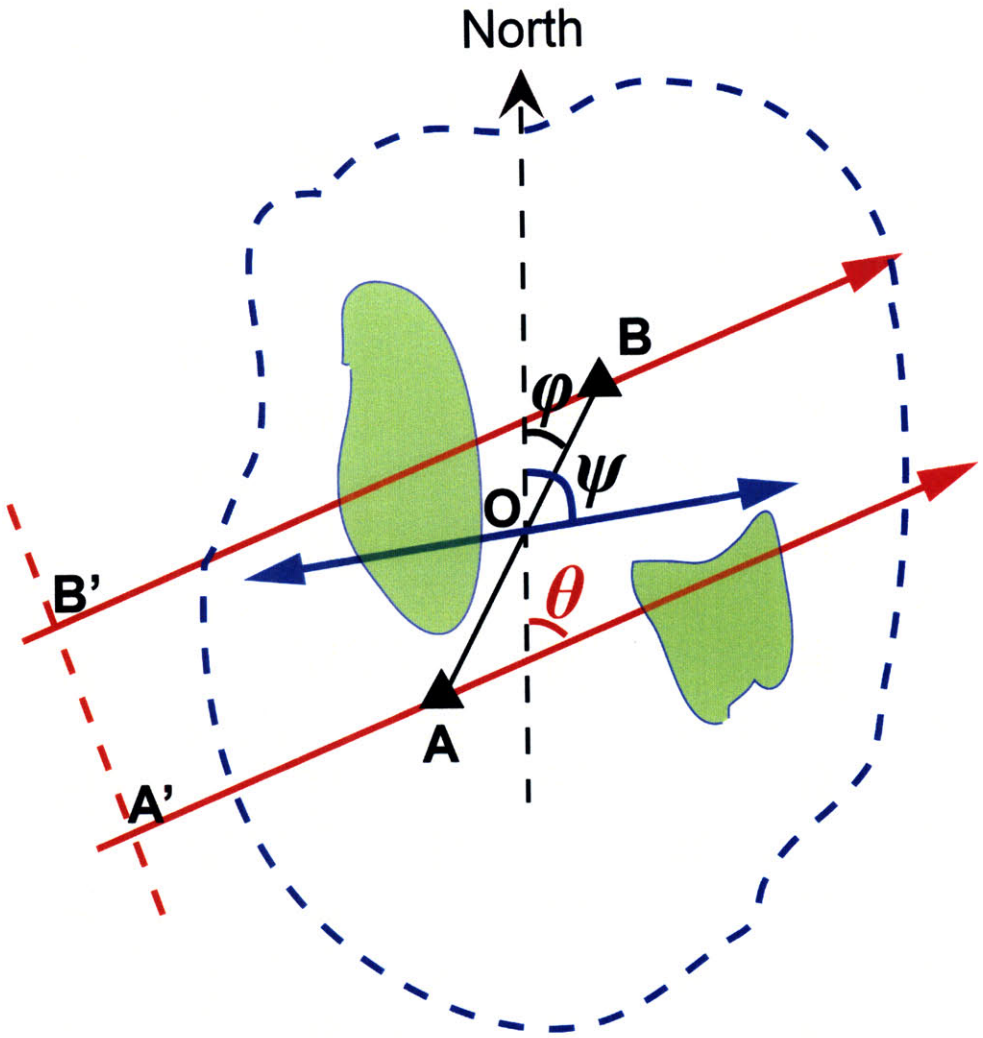

Figure 5-1. Geometry of the plane-wave modeling. The incoming plane wave with azimuth angle θ is shown as the red lines with arrow. Red dashed line shows the wave front of the plane wave which is perpendicular to the ray paths. The two stations are located at A and B, shown as the black triangles, with the central point at O and azimuth angle φ (from A to B). The green patches are the regions with velocity anomalies. The fast direction with the azimuth angle ψ of the azimuthal anisotropy at point O is shown as the blue bar with arrows at both ends.

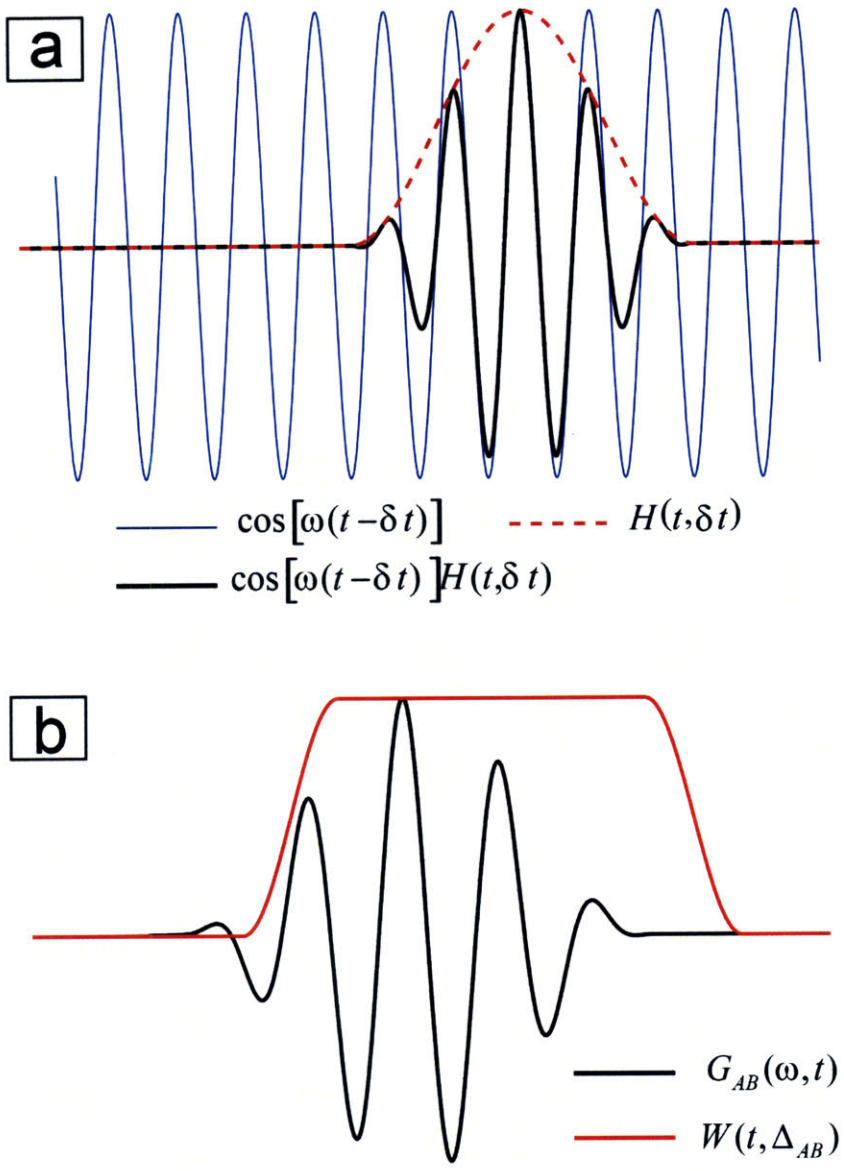

Figure 5-2. (a) Taper function $H(t,\delta t)$, shown as the red dashed trace, as given by equation (5-2). The blue trace show the single sinusoid cross correlation function $\cos[\omega(t-\delta t)]$ of incoming plane wave and the black trace gives the product of $H(t,\delta t)$ and $\cos[\omega(t-\delta t)]$. (b) Surface wave window function $W(t,\Delta_{AB})$, shown as the red trace, as given by equation (5-7). The black trace shows the theoretical Green's function given by equation (5-6).

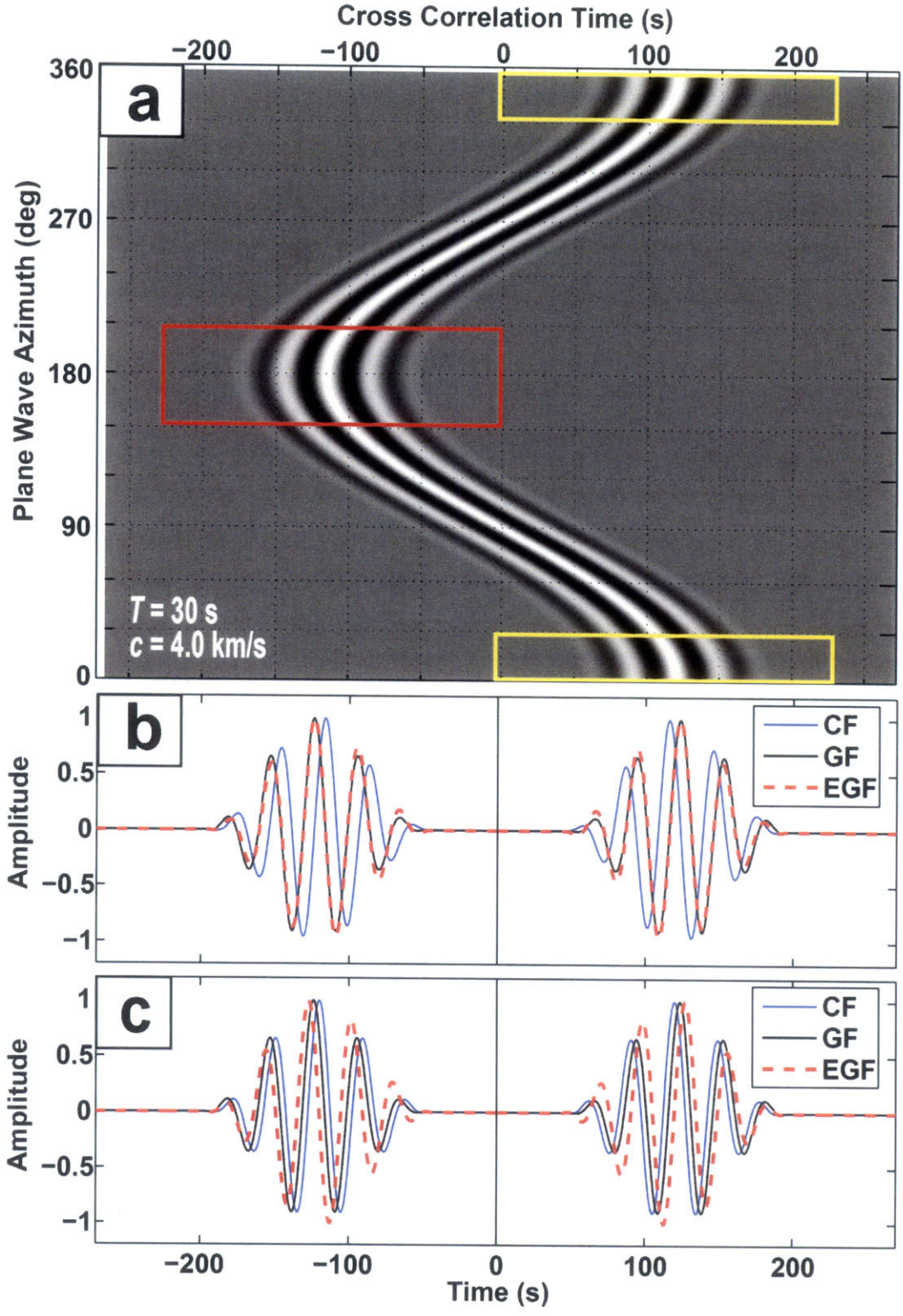

Figure 5-3. Illustration of the construction of Green's function from 30 s period plane wave interferometry in a homogeneous and isotropic medium with phase velocity c = 4

km/s at period 30 s. (a) Cross-correlagram for a south-north station pair apart from 480 km with isotropic plane wave energy distribution. Each horizontal line in the cross-correlagram gives the individual cross correlation function, given by the integrand of equation (1). The white color represents the positive values while the black color shows for negative values. The red box shows the first Fresnel zone of plane wave interferometry, given by equation (5-10), for the construction of the anti-causal part Green's function, while the yellow boxes shows that for the causal part Green's function. (b) Comparison of the cross correlation function (CF), empirical Green's function (EGF), and the theoretical Green's function (GF) for isotropic noise energy distribution with cross-correlagram shown in (a). CF (blue trace) is the stack of all individual cross correlation functions, i.e., vertical directional stack of the cross-correlagram in (a). EGF (red dashed trace) has $\pi/2$ phase shift to CF but is almost identical to the theoretical GF (black trace). (c) Comparison of the CF, EGF, and GF when plane wave energy is 1 only at azimuth angle $\theta = 0^{\circ}$ and 180° but zero elsewhere. In this case, the EGF has $\pi/4$ phase shift away from zero time compared to the GF.

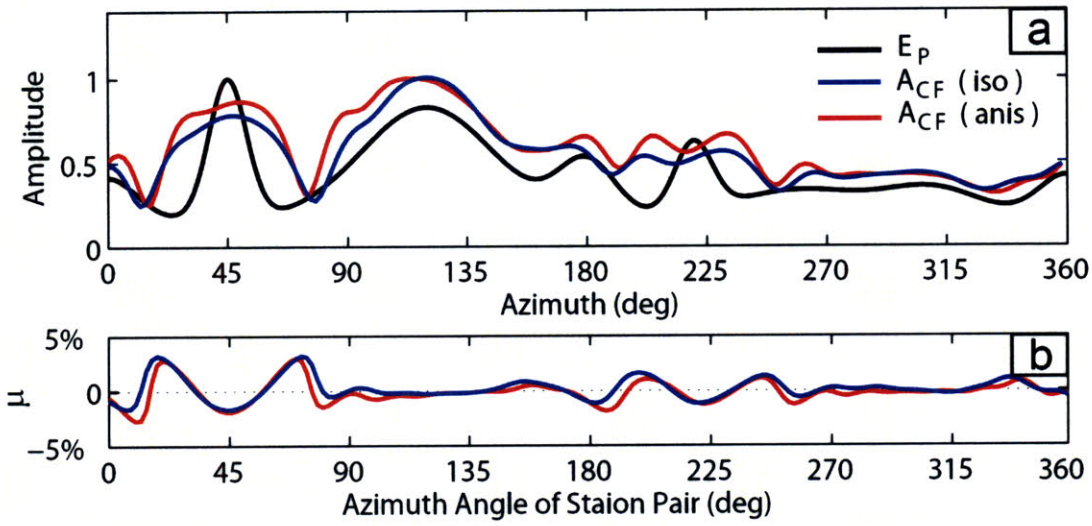

Figure 5-4. Bias of phase velocity measurements from plane wave interferometry in case of non-isotropic plane wave energy distribution in homogeneous medium with or without azimuthal anisotropy: (a) azimuthal distribution of ambient noise energy E_P (shown as the black curve) and normalized surface wave amplitudes A_{CF} of the cross correlation functions (blue or red curve); and (b) relative phase velocity bias (μ) between the EGF and GF as given by equation (5-9). The blue curve represents for the bias for a homogeneous and isotropic medium and the red curve for a homogeneous medium with 5% azimuthal anisotropy with fast direction ψ= 45°. The geometry of the station pair is described in Section 5.3.

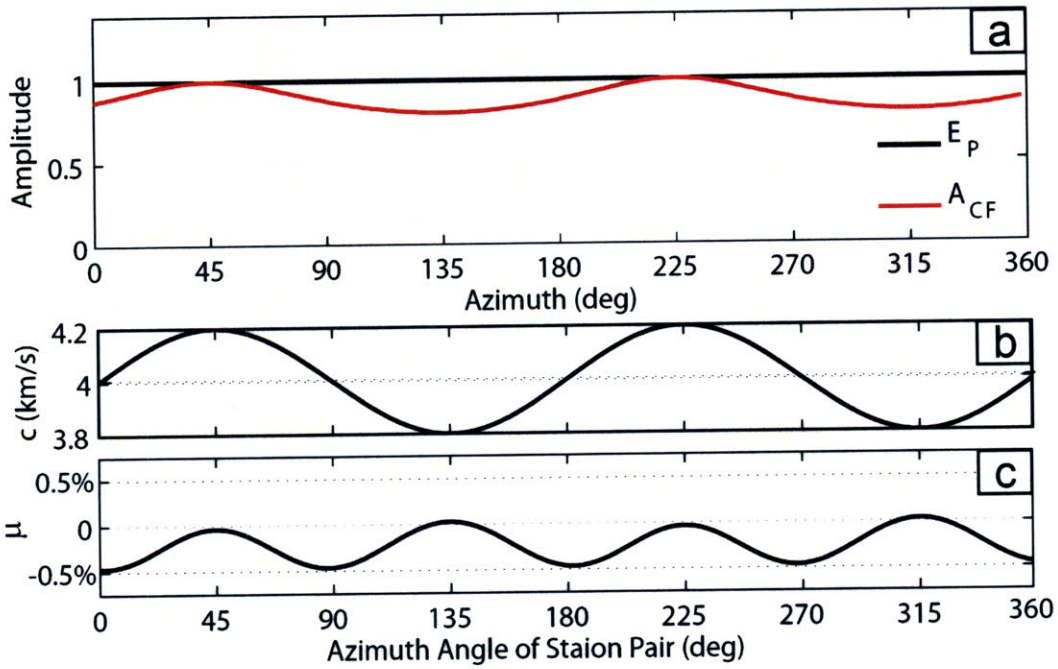

Figure 5-5. Relative phase velocity bias (μ) (black line in (c)) for an isotropic ambient noise energy distribution (black line in (a)) in a homogeneous medium with 5% azimuthal anisotropy with fast direction ψ= 45°. In (a) the red line shows the normalized surface wave amplitudes A_{CF} of the cross correlation functions. In (b) the black line shows the interstation phase velocity with different azimuth angles.

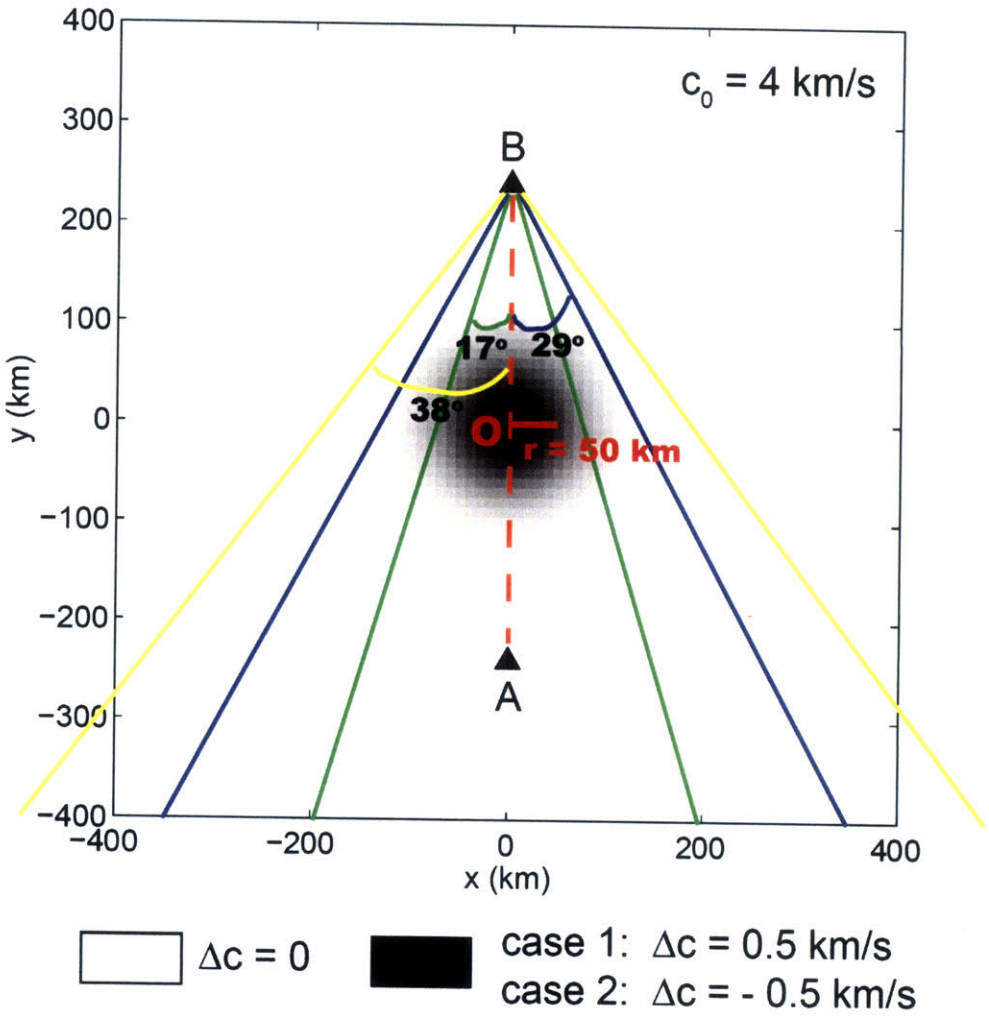

Figure 5-6. Geometry of plane wave interferometry for a heterogeneous and isotropic medium (Section 5.3.3.1) with isotropic ambient noise energy distribution. The velocity distribution is $c(x, y) = c_0 + \Delta c \cdot \exp\{-0.5(x^2 + y^2)/r^2\}$, with the background velocity c_0 = 4 km/s shown as the white region and the 2-D Gaussian shape anomaly centered at O(0, 0) shown as the black-shaded region with the horizontal scale r. The largest anomaly, Δc = 0.5 km/s for case 1 or Δc = -0.5 km/s for case 2, is shown with black. The two stations at A (0, -240) and B (0, 240) are shown as the black triangles. For an anomaly with the horizontal scale r = 50 km and Δc = 0.5 km/s, the half width of the first Fresnel zone for interferometry (see equation (5-11)) with respect to the two-station path (from A to B) is about 17°, 29°, and 38° for T = 10 s, 30 s, and 50 s, as bounded with the green, blue, and yellow lines, respectively.

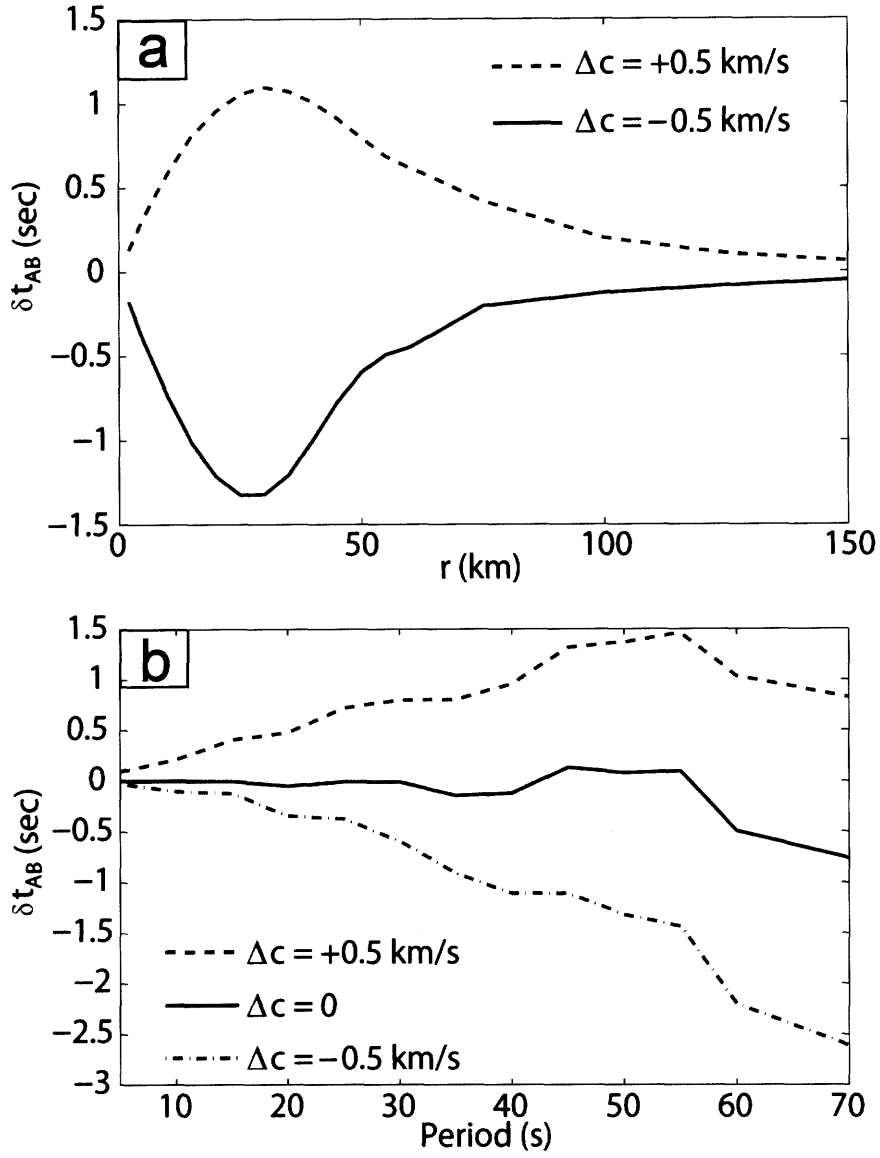

Figure 5-7. The phase travel time difference δt_{AB} between the EGF and the theoretical GF for a heterogeneous and isotropic model (Figure 5-7) with isotropic ambient noise energy distribution. In (a), we show δt_{AB} as a function of the horizontal scale of the anomaly (r) with the dashed line for a positive anomaly (Δc = 0.5 km/s, case 1 in Figure 5-7) and solid line for a negative anomaly (Δc = -0.5 km/s, case 2 in Figure 5-7). In (b), we fix the horizontal scale of the anomaly r = 50 km and change the period of incoming plane waves. The dashed, solid, and dash-dotted lines show the results for a positive anomaly (Δc = 0.5 km/s), no anomaly (Δc = 0), and a negative anomaly (Δc = -0.5 km/s), respectively.

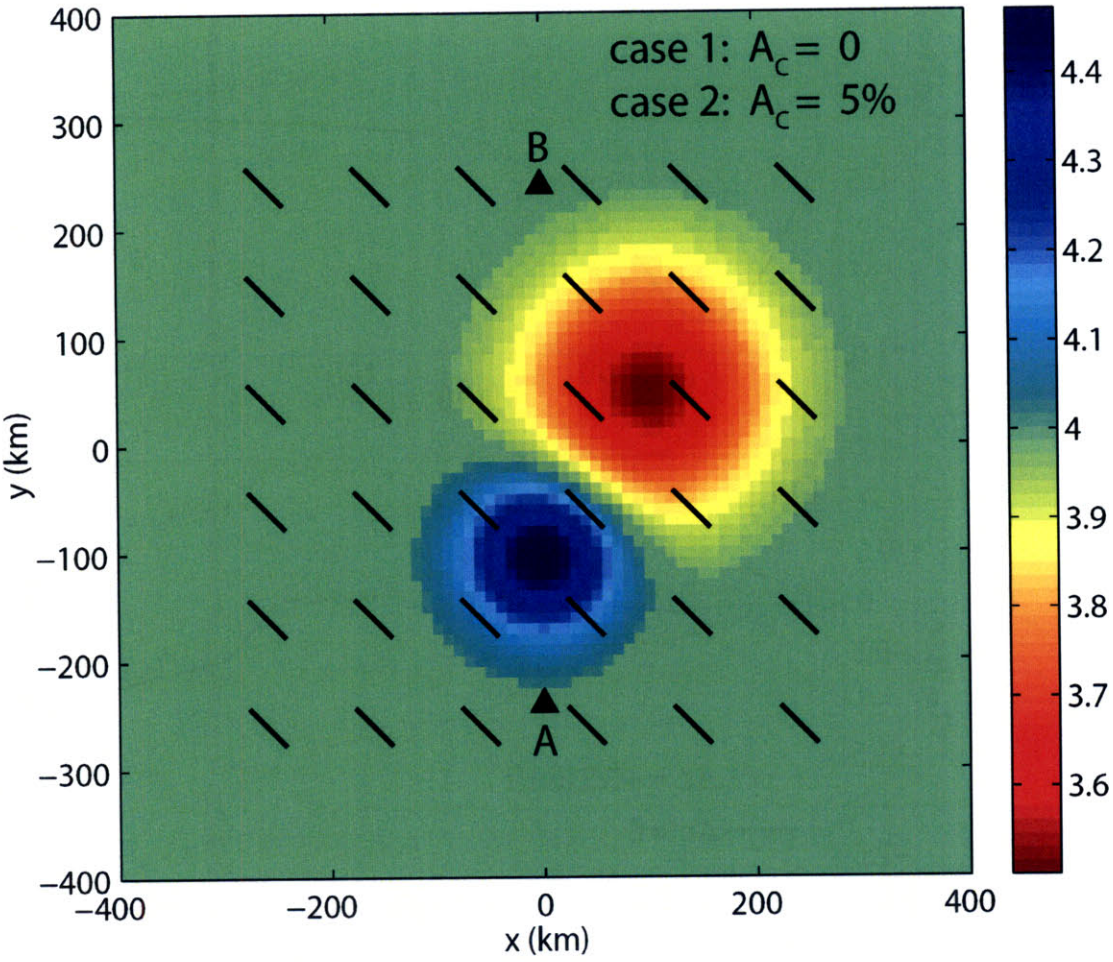

Figure 5-8. Heterogeneous model (with or without azimuthal anisotropy) for investigating the Green's function retrieval. The velocity model is $c(x, y) = c_0(x, y)\{1 + A_c \cos 2(\theta - \psi)\}$. The color bar shows the value of the isotropic part of the velocity $c_0(x, y)$ (km/s). The short bars, all with azimuth angle ψ=135° showing the fast propagation direction, give the azimuthally anisotropic part of the velocity with amplitude A_c = 0 for case 1 (no azimuthal anisotropy) and A_c = 5% for case 2 (with azimuthal anisotropy).

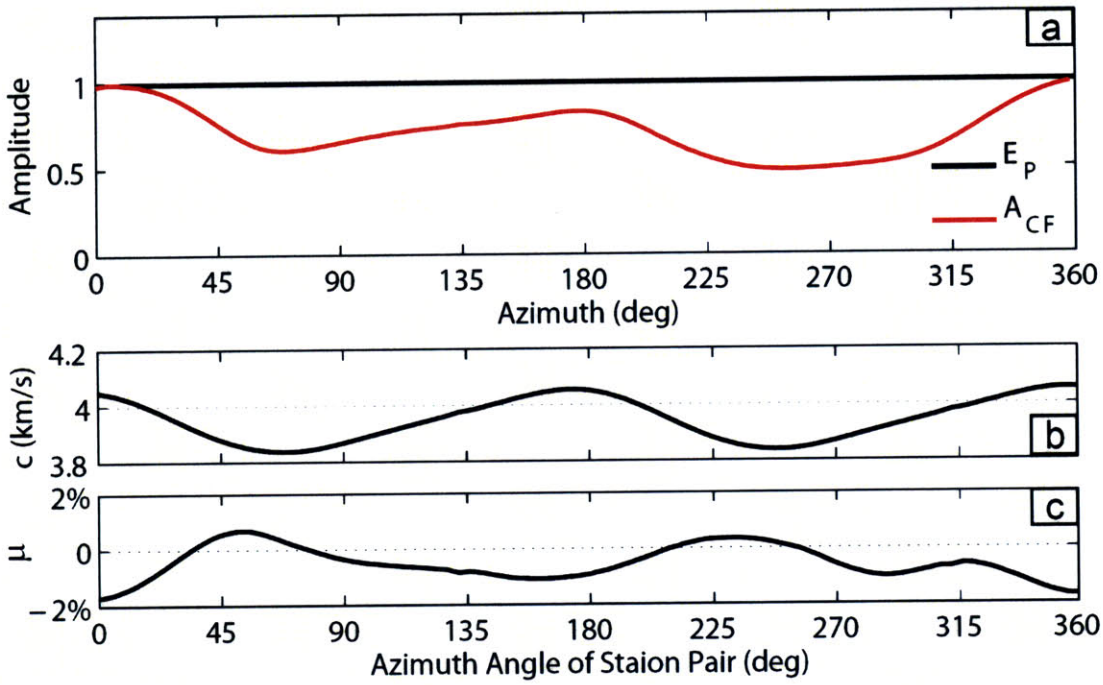

Figure 5-9. Same as in Figure 5-5 with isotropic ambient noise energy distribution in the heterogeneous medium without azimuthal anisotropy (case 1 of the model in Figure 5-8).

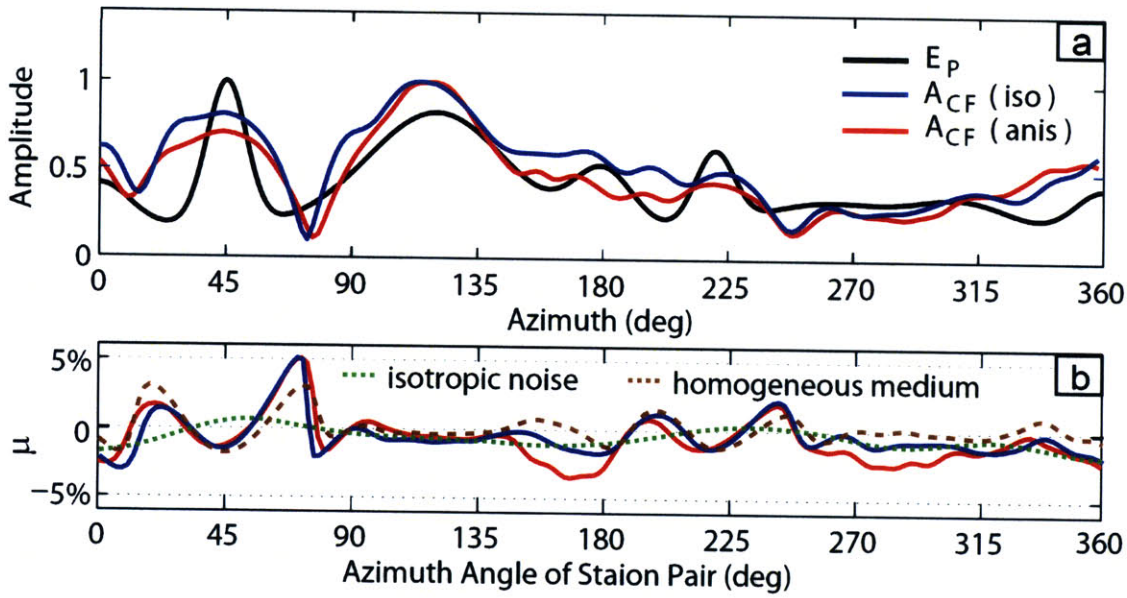

Figure 5-10. Same as in Figure 5-4 with uneven ambient noise energy distribution in the heterogeneous medium as shown in Figure 5-8 with blue curves showing the results without azimuthal anisotropy (case 1 in Figure 5-8) and red curves showing the results with 5% azimuthal anisotropy (case 2 in Figure 5-8). In (b) the green dashed line shows the relative phase velocity bias with isotropic ambient noise energy distribution in the heterogeneous medium (case 1 in Figure 5-8), same as the black line in Figure 5-9c. The brown dashed line shows the relative phase velocity bias with uneven ambient noise energy distribution (black curve in (a)) in the homogeneous and isotropic medium with velocity 4 km/s.

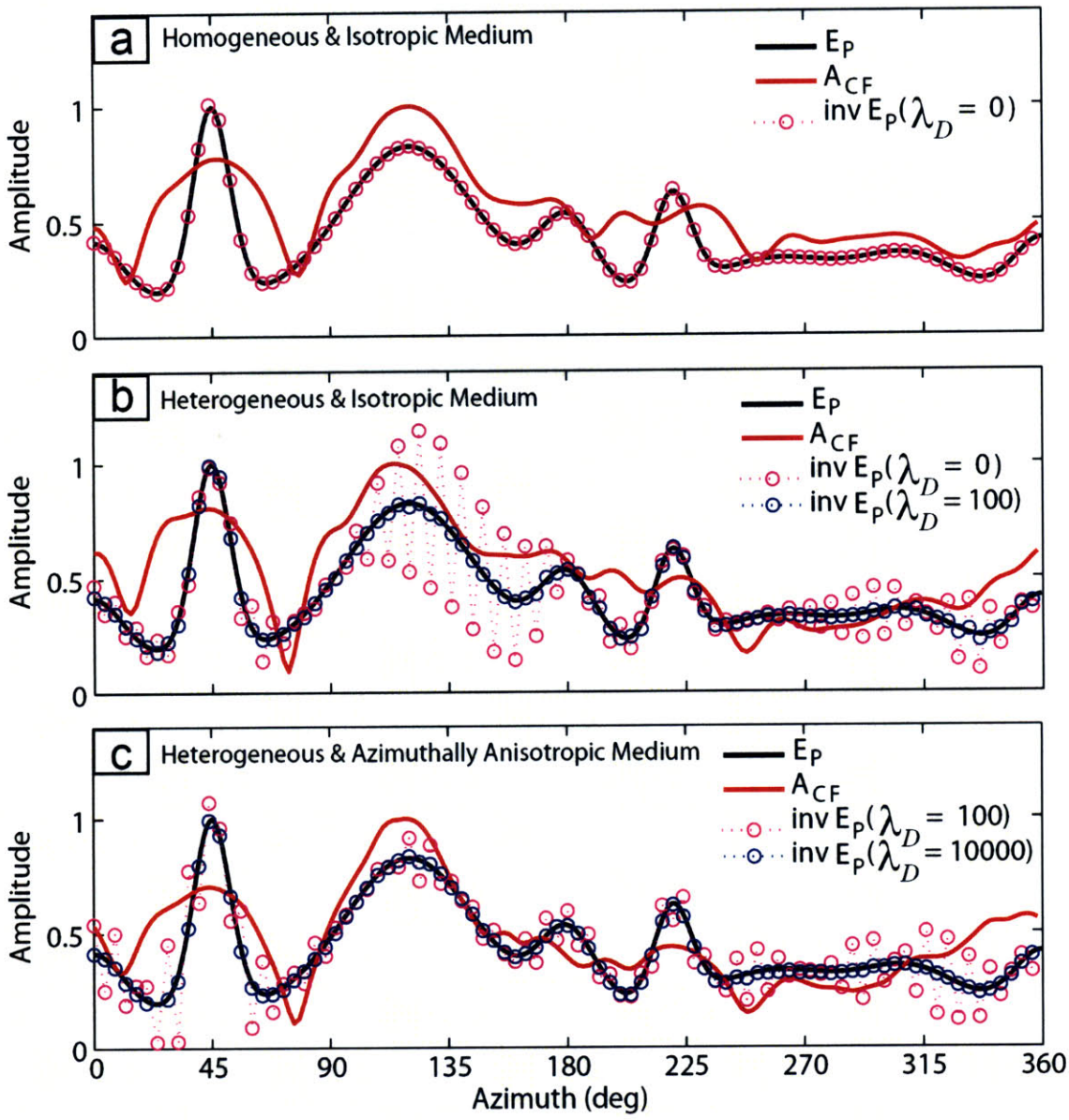

Figure 5-11. Recovery of the azimuthal distribution of ambient noise energy (magenta or blue open circles) from the cross correlation functions as described in Section 5.4 for (a) the homogeneous and isotropic medium (Section 5.3.1.1) without adding damping (λ_D = 0), (b) the heterogeneous medium without azimuthal anisotropy (case 1 in Figure 5-8) with the damping values λ_D = 0 (for the magenta circles) and λ_D = 100 (for the blue circles), and (c) the heterogeneous medium with 5% azimuthal anisotropy (case 2 in Figure 5-8) with the damping values λ_D =100 (for the magenta circles) and λ_D = 10000 (for the blue circles). The input ambient noise energy E_P is shown as the black line. The red line shows the amplitude of the cross correlation functions.

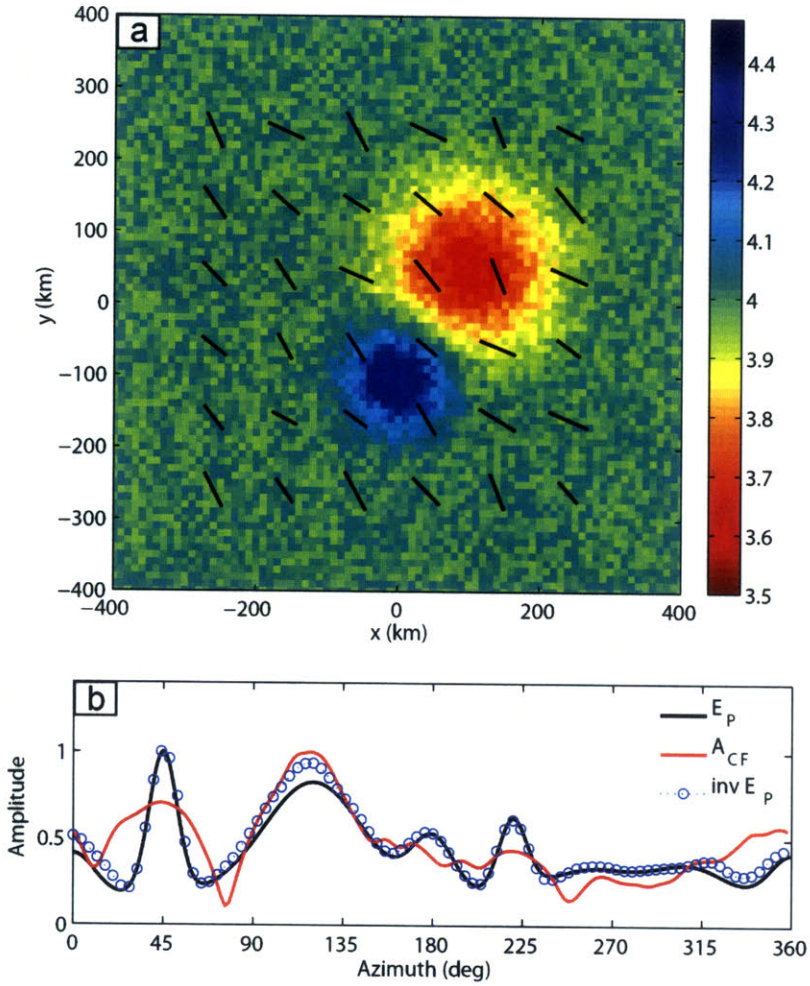

Figure 5-12. (a) A modified velocity model for the modeling in the inversion using equation (5-21). The original velocity model is shown as the case 2 of the model in Figure 5-8, which is used for the calculation of the cross correlation functions from equation (5-1). The amplitude of the velocity anomaly (isotropic part) in the modified model is 75% of that in the original velocity model. And a maximum of 0.05 km/s random noise is added to the isotropic part of the modified velocity model. For the azimuthal anisotropic part, we add a maximum of 25° random noise to the azimuth of the fast propagation direction and a maximum of 2% random noise to the amplitude of azimuthal anisotropy (originally 5%). (b) Recovery of the ambient noise energy (blue open circles) when using the modified velocity model (a) in the inversion but the original velocity model for calculating the cross correlation functions. In (b), the input ambient noise energy is shown as the black curve and the red curve shows the amplitude of the cross correlation functions.

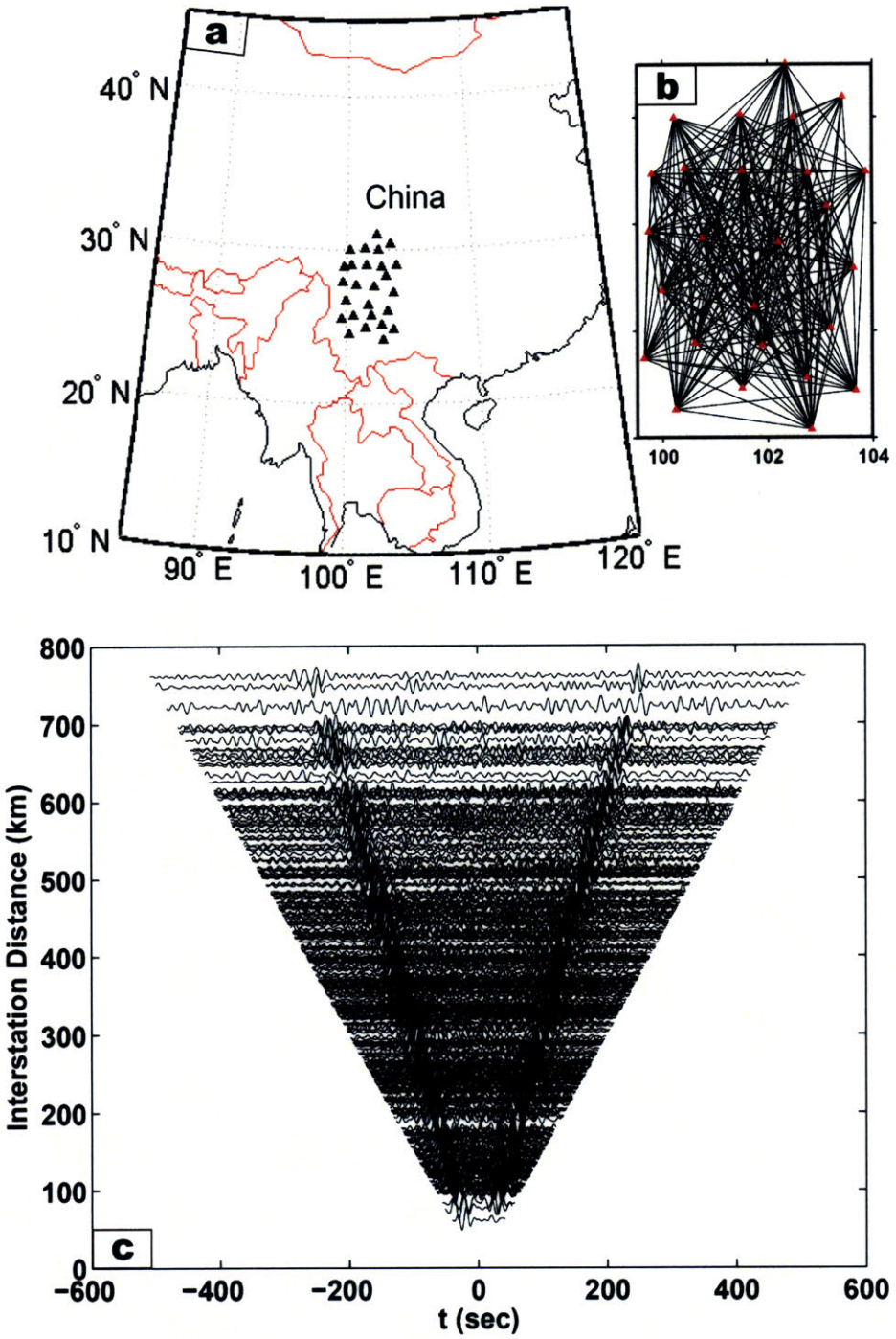

Figure 5-13. (a) Location of the MIT array in SE Tibet, China. (b) Ray path coverage for interstation phase velocity measurements at T = 25 s from the EGFs retrieved from one month data (January 2004) of the MIT array. (c) All interstation cross correlation functions in the period band 10 – 30 s from one-bit cross correlation of one month MIT array data (January 2004). The maximum amplitude of each trace is normalized.

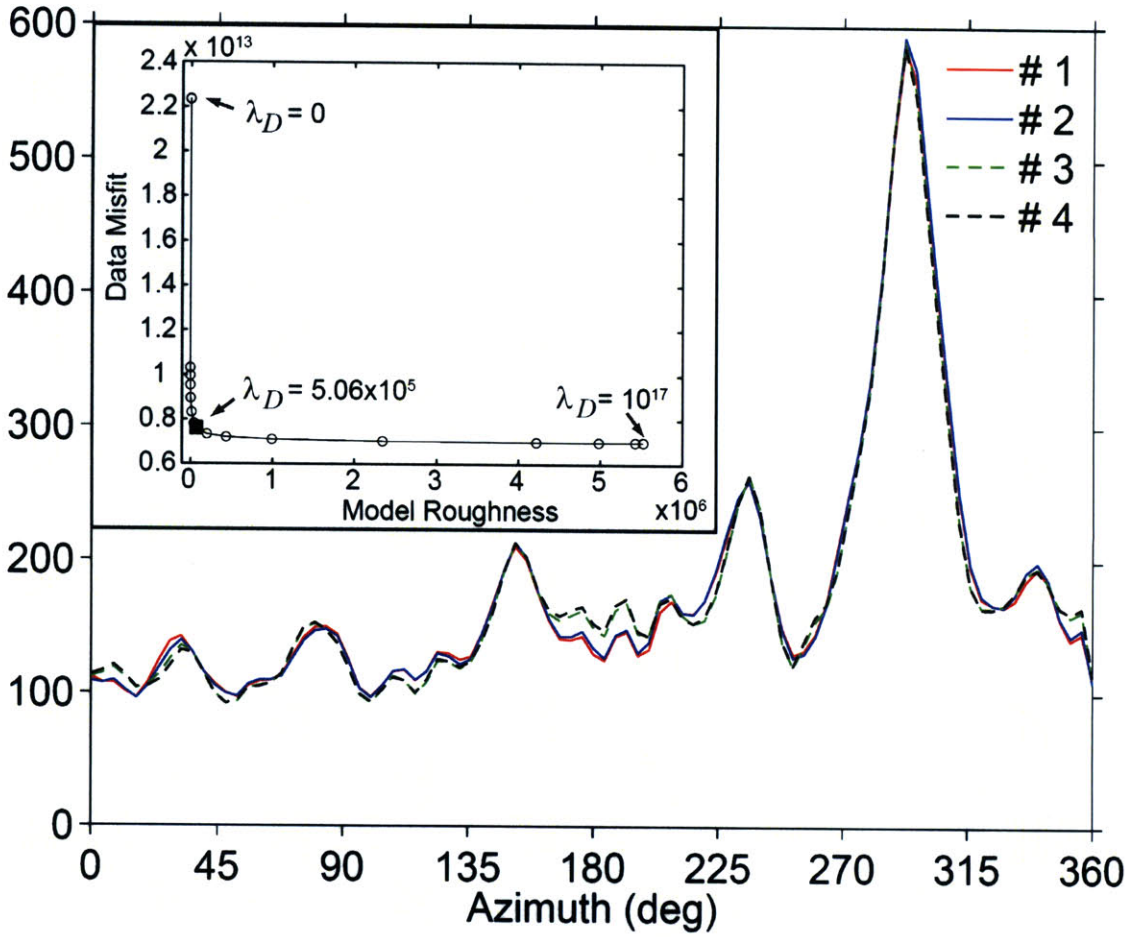

Figure 5-14. The inversion results of ambient noise energy distribution at T = 25 s with respect to the MIT array using plane-wave modeling and an iterative approach. The results for the first four iterations are shown as the red, blue, green dashed, and black dashed lines, respectively. The first two iterations are based on the isotropic phase velocity maps and the 3rd and 4th iterations use the azimuthally anisotropic phase velocity maps. In the upper left inset figure, we show the tradeoff curve between the data misfit and model roughness (defined in Section 5.2). The open circles show the trial damping values in the inversion and the black solid square shows the final choice of damping value for the inversion of ambient noise energy. Note that the horizontal axis shows the azimuth angle of the direction of the incoming noise energy propagating into the array. The maximum noise energy appears at about 300°, which is about to the east of the array.

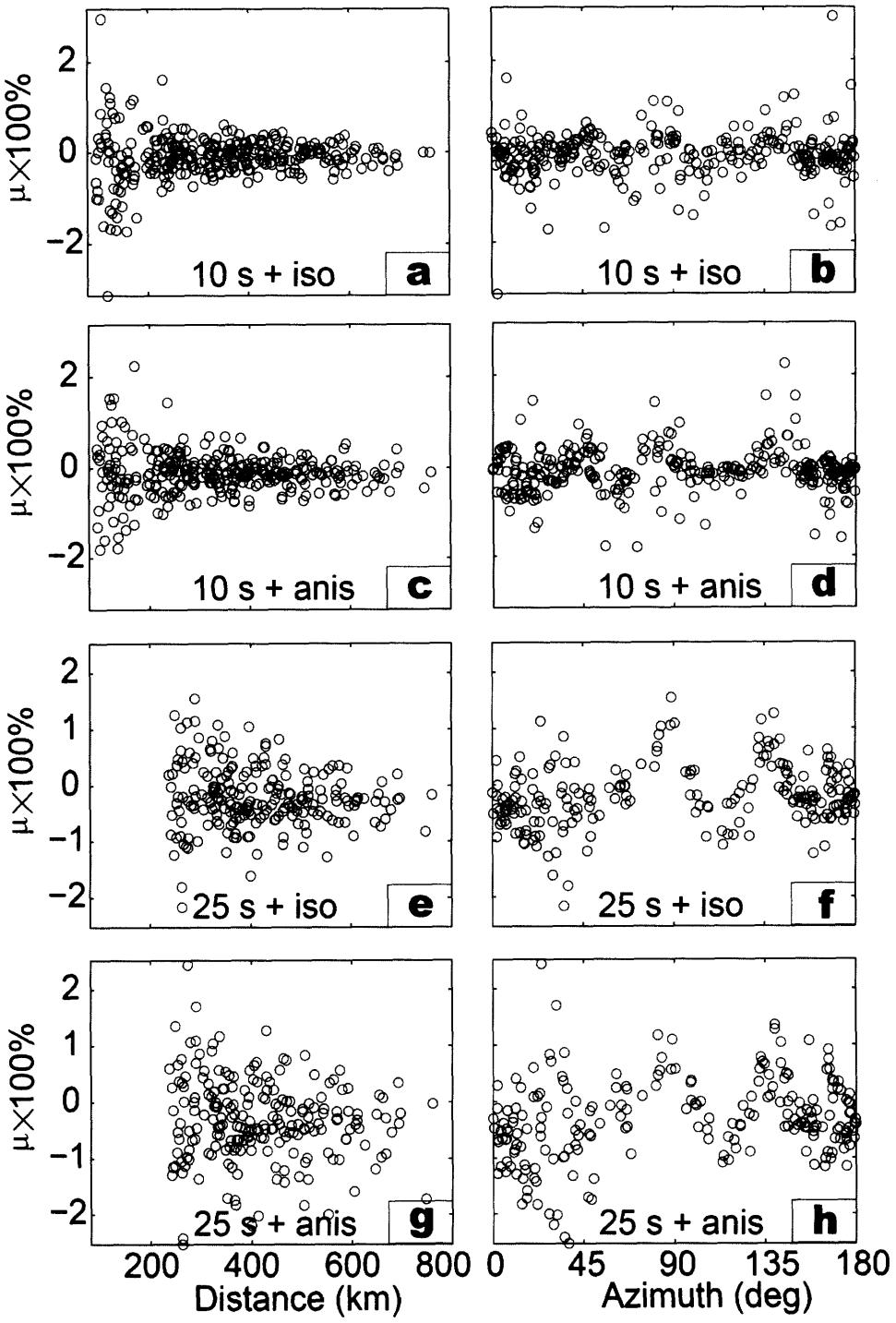

Figure 5-15. Relative bias (μ) of phase velocities between the EGF and GF v.s. interstation distance (left column) or azimuth (right column) for the periods T = 10 s (a-d) and T = 25 s (e-h) using either isotropic phase velocity maps (a, b, e, f) or azimuthally anisotropic phase velocity maps (c, d, g, h) for the forward (plane-wave) modeling.

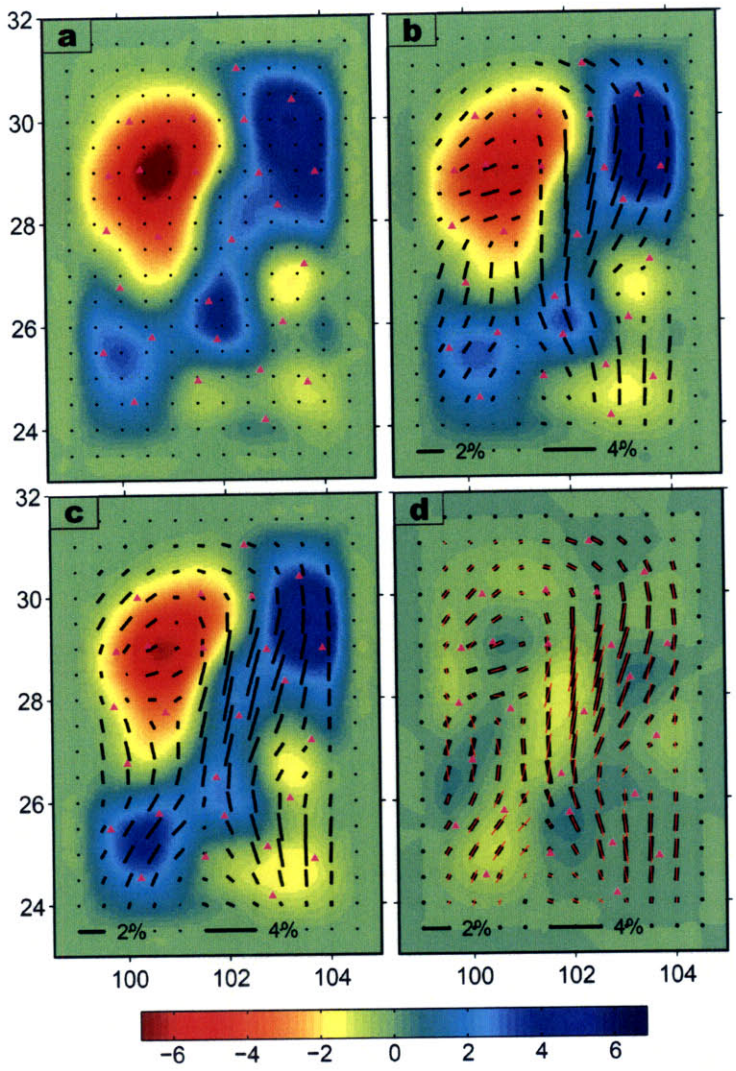

Figure 5-16. Distribution of 2-D phase velocity maps (in per cent with respect to the average value) at T = 25 s using (a) uncorrected phase velocity measurements without azimuthal anisotropy inversion, (b) uncorrected phase velocity measurements with azimuthal anisotropy inversion, and (c) corrected phase velocity measurements with azimuthal anisotropy inversion as described in Section 5.2. The background image of (d) shows the difference (in per cent) of phase velocities between the isotropic part of phase velocity maps of (b) and (c). On (d) the thick black bars and red thin bars show the comparison of azimuthal anisotropy from (b) and (c), respectively. The color bar gives the magnitude of perturbation (in per cent) of isotropic phase velocities and the two horizontal bars at the bottom of (b-d) gives the magnitude of azimuthal anisotropy.

Chapter 6

Structure and deformation of the crust and upper mantle beneath SE Tibet from surface-wave array tomography[5]

Abstract

The southeastern part of Tibetan Plateau and its margin in SW China have been subjected to several driving forces throughout its geological history. The understanding of dynamic evolution and deformation pattern in SE Tibet requires insight into the isotropic and anisotropic structure of the crust and upper mantle. In this study, with data from 75 broad band stations, we use surface-wave array tomography from ambient noise interferometry and teleseismic surface waves to investigate the 3-D shear velocity structure and azimuthal anisotropy in the crust and upper mantle in SE Tibet around the eastern Himalayan syntaxis. The (short-period) surface wave data resolve (1) widespread inter-connected low velocity (and, presumably, mechanically weak) zones in the middle and lower crust and (2) variations with depth of the pattern of azimuthal anisotropy (and, presumably, deformation), which is inconsistent with simple vertically coherent deformation in the crust and upper mantle. We compare the azimuthal anisotropy from surface wave tomography with inferences from GPS measurements of (present day) surface motion and with results of shear wave splitting. Collectively, our findings are most consistent with a large level of decoupling between deformation in upper crust and upper mantle beneath SE Tibet. This corroborates models of crustal channel flow, but the major faults and upper mantle processes may influence and, perhaps, locally obstruct such flow.

[5] In preparation as: Yao H., van der Hilst, R.D., Montagner, J.-P., 2009. Structure and deformation of the crust and upper mantle beneath SE Tibet from surface-wave array tomography, to be submitted to *J. Geophys. Res.*

6.1 Introduction

The uplift and development of the Tibetan Plateau produced by India-Eurasia plate convergence since early Cenozoic time (Molnar et al., 1993, and ref. therein) have been the focus of much geological and geophysical research since the prime work by Argand some 90 years ago (Argand, 1924); for recent reviews, see Molnar et al. (1993) and Royden et al. (2008) and references therein. However, the deformation mechanisms of the plateau are still widely debated among various hypotheses. The geological evolution of the southeastern Tibetan Plateau is controlled by the northward subduction of the Indian lithosphere along the Indus-Tsangpo suture (ITS) west of the eastern Himalayan Syntaxis (EHS) (Yin & Harrison, 2000) and the eastward subduction of Burmese microplate along the Burma arc south of the EHS (Ni et al., 1989 ; Li et al., 2008) (Figure 6-1a). As a consequence, the crust in between EHS and Sichuan basin (a mechanically rigid part of the Yangtze or South China craton) has undergone clockwise deformation around the EHS (Zhang et al., 2004). This so-called "indenter corner" also represents the southern extremity of the trans-China seismic belt. Investigating the lithosphere in SE Tibet can help understand the processes involved in plateau building and (eastward) expansion as well as the seismotectonics and seismicity of this region.

Geological studies have revealed that the relatively recent uplift (<15 Ma) of the eastern part of the Tibetan plateau occurred without substantial crustal shortening or eastward motion of the deformation front (see Royden et al. (2008) for a review). The lack of the significant upper-crustal shortening, the dominance of strike-slip faults, and the regional topographic gradients suggest that uplift of SE Tibet results mainly through material transport from the central Plateau by means of ductile channel flow in the deep crust (Royden et al., 1997; Shen et al., 2001; Cook & Royden, 2008). The presence of crustal zones of low mechanical strength (rigidity) is supported by recent surface wave array tomography in the southeastern margin of the Tibetan Plateau which reveals the wide existence of low (shear) velocity layers at mid- or lower-crustal depth (Yao et al., 2008; Chapter 3). Receiver function studies (Xu et al., 2007; Liu et al., 2008; Wang et al., 2009, in preparation) also find intra-crustal low velocity layers in this region. Magnetotelluric results (Bai et al., 2006) show prominent low resistivity layer at middle or middle to

lower crustal depth in southeastern Tibetan Plateau. These results indicate a generally weaker middle/lower crust in the southeastern margin of the Tibetan Plateau.

In the Himalayan orogen and southern Tibet, seismic and magnetotelluric surveys of INDEPTH projects suggest partial melt at the mid-crustal depth (Nelson et al., 1996; Unsworth et al., 2005), which may significantly reduce the viscosity. A thermomechanical channel-flow model with a weak middle crust was proposed to investigate the Himalayan-Tibetan tectonics (Beaumont et al., 2001, 2004), e.g., the southward extrusion of the Tibetan middle crust toward the Indian foreland (Hodges et al., 2001), which is further supported by recent geochemical and geological observations (e.g., Lee & Whitehouse, 2007; King et al., 2007).

Efficient large-scale crustal channel flow requires sufficient inter-connectivity of mechanically weaker zones. Although individual studies have revealed the existence of crustal low velocity or resistivity zones, in SE Tibet and around the EHS their 3D architecture and inter-connectivity remains unclear. Preliminary results from surface wave array tomography with data from the MIT array in SE Tibet suggest that the pattern of low velocity zones – and, presumably, flow – in the crust is complicated and that major faults may locally obstruct lateral flow (Yao et al., 2008; Chapter 3).

Channel flow models require that the viscosity in the mechanically weaker layer is at least several orders magnitude less than that of the upper rigid crust (Royden et al., 1997; Cook and Royden, 2008). Therefore the low viscosity channel in the middle/lower crust effectively decouples deformation of the upper crust from that of the mantle lithosphere. However, both the extent of decoupling and the geographical regions where this might occur are still hotly debated. Joint analysis of GPS, surface geology, and shear wave splitting measurements have been used to argue for vertically coherent deformation in the crust and upper mantle in Tibet but decoupling in Yunnan, SW China (Flesch et al., 2005). Shear wave splitting data from 25 MIT array stations in SW China also support models of crust-mantle decoupling south of ~ 26°N in Yunnan (Lev et al., 2006). Using more shear wave splitting data on SE Tibet around the eastern Himalayan syntaxis

(including data from Lev et al. (2006)) and joint interpretation with surface strain field from GPS data, Sol et al. (2007) argue for mechanical coupling across crust-mantle interface beneath much of SE Tibet except at southeastern margin in Yunnan. The most recent results by Wang et al. (2008) argue for crust-mantle mechanic coupling in Tibet and also surrounding regions (including Yunnan) using joint analysis of 178 shear wave splitting measurements and ~2000 GPS observations. Their results also suggest simple shear deformation of lithosphere in the plateau and pure shear deformation in the surrounding area.

Shear wave splitting measurement represents the integrated effect of seismic anisotropy along the ray path and has poor depth resolution (e.g., Savage, 1999, for a review); it is often assumed that the main contribution to the splitting signals comes for anisotropic structure in the upper mantle, but in Tibet the effect of the thick, anisotropic crust should, perhaps, not be ignored. GPS derived strain rate fields only give the current rate of surface deformation, not the entire deformation history, and provide little insight about deformation in the deeper crust. In view of these complexities, the inference of differences in deformation pattern (e.g., coupling or decoupling) between crust and mantle through comparison of surface instantaneous strain field with shear wave splitting data is fraught with considerable uncertainty.

We would understand the deformation of crust and upper mantle much better if we knew seismic anisotropy at different depths. Surface waves can resolve depth dependent shear velocity structure and azimuthal anisotropy (e.g., Montagner & Tanimoto, 1991, Simons et al., 2003) in the crust and upper mantle, and the anisotropy thus derived can be compared directly with shear wave splitting measurements (Montagner et al., 2000; Simons et al., 2002) and (under specific assumptions) with the surface strain rate field. In this study we investigate structure and deformation of the lithosphere across the southeastern part of the Tibetan Plateau from high resolution surface wave tomography using data from temporary seismograph arrays (Figure 6-1a). We present 3D models of crust and upper mantle heterogeneity and azimuthal anisotropy. These models reveal the

3D architecture of crustal low velocity zones and constrain the deformation of the lithosphere in SE Tibet.

6.2 Data and dispersion analysis

In 2003 and 2004, MIT and Lehigh University, in collaboration with Chengdu Institute of Geology and Mineral Resources in China, deployed 73 broad band seismograph array stations in SE Tibet and SW China around EHS (Figure 6-1a). Data from these arrays are analyzed along with data from permanent stations in Kunming (KMI) and Lhasa (LSA), which are part of the Global Seismography Network.

To obtain high resolution images of the thick crust and underlying lithospheric mantle we use the method developed by Yao et al. (2006, 2008) – see Chapters 2 and 3 of this thesis – which combines phase velocity dispersion measurements from ambient noise interferometry and (for selected earthquakes) two-station analysis.

We use 10 months vertical component data between November 2003 and August 2004 to obtain the empirical Green's function (EGF) between every two-station pair from ambient noise interferometry; from these EGFs we measure inter-station Rayleigh wave phase velocity dispersion curves within the period band 10 – 50 s. For details of the data processing we refer to Yao et al. (2006, 2008). The uneven distribution of ambient noise energy (Yao et al., 2009; Chapter 4) may cause an azimuth-dependent bias of inter-station phase velocity measurements from EGFs. However, for the arrays in SE Tibet the effect of the bias is small – and ignored here – if we stack causal and anti-causal EGFs from 10 month long records (Yao & van der Hilst, 2009; Chapter 5).

We also measure about 16,000 inter-station Rayleigh wave phase velocity dispersion curves within the period band 20 – 150 s from two-station (TS) analysis using recordings from about 150 earthquakes at teleseismic distances. Under the assumption of ray theory, the TS dispersion is only sensitive to structure in between two stations on the same great circle path. However, at finite frequency the inter-station phase velocity measurements are also sensitive to the structure outside the two-station path (Appendix Figure A-1). The

earthquakes used for our TS analysis are mostly distributed to the east and south of the array, and surface waves from these sources propagate across seismically fast structures in southern China, such as the Sichuan Basin, where the crust is thinner than beneath the arrays on the Tibetan Plateau. We thus expect that finite frequency phase velocity measurements at intermediate periods to be higher than those based on the (great circle) ray theory used to construct phase velocity maps (Section 6.3). Figure A-2 (Appendix A) suggests that for periods of 20-50 s the average phase velocity from finite frequency measurements will indeed be 0.4-0.8% higher than those from ray theory; we correct for this phase velocity difference in order to suppress the effects of structure outside the array area.

Figure 6-2 presents histograms of the difference in inter-station dispersion curve from EGF and TS analysis (after suppressing the finite frequency effect) for periods of 20 – 50 s. At each period, the mean difference of phase velocity between the EGF and TS analysis ($C_{TS} - C_{EGF}$) is almost zero, but the standard error of the difference increases from ~0.05 km/s between 20 – 40 s to 0.082 km/s at 50 s (which reflects the difficulty of recovering EGFs from long period data). Based on this analysis we decided to average the EGF and TS dispersion data (using the scheme from Yao et al. (2008)) only for periods at 20 – 40 s (yielding 2232 dispersion curves). For periods less than 20 s we take measurements from the EGF analysis, and for periods larger than 40 s we only use measurements from the TS analysis.

We thus obtain 2413 dispersion curves within the period band 10 – 150 s. The number of measurements at each period is shown in Figure 6-3a and the average phase velocity dispersion curve (representative of the entire region under study) is shown in Figure 6-3b. We note that the decrease of measurements with increasing periods is an effect of the far field approximation that allows us to use a plane-wave representation of surface-wave propagation. The ray path coverage at 30s and 100s is shown in Figure 6-4. The excellent spatial and azimuthal data coverage at periods less than ~100 s allows for inversion of both isotropic and azimuthally anisotropic phase velocity maps.

6.3 Phase velocity maps and azimuthal anisotropy

We use the continuous regionalization method due to Montagner (1986) to invert path averaged phase velocities at each period for 2-D phase velocity variations, following the generalized inversion scheme of Tarantola and Valette (1982). We express the local azimuthally varying Rayleigh-wave phase velocity $c(\omega, M, \psi)$ at location M, for each angular frequency ω and azimuth ψ, as follows (Smith & Dahlen, 1973):

$$c(\omega, M, \psi) = c_0(\omega)[1 + a_0(\omega, M) + a_1(\omega, M)\cos 2\psi + a_2(\omega, M)\sin 2\psi], \qquad (6\text{-}1)$$

where $c_0(\omega)$ is the reference (transversely isotropic) phase velocity (usually the average of all observed phase velocities at a certain frequency), and a_0 and a_i (with i = 1, 2) are the isotropic phase velocity perturbation and the azimuthally anisotropic coefficients, respectively. The inversion for a_i (i = 0, 1, 2) is controlled by three parameters: the standard error of phase velocity measurements σ_d, the a *priori* parameter error σ_p, which constrains the anomaly amplitude, and the spatial correlation length L, which constrains the smoothness of the model parameters.

Our analysis of phase velocity measurements suggests that σ_d is about 1-2% and for the inversion we set it to 2% for all measurements. As with regularization, the choice of σ_p and L is somewhat subjective; in our study they are determined empirically from a series of test inversions. For a_0, σ_p is set to be twice that of the standard deviation (in per cent) of all observed phase velocities at each period, which is much larger at intermediate periods (e.g., 6% at 30s) than at long periods (e.g., 2.5% at 120s). For a_1 and a_2, σ_p is set to be 1%. The correlation length L_{iso} for the isotropic term is determined by the path coverage and the half-wavelength of the surface waves at each period, e.g., L_{iso} = 50, 50, 115, 182, 250 km at 10, 30, 60, 90, and 120s, respectively. The correlation length for the azimuthally anisotropic parameters is set to be $2\times L_{iso}$ at the corresponding period, with a minimum value of 150 km in order to obtain a robust pattern of azimuthal anisotropy.

The variations of isotropic phase velocities and azimuthal anisotropy at periods 10, 30, 60, and 100s are shown in Figure 6-5. Figure 6-6 gives the posterior errors of the isotropic

phase velocities and the magnitude of azimuthal anisotropy after the inversion, which are much smaller than the perturbation of phase velocities and the magnitude of azimuthal anisotropy in the array area. This demonstrates the significance of the variations in isotropic phase velocity and azimuthal anisotropy (for the periods of interests) within the array area. Resolution tests (Figure 6-7) show that the lateral resolution of isotropic phase velocities in the array area is about 100 km or less in the short and intermediate periods (10 – 50 s), about 100 – 200 km between 50 s and 100 s, and 200 – 350 km at periods larger than 100 s.

In the next section we invert for depth-dependent variations of shear velocity and azimuthal anisotropy from surface wave azimuthal anisotropy. Even without inversion, however, we can readily see some interesting features from the variations of isotropic part phase velocity maps and the patterns of Rayleigh wave azimuthal anisotropy. For example, at T=30 s Rayleigh wave propagation is slow beneath the plateau area and fast beneath the Yangtze block in SW China. At T=60 s, low phase velocities are observed along the western margin of Yangtze block, which may indicate that at mantle depths the shear velocity is relatively low around the block boundary. At T=10 s, at which the Rayleigh wave is sensitive to the structure between ~5-15 km depth, the fast polarization axes of Rayleigh waves reflect the conspicuous pattern of the clockwise rotation around the eastern Himalayan syntaxis in the GPS surface velocity field (Zhang et al., 2004). At T=60 s and T=100 s the fast polarization pattern appears to be (very) different from that at 10 s, suggesting changes of deformation pattern from the upper crust to upper mantle.

6.4 Inversion of shear velocity structure and azimuthal anisotropy

We use the linearized inversion scheme due to Montagner and Nataf (1986) to invert for 3-D shear velocity structure and azimuthal anisotropy in the crust and upper mantle in SE Tibet. To ensure optimal performance and reduce trade-offs between crust and mantle structures we made an effort to find a starting model, in particular for Moho depth, which is close to the true model. In order to account for the large variation in Moho depth (between 40 – 75 km), for each grid point we use a reference model with a crustal thickness that was obtained from the model space search (using neighborhood algorithm)

by Yao et al. (2008) using dispersion data (Yao et al., 2006), receiver functions (Zurek et al., 2005; Xu et al., 2007), and – outside the array region – the global references model Crust 2.0 (http://mahi.ucsd.edu/Gabi/rem.html). Initial values of the reference wavespeeds in the upper mantle are from *ak135* (Kennett et al., 1995), but after a series of convergence test we set reference values for Vs, Vp, and density in the crust to 3.6 km/s, 6.3 km/s, and 2700 kg/m^3, respectively. We note, however, that because of the excellent depth resolution of the short period dispersion data, the inversion results are not very sensitive to these reference values.

In the linearized inversion for anisotropic parameters, the Rayleigh wave phase velocity perturbation $\delta c_R(M,\omega,\psi)$ is expressed at location M for angular frequency ω and azimuth ψ as:

$$\begin{aligned}\delta c_R(M,\omega,\psi) = \int_0^H \Bigg[& \frac{\partial c_R}{\partial A}\left(\delta A + B_c \cos 2\psi + B_s \sin 2\psi\right) \\ & + \frac{\partial c_R}{\partial C}\delta C + \frac{\partial c_R}{\partial F}\left(\delta F + H_c \cos 2\psi + H_s \sin 2\psi\right) \\ & + \frac{\partial c_R}{\partial L}\left(\delta L + G_c \cos 2\psi + G_s \sin 2\psi\right)\Bigg] \frac{dz}{\Delta h}\end{aligned} \qquad (6\text{-}2)$$

The five parameters (A, C, F, L, N) describe the equivalent transverse isotropic medium with a vertical symmetry axis, which corresponds to the average over all azimuths. The other six parameters $B_{s,c}$, $G_{s,c}$, and $H_{s,c}$ give the 2ψ azimuthal variations of A, L, and F. Note that, as before, we ignore the 4ψ and higher order terms. For each grid point, the kernels $\partial c_R / \partial p_i$ are calculated from 1-D reference model at that location using a normal mode method (Montagner & Nataf, 1986). H is the maximum depth in the inversion, which we set to 350 km. Δh is the normalization thickness for the calculation of sensitivity kernels. In this inversion we take into account the posterior errors on phase velocity maps (Section 6.3, Figure 6-6), and the final errors on the parameters are estimated from the posterior covariance matrix. In this inversion we use a Gaussian correlation function with a correlation length that increases linearly from 25 km at the surface to 50 km at 350 km depth. Since Rayleigh phase velocities are mainly sensitive to L, only three parameters (L, G_c, G_s) can be resolved – see Simons et al. (2002) for further

discussion. Finally the azimuthally anisotropic velocity of vertically polarized shear wave is given by

$$\hat{\beta}_{SV} \approx \sqrt{\frac{L + G_c \cos 2\psi + G_s \sin 2\psi}{\rho}}, \tag{6-3}$$

where ρ is the density. G_c and G_s are usually much smaller than L, therefore equation (6-3) can be approximated as

$$\hat{\beta}_{SV} \approx \beta_{SV}\left(1 + \frac{G_c}{2L}\cos 2\psi + \frac{G_s}{2L}\sin 2\psi\right), \tag{6-4}$$

where $\beta_{SV} = \sqrt{L/\rho}$ is the isotropic part velocity of vertically polarized shear wave (Simons et al., 2002). The magnitude of the shear velocity azimuthal anisotropy is given by $A_{SV} = \frac{1}{2L}\sqrt{(G_c)^2 + (G_s)^2}$ and the azimuth angle of the fast polarization axis is $\phi = \frac{1}{2}\tan^{-1}(G_s/G_c)$.

6.5 3-D shear velocity structure and azimuthal anisotropy

From the 1-D velocity structures thus obtained we construct a 3-D azimuthally anisotropic shear velocity model. Figure 6-8 shows the horizontal variation of absolute shear wavespeeds and azimuthal anisotropy in the crust and upper mantle. Figure 6-9 and 10 show, respectively, the absolute Vs and the perturbation of Vs with respect to the reference model for a series of (vertical) crust-mantle sections across SE Tibet. Since the azimuthal data coverage degrades at long period (e.g., T > 100 s) we only show the results for azimuthal anisotropy up to 150 km (Figure 6-8).

The Lhasa Block, north of the Himalayan Thrust Belt, generally shows prominent low shear wavespeeds at middle crustal depth. The Songpan-Ganze Fold belt shows clear low wavespeeds at middle/lower crustal depth, with variation of intensity or depth/thickness of low velocity layer. The Yangtze Block generally exhibits fast wavespeeds in the crust except the southern fault zone regions where low wavespeeds dominate, e.g., the upper crust north of the Red River fault, the middle crust of Xiaojiang fault zone, and the

middle and lower crust around Lijiang fault. At uppermost mantle depth (e.g., 80 km and 110 km in Figure 6-8), the Qiangtang Block appears fast, while wavespeeds beneath the Lhasa Block are close to the reference values. The data reveal a conspicuous low velocity zone around the western margin of the Yangtze Block in the uppermost mantle (e.g., at 80 and 110 km depth).

The pattern of fast directions and magnitudes of azimuthal anisotropy changes substantially from the upper crust to the upper mantle. In general, the magnitude of azimuthal anisotropy appears to be relatively small in the upper and middle crust. At 10 km depth, the azimuthal anisotropy reveals a clear curvilinear pattern around the eastern Himalayan syntaxis. At 25 km depth, the fast direction is nearly NE-SW in the Yangtze block, which is different from the N-S direction at 10 km.

Figure 6-8 reveals a dramatic change in the pattern of azimuthal anisotropy from middle/lower crust (e.g., at 50 km depth) to the uppermost mantle (80 and 110 km). The fast direction of shear waves near Indus-Tsangpo suture around 93°E changes from E-W direction at 50 km depth to S-N direction at 80 and 100 km depth. At 50 km depth, the fast direction in the Songpan-Ganze Fold Belt and Yangtze Block is predominantly S-N direction. However, in the uppermost mantle, the fast axes generally follow the shape of the slow structure along the western margin of Yangtze Block. We also notice a difference in the pattern of azimuthal anisotropy north and south of 26°N. At about 150 km, the fast direction is nearly E-W direction south of 26°N, which is possibly related to the eastward subduction of Burma microplate along the Burma arc.

6.6 Discussion

6.6.1 Crustal low velocity zone (LVZ)

We note that throughout SE Tibet the crust is seismically slower than average crust; this may suggest that the entire crust of SE Tibet is relatively weak. It is, therefore, important to stress that the crustal LVZs identified here represent substantial anomalies even with regard to this average slow/weak crust.

We observe widespread crustal LVZs (Figures 6-8 – 6-10) in SE Tibet with significant 3D variations in intensity. The pronounced and widespread mid-crustal LVZ beneath the Lhasa Block in southern Tibet is consistent with the magnetotelluric results that exhibit high conductivity at the mid-crustal depth (Unsworth et al., 2005; Wei et al., 2001) and which suggest a weaker and partial molten middle crust. The N-S oriented rifts due to E-W extension in southern Tibet (near 90° E), with short wavelength shoulders and rift-flank uplift, also suggest a thin brittle upper crust underlain by a low-viscosity weaker layer (Mazek et al., 1994). Numerical models with a low-viscosity and partially molten middle crust and denudation show how mid-crustal rocks may have been exhumed to the surface (Beaumont et al., 2004), consistent with the surface exposure of high-grade metamorphic rock and intrusions of the High Himalayan Series (e.g., Grujic et al., 2002). Recently, King et al. (2007) provided field evidence for the southward migration of Asian-affinity, mid-crustal material south of the Indus-Tsangpo suture during Miocene. The normal lower crust of southern Tibet underlying the mid-crustal LVZ observed here consists of strong and dry granulite and may represent the subducted Indian lower crust (Percival et al., 1992; Priestley et al., 2008). This feature is consistent with Priestley et al. (2008)'s observations of earthquakes in the shallow crust and in the deep crust beneath southern Tibet, indicating a cool, brittle upper 'Tibetan' crust and a cold brittle low 'Indian' crust, separated by a ductile, aseismic middle crust.

Crustal LVZs, that is, zones of anomalously low wavespeed, are ubiquitous beneath SE Tibet. The southern part of the Songpan-Ganze Fold Belt shows prominent velocity anomalies in both middle and lower crust, but LVZs also occur in the Yangtze Bock. Similarly to the inversion of MIT array data (Yao et al., 2008), in some – but not all – areas, the termination of LVZs in the crust seems to coincide loosely to major faults in this area, e.g., Xianshuihe fault, Anninghe fault, Lijiang-Muli fault, and Luzhijiang fault (Figures 6-9 and 6-10). However, the spatial resolution is (still) not sufficient to draw more definitive conclusions.

The widespread crustal LVZs generally corroborate models that invoke ductile channel flow beneath the eastern Tibetan plateau (e.g., Royden et al., 1997; Shen et al., 2001 ;

Clark et al., 2004 ; Cook & Royden, 2008). The flow models (e.g., Royden et al., 1997, Cook & Royden, 2008) require sufficient connectivity of low viscosity layers in the crust for the efficient development of channel flow. Isolated patches of low viscosity zone in the mid-lower crust may be important for deformation on a local scale but are unlikely to produce large scale crustal channel flow. To first order, the LVZs inferred from our tomographic studies appear well-connected at middle and/or lower crustal depth in SE Tibet although with variations of depth range and thickness. If the LVZs mark significantly reduced rigidity due to, e.g., partial melt, which would be consistent with the steep geothermal gradients in SE Tibet (Hu et al., 2000), it is likely that large scale crustal flow can occur underneath SE Tibet.

We note, however, that from wavespeed variations we can neither confirm nor refute the very low viscosities that have been assumed in the channel flow models. Furthermore, the 3D geometry and the variations in intensity and of crustal LVZs suggest the pattern of channel flow, if indeed it exists, will be more complicated than that predicted by simple lower crustal flow models with depth dependent viscosity. As we mentioned above, some crustal LVZs may be truncated by some major faults at depth. This observation, still tentative, would suggest that major faults can influence the pattern of flow and, hence, the style of regional deformation. This is an important target for future research.

6.6.2 Crust and uppermost mantle deformation

Shear wave splitting results from anisotropy due to deformation over long periods of geological time (finite strain); in contrast, the GPS velocity field is related to the instantaneous (present-day) deformation at the surface. Furthermore, the relationship between deformation and the resulting anisotropic fabric depends on the type of deformation (e.g. simple vs. pure shear). Finally, the GPS velocity field itself is not an invariant (like strain) and will depend on the geographical reference frame. Comparing these two measures of strain is not straightforward and requires several assumptions.

Shear wave splitting measurements have poor depth resolution because the splitting can, in principle, be produced by anisotropic structure anywhere from the core-mantle

boundary to the surface (even though finite frequency theory suggest that splitting is most sensitive to relatively shallow structures (Saltzer et al., 2000; Chevrot, 2006; Long et al., 2008; Sieminski et al., 2008). It is often assumed that the signal that is observed at the surface has an upper mantle origin, which constrains the style of deformation in the crust-mantle system (e.g., Flesch et al., 2005; Sol et al., 2007; Wang et al., 2008), but the thick crust underlying the Tibetan plateau could produce a significant – and probably complicated – signal. The (gradient of the) GPS velocity field gives information about the instantaneous (current) surface (or upper crust) deformation rate, with little information about middle or lower crustal deformation and no information about the deformation history (which influences the finite strain measured by shear wave splitting). The instantaneous surface strain field from GPS data would represent the accumulated finite strain field only if deformation has been constant for sufficiently long periods of time. However, in areas with complicated deformation histories, the derived instantaneous surface strain field may not reflect the long term finite strain.

In this section, we first compare the GPS velocity field and derived present-day surface deformation pattern with the azimuthal anisotropy obtained from surface wave array tomography. Subsequently, we calculate the shear wave splitting time and fast polarization direction from the 3D tomographic model of azimuthal anisotropy and compare them to the observed shear wave splitting measurements. Finally, we discuss the possible deformation pattern in the crust and uppermost mantle and its dynamic implication.

6.6.2.1 Comparison of upper crust deformation with GPS results

In case of simple shear deformation (that is σ_1 and σ_3 horizontal), medium fabric tends to develop along the direction of shear. Therefore, the fast axis of seismic anisotropy will be parallel to the direction of shear, which is generally not the axis of finite strain maximum-compression (σ_1). However, in the case of pure shear, e.g., deformation due to horizontal tectonic stresses (σ_1 horizontal, σ_3 vertical), fabric or fast polarization axis of seismic waves tends to be perpendicular to the direction of maximum-compression (σ_1). The fast axis of seismic anisotropy is thus expected to be nearly perpendicular or at large angle to

the direction of flow (velocity field) near boundaries where maximum-compression force is exerted. Estimating finite strain from GPS is difficult because the instantaneous strain-rate cannot be integrated over sufficiently long periods of deformation history. Under the assumption that the style of deformation has been constant over sufficiently periods of time, and, thus, that the finite strain is parallel to the present-day infinitesimal strain, then the comparison of the GPS velocity field with upper crust anisotropy may provide information about the dominant type of shear deformation in the rigid upper crust in the geological history.

In SE Tibet, the GPS velocity field (Chen et al., 2000; Zhang et al., 2004; Sol et al., 2007) reveals clock-wise rotation around the eastern Himalayan syntaxis (Figure 6-11). In this region, the angle difference between the surface velocity field and the fast axes of upper crustal azimuthal anisotropy is generally small (Figure 6-12a,b). This is consistent with a predominance of simple shear deformation, accommodated by major strike-slip faults, such as the Xiaoshuihe-Xiaojiang fault zone (e.g., Wang & Burchfiel, 2000). In other regions the surface velocity vectors are at large angle (60° - 90°) to the fast polarization axes of seismic anisotropy, which suggests a predominance of deformation by pure shear (e.g., crustal shortening). This is the case, for instance, around 93°E in the Lhasa block of southern Tibet, near the southeastern corner of the Qiangtang block (near the Bangong-Nujiang suture), around the western margin of the Sichuan Basin and Longmenshan fault zone, and along the southeastern margin of the Tibetan Plateau (Figures 6-11 and 6-12a),

From the GPS velocity field in central Asia, Wang et al. (2008) calculated the velocity gradient tensor and strain rate tensor and then infer the current pattern of shear deformation by calculating the kinematic vorticity number W_k (McKenzie, 1979; Fossen & Tickff, 1993). From their results, the current surface deformation is dominated by simple shear (red triangles) in SE Tibet except in the regions around the Indus-Tsangpo suture, part of the Bangong-Nujiang suture where Qiangtang block joins with Lhasa block, part of Songpan-Ganze fold belt, and most of the Yunnan province in SW China (about south of 25°-26°N), where pure shear (blue triangles) dominates.

6.6.2.2 Comparison with results from shear wave splitting

From the azimuthal anisotropy inferred from surface wave array tomography we can calculate the predicted maximum splitting time and fast polarization direction for vertically incident shear waves using the expression by Montagner et al. (2000) for simple medium with a horizontal symmetry axis (see also Simons et al., 2002). We first calculate the splitting time and polarization only for the crust (Figure 6-13a). The predicated split time from crustal anisotropy is fairly large (about 1 s) in the plateau area, where the crust is 70-80 km thick, but (negligibly) small off-plateau in Yunnan. Since the observed splitting time is about 1 s (Lev et al., 2006; Sol et al., 2007; Wang et al., 2008), the contribution from crust in the Tibetan plateau cannot be neglected. The estimated split times and directions in the upper mantle (between Moho and 150 km depth) are substantially different from those due to crustal anisotropy (Figure 6-13b). The most obvious feature is the increase in split time in Yunnan (> 1s). The direction of splitting in the upper mantle to 150 km depth shows primarily the E-W or ESE-WNW direction south of 27°N, while north of 27°N the splitting direction is mainly S-N direction. This implies a change of upper mantle deformation pattern around 27°N in the southeastern margin of the Tibetan plateau. In southern Tibet, west of 93.5°E, the fast polarization direction estimated from azimuthal anisotropy in the crust is quite different around the Bangong-Nujiang suture and Indus-Tsangpo suture, implying very different deformation pattern in the crust and upper mantle around these suture zones.

The splitting parameters calculated from the azimuthal anisotropy in crust and upper mantle together (Figure 6-13c) are generally more similar to that from the upper mantle (Figure 6-13b) than that from the crust (Figure 6-13a), reflecting – in general – a larger contribution by upper mantle anisotropy. For observations with split time larger than 0.4 s we compare observed shear wave splitting parameters (Lev et al., 2006; Sol et al., 2007; Wang et al., 2008) with predictions from our 3D model (Figure 6-14). Overall, larger angle differences appear in the southern Tibet (Lhasha and Qiangtang blocks) and smaller difference in the southeastern margin of Tibetan plateau (Figure 6-14a). The statistical histogram of these angle differences (Figure 6-14b) shows that only about 55% percent of

the predicted splitting direction is similar to the observed splitting direction (with angle difference less than 36°).

This discrepancy can have several causes. Firstly, the predicted splitting is only from the seismic anisotropy between the surface and 150 km depth, so any anisotropy deeper in the mantle is ignored. Subduction beneath the Himalaya and Burma ranges may, however, cause complex (and non-negligible) anisotropy in the lithosphere and asthenosphere beneath SE Tibet. Secondly, some observed splitting directions have large uncertainty caused by uneven azimuthal data coverage and noisy records. Thirdly, the directions inferred from surface wave array tomography also have uncertainties due to uneven azimuthal coverage and regularization of the inversion (see sections 6.3 and 6.4). Finally, the calculation of the splitting parameters is based on the assumption of a horizontal orientation of the fast axis, but dipping axes cannot be excluded (Simons et al., 2000).

The above observations suggest a complex origin of seismic anisotropy in the crust and upper mantle beneath SE Tibet. In the region west of Sichuan Basin and north of 26°N where the crust is thick, the contribution to splitting time from the crust is at least as important as from the upper mantle (Figure 6-13). However, in the region south of 26°N, in Yunnan, the splitting mainly originates from upper mantle anisotropy (Figure 6-13). The observed splitting data and the 3D model of azimuthal anisotropy suggest substantial depth dependence of anisotropy. In regions as complex as SE Tibet, such depth dependence cannot be resolved with traditional shear wave splitting measurements (e.g., Lev et al., 2006), but in the future it may be possible to constrain depth variations with, for instance, finite frequency shear wave splitting tomography (Long et al., 2008).

6.6.2.3 Coupled or decoupled crust and upper mantle in SE Tibet?

Previous arguments for crust-mantle coupling in Tibet and coupling or decoupling in Yunnan of SW China (Silver, 1996; Holt, 2000; Flesch et al., 2005; Lev et al., 2006; Sol et al., 2007; Wang et al., 2008) are primarily based on the comparison between the instantaneous surface strain field from GPS observations and shear wave splitting

measurements. As we discussed above (section 6.6.2), this involves strong assumptions about deformation mechanisms, histories, and reference frames, which can easily be violated in areas with a complicated tectonic history and with thick and highly deformed crust, such as SE Tibet. The conclusion by Flesch et al. (2005), Sol et al. (2007), and Wang et al. (2008) that crust and mantle deform coherently follows from the assumption that the observed splitting at the surface originates in the upper mantle. However, the predicted splitting from our 3D anisotropic model shows that the contribution to splitting from the crust is at least as important as from the upper mantle in the region west of Sichuan Basin and north of 26°N. From our inversion of surface wave data, we obtain a complicated pattern of crust and upper mantle azimuthal anisotropy in SE Tibet (Figure 6-8). The fast direction of azimuthal anisotropy and the direction of the current observed GPS velocity field are highly correlated at upper crustal depth (Figure 6-12a, b). However, at middle crustal depth (Figure 6-12c,d) there is no significant correlation, and at upper mantle depths (Figure 6-12e,f) the correlation is negative. These observations are not readily consistent with vertically coherent deformation of the crust-mantle system beneath SE Tibet, as was proposed by, for instance, Flesch et al. (2005), Sol et al. (2007), and Wang et al. (2008), and suggest, instead, that parts of the crust and upper mantle deform (or have in the past deformed) differently from one another.

The predominance of crustal LVZs at middle/lower crustal depth in SE Tibet and the apparent change of pattern of azimuthal anisotropy from the upper crust to upper mantle (Figures 6-8 and 6-12) are most consistent with models that allow (at least partial) mechanical decoupling between the upper crust and the upper mantle and would, thus, corroborate channel flow in the deep crust (Royden et al., 1997; Cook & Royden, 2008; Royden et al., 2008). However, given resolution limitations and errors in the tomographic models it is still difficult to quantify the degree of decoupling. In general, there is no apparent correlation between the presence of LVZs and the strength of azimuthal anisotropy. In general, lower crust (e.g., in Songpan-Ganze Fold Belt) shows much larger azimuthal anisotropy (~4%) than that in the middle crust (~2%). This might be indicative of more efficient crustal channel flow deeper in the crust, for instance due to much lower

viscosity related to higher temperature in the lower crust (Hu et al., 2000), or compositional differences between the middle and lower crust.

6.7 Conclusions

High resolution surface wave tomography from ambient noise interferometry and teleseismic surface wave analysis provides important constraints on the shear wave velocity structure and azimuthal anisotropy in the crust and upper mantle beneath SE Tibet. These constraints are essential for the understanding of dynamic evolution and deformation pattern of SE Tibet. The main conclusions are:

(1) The entire crust is seismically slow and, perhaps, mechanically weak.

(2) SE Tibet is dominated by LVZs in the middle or lower crust or both. These LVZs are anomalous compared to the average slow crust and show complicated geometry with both lateral and vertical variations.

(3) Although some LVZs may be truncated by major faults in this area, the LVZs seem to form a well-connected channel at middle/lower crustal depth in SE Tibet around the eastern syntaxis (with horizontal resolution about 100 km), which supports models of crustal channel flow in this area.

(4) The pattern of crustal flow may be complicated as inferred from the 3D geometry of LVZs. And it is possible that upper mantle processes are involved also.

(5) The deformation of upper crust in SE Tibet, especially in southeastern plateau margin, is probably dominated by simple shear, which is similar to that inferred from current GPS velocity field. However, deeper in the crust and in the uppermost mantle, simple shear cannot explain the observed pattern of azimuthal anisotropy. This implies radial changes of deformation mechanism.

(6) The patterns of splitting from SKS observations and from our 3D anisotropic model are similar beneath the plateau margin, but different in southern Tibet, which may require sources of seismic anisotropy below the depth considered in our model (150 km). In the region south of 26°N (Yunnan) splitting signal mainly originates from upper mantle anisotropy. However, in the region west of Sichuan Basin and north of 26°N, the predicted splitting from the crust is at least as important as from the upper mantle, suggesting that the previous conclusion of crust-mantle coupling in Tibet

from comparison of splitting and GPS observations needs to be reconsidered.

(7) The apparent change of pattern of azimuthal anisotropy from the upper crust to upper mantle and the widespread and well-connected crustal LVZs argues against vertically coherent deformation of Tibetan lithosphere and implies that beneath SE Tibet the deformation of the upper crust is largely decoupled from that of the upper mantle.

Appendix. Correction of phase velocity measurements from the TS analysis

Ray theory is commonly used in traditional surface wave tomography, in which phase velocity or travel time is only sensitive to the structure along the great circle ray path. The average phase velocity at frequency ω between two stations at A ($\mathbf{r}_A$) and B ($\mathbf{r}_B$) in a perturbed earth mode can be expressed as

$$\bar{c}_{AB}^{RT} = \Delta_{AB} / t_{AB}^{RT}(\omega) = \Delta_{AB} \Big/ \int_A^B \frac{dl}{c(\omega,\mathbf{r})}, \tag{A-1}$$

where $c(\omega,\mathbf{r}) = c_0(\omega) + \delta c(\omega,\mathbf{r})$ gives the 2-D phase velocity distribution with c_0 the reference phase velocity and $\delta c(\omega,\mathbf{r})$ the 2-D phase velocity perturbation, Δ_{AB} is the great circle distance between A and B, and the integration is taken along the great circle path between A and B.

Considering the finite frequency effect of surface wave propagation, we can express the phase travel time between S ($\mathbf{r}_S$) and A as

$$t_{SA}^{FK}(\omega) = t_{SA}(\omega) + \frac{1}{\omega} \iint_\Omega K_\phi^c(\omega,\mathbf{r};\mathbf{r}_S,\mathbf{r}_A)(\delta c / c_0) d\Omega, \tag{A-2}$$

where $t_{SA}(\omega) = \Delta_{SA} / c_0$ is the reference travel time between S and A, $K_\phi^c(\omega,\mathbf{r};\mathbf{r}_s,\mathbf{r}_A)$ is the 2-D phase sensitivity kernel to phase velocity, and the integration is computed at the spherical surface Ω of the Earth. Δ_{SA} (or Δ_{SB}) is the great circle distance between S and A (or B). Therefore, the finite frequency travel time of surface waves based on cross-correlation method between the two stations at A and B is given by

$$t_{AB}^{FK}(\omega) = t_{SB}^{FK} - t_{SA}^{FK} = (t_{SB} - t_{SA}) + \frac{1}{\omega} \iint_\Omega K_\phi^c(\omega,\mathbf{r};\mathbf{r}_S)_{AB}(\delta c / c_0) d\Omega, \tag{A-3}$$

where $t_{SB} - t_{SA} = \frac{\Delta_{SB}}{c_0} - \frac{\Delta_{SA}}{c_0}$ is the differential reference travel time between A and B, and $K_\phi^c(\omega,\mathbf{r};\mathbf{r}_S)_{AB} = K_\phi^c(\omega,\mathbf{r};\mathbf{r}_S,\mathbf{r}_B) - K_\phi^c(\omega,\mathbf{r};\mathbf{r}_S,\mathbf{r}_A)$ is the 2-D differential phase sensitivity kernel. Figure A-1 shows one example of the windowed differential kernel at T = 30 s with a reference phase velocity 3.6 km/s using the phase kernel expression in Zhou et al. (2004). The average inter-station phase velocity in the TS method based on finite frequency theory can be approximated as

$$\bar{c}_{AB}^{FK} = (\Delta_{SB} - \Delta_{SA}) / t_{AB}^{FK}(\omega), \tag{A-4}$$

provided that the source is almost along the great circle path linking the two stations (see Yao et al.(2006)).

$\bar{c}_{AB}^{FK}$ may be different from $\bar{c}_{AB}^{RT}$ in general heterogeneous medium. However, our approach to invert for both isotropic and azimuthally anisotropic phase velocity maps (Section 6.3) is based on the ray theory. In order to suppress the effect of structure outside the ray path on the tomographic inversion results due to finite frequency effect, we perform the following scheme to calculate an approximately ray-theory-based inter-station phase velocity measurements from the observed finite frequency measurements. First we use the global crust and upper mantle model from Shapiro & Ritzwoller (2003) to calculate the phase velocity map $c(\omega, \mathbf{r})$ at each frequency ω and consequently the reference (average) phase velocity c_0 and the phase velocity perturbation $\delta c(\omega, \mathbf{r})$. From the model, we then calculate the difference of phase velocities between finite frequency approach and ray theory approach as

$$\delta c_{FKmRT}(\omega) = \bar{c}_{AB}^{FK}(\omega) - \bar{c}_{AB}^{RT}(\omega). \tag{A-5}$$

If the observed average inter-station phase velocity from the TS approach (Yao et al., 2006) is $\bar{c}_{AB}^{TS}(\omega)$, the corrected inter-station phase velocity after suppressing the finite frequency effect is given by

$$\tilde{c}_{AB}^{TS}(\omega) = \bar{c}_{AB}^{TS}(\omega) - \delta c_{FKmRT}(\omega). \tag{A-6}$$

We repeat this process for every station pair for each earthquake at every period for our TS measurements and finally obtain the corrected inter-station phase velocity measurements $\tilde{c}_{AB}^{TS}(\omega)$ within the period band 20-150 s for 16386 inter-station paths. For each station pair, we average the dispersion curves from different events and finally obtain 2232 inter-station average dispersion curves. The average phase velocity dispersion curve in the study area is thus calculated by taking the mean of all the inter-station average dispersion curves. As shown in Figure A-2, the original average phase velocity dispersion which is subjected to finite frequency effect will be 0.4-0.8% higher between 20 – 40 s than that after suppressing the finite frequency effect. This is mainly

due to the fact that surface waves from the earthquakes used in this study, which are mainly located to the east and south of our array, sample faster structure in southern China and Sichuan Basin where the crust is much shallower than in the Tibetan Plateau area. Hopefully through our approach of suppressing finite frequency effect on the dispersion measurements, we can mitigate the effect of structure outside the array area on the tomographic phase velocity maps.

References

Argand, E., 1924. La tectonique de l'Asie, *Int. Geol. Cong. Rep. Sess.*, 13(1), 170-372.

Bai, D., Meju, M., Arora, B., Ma, X., Jiang, C., Zhou, Z., Zhao, C., and Wang, L., 2006. Large crustal-mantle channel flow in central Tibet and eastern Himalaya inferred from magnetotelluric models, *Eos Trans. AGU*, 87(36), West. Pac. Geophys. Meet. Suppl., Abstract S45A-07.

Beaumont, C., Jamieson, R. A., Nguyen, M. H. and Lee, B., 2001. Himalayan tectonics explained by extrusion of a low-viscosity channel coupled to focused surface denudation, *Nature*, 414, 738-742.

Beaumont, C., Jamieson, R. A., Nguyen, M. H. and Medvedev, S., 2004. Crustal channel flow: 1. Numerical models with applications to the tectonics of the Himalayan-Tibetan orogen, *J. Geophys. Res.*, 109, B06406, doi:10.1029 /2003JB002809.

Chen, Z., Burchfiel, B.C., Liu., Y., King, R.W., Royden, L.H., Tang, W., Wang, E., Zhao, J., Zhang, X., 2000. Global positioning system measurements from eastern Tibet and their implications for India/Eurasia intercontinental deformation, *J. Geophys. Res*, 105, 16215-16227.

Chevrot, S., 2006. Finite-frequency vectorial tomography: a new method for high-resolution imaging of upper mantle anisotropy, *Geophys. J. Int.,* 165, 641–657.

Clark, M. & Royden, L. H., 2000. Topographic ooze: building the eastern margin of Tibet by lower crustal flow, *Geology*, 28(8), 703-706.

Cook, K.L. and Royden, L.H., 2008. The role of crustal strength variations in shaping orogenic plateau, with application to Tibet, *J. Geophys. Res.*, 113, B08407, doi:10.1029/2007JB005457.

Flesch, L.M., Holt, W.E., Silver, P.G., Stephenson, M., Wang, C.-Y., and Chan, W.W., 2005. Constraining the extent of crust-mantle coupling in central Asia using GPS, geologic, and shear wave splitting data, *Earth Planet. Sci. Lett*, 238, 248-268.

Fossen, H. and Tikoff, B., 1993. The deformation matrix for simultaneous simple shearing, pure shearing, and volume changes, and its application to transpression/ transtension tectonics, *J. Structural Geology*, 15, 413-422.

Grujic, F., Hollister, L.S., and Parrish, R.R., 2002. Himalayan metamorphic sequence as an orogenic channel; insight from Bhutan, *Earth Planet. Sci. Lett.*, 198, 177-191, doi:10.1016/S0012-821X(02)00482-X.

Hodges, K.V., Hurtado, J.M., and Whipple, K.X., 2001. Southward extrusion of Tibetan crust and its effect on Himalayan tectonics, *Tectonics*, 20(6), 799-809.

Holt, W.E., 2000. Correlated crust and mantle strain fields in Tibet, *Geology*, 28, 67-70.

Hu, S., He, L., & Wang, J., 2000. Heat flow in the continental area of China: a new data set, *Earth Planet. Sci. Lett.*, 179, 407-419.

Kennett, B. L. N., Engdahl, E. R. & Buland, R., 1995. Constraints on the velocity structure in the earth from travel times, *Geophys. J. Int.*, 122, 108–124.

King, J., Harris, N., Argles, T., Parrish, R., Charlier, B., Sherlock, S., and Zhang, H.F., 2007. First field evidence of southward ductile flow of Asian crust beneath southern Tibet, *Geology*, 35, 727 – 730.

Lee, J. and Whitehouse, M.J., 2007. Onset of mid-crustal extensional flow in southern Tibet: evidence from U/Pb zircon ages, *Geology*, 35, 45-48.

Lev, E., Long, M., van der Hilst, R.D., 2006. Seismic anisotropy in Eastern Tibet from Shear-wave splitting reveals changes in lithosphere deformation. *Earth Planet. Sci. Lett.* 251, 293–304.

Li, C., Van der Hilst, R.D., Meltzer, A.S., Sun, R., and Engdahl, E.R., 2008. Subduction of the Indian lithosphere beneath the Tibetan Plateau and Burma, *Earth Planet. Sci. Lett,* 274, 157-168.

Liu QY, Li Y, Chen JH, 2009. Wenchuan M(S)8.0 earthquake: preliminary study of the S-wave velocity structure of the crust and upper mantle, *Chinese J. Geophys.* (in Chinese), 52 (2), 309-319.

Long, M.L., De Hoop, M.V., and Van der Hilst, R.D., 2008. Wave-equation shear wave splitting tomography, *Geophys. J. Int.,* 172, 311-330

Masek, J.G., Isacks, B.L., and Fielding, E.J., 1994. Rift flank uplift in Tibet: Evidence for a viscous lower crust, *Tectonics*, 13(2), 659-667.

McKenzie, D., 1979. Finite deformation during fluid flow, *Royal Astron. Soc. Geophys. J,* 58, 689-715.

Montagner, J.-P., 1986. Regional three-dimensional structures using long period surface waves, *Ann. Geophys.*, 4, 283–294.

Montagner, J.-P. & Nataf, H.-C., 1986. A simple method for inverting the azimuthal anisotropy of surface waves, *J. geophys. Res.*, 91, 511–520.

Montagner, J.-P. & Tanimoto, T., 1991. Global upper mantle tomography of seismic velocities and anisotropies, *J. geophys. Res.*, 96, 20 337–20 351.

Montagner, J.-P., Griot-Pommera, D.-A. & Lav´e, J., 2000. How to relate body wave and surface wave anisotropy?, *J. geophys. Res.*, 105, 19 015–19 027.

Nelson, K.D., Zhao, W.J., Brown, L.D., Kuo, J., Che, J., Liu, X., Klemperer, S.L. Makovsky, Y., et al., 1996. Partially molten middle crust beneath Southern Tibet: Synthesis of Project INDEPTH results, *Science*, 294, 1684-1688.

Ni, J.F., Guzman-Speziale, M., Bevis, M., Holt, W.E., Wallace, T.C., Seager, W., 1989.Accretionary tectonics of Burma and the three-dimensional geometry of the Burma subduction zone. *Geology*, 17, 68–71.

Percival, J., Fountain, D., and Salisbury, M., 1992. Exposed crustal cross sections as windows on the lower crust, in *Continental Lower Crust*, 317-363, eds Fountain, D., Arculus, R. and Kay, R. Elsevier Pub., Amsterdam.

Priestley K., Jackson, J., and McKenzie, D., 2008. Lithospheric structure and deep earthquakes beneath India, the Himalaya and southern Tibet, *Geophys. J. Int.*, 172, 345-362, doi:10.1111/j.1365-246X.2007.03636.x

Royden, L. H., Burchfiel, B. C., King, R. W., et al., 1997. Surface deformation and lower crustal flow in eastern Tibet, *Science,* 276, 788-790.

Royden, L.H., Burchfiel, B.K., and Van der Hilst, R.D., 2008. The geological evolution of the Tibetan Plateau, *Science*, 321, 1054-1058.

Saltzer, R.L., J. Gaherty and T.H. Jordan, 2000. How are shear wave splitting measurements affected by variations in anisotropy with depth?, *Geophys. J. Int.* 141, 374–390.

Savage, M.K., 1999. Seismic anisotropy and mantle deformation: what have we learned from shear wave splitting? *Rev. of Geophys.*, 37, 65-106.

Sieminski, A., Paulssen, H., and Trampert, J., 2008. Finite-frequency SKS splitting: measurement and sensitivity kernels, *Bull. Seismo. Soc. Amer.*, 98(4), 1797-1810, DOI: 10.1785/0120070297

Shapiro, N., Ritzwoller,M., 2002. Monte-Carlo inversion for a global shear-velocity model of the crust and upper mantle, *Geophys. J. Int.* 151, 88–105.

Shen, F., Royden, L. H. and Burchfiel, B. C., 2001. Large-scale crustal deformation of the Tibetan Plateau, *J. Geophys. Res.*, 106(B4), 6793-6816.

Silver, P.G., 1996. Seismic anisotropy beneath continents: Probing the depths of geology, *Annu. Rev. Earth Planet. Sci.*, 24, 385-432.

Simons, F. J., van der Hilst, R. D., Montagner, J. P., and Zielhuis, A., 2002. Multimode Rayleigh wave inversion for heterogeneity and azimuthal anisotropy of the Australian upper mantle, *Geophys. J. Int.*, 151, 738-754

Smith, M.L. & Dahlen, F.A., 1973. Azimuthal dependence of Love and Rayleigh-wave propagation in a slightly anisotropic medium, *J. Geophys. Res.*, 78, 3321-3333.

Sol, S., Meltzer, A., Burgmann, R., Van der Hilst, R.D., et al., 2007. Geodynamics of southeastern Tibet from seismic anisotropy and geodesy, *Geology*, 35, 563-566, doi: 10.1130/G23408A.1.

Tarantola, A., and B., Valette, 1982. Generalized nonlinear inverse problem solved using the least squares criterion, *Rev. Geophys. Space Phys.*, 20(2), 219-232.

Unsworth, M. J., Jones, A. G., Wei, W., Marquis, G., Gokarn, S.G., Spratt, J.E., 2005. Crustal rheology of the Himalaya and southern Tibet from magnetotelluric data, *Nature*, 438, 78-81.

Wang, C.-Y., Flesch, L.M., Silver, P.G., Chang, L.-J., and Chan, W.W., 2008. Evidence for mechanically coupled lithosphere in central Asia and resulting implication, *Geology*, 36, 363-366, doi:10.1130/G24450A.1

Wang, E. & Burchfiel, B.C., 2000. Late Cenozoic to Holocene deformation in southwestern Sichuan and adjacent Yunnan, China, and its role in formation of the southeastern part of the Tibetan Plateau, *Geol. Soc. Am. Bull*, 112, 413-423.

Wei, W., Unsworth, M., Jones, A., Booker, J., Tan, H., Nelson, D., Chen, L., Li, S., et al., 2001. Detection of widespread fluids in the Tibetan crust by magnetotelluric studies, *Science*, 292, 716-718.

Xu, L., Rondenay, S., Van der Hilst, R.D., Structure of the crust beneath the Southeastern Tibetan Plateau from teleseismic receiver functions, *Phys. Earth Planet. Int.*, 176-193, doi:10.1016/j.pepi.2007.09.002

Yao, H., Van der Hilst, R.D., & de Hoop, M.V., 2006. Surface-wave array tomography in SE Tibet from ambient seismic noise and two-station analysis – I. phase velocity maps, *Geophys. J. Int.*, 166, 732-744.

Yao, H., Beghein, C., and Van der Hist, R.D., 2008. Surface-wave array tomography in SE Tibet from ambient seismic noise and two-station analysis: II – Crustal and upper-mantle structure, *Geophys. J. Int.*, Vol. 163, 205-219, doi: 10.1111/j.1365-246X.2007.03696.x.

Yao, H., Campman, X., De Hoop, M.V., and Van der Hilst, R.D., 2009. Estimation of surface-wave Green's function from correlations of direct waves, coda waves, and ambient noise in SE Tibet, *Phys. Earth Planet. Inter.*, under review

Yao, H. and Van der Hilst, R.D., 2009. Analysis of ambient noise energy distribution and phase velocity bias in ambient noise tomography, with application to SE Tibet, *Geophys. J. Int.*, under review

Yin A. and Harrison, T.M., 2000. Geologic evolution of the Himalayan-Tibetan orogen, *Annu. Rev. Earth Planet. Sci.,* 28, 211-280.

Zhang P., Shen, Z., Wang, M., et al., 2004. Continuous deformation of the Tibetan Plateau from global positioning system data, *Geology*, 32(9), 809-812.

Zhou Y., Dahlen, F. A., and Nolet, G., 2004. Three-dimensional sensitivity kernels for surface wave observables, *Geophys. J. Int.*, 158, 142-168.

Zurek, B., Meltzer, A., Sol, S., Zhang, X., and Zhang, J., 2005, Measurements of crustal thickness and Poisson's ratio in southeastern Tibet from receiver functions, *Eos (Transactions, AGU)*, v. 86, abstract T41A–1283.

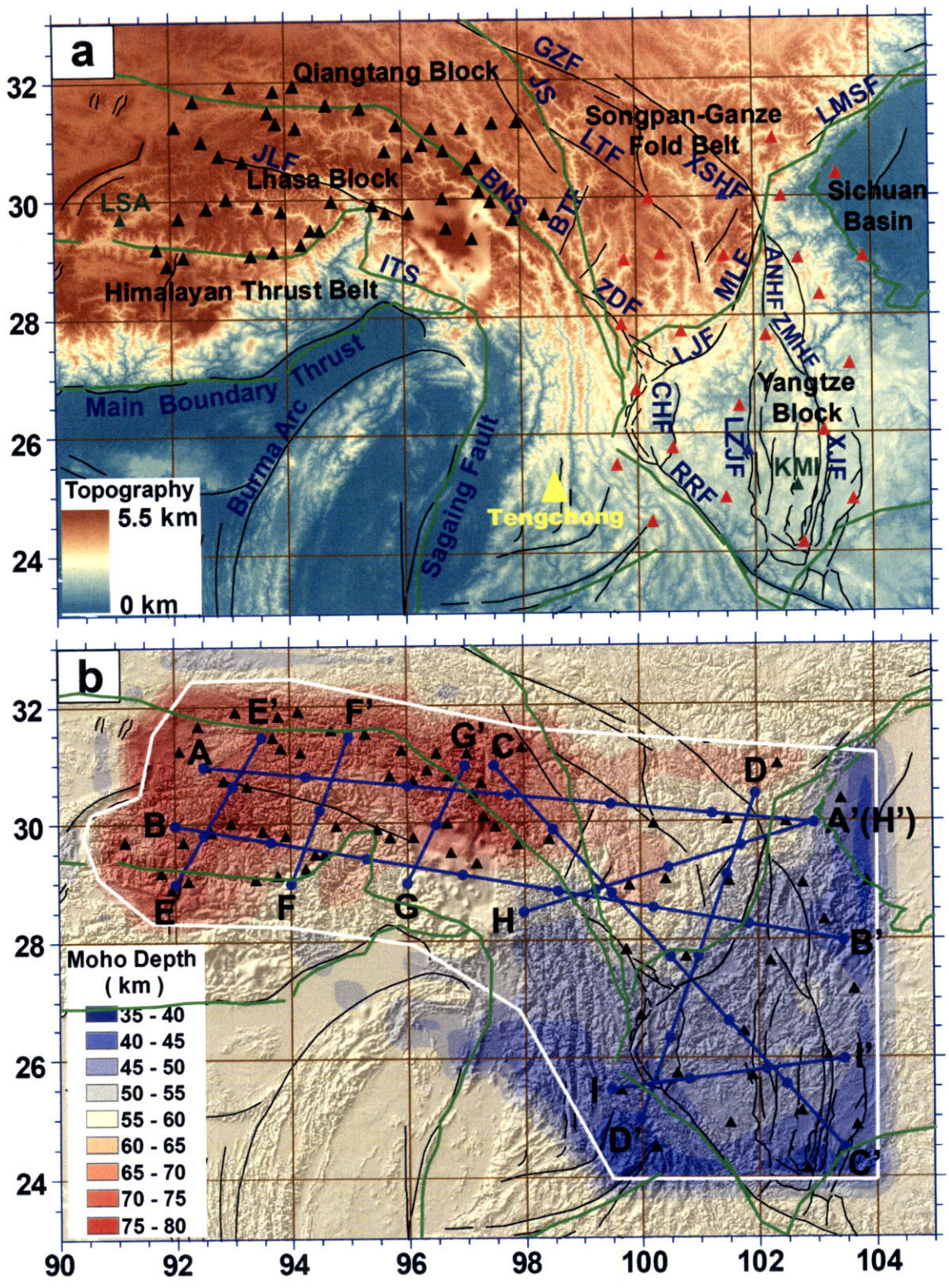

Figure 6-1. (a) Topography, tectonic elements and fault systems in the southeastern part of the Tibetan Plateau around the eastern Himalayan syntaxis (EHS). (b) The depth of

Moho discontinuity from surface wave array tomography with reliable results within the region enclosed by the white line. Tectonic boundaries (modified from Li, 1998 and Tapponnier et al., 2001) are shown as dark green lines and the major faults are depicted with thin black lines (after Wang et al., 1998; Wang & Burchfiel, 2000; Shen et al, 2005). Abbreviations are: JLF – Jiali Fault, GZF – Ganzi Fault, LMSF – Longmenshan Fault, XSHF – Xianshuihe Fault, LTF – Litang Fault, ANHF – Anninghe Fault, ZMHF – Zemuhe Fault, ZDF – Zhongdian Fault, LJF – Lijiang Fault, MLF – Muli Fault, CHF – Chenghai Fault, LZJF – Luzhijiang Fault, XJF – Xiaojiang Fault, RRF – Red River Fault, EHS – Eastern Himalaya Syntaxis, JS – Jingsha Suture, BNS – Bangong-Nujiang Suture, ITS – Indus-Tsangpo suture. In (a) red and black triangles are temporary stations deployed by MIT and Lehigh Univeristy, respectively. The two pernament stations (dark green triangles) are located at Kunming (KMI) and Lhasa (LSA), China. The Tengchong volcanic area is depicted as the yellow triangle. In (b), the blue lines show the location of vertical shear wavespeed profiles in Figures 6-9 and 6-10.

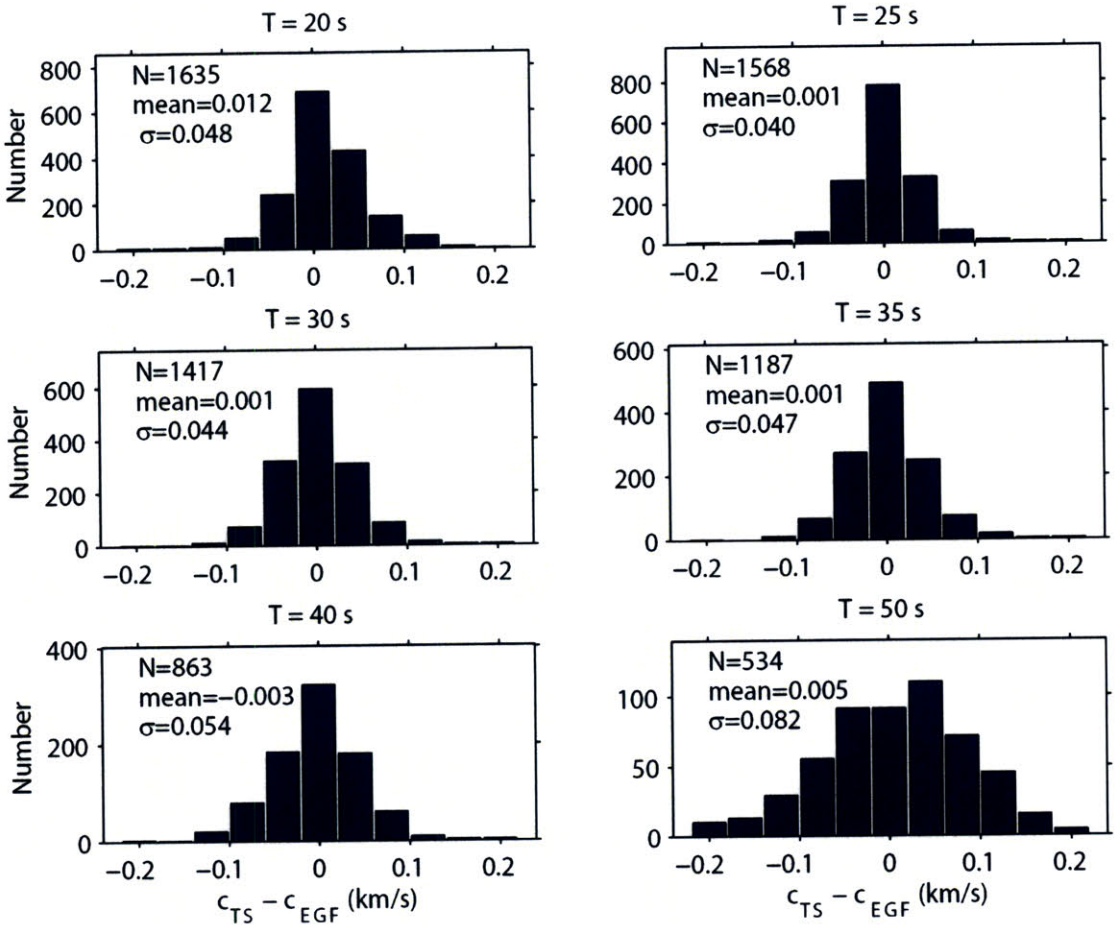

Figure 6-2. Histogram to show the comparison of inter-station Rayleigh wave phase velocity measurements from the EGF analysis and TS analysis (after suppressing the finite frequency effect) at overlapping periods (20 – 50 s). The horizontal axis show the difference between the phase velocity from the TS analysis (C_{TS}) and that from the EGF analysis (C_{EGF}), i.e., $C_{TS} - C_{EGF}$, while the vertical axis shows the number of inter-station paths which falls in the different $C_{TS} - C_{EGF}$ interval each with a width of 0.04 km/s. In each plot, 'N' is the total number of paths for comparison and 'mean' is the average difference (km/s) of $C_{TS} - C_{EGF}$ for all paths at that period with 'σ' the standard deviation of the differences in the histogram.

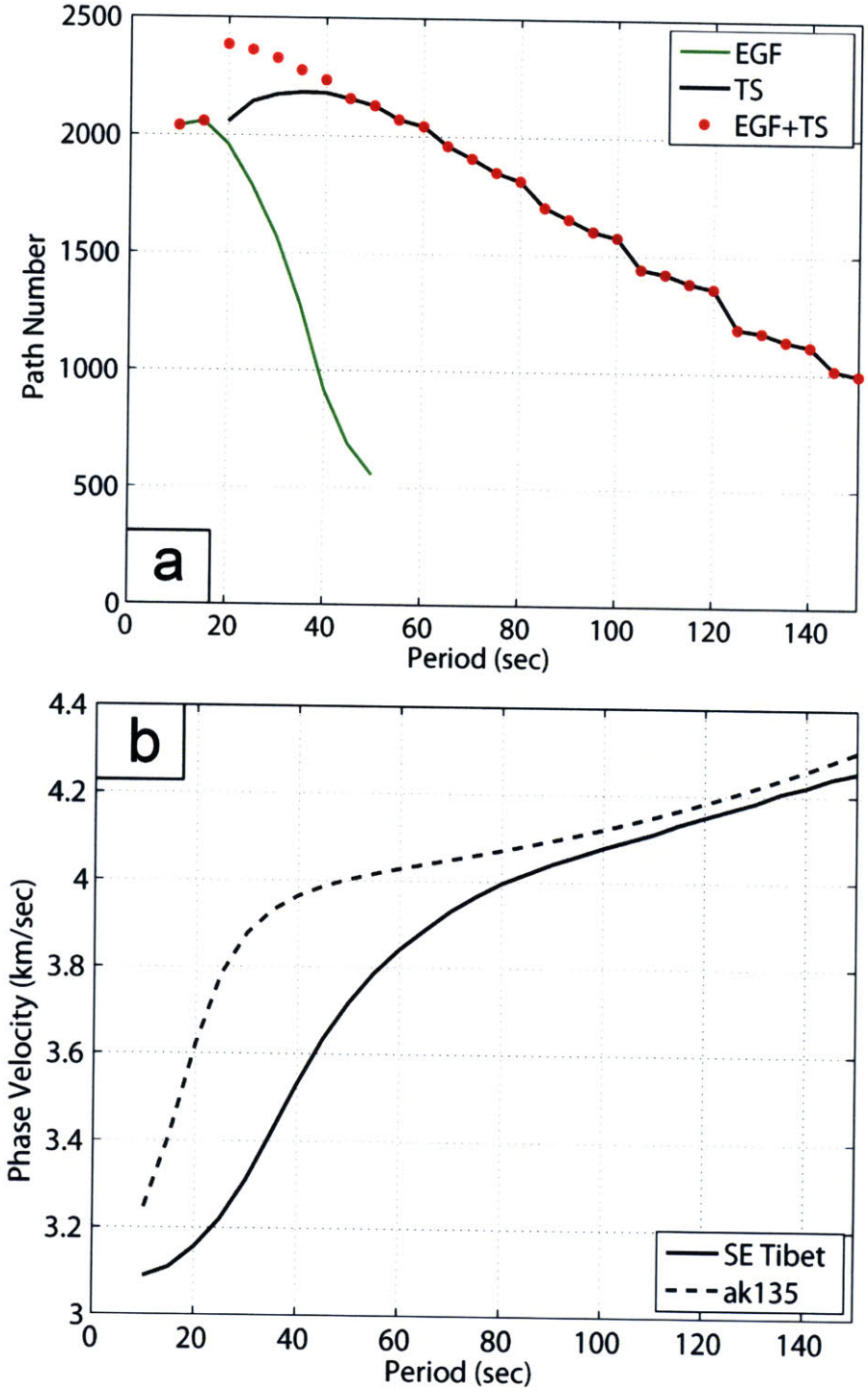

Figure 6-3. (a) Comparison of the number of inter-station phase velocity measurements from EGFs using ambient noise interferometry, TS analysis, and combination of EGF and TS analyses. (b) Average Rayleigh wave phase velocity dispersion curve of SE Tibet (black line) and that of the *ak135* global 1-D reference model (dashed line).

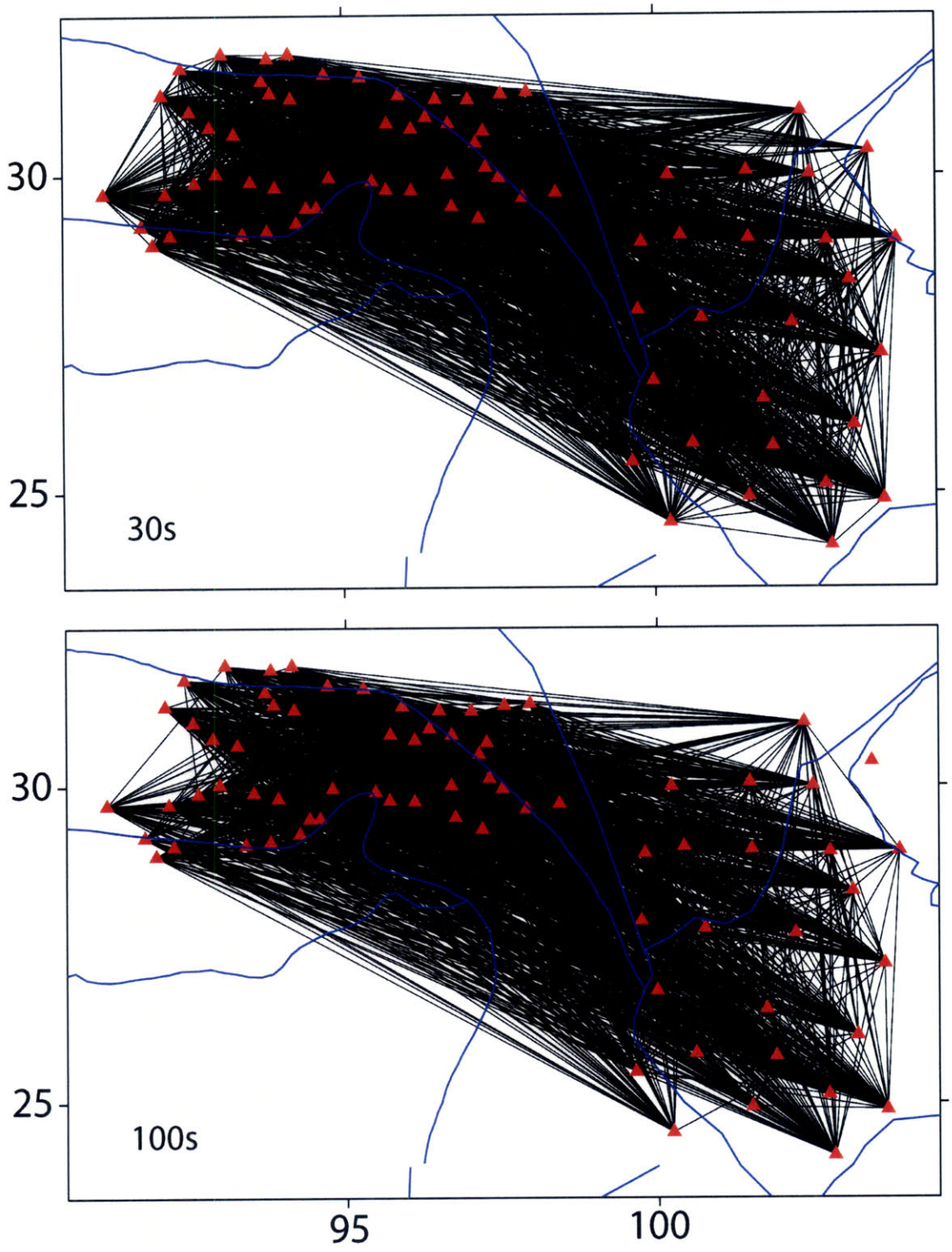

Figure 6-4. Ray path coverage at 30 s and 100 s. The number of ray paths at 30 s and 100 s is 2300 and 1500, respectively.

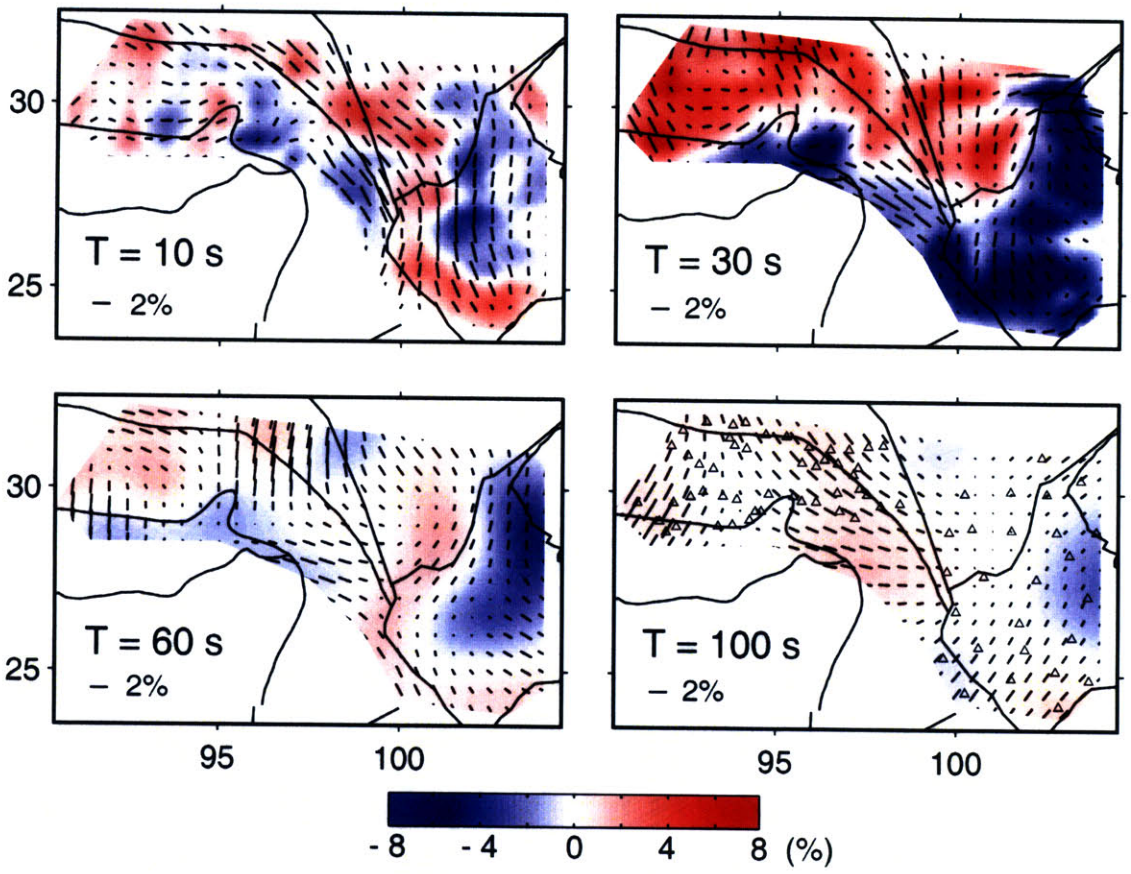

Figure 6-5. Variation of isotropic phase velocities and azimuthal anisotropy at 10, 30, 60, and 100 s. Colorbar shows the value of phase velocity perturbation in per cent with respect to the average value in Figure 6-3b. The black bars show the magnitude (in per cent) and fast polarization direction of azimuthal anisotropy. Open triangles show the location of stations.

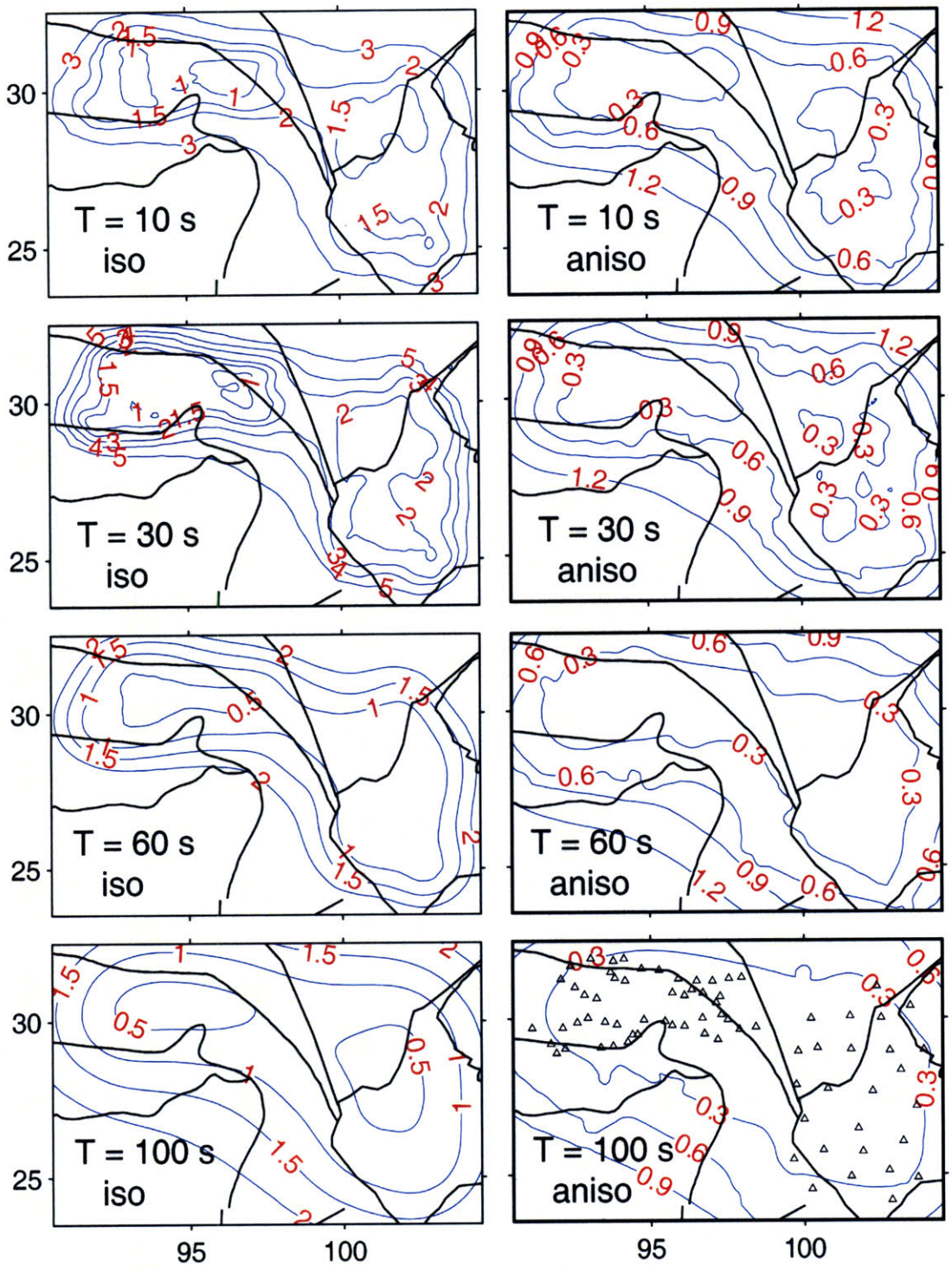

Figure 6-6. Posterior errors (in per cent) of isotropic phase velocities (left column) and the magnitude of azimuthal anisotropy (right column) at 10, 30, 60, and 100 s. The corresponding phase velocity and azimuthal anisotropy variations are shown in Figure 6-4.

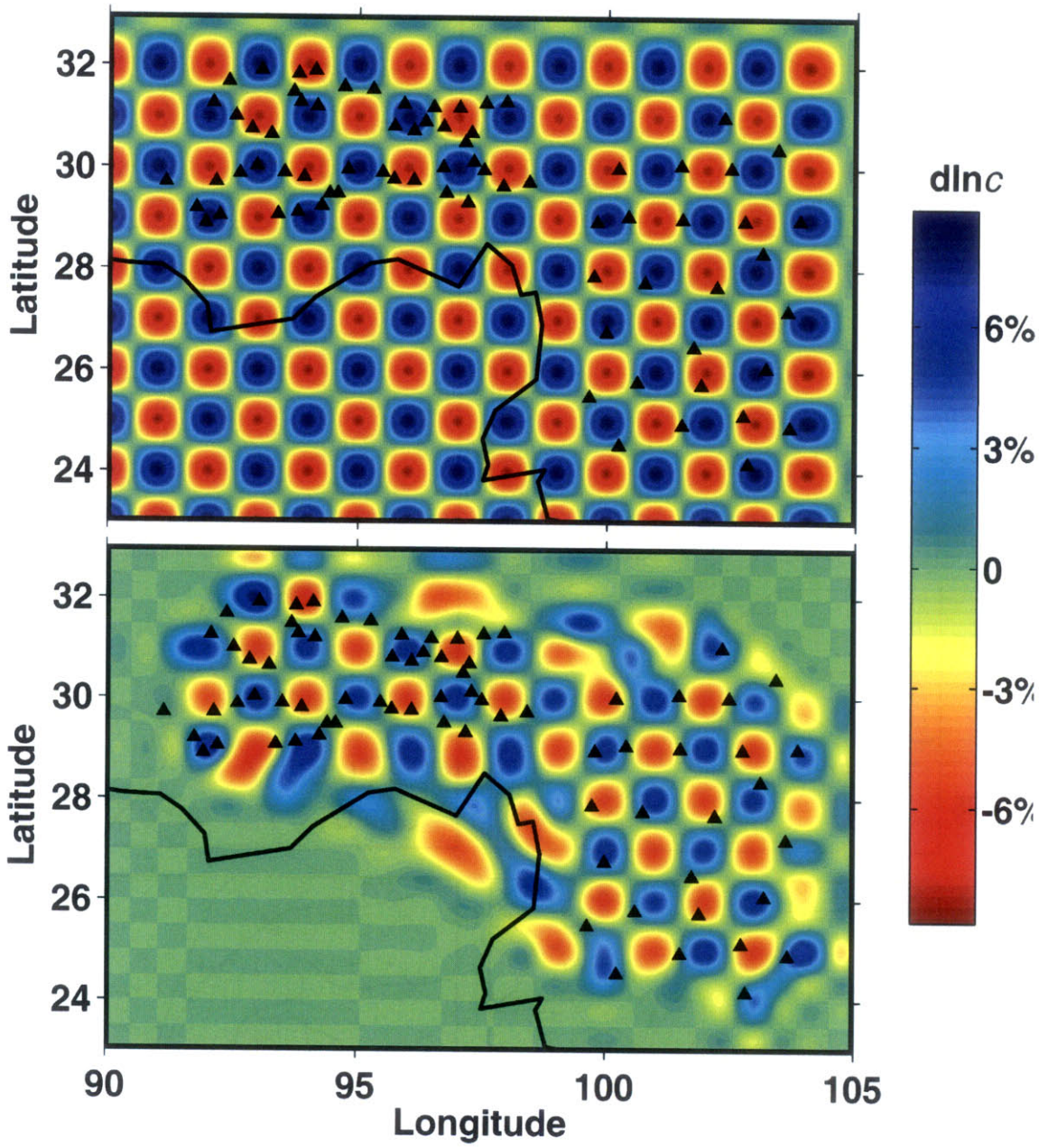

Figure 6-7. 1°×1° checkerboard test for the ray path coverage at T = 30 s for the inversion of isotropic phase velocity map. The top one shows the input phase velocity variation and the bottom one showing the output.

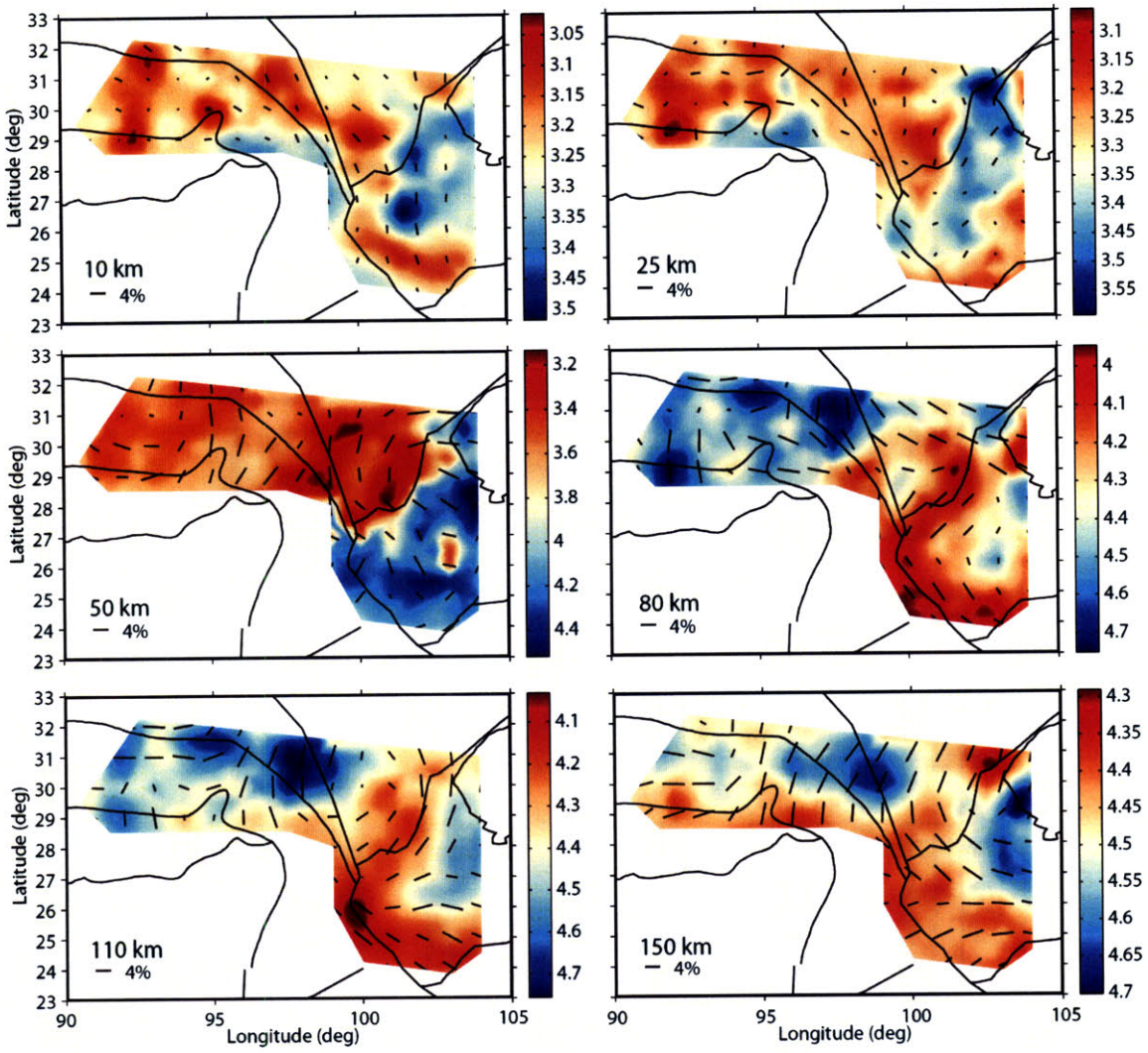

Figure 6-8. Variation of isotropic shear velocity structure (color image) and its azimuthal anisotropy (short black bars) in the crust and upper mantle beneath SE Tibet. The color bars show the absolute shear wave velocities (km/s). The tectonic boundaries are shown as the black lines.

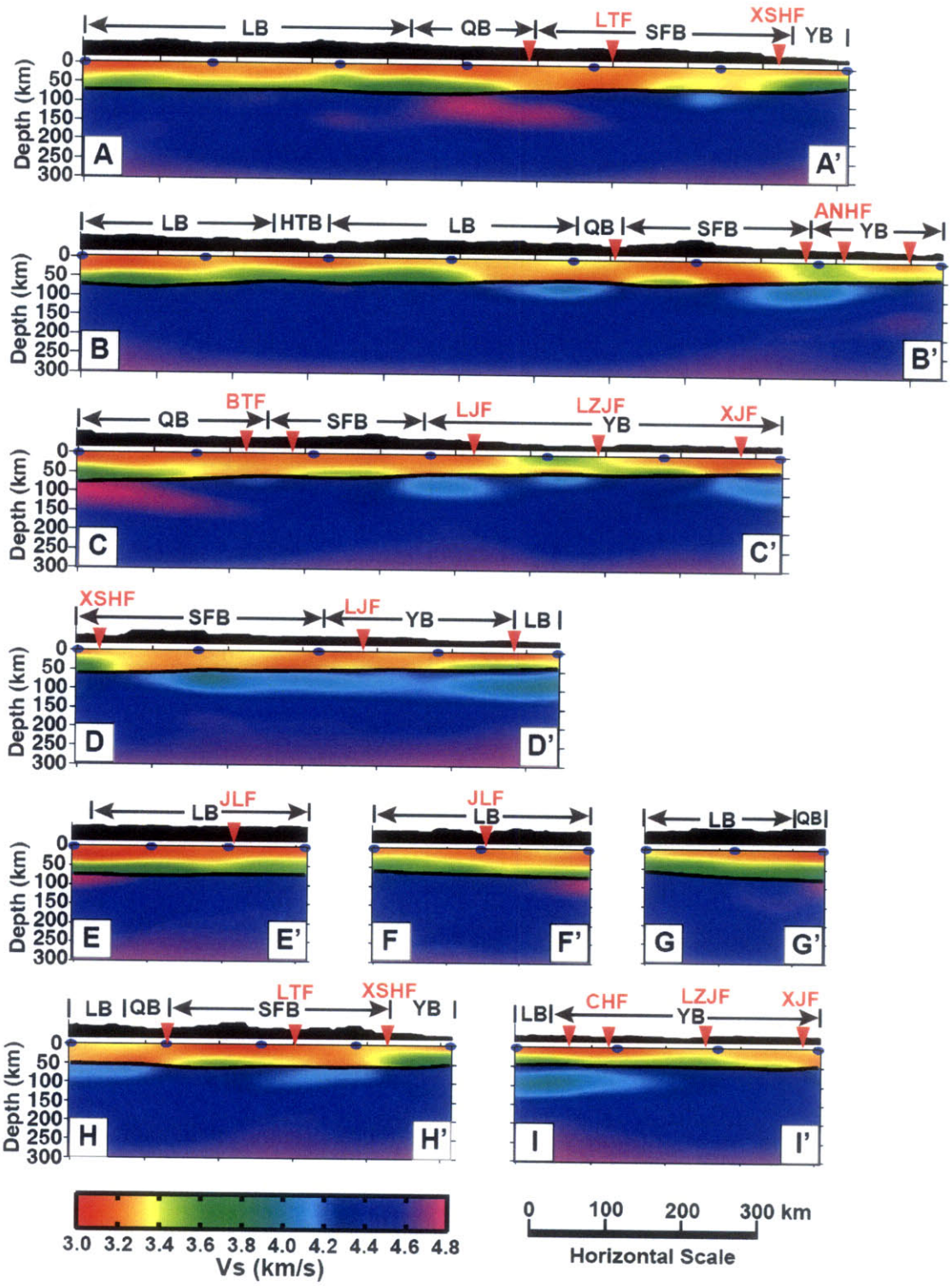

Figure 6-9. Absolute isotropic shear wavespeeds across the nine profiles shown in Figure 6-1b (blue lines). Topography is depicted above each profile as the black area and the red triangles above it mark the location of major faults along each profile. The abbreviations

for fault names (red) are the same as in Figure 6-1. The tectonic unit boundaries are shown as the black vertical lines on each topographic area. The abbreviations for the tectonic unit are: LB – Lhasa Block, QB – Qiangtang Block, SFB – Songpan-Ganze Fold Belt, YB – Yangtze Block, and HTB – Himalayan Thrust Belt. The thick black line (around 50 km depth) on each color profile indicates the Moho discontinuity. The wavespeed (km/s) color scale and the horizontal length scale of profiles are shown as the colorbar and scale ruler at the bottom of this figure, respectively.

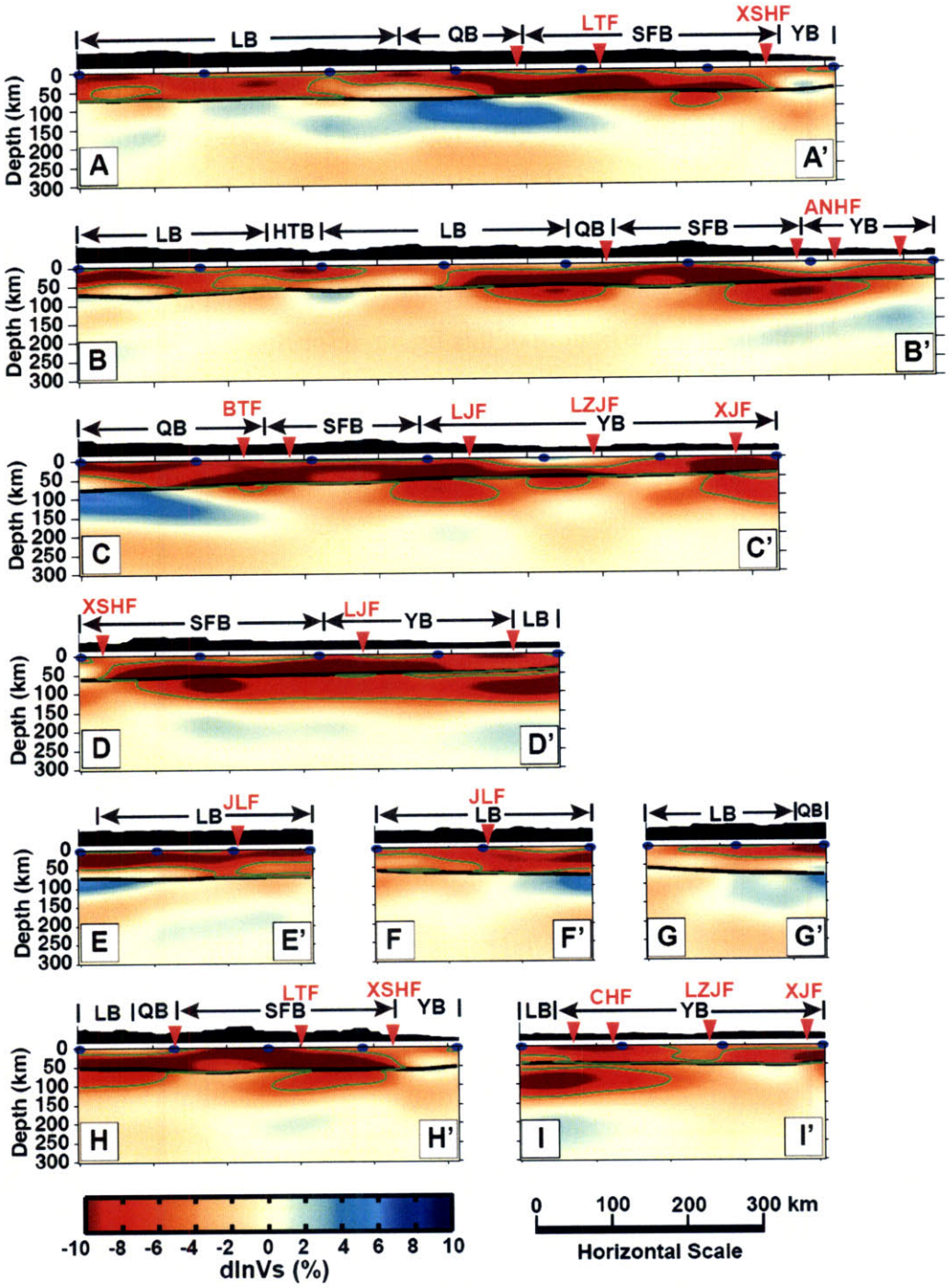

Figure 6-10. Same as Figure 6-9 but for the perturbation of shear wavespeeds with respect to the reference model. The reference Vs in the crust linearly increases from 3.4 km/s at the surface to 3.85 km/s at Moho depth, which is inferred from the Crust 2.0 model (http://mahi.ucsd.edu/Gabi/rem.html). The reference Vs in the upper mantle is from the global *ak135* model (Kennet et al., 1995). The Green lines enclose the region with Vs less than 6% of the reference value.

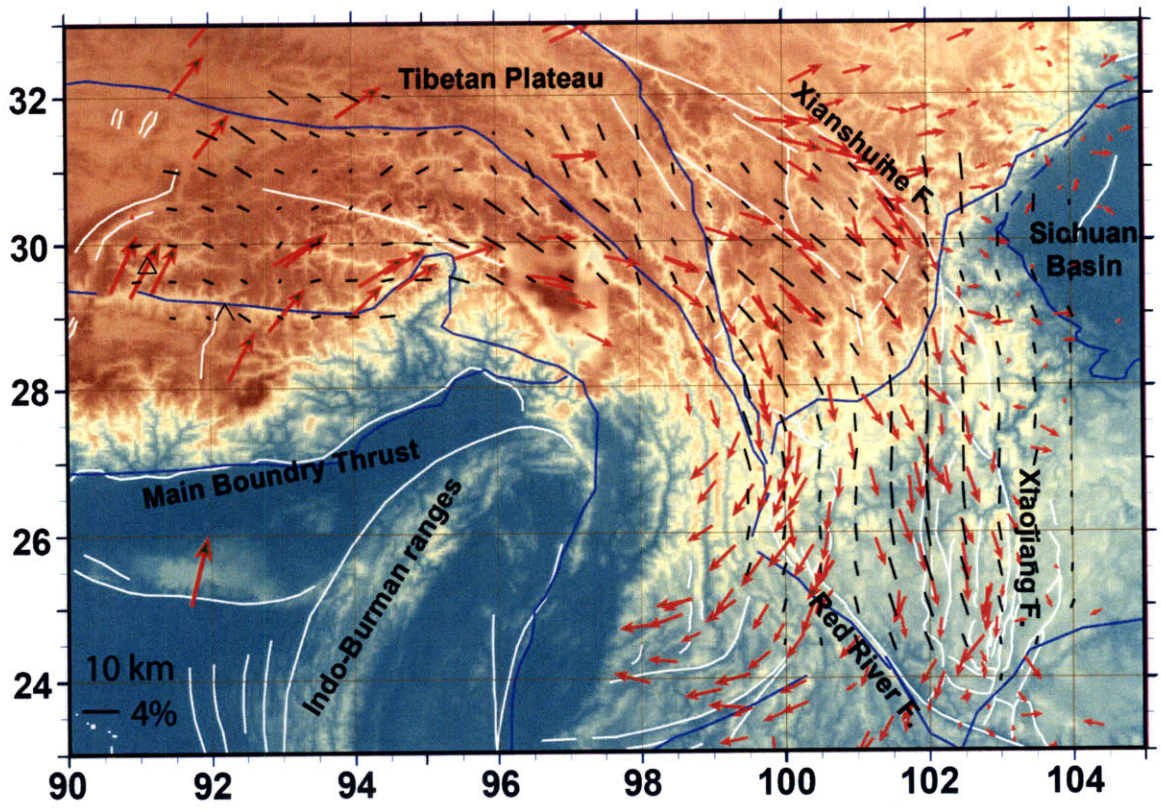

Figure 6-11. Comparison of shear wave azimuthal anisotropy at 10 km (black bars) and the GPS velocity fields (red arrows). The GPS data are from Chen et al. (2000), Zhang et al. (2004), and Sol et al. (2007). The white lines show the faults and the blue lines are the block boundaries.

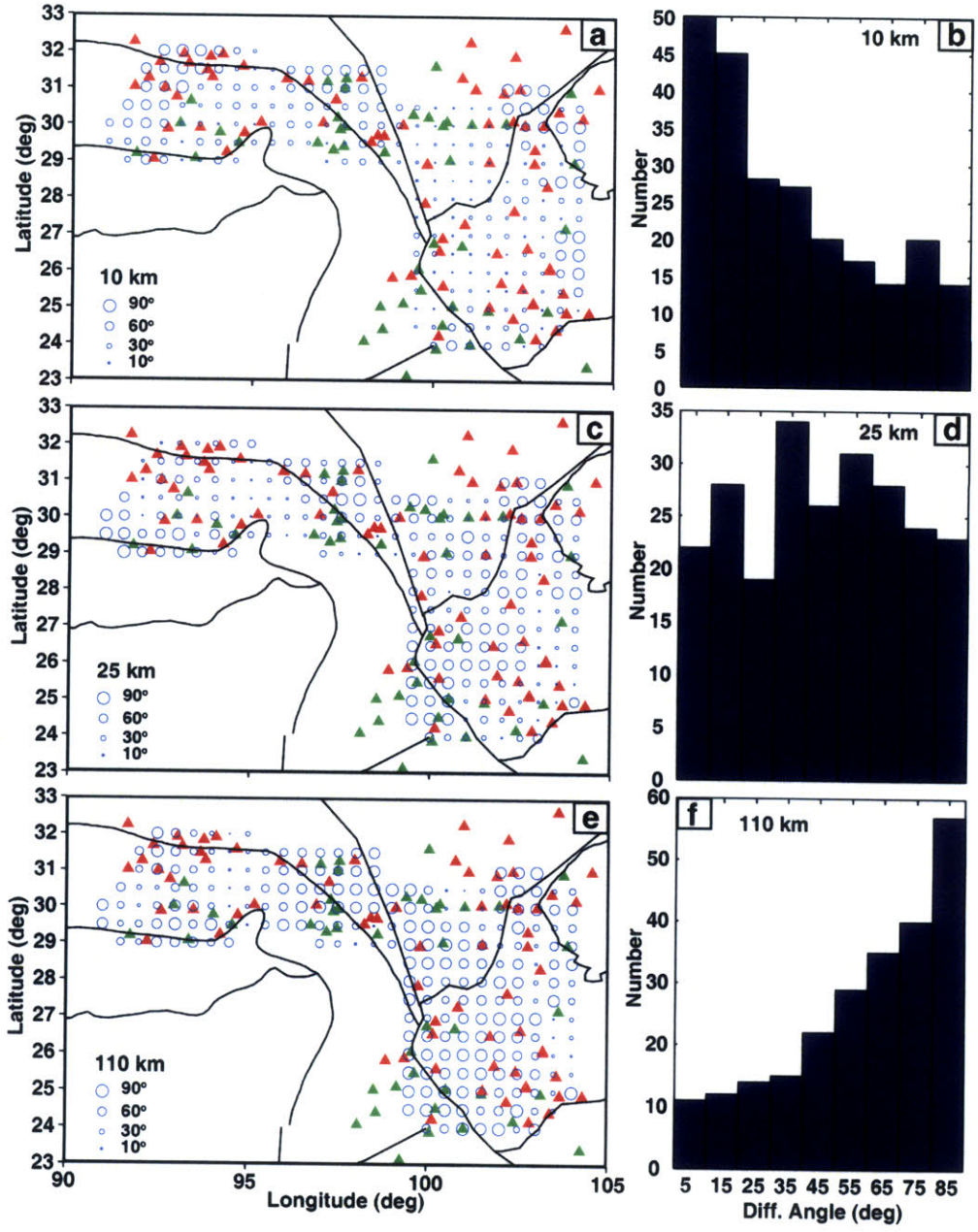

Figure 6-12. Comparison of angle difference between the fast axes of shear wave azimuthal anisotropy at 10, 25, and 100 km and GPS velocity vector in Figure 6-11. The three figures in the left column show the spatial distribution of the angle difference using open circles and the figures in the right column show the histogram of this angle difference. The red and green triangles represent the region with surface currently dominated by simple shear or pure shear, respectively, which is derived from the GPS velocity field (from Wang et al., 2008).

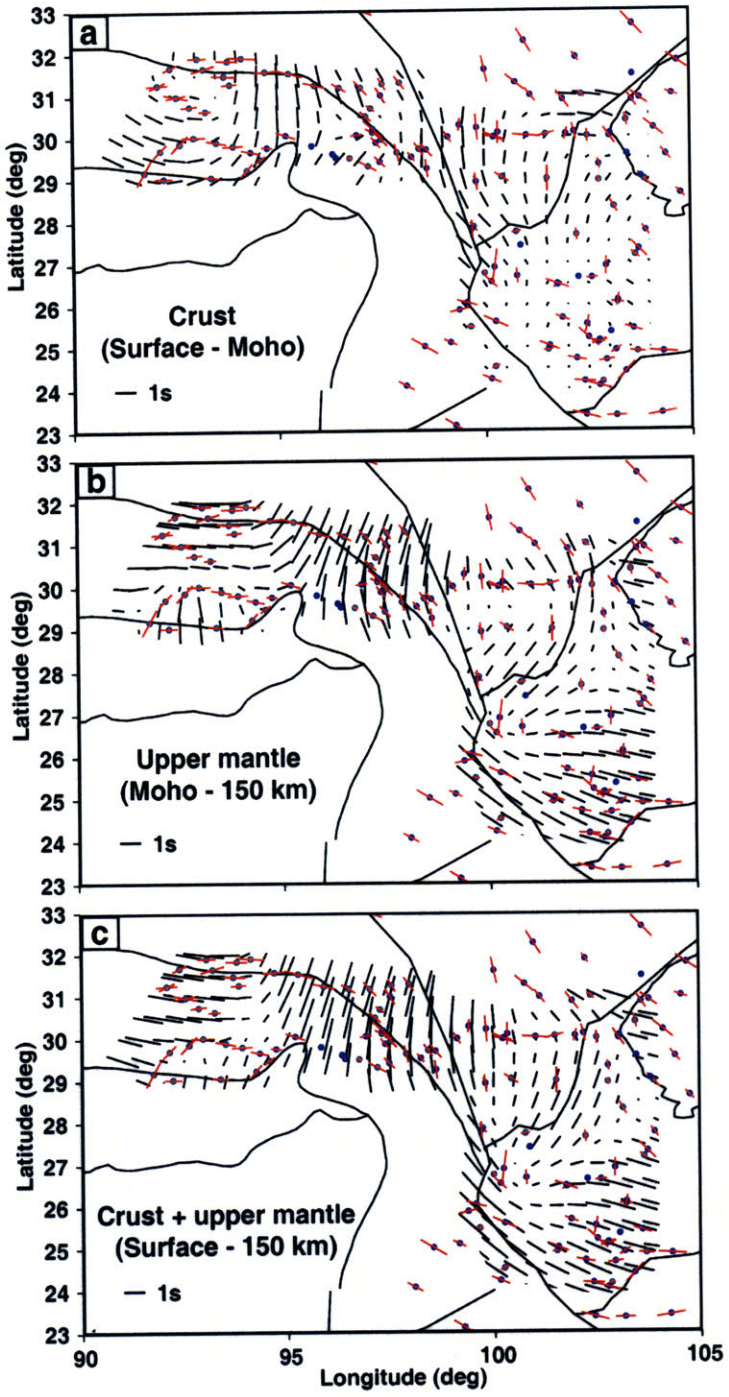

Figure 6-13. Comparison of the observed shear wave splitting measurements (red bars, from Lev et al.(2006), Sol et al.(2007), and Wang et al.(2008)) with the predicted shear wave splitting time and fast direction (black bars) in the crust (from surface to Moho depth, upper panel), upper mantle (from Moho to 150 km depth, middle panel), and crust and upper mantle (from surface to 150 km depth, low panel) using the obtained 3-D azimuthally anisotropic model in this study (Figure 6-8). Dots are the stations.

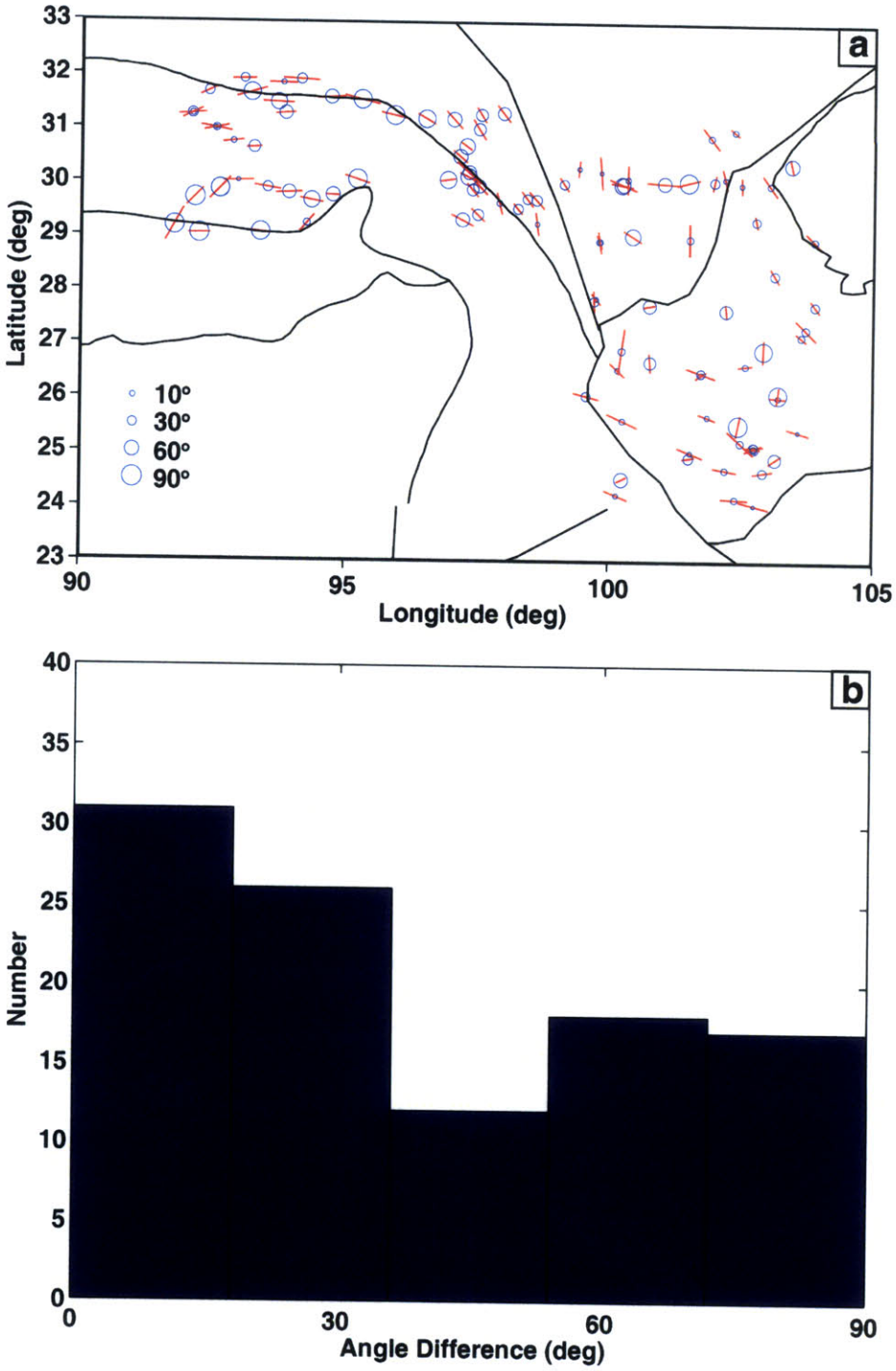

Figure 6-14. (a) The spatial distribution of the angle difference (in degree, shown as the open circles) between the fast axis of predicted shear wave splitting in the crust and upper mantle (lower panel in Figure 6-13) and that of the observed shear wave splitting (shown as red bars) with splitting time larger than 0.4 s. (b) Histogram of the angle differences of fast splitting axes in (a), with the vertical axis the number of observations for comparison.

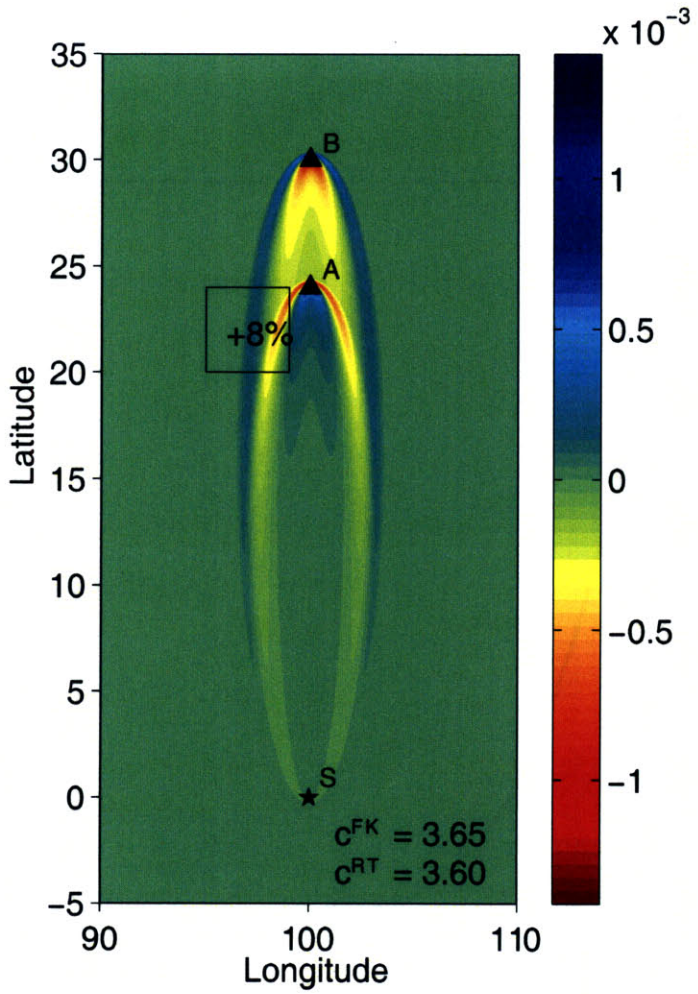

Figure A1. Surface wave finite sensitivity differential kernel $K_{\phi}^{c}(\omega,\mathbf{r};\mathbf{r}_{S})_{AB}$ (equation A-3) at 30 s for two-station phase velocity analysis. The source is at S (star) and the two stations are at A and B (triangles). The background phase velocity is 3.6 km/s with anomaly (+8%) in the box near A. The calculation of the kernel is based on the method by Zhou et al. (2004) without considering the effect of source mechanism. The phase velocity between A and B based on ray theory (c^{RT}) is 3.6 km/s. The inter-station phase velocity based on finite frequency theory (c^{FK}), e.g., from two-station cross-correlation analysis, is 3.65 km/s, which is about 1.5% larger than the ray based measurement, due to the effect of fast structure in the box but not on the ray path between A and B.

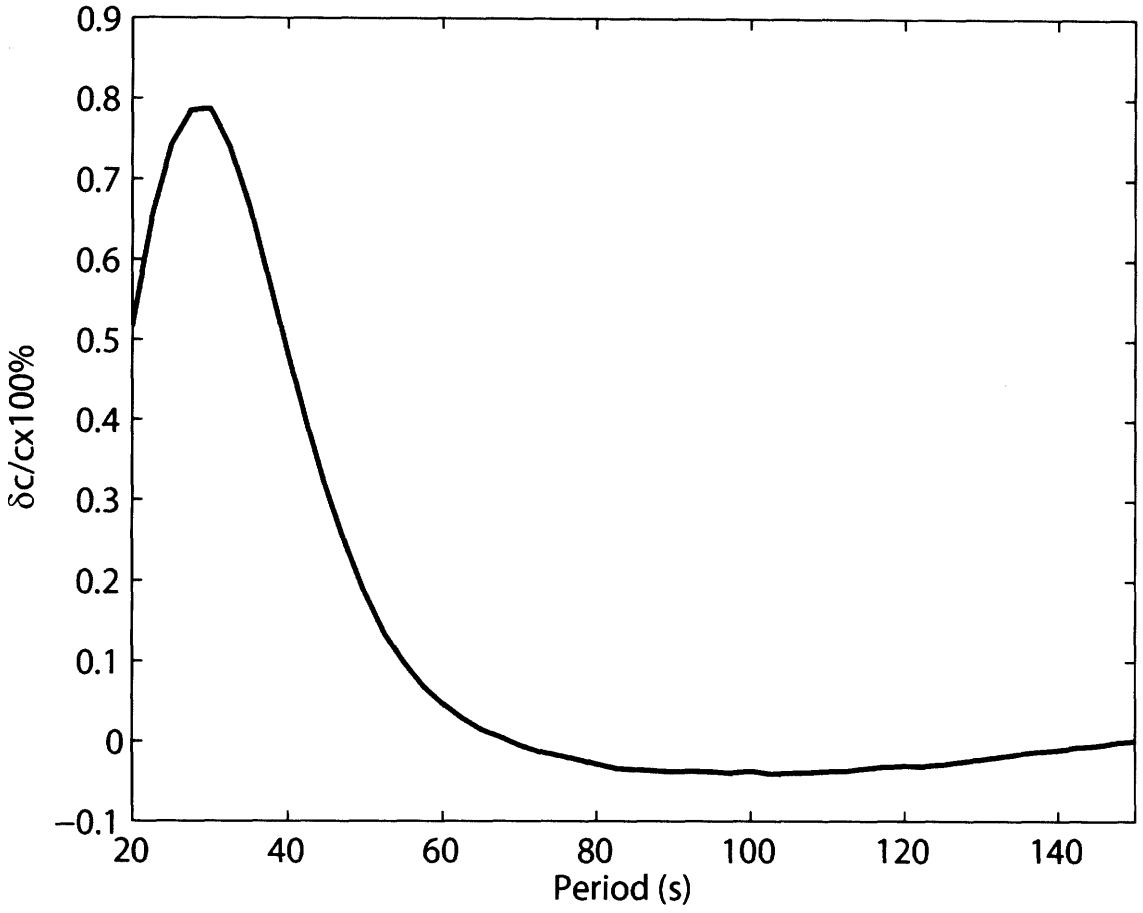

Figure A2. Difference between the original average inter-station phase velocity measurements from TS analysis in SE Tibet and those after suppressing the finite frequency effect using equation (A-6). The average phase velocities between 20 s and 40 s is about 0.5 – 0.8% larger before suppressing the finite frequency effect due to the fast structure (thinner crust) to the east and south of the array.